AN INVESTIGATION INTO THE EFFECT OF STRESS ON THE FORMATION AND STABILITY OF CARBON S-PHASE ON AUSTENITIC STAINLESS STEEL

By **Wei Li**

A thesis submitted to the
University of Birmingham
for the degree of

DOCTOR OF PHILOSOPHY

School of Metallurgy and Materials
College of Engineering and Physical Sciences
The University of Birmingham
September 2011

Synopsis

Due to its excellent corrosion resistance, adequate mechanical properties and good fabricability, AISI 316 austenitic stainless steel is used in a wide range of applications. However, it is well known that austenitic stainless steels are characterised by poor tribological properties because of their low hardness and strong tendency to adhesion.

S-phase can be created in austenitic stainless steels by low-temperature thermochemical treatments, which can greatly enhance their hardness, wear resistance and fatigue properties because of the supersaturation by interstitials. Without the precipitation of carbides or nitrides, the good corrosion resistance of austenitic stainless steel can be maintained, which is, in some cases, even better than untreated material.

One of the technological challenges associated with S-phase surface engineering is that the maximum layer thickness of the S-phase layers is much thinner than that formed during the nitriding and carburising of other steels. The thickness of S-phase is restricted by its metastability and precipitation of carbides or nitrides will occur as a result of prolonged treatment.

In this project, the effect of *in situ* tensile stress on the formation of S-phase on 316L austenitic stainless steel was investigated and it was demonstrated that the tensile stress thickened the S-phase layer by promoting the carbon diffusion in austenitic substrate. However, carbides including metastable CrC and $Cr_{23}C_6$ also precipitated from the S-phase

when applied tensile stress exceeded 40MPa. The decomposition of S-phase was studied through TEM observation and thermodynamic calculation.

The thermo-mechanical stability of carbon S-phase was studied by creeping (tensile stress) and HIPping (compressive stress) tests. The results show that at elevated temperature, the compressive stress applied on carbon S-phase by HIPping was proved to retard the decomposition of S-phase by impeding the carbon diffusion; on the other hand, tensile stress applied on carbon S-phase by creep equipment also verified the favourable effect on interstitial carbon diffusion, promoting decomposition of S-phase.

The residual compressive and shear stresses in carbon S-phase was measured by X-ray diffraction $\sin^2\psi$ method to be 2.2 GPa and 132 MPa, respectively. The wear behaviour of carbon S-phase was studied by dry and oil lubricated reciprocating wear. A very thin surface layer of S-phase case was transformed to martensite during unlubricated reciprocating sliding wear. In contrast, carbon S-phase is stable under lubricated sliding wear conditions up to a very high load, which is desirable for high load wear application.

Acknowledgement

In first place, I would like to express my sincere gratitude to Prof. H. Dong for giving me the chance to carry out this research and invaluable supervision of the work, for his generous mentoring and patience during the previous years.

I am grateful to Dr. Y. L. Chiu and Dr. X. Y. Li for their continuous support and kind help in the work. Thanks are due to all members of the Surface Engineering Group, especially Dr. J. Chen, for his help and encouragement; and people in the school of Metallurgy and Materials Dr. M. Chu, Dr. A. Bloyce, Dr. Y. Li , Dr. M. Attallah and Dr. M. P. Taylor, for their assistance and discussion. Thanks to all my friends.

I also wish to acknowledge the financial sponsors: EPSRC, UK (EP/F006926/1) and EU FP7 (NMP3-SL-2008-213600), the Overseas Research Studentship Award and the studentship from School of Metallurgy and Materials.

Finally, I would like to take this opportunity to express my deepest gratitude to my family for their continued support and inspiration over the years. I wish to dedicate this work to them, especially my daughter, whose birth brings me infinite happiness and confidence.

Publications

(Related to PhD study)

1. Wei Li, Yulong Chiu, Hanshan Dong. 'A preliminary study of thermo-mechanical stability of carbon S-phase formed in austenitic stainless steel', Proceedings of the International Federation for Heat Treatment and Surface Engineering, 2010

2. Wei Li, Xiaoying Li, Hanshan Dong. 'Effect of tensile stress on the formation of S-phase during low-temperature plasma carburizing of 316L foil', *Acta Materialia*, **59** (2011), 5765–5774.

Table of Contents

List of Tables

List of Figures

1 Introduction

1.1 Background

Due to its excellent corrosion resistance, adequate mechanical properties and good fabricability, AISI 316 austenitic stainless steel is used in a wide range of applications, from normal decorative material used in kitchen units and furniture to working pieces in mechanical devices and machines, to critical components in nuclear and space industries. However, it is well known that austenitic stainless steels are characterised by poor tribological properties mainly because of their low hardness and strong tendency to adhesion [1]. Accordingly, austenitic stainless steels are normally limited to non-tribological applications.

Thermochemical surface engineering (such as carburising and nitriding) has long been used to improve the hardness and tribological properties of many types of metallic materials. However, conventional thermochemical treatments are not suitable for austenitic stainless steel because the increased hardness and wear resistance is achieved at the price of reduced corrosion resistance due to the precipitation of chromium carbides or nitrides and depletion of chromium in solid solution. This technical challenge was not addressed until the mid-1980s when interstitially supersaturated austenite, so-called S-phase was created in austenitic stainless steel by low-temperature thermochemical treatments [2].

The formation of S-phase on the outer surface can greatly enhance the mechanical properties of austenitic stainless steels such as hardness, wear resistance and fatigue

properties arising from the supersaturation by interstitial alloying elements [3]. Without the precipitation of carbides or nitrides, the good corrosion resistance of austenitic stainless steel can be maintained, which is, in some cases, even better than untreated material [4].

One of the technological challenges associated with S-phase surface engineering is that the maximum S-phase layer is much thinner than that formed during the nitriding and carburising of other steels. This is because S-phase is thermodynamically metastable and precipitation of carbides or nitrides will occur as a result of prolonged treatment [5]. Therefore, it is scientifically interesting and technologically important to study the effect of applied stress on the formation of S-phase.

Another technological challenge for the long-term application is the stability of S-phase under different stress (tensile and compressive stresses) conditions at elevated temperatures as well as under wear conditions. Investigation into the stability of S-phase can advance the scientific understanding of diffusion of interstitials and metastability of S-phase. Moreover, the study of on the stability of the S-phase has real value in some engineering applications. For example, S-phase surface engineered austenitic stainless steel tubes have been used in nuclear reactors under actions of elevated temperature, mechanical loading and corrosive environments [6].

However, the effect of stress on the formation of S-phase and the effect of stress and temperature on the stability of S-phase are almost absent from literature. These effects

may be crucial for critical components like those described above since the decomposition of S-phase and the formation of chromium carbides or nitrides will dramatically reduce their corrosion resistance, which could lead to serious safety problems.

1.2 Aims of this project

Therefore, the present project was directed at investigating the effect of stress on the formation of S-phase during low temperature plasma carburising, the stability of carburised S-phase under different stress (tensile and compressive stresses) conditions at elevated temperatures and under conditions of wear . The scientific and technological objectives of the present project were as follows:

- To investigate the effect of *in situ* applied stress on the formation and decomposition of S-phase, thus exploring the possibility of increasing the S-phase layer thickness by applying tensile stress during treatment.

- To study the stability and decomposition of carburised S-phase and diffusion of interstitial carbon atoms under isostatic compressive stress and tensile stress at elevated temperatures.

- To study the wear behaviour and phase transformation of carburised S-phase during dry and oil lubricated reciprocating wear under various loads.

2 Literature Review

2.1 Stainless Steels and Austenitic Stainless Steel

2.1.1 Stainless Steel

2.1.1.1 Introduction

Among all the common materials used in our life, stainless steels are without doubt one class of the most important metal alloys. Their advantages over some other materials, and certainly many steels, are clear from the name 'stainless' and are manifested in a plenitude applications, from normal decorative materials used in the kitchen and furniture to working pieces in mechanical devices and machines, and even in components found in more demanding applications like nuclear plants and space vehicles. The annual consumption of stainless steel has increased at a compound growth rate of 5% from 1986 to 2006, surpassing the growth rate of other materials [7].

The corrosion resistance of iron-chromium alloys, was recognised quite earlier in 1821 by Berthier [8],to resist against the attack from some acids. However, at that time, it was impossible to produce the alloys with low carbon and high chromium. So the high-chromium alloys were too brittle to be used as engineering materials. It was at the early time of 20^{th} century that the commercial potential of such alloys became practical [8]. With the great effort of these researchers (e.g. Strauss, Guillet ,Maurer, Monnartz and Brearley *et al.*) [8], the development of stainless steels began to be driven by actual applications. Among them, Brearley was referred as the inventor of a ferritic Fe - 13% Cr alloy and the first one to announce the discovery of 'non-rusting steel' and applied it to

commercial usage as table cutlery in 1915 [9]. In parallel, Haynes was granted a U.S. patent on a martensitic stainless steel [10] while Strauss and Maurer patented austenitic stainless steel in Europe [11].

Defined as steel, and Fe-C alloy, the 'stainless' property is attributed to the addition of Chromium (Cr) into steels through an alloying process. To make stainless steels resistant to staining, rusting or corroding, the addition of Cr to the amount of at least about 10wt% [12] is necessary. It is now generally believed that the good corrosion resistance could be contributed to the thin protective film of oxide forming on the surface of stainless steel. This so called "passive film" forms spontaneously on the steel surface when it is exposed to air or to some other gas or liquid which can supply oxygen to the steel [13]. The film is transparent because of its thickness (about several nm) and composed mainly of amorphous chromium oxides [14]. However, it is tightly adherent to the steel and insoluble in many liquids and also impermeable to many gases. When it remains intact and tightly adherent to the steel surface, the steel is protected from corrosive attack. Even if the oxide film is broken locally and the metal is exposed to the corrosive environment, serious corrosion still can be evaded because this passive film is self-repairing and protect the steel again quickly.

However, to protect the steel against pitting or corrosion in more harsh environments (like warm seawater or chemical fluid), more alloying elements (e.g. higher chromium, nickel, molybdenum) are needed, contributing to the sophisticated research on and diverse applications for stainless steel.

There is no doubt that corrosion resistance is the most distinctive property of stainless steel. However, when used in various engineering applications, many other factors should be considered, such as strength, hardness, weldability, creep resistance, toughness etc. There are three main types of microstructures in stainless steels, ferrite, austenite and martensite and they are dictated through the alloy chemical composition. It is well known that microstructural constitution is the major influence on the different properties of materials. Therefore the desired properties of stainless steel for different applications may be controlled through the alloying process.

2.1.1.2 Classification of Stainless Steels

Stainless steels are usually classified on the basis of microstructure. It is widely accepted that they are categorised into these following classes: austenitic stainless steels ; ferritic stainless steels; martensitic stainless steels; duplex stainless steels; precipitation hardening stainless steels; Mn-N substituted austenitic stainless steels [1]. In subsequent sections, each class will be briefly discussed in terms of constitution, alloy compositttion and properties.

When pure iron is heated up to 912˚C, the BCC structural ferrite (α-iron) will change to FCC structure called γ-iron or austenite. Further heating over 1394˚C will transform the austenite back to ferrite again; and it is called δ-iron to distinguish from that ferrite of lower temperatures. The reverse transformations take place on cooling at the same temperature as on heating.

With the alloying addition of carbon, the phase transformation becomes more complex. As shown in Figure 2-1 the Fe-C diagrams [15], there is a stable phase in Fe-C alloys with the chemical formula Fe_3C, named cementite. The carbon is almost insoluble in ferrite while austenite is able to dissolve an appreciable amount of carbon. The homogeneous solution of carbon in austenitic iron is stable over a wider range of temperature than pure γ-iron. When it is cooled rapidly, the austenite remains intact until even lower temperatures are reached. With rapid quenching, the carbon dissolved in austenite has no time to diffuse, precipitate and grow separate carbides and remains in solution when a shear, rather than diffusion, transformation takes place to form a BCT structure called 'martensite'.

In stainless steels, with more alloying elements added, the stability of these phases is dictated by all of the alloying elements. The presence of the two major phases in stainless steel austenite and ferrite is dictated by the alloying elements which could be separated in two main groups: γ forming and α forming elements. Two main constituents of stainless steels, chromium and nickel are representative due to their effects on enclosing and expanding the austenitic loop in the phase diagrams. Therefore it is customary to express the contribution of all the elements in stainless steel as 'chromium equivalent' and 'nickel equivalent' [13].

The values of 'chromium equilibrium' and 'nickel equilibrium' are from the accumulated data from hundreds of experiments over many years. However, these equivalents are complicated applying to different alloying compositions considering the mutual effects on

each other. One simple case from 18Cr-8Ni type alloys [16] gave the equation as follows:

$$w(Cr') = w(Cr) + 1.5w(Si) + w(Mo) \quad (2.1)$$

$$w(Ni') = w(Ni) + 30w(C + N) + 0.5w(Mn) + 0.64w(Co) \quad (2.2)$$

Here, w(X) means weight percent of alloying elements X in steel.

And through Figure 2-2, is could be known the composition of δ ferrite and austenite in the steels after cooling.

2.1.1.3 Austenitic Stainless Steel

Austenitic stainless steel (ASS) is undoubtedly the most widely used one among all the stainless steels [17]. The most common composition of these steels is based around 18Cr-8Ni. Although there are more highly alloyed Cr-Ni ASS grades such as Cr20Ni10 and Cr18Ni20Mo2Cu2Nb, it is economic to use the 18Cr-8Ni type most commonly because it is the minimised nickel and chromium composition for the steel to keep a fully austenite microstructure to room temperature. ASS has very good toughness especially at low temperature and shows no ductile-brittle transition temperature. At elevated temperatures above 600°C, its strength is also superior to other types of stainless steels. It is non-magnetic and suitable for stretch forming due to the fully austenitic structure. All these special properties make ASS the first choice in the corrosive conditions. Nevertheless, its low resistance to stress corrosion cracking, low ultimate stress and low hardness lead to some limitations in applications.

The choice of alloying elements and their quantity are dictated by the industrial demand. For instances, the carbon content of these alloys is usually very low to avoid precipitation of $Cr_{23}C_6$ at grain boundaries, which significantly reduces their corrosion resistance. Additions of Mo and other alloying elements further increase its outstanding resistance to general and pitting corrosion. Ti and Nb can be added to produce the ASS grades which reduce the tendency of grain boundary corrosion. And some other minor elements like W, Ti, V, S and RE elements have specific effects on the mechanical properties of austenitic stainless steel. The most commonly used commercial grade of ASS and their compositions are listed in Table 2-1 [12]. However, austenitic stainless steels are not always uniform in the applications or processing conditions. For example, martensitic phase transformation may occur during deformation in 18Cr-8Ni ASS.

In general, different compositions and processing conditions have a profound influence on the type of second phases in ASS. The most significant second phases will be described in latter sections (e.g. martensite α', carbides and intermetallic phases (σ, χ and Laves phases). A detailed and comprehensive description of the secondary phases observed in ASS is out of the scope of this review and only those most significant to the material under study (i.e. AISI 316) will be discussed in latter sections.

2.1.1.4 Ferritic Stainless Steel

These alloys, as indicated by their name, keep the ferritic structure up to the melting point. The ferritic stainless steels normally contain 17% to 26% Cr with little addition of nickel [18]. Only a small fraction of austenite forms at high temperature depending on the

amount of other alloying elements, mainly C and N. The advantages of ferritic stainless steel over austenitic stainless steel appear in two main sections. On the one side, the ferritic structure is stronger than the austenitic; on the other side, the production cost is reduced significantly due to the absence of Ni in their composition as compared to the austenitic counterparts. However, they are weaker in many factors such as corrosion resistance, formability and toughness.

The occurrence of Fe-Cr σ phase, Fe-Cr-Mo χ phase and Cr rich α' phase is of importance in ferritic stainless steel because embrittlement is attributed to their presence [19]. In alloys with high content of austenite forming elements, it is necessary to avoid embrittlemet caused by martensitic transformation of the retained austenite present at grain boundaries. Furthermore, the carbides ($M_{23}C_6$, M_7C_3) and nitrides (M_2N), together with some intermetallic compounds in alloys containing Ni, Co, Mo ,Ti, Al could reduce the toughness [1]. All these embrittlement effects explain the arising of ductile to brittle transition which is typical in ferritic stainless steels.

Ferritic stainless steels have higher yield strength and ultimate strength than the austenitic stainless steels. They have low work hardening rate which reduce the flow stresses upon forming. On hot rolling, ferritic stainless steels are soft and easy to shape. The corrosion resistance of ferritic stainless steels is adequate in mild corrosive environments. Although in the most severe environments they serve not as well as austenitic stainless steels, their higher resistance to stress corrosion cracking is significant for their applications in chemical plants.

With the constant increasing price of nickel, ferritic stainless steels are increasingly developed in improving their weldability and toughness to substitute austenitic stainless steels in some less demanding situations.

2.1.1.5 Martensitic Stainless Steel

The concept of martensitic transformation was explained briefly prior to the introduction of martensitic stainless steel. As mentioned above, martensite is a metastable phase occurring when steels are quenched from austenite. Generally, there are three temperature marks to characterise the martensite transformation: M_s, M_f and M_d. The first two values are corresponding to the starting temperature and finishing temperature of the martensite transformation while M_d represents the highest temperature of martensite transformation caused by deformation. The experienced equation of Ms in 18Cr-8Ni type stainless steel could be written as[20, 21]:

$$M_s(℃) = 1305 - 41.7w(Cr) - 61.1w(Ni) - 1667w(C+N) - 33.3w(Mn) - 27.8w(Si) \quad (2.3)$$

And the alloying elements should be within the range of following:

Cr 10%-18% Ni 6%-12% C 0.004%-0.12% Si 0.3-2.6% Mn 0.6-5% N 0.01%-0.06%

The highest M_s from equation 2.3 is about 470 °C taking the lowest alloying compositions.

It is deduced from this equation that if martensitic stainless steel are designed, M_s should

be as high as possible and M_f should be above the room temperature. Otherwise there would be austenitic stainless steel retaining in the structure. Meanwhile, the M_d is higher than M_s for about 170°C in 18Cr7Ni stainless steels [22, 23].

The common designs of martensitic stainless steels allow the composition of 12% to 17% Cr and 0.1% to 1.0% C with additions of other alloying elements such as Mo, V, Nb, Al and Cu. The austenitic structure which is stable over 1050°C, undergoes full martensitic transformation on cooling [13]. The martensite structures grant these stainless steels high strength and hardness but low toughness. It is of importance in martensitic stainless steels, as with non-stainless martensitic steels, to temper them at appropriately high temperature to obtain a good combination of mechanical properties including strength, ductility and toughness. Alloying elements are also very crucial in the properties of martensitic stainless steels. The addition of C and N is limited because these elements will reduce the toughness. Mo, W and V are added to increase the temper resistance by secondary hardening reactions, which increase the strength but reduce the toughness and resistance to stress corrosion. Meanwhile, their tendency to retain δ ferrite needs to be balanced by austenite forming elements so that Ni, Co, Mn and Cu have to be used, and this will increase the cost of the alloys. However, the austenite forming elements could initiate some problems in limiting the range of tempering conditions by lowering the A_{C1} temperature, depressing the M_s-M_f temperature range. Therefore some retained austenite at grain boundaries would transform to martensite during tempering, which could cause distortion and embrittlement [13].

The precipitation of intermetallic compounds instead of the carbides and nitrides provides another hardening and strengthening mechanism. And this effect could be achieved by adding the alloying elements such as Ti, Al, Cu and Mo. By changing the tempering temperature, a good combination of strength and ductility according to the industrial demand can be obtained. But it should be with caution to avoid over-aging because some large intermetallic particles (Fe_2Mo) and secondary phases (e.g. Cr rich α' phase and Fe-Cr-Mo χ phase) would form and lead to embrittlement [24].

In general, martensitic stainless steels are superior to ASS in their high strength and hardness at the expense of corrosion resistance. It is rather complicated to adjust the composition and tempering conditions of these stainless steels to keep a balance in strength and toughness. Some applications of martensitic stainless steels have origins in high strength demanding and mild corrosive conditions, such as tools, gears, shafts, valves, bearing and wear resistant parts in chemical and petrochemical industry, hydroelectric power generation and aeronautic applications.

2.1.1.6 Duplex Stainless Steel

Duplex stainless steels are constituted by a ferritic-austenitic or ferritic-martensitic duplex structure with typical composition of 18% to 30% Cr, relatively low Ni and some additions of Mo, Nb and Ti [25]. These steels were designed to keep the positive aspects of austenitic and ferritic alloys with high strength and good ductility. Also the reduction of alloying nickel has advantage in the express of production cost. Moreover, compared to normal austenitic stainless steel, they have even better in resistance to corrosion and

pitting corrosion in many harsh conditions.

The presence of ferrite and the induced reduction in the grain size of austenite increase the strength of duplex stainless steel. Moreover, the austenite transforms into martensite during deformation and increases the strength to levels even higher than the pure ferrite structures. And there is no significant toughness reduction accompanying the increment of strength because of the two-phase structures. By changing the composition of alloying elements and processing conditions, the fraction of the two phases can be changed, thus adjusting the balance of toughness and strength, satisfying the various demands of industrial applications. The secondary phases are also very commonly occurring in duplex stainless steel and they should be carefully monitored to avoid the embrittlement effects. Besides, between the austenitic and ferritic phases, partitioning of alloying elements would also occur which is normal for dual phase structure. It is necessary to use appropriate heat treatments and cooling rates to avoid the embrittlement.

Although duplex stainless steels have the advantages of both ferritic and austenitic stainless steels, they are limited in useful temperature range, normally below 250°C and the welding requirements are more restrict than austenitic stainless steel. Their use is expanding fast due to high corrosion resistance and good mechanical properties and applications include chemical, petrochemical, oil, wood pulp, pharmaceutical, textile and nuclear industries.

2.1.1.7 Precipitation hardening stainless steel

These alloys are based on the combination of martensitic transformation and precipitation hardening. To develop a stainless steel with fully hardened condition to resist corrosion and tempering, there was a requirement for a stainless steel with preliminary austenitic structure to permit good formability, and subsequently undergo martensitic transformation and produce precipitation hardening.

In stainless steel, there are many different types of carbides. Among them, $M_{23}C_6$ is the most extensively studied carbides on grounds of its ubiquitous occurrence in stainless steel. This carbide has a crystal structure of face centred cubic (fcc) lattice. The micro structural characterisation has been carried out under TEM studies in well developed state [26-29]. However, the studies of formation of precipitates on does the reference bracket come before or after the full-stop? the very early stage are quite rare until recent studies fulfilled the gap [30]. It was revealed by DSC and HRTEM that the precipitation of $M_{23}C_6$ was preceded by the formation of unidentified, plate-like precipitates, which measure just a few atomic planes, at dislocations and grain boundaries. Another study using positron annihilation spectroscopy observed the very early stage of the formation of $M_{23}C_6$ [31]. This study revealed that the formation of carbides begins with the association of carbon atoms with vacancy clusters.

The martensitic transformation can be induced by deep cooling to sub-zero temperature or by a primary ageing treatment to precipitate $M_{23}C_6$ and control the amount of C in solution. Thus it is available for the martensitic transformation by increasing M_S. However,

to control the M_s-M_f range accurately is not easy due to the need for even more precise control of alloying composition. Therefore, most of these alloys are manufactured in the fully transformable and precipitation hardened condition.

The applications are very limited due to its relatively hard processing conditions and those alloys have been used in the shell of high speed aircraft, fasteners, spring, measuring instruments, wire and cables.

2.1.1.8 Mn-N substituted austenitic stainless steel

These alloys are recently developed austenitic stainless steels. The basic idea is to substitute Ni with Mn-N to produce low nickel or nickel-free ASS. One of the main problems associated with the Ni in stainless steel is its probability of causing allergy in human bodies [32]. Moreover, Ni and Ni alloys are suspected of being carcinogenic to humans [33]. Because the potential hazards of Ni may bring to humans, a significant amount of research has been devoted to Ni-free/ultra-low-Ni stainless steel and applied it in the medicine [34-41]. The most commonly used austenitising substitutes for Ni are Mn, C and N. These CrMnN steels could contain very high Cr and Mn contents and relatively high Ni. For examples, one of the commercial Ni-free austenitic stainless steel called BioDur 108. It contains 23% Mn, 21% Cr and 0.97%N and is an essentially nickel-free austenitic stainless alloy with high nitrogen content to maintain its austenitic structure. The alloy's tensile and fatigue strength is superior to that of grade 316L. Its pitting and crevice corrosion resistance is superior to grade 316L and equivalent to 22Cr-13Ni-5Mn alloy. However, such a high level of Mn in stainless steel is prone to cryogenic

intergranular fracture [42]. Too much nitrogen is also believed to deteriorate the cryogenic toughness and impact of austenitic stainless steels [43]. To address this problem, some researchers recently found that electrolslag melting and alloying with Cr and Mo could be beneficial[44]. Although many compositions and properties of these alloys have analysed, the development of Mn-N substituted austenitic stainless steel is still at the frontier of new steel research. With deeper understanding of the mutual effects of alloying elements including substitutions and interstitials, more and more new stainless steels will be designed and developed to serve in more severe conditions and satisfy higher demand of industrial applications.

2.1.2 Surface engineering of stainless steel

In many cases, damage or failure occurs at the surface or near the surface in engineering alloy components. Therefore, surface engineering is of great importance and a large amount of research has focused on enhancing the surface properties of stainless steels In order to broaden their successful areas of application.

2.1.2.1 Traditional surface hardening

Carburising is a process for case hardening that has been carried out for many years [13]. By heating the article for an appropriate period in contact with a carburising medium, a surface volume of higher carbon may be formed on the steel surface. Early carburization used a direct application of charcoal to harden steel weapons, a process which could be traced back to ancient China over two thousand years ago [45]. The carburising operation results in the production of a surface layer containing about 1wt.% carbon. Traditional

carburising treatment is immersing the steel in a molten cyanide bath for a suitable time. High surface hardness is obtained but their resistance to corrosion is thereby lowered due to the formation of chromium carbides. These carbides exist as separate particles in the finally hardened article, and chromium in this form has no beneficial effect on corrosion resistance.

With the development of industry, people use gaseous medium as carbon source and make the carburising process more effective and controllable. For instance, W. E. Makin and W.C. Troy [46] found a method for the production of hardened article of 12-14 per cent chromium steel in a specially designed furnace purged with an atmosphere of cracked ammonia. They found, that if they added 1 per cent of methane to this atmosphere of cracked ammonia the steels were carburised to some extent on the surface, and thereby surface hardness values of 700-750 HV were obtained. The degree of carburization depended on the hardening temperature and the length of time the steel was treated. Heating articles of steel containing 0.3 per cent carbon and 14 per cent chromium at 950˚C for an hour in this special atmosphere produced a carburised skin about 0.01 inch (250μm) thick; increasing the time to 2.5 hours doubled this thickness. The use of higher temperatures than 950˚C increased the amount of carbon absorbed but tends to give a softer skin, because the austenite existing at the hardening temperature was partly retained in the cooled sample instead of being transformed completely to martensite. However, traditional carburising is not suitable for all kinds of stainless steels, e.g. no carburising process should be applied to austenitic stainless steels. Although absorbing carbon readily, they are not thereby hardened to any useful extent, and

detrimental effects on properties such as corrosion resistance are likely.

Nitriding can be applied to more forms of stainless steels, and could produce intensely harder surfaces than carburising. Nitriding is carried out in the normal way by treating the steels for up to about 90 hours in an atmosphere of ammonia at 500˚C or 550˚C. Before stainless steels can be successfully and uniformly nitrided, the thin passive oxide skin must be removed, otherwise nitrogen cannot penetrate into the steel. The oxide may be removed by pickling in some solutions containing hydrochloric acid or phosphoric acid or sulphuric acid [13]. After that the article would need to be washed preliminarily in water and directly put into the nitriding vessel. In the case of the austenitic chromium-nickel-tungsten steels, the nitrided layer could be hardened up to 1000 HV but the thickness was shallow. However, it considerably reduces the corrosion resistance of the austenitic stainless steel due to the precipitation of fine particles of chromium nitrides.

Flame hardening is a process of surface hardening which could only applied to hardenable (i.e. martensitic) types of stainless steels. It is carried out in a higher temperature and no cooling of the surface by quenching is needed. The articles to be hardened in this way should first be hardened and tempered so as to produce the required core strength. The surface hardness attained depends on the composition of the steel. And it does not cause any loss in corrosion resistance and the hardened surface is, on the contrary, more resistant than the fully tempered core.

2.1.2.2 Surface modification with modern technologies

Besides traditional surface hardening processes, a multitude of surface modification methods have been developed in recent years.

Surface grain refinement technologies including ultrasonic peening[47], high-energy shot peening [48], ultrasonic shot peening [49, 50], surface mechanical attrition[51-54] and sandblasting [55, 56] have been utilised to improve the surface properties of stainless steel. The nanostructuring surface layer caused by severe plastic deformation due to these procedures is very beneficial in some aspects of application. For example, the fatigue life is prolonged because the surface nanocrystalline structure could impede the movement of dislocations and the mass compressive residual stress could delay the crack initiation. The nanostructuring mechanism involved in these techniques have been discussed and explained in different steels. According to experiments and analyses, a high density of dislocations, sheer bands or twins are the main source of grain subdivision.

Laser surface modification techniques have been used to enhance the surface property of stainless steel as well. These methods include surface melting [57-61], laser annealing [62, 63], laser alloying [64-67], laser cladding [68, 69], laser peening [70] and laser transformation hardening [71]. The main aim has been to form some intermetallics and carbides to stainless steel and enhance tribological properties. Laser annealing and peening could also introduce large compressive residual stress to the surface layer and improve the fatigue property and resistance to corrosion cracking as well. However, laser surface melting could have some negative effect [58, 72, 73]. For example, the cavitation

erosion resistance of some steels may be degraded by laser surface melting because the delta ferrite forms and make the steel susceptible to cavitation erosion. Low temperature carburising/nitriding to form S-phase is another recent developed technology to improve the surface properties of stainless steel, especially austenitic stainless steel. The understanding of S-phase is critical to understanding this research that a detailed review of this subject is described below.

2.2 Plasma surface engineering

2.2.1 Overview of plasma

Plasma is considered to be the fourth state of matter besides solid, liquid and gas. Like gas, plasma does not have a definite shape or a definite volume unless enclosed in a container; unlike gas, in the influence of a magnetic field, it may form structures such as filaments, beams and double layers. The definition of plasma by ASM society [74, 75] is an electrically generated 'gaseous' mixture consisting of positively and negatively charged particles as well as neutral species.

Plasma phenomena are very widespread in our surroundings. They could be observed in laboratory, in industry and even in nature, in our dailey life. For example, sun and other stars, aurora, neon lamps in the streets or plasma display of TV sets are all plasmas. They are very different and by their characteristics can be divided into many types as illustrated in Figure 2-3 [76]. The schematic shows each kind of plasma in certain regions according to their parameters. The axis's units are explained as follows: left Y axis is the logarithm of plasma temperature, right Y axis is also temperature related but has energetic meaning

corresponding to the particle energy, upper X axis reflects “plasma frequency” (density of charges divided on density of total gas), lower X axis shows logarithm of ions density (number of ions in a unit of volume). In the schematic, the parameters of some plasma phenomenon can be compared to each other. Among these categories, the glow discharge plasma labelled in red area is very important for the research of plasma surface alloying processes.

2.2.2 The principal of plasma surface alloying

The dc glow discharge has been historically important, both in applications of weakly ionised plasma and in studying the properties of the plasma medium. The usual pressure range of operation is between 1.333 Pa and 1333 Pa. Between the anode and cathode, many light and dark regions have been identified in Figure 2-4. All these regions can be described briefly as follows.

2.2.2.1 Positive Column

Positive column is a luminous glow area close to the anode. Its performance declines with increasing bombardment by electrons or ions [77]. As shown in Figure 2-4 near zero bias voltage of the substrate, the positive column has a minimum value in dark conductivity and a maximum in photoconductivity [78].

2.2.2.2 Cathode Sheath

The cathode sheath is the region over which most of the voltage drop occurs, it is also known as the cathode fall or Crookes dark space. The electrons carrying current in the

positive column are prevented from reaching the cathode. The electron density increases exponentially from the cathode, with the exponent known as the first Townsend coefficient [79]. This mechanism is important for the steady-state discharge before breakdown happens.

2.2.2.3 Negative Glow and Faraday Dark Space

The dramatic increasing density of high-velocity electrons near the cathode leads to a bright cathode glow where the light intensity increases to a peak. Meanwhile, the electric field decrease rapidly at the end of this region. Before the equilibrium conditions of the positive column can be established, the high electron velocities need to be dissipated by elastic and inelastic collisions. In this process the electrons lost almost all of their energy and then are reaccelerated in a weak field which is called the Faraday dark space, the transition to the positive column could be rather complex and the Faraday Dark Space can be very long [80].

2.2.2.4 Anode fall

The anode fall area is located between the positive column and the anode. The drift velocity of the electrons in the positive column is less than their thermal velocity. The anode must be positive with respect to the positive column to maintain the current. And a retarding electric field near the anode is required to prevent the full thermal electron current from reaching the anode. As a result, a double layer forms just like other types of discharge but with a smaller voltage drop in this region.

The typical voltage-current characteristic of a dc discharge is shown in Figure 2-5 [81]. From the low currents, the region below I_A is called a dark or Townsend discharge. Then the glow gradually builds up until a transition is reached, with hysteresis, entering the flatten region at a voltage V_s. This flatten region with slightly negative slope dV/dI is called normal glow. The voltage remains almost constant as the current increases till I_B, at which point the voltage increases with increasing current. This region is called abnormal glow. Further increment in current causes a rather abrupt transition at point I_C, with hysteresis, to a considerably lower voltage discharge known as an arc discharge. The voltage continues to decrease with increasing current.

2.2.2.5 Sputtering

Sputtering is a phenomenon apart from the discharge dynamics, but is important for applications and in limiting the use of glow discharge. The voltage drop across a cathode sheath is about several hundred volts and the ion-bombarding voltage leads to severe sputtering of the cathode surface and deposition of material on other surfaces. Although the large voltage drop in the cathode sheath is hard to control, there are several configurations that enhance the sputtering efficiency, for example, hollow cathode discharges [82] and dc planar magnetron discharge [83].

2.2.2.6 Glow discharge plasma

Glow discharge plasma is a non-thermal plasma generated by the application of DC or low frequency RF (<100 kHz) electric field to the gap between two metal electrodes [84]. The glow discharge plasma which contains high density of electron with intermediate energy

ranging from 1 to 10 electron volts is very commonly used in the plasma surface alloying processes. Due to the effective impact on ionising and dissociating diatomic molecules of this energy range, glow discharge plasma could provide a ready and prolific source of chemically active atoms, therefore appropriate for plasma surface alloying i.e. plasma carburising and plasma nitriding.

A glow discharge plasma may be obtained by applying a DC voltage to a gap of low pressure gas between two electrodes in a vacuum vessel. Discharge or ionization can be triggered by the collision between electrons and gas atoms. The collisions ionised the gas atoms and consequently result in even larger emission of electrons. The effect will also be accompanied by excitation of visible light and make the gas glow. The application of glow discharge include fluorescent light, DC plasma reactor, magnetron discharged deposition, and electro bombardment plasma source etc. During a plasma surface alloying treatment, the article to be treated is served as the cathode while the furnace interior wall is the anode. The chamber is first evacuated and then filled with specified mixture of gasses, for instance, methane (CH_4) and hydrogen (H_2) for carburising. The gas flow is controlled by pump to keep the pressure at required values (normally several mbar for plasma carburising). Treatment is initiated by the application of an electrical potential of several hundred volts between the components (cathode) and the vacuum chamber (anode)[85]. This causes the formation of glow discharge plasma around the components.

An anomalous glow discharge is utilised in the process in order to ensure complete coverage of the cathode and also to provide sufficient power to heat the components up

to treatment temperature.

2.2.3 Advantages of plasma surface engineering

This plasma surface engineering technology offers a number of advantages over the conventional methods currently used for thermo chemical heat treatment. the benefits for the plasma carburising surface engineering in particular compared with other carburising methods such as gas carburising. It has been mentioned by many researchers and concluded by Bell [85] as follows:

(a) Reduced treatment times arise because of a more rapid saturation of the surface owing to the enhanced mass transfer through the plasma.

(b) Reduced energy consumption is achieved both because the treatment time is reduced and also because only the cathode is heated; heat loss occurs only by radiation through the vacuum to the cold chamber wall.

(c) Reduced gas consumption with 95% savings are claimed, gas quantities used being of the order of tens of litres per hour.

(d) No environmental hazards arise, *e.g.* no toxic wastes requiring disposal and no risks of explosion.

All these advantages are more and more important in modern industry. Eco-friendly designs and energy- saving installations are so important that lead the whole human society to the future.

2.3 S-Phase

2.3.1 Origin and Determination of S-Phase

S-Phase was reported for the first time by Zhang and Bell in 1985, [2]. It was noted as a hard and corrosion resistant layer formed on AISI 316 stainless steel by low temperature-plasma nitriding. Parallel research work was made by Ichii *et al.* [86], who found that in the XRD pattern of low temperature (400°C) plasma nitrided AISI 304 austenitic stainless steel, there were five extra peaks which were shifted to the lower diffraction angles relative to the corresponding γ peaks. These five peaks were denoted as S1-S5 and Ichii coined the term 'S-phase' to describe this new found phase.

The lattice expansion of austenite in N ion implanted AISI 304 austenitic stainless steel was observed for many years. It was in 1993 by Leyland [87]that the term 'expanded austenite' was first applied to the new phase which was still FCC structure. However, Marchev [88] argued that the S-phase probably was body centred tetragonal structure like martensite in steel and denoted it as 'M-phase'. Although there is no widely accepted name for this new phase, 'S-phase' and 'expanded austenite' are the most commonly used names for the new phase, and they could be interchangeable in the literature. The name 'S-phase' is used in this thesis for convenience and consistency.

S-phase research has received extensive scientific interest and several techniques have been developed to form S-phase in ASS such as low-temperature plasma nitriding [89], low-temperature plasma carburising [90], ion implantation [91], plasma immersion ion implantation (PIII)[92] [93], gas carburising [94] [95] as well as physical vapour

deposition(PVD)[96].

2.3.2 Structure of S-phase

Initially, S-phase was described as a duplex layer consisting of a mixture of face centered cubic $[Fe,Cr,Ni]_4N$ and austenit [2], or a compound layer of type $[Fe,Cr,Ni]_4N$ structure [86].

The crystallographic structure of the S-phase arouses a lot of research interest and has been a debate for a long time. The peaks of S-phase in XRD profiles shift to small angles comparing with the original FCC peaks and the degree of peak shift also depended on the type and amount of interstitials introduced into the substrate. Further examination of the S-phase peaks revealed that the shift of peaks S2(200) is greater than S1(111) [86, 87, 97]. This unequal shifting could be attributed to the distortion of the FCC structure and based on the special peak shift, some researchers agreed with the face centred tetragonal structure(FCT) [98, 99]. But the tetragonal structure should have extra peaks which never appeared in any XRD profiles given by researchers [93]. Other explanation of S-phase structure was body-centred tetragonal structure (BCT) [88, 100] which was also not very accurate. Researchers found that the uneven peak shift of S2(200) is very similar to that caused by the stacking faults in untreated austenitic stainless steels by cold work [101]. Therefore, it is reasonable to believe that the anomalous peak shift in S-phase could be related to the stacking faults and it is well established that stacking faults could shift the XRD peaks positions of FCC structure and the degree of which depends on the probability of stacking faults [102, 103]. Up till now, the best recognised description is that S-phase is an expanded FCC with a high density of stacking faults, dislocation, slip lines and

deformation twins [93, 104-107]. The high compressive stress after treatment induced plastic deformation to the FCC austenitic substrate so that dislocations, slip lines twins and stacking faults can been found by using different characterisations. However, the lattice strains associated with high stacking faults density may cause disturbance in identifying the crystallography of S-phase. Thomas Christiansen *et al.* recently analysed homogeneous stress-free S-phase synthesised by gaseous nitriding of 316 stainless steels powders and proved that the S-phase has a FCC structure [105].

2.3.3 S-phase formation conditions

2.3.3.1 Substrate crystallography requirement

S-phase, mentioned by Bell [108], is formed when a large amount of either nitrogen or carbon(or both) are dissolved in the surface of an austenitic stainless steel forming a supersaturated solid solution without the precipitation of chromium nitrides or carbides.

It is known that N and C atoms occupy the octahedral interstitial sites in FCC and are surrounded by six nearest neighbour metal atoms in substitution sites [109]. It is generally believed that Face Centric Cubic (FCC) crystal structure is essential for the formation of S-phase [110]. Recent work [97] on low-temperature plasma carburising of Co-Cr biomedical alloys revealed that S-phase could be formed in dual phased with hexagonal close-packed structure (HCP) and FCC crystal structure. And inward diffusion of carbon can convert the HCP phase into FCC phase to form S-phase because of the stabilization of austenite due to carbon's alloying effect. However, all the research results have revealed that although phase transformation may accompany with the saturation of interstitial

atoms, FCC structure of substrate is necessary for S-phase to form.

2.3.3.2 Alloying elements effect

As discussed above, S-phase is an interstitial supersaturated solid solution. Therefore, the interaction between the substitutional alloying elements (e.g. Cr, Ni, Fe, etc.) and interstitial alloying elements (e.g. C, N) is important.

2.3.3.2.1 Effect of nitride/carbide forming alloying elements

X-ray photoelectron spectroscopy(XPS) analysis of N implanted AISI 304L by Riviere *et al.* [111] revealed the existence of a selective and dominant bonding of N to Cr, which was lower than that for CrN. Meanwhile, Fe was detected in the metallic state in the S-phase, suggesting that Fe played trivial role in the long range transport of N and the formation of S-phase. Similar results were found by Dahm *et al.* [112] in the magnetron sputtering deposited S-phase coating showing that Cr was the only metallic species altered by the presence of N.

The clustering Cr-N was observed earlier by Shanker *et al.* using high resolution TEM [113]during aging at 850C/25h for AISI 316LN(0.078wt.% N). The high negative enthalpy of binding between Cr and N may result in a high driving force for the formation of Cr-N clusters in austenitic matrix.

Besides Cr-N clusters, Mo-N pairs were also found to be uniformly distributed in the 316 ASS based austenite phase by Murayama *et al.* [114] through 3DAP mass spectrum. The

affinity of these alloying elements especially Cr is essential for S-phase formation which was indicated by Oddershede *et al.* [115]. They investigated the Cr-N bonding in low temperature(718K) gas nitride 316ASS flakes with 0.4-1.2μm thick by extended X-ray absorption fine structure analysis. Most Cr atoms was found to be associated with a Cr-N bond distance comparable to the chemical compound CrN, but only a small fraction of the Cr atoms could be detected as CrN with XRD analysis.

Makishi *et al.* [116] reported that binary nickel alloys with either Ti, V, Nb, Cr or Mn can form a detectable S-phase layer under XRD and optical microscopy. Williamson *et al.* [110]found a trend of reduced amounts of the S-phase with increasing concentrations of Ni within the Ni-rich alloys and pure Ni fails to form S-phase. Alloy elements such as Ti, V, Nb, Cr, Mn and Mo could increase the N solubility in binary nickel alloys in a descending order.

As for the S-phase formed by carburising, a similar scenario occurs to the clustering bond between carbon and alloying elements. Heuer [117] studied the internal friction of the interstitial defects in gas carburised 316ASS and a major friction peak was obvious which is related to the anelastic relaxation of a composite cluster.

Based on thermodynamic calculations, Michal *et al.* [118] investigated the effect of strong carbide forming elements such as Ti, V, Nb, Al,Cr, Mo and Mn together with Ni and Si on the carbon solubility in Fe based austenitic alloys at 477 °C as shown in Figure 2-6. All strong carbide forming elements can increase the carbon solubility while Ni and Si

decrease it. This could provide important information on achieving high performance S-phase on developing new compositional austenitic stainless steel.

Therefore, it follows that strong nitride/carbide forming elements such as Ti, V, Nb, Al, Cr, Mn and Mo have strong affinity with N and C and increase their solid solubility in austenitic stainless steel, and thus are beneficial for the formation of S-phase.

This point of view has been partially supported by the following research works. Sun *et al.* [119] studied the response of three austenitic stainless steels with similar Cr and Ni content but different Mo or Ti contents and found the threshold temperature for S-phase forming increased with the content of such strong nitride/carbide forming elements. Similar results were found by Tsujikawa *et al.* [120] in plasma carburising of AISI 304 and AISI 316 (AISI 316 is 2.67wt.% rich in Mo than AISI 304). Carbon diffused faster and the lattice expansion was also larger in AISI 316 than that in AISI 304 which might due to the Mo-C clusters.

2.3.3.2.2 Effect of other alloying elements

Among all the other alloying elements in stainless steel, nickel is obvious very important not only because of the relative high portions in the composition (above 10wt.% in AISI 316) but also because Ni is the element to stabilise the FCC austenitic structure at room temperature. F. Ernst *et al.* [121] mentioned Ni is required for retarding the undesired precipitation of carbides during low-temperature carburization. Therefore, it is generally believed that Ni is favourable for the forming of S-phase. However, the role of Ni differs

greatly from Cr in the formation of S-phase on austenitic stainless steels. Recent work [122] demonstrated clearly that S-phase could form on Ni-free, high Mn austenitic stainless steel by plasma carburising. Therefore, Ni is not necessary for the formation of S-phase in austenitic stainless steel. But with the substitution of Mn, it is easier to form precipitates especially for plasma nitriding because of its stronger affinity with N.

Other minor, non-carbide forming elements might also have some effect on the formation of S-phase. Research results [123] found that Cu could also enhance carbon supersaturation in the S-phase during low temperature carburising of austenitic stainless steel. Lutz *et al.* [124] compared the response of Fe-Cr-Ni Co-Cr-Mo and Co-Ni-Cr-W-Fe alloys after nitriding under the same conditions. They found that the thickness of S-phase of these alloys increased in the order of Ni, Co and Fe.

As a whole, the diffusion of C and N in the austenitic matrix and long range order of these interstitial atoms might be related to the outer electron structures and magnetic property of the alloys. S. Shang *et al.* [125] investigated the hyperfine interactions in ε-Fe_6N_x by Mössbauer spectroscopy and *ab initio* calculations. The values of hyperfine field (HFF) are influenced by the Fe atomic volume and Curie temperature whilst isomer shift (IS) is increased with the iron atoms surroundings An (n=0,1,2,3nitrogen atoms) and nitrogen content of the ε phase. They also [126] analysed the phase stability in binary and ternary interstitial phases ε-Fe_6C_x, ε-Fe_6N_x and ε-$Fe_6C_xN_y$ by using the first-principles projector-augmented wave method. It was found that the interaction between interstitial atoms (C and N) was of a repulsive nature in the ε phases and revealed different magnetic

properties [127, 128]. These calculation based on first principle opened a window for understanding the effect of alloying elements on the transition of S-phase to precipitation.

In general, to form S-phase in 3-d transitional metal alloys such as Fe, Co, Ni with FCC structures, it is important that a certain amount of Cr may be necessary. For example, ASS and Co-Cr normally own more than 10wt% and 20wt% Cr respectively. Some nitride/carbide forming elements play beneficial role on the formation of S-phase and other alloying elements like Ni, Cu affect the diffusion coefficient and solution ability of N, C in austenitic substrate. However, the mixing effects of alloying elements seem complicated and mutually tangled within both substitutional and interstitial atoms.

2.3.4 Diffusion modelling and simulation of S-phase

The diffusion profile is important for analysing the formation mechanism of S-phase. As mentioned above, S-phase is an interstitial supersaturated single phase without precipitates. This significant supersaturation, which has been demonstrated by many researchers [95, 99, 129, 130], is about 12at.% in carburised S-phase and about 25-30at.% in nitride S-phase. The earlier prediction of N depth profiles in plasma nitride ferrite steel containing nitride forming elements was developed by Sun and Bell [131] and several models have been proposed to explain the tremendous uptake of nitrogen in S-phase. One is the trapping and detrapping model which was pointed out by S. Parascandola *et al.* [132] considering the assumption that diffusion of nitrogen is under the influence of trap sites formed by local chromium. By assuming every trap site of Cr holds one nitrogen atom, they modulated results fitting well with the experimental curves of $^{14}N/^{15}N$ nitriding

results. Also they calculated the diffusion activation energy of 1.1eV and detrapping activation energy above 1.45eV.

Another model by S. Mandl *et al.* assumed that [133] N diffusion in S-phase was concentration dependent nitrogen. In all cases step-like behaviour, with a high value for high nitrogen contents and low value for low ones, was found in the research work. They [134] also observed a scatter of transition point for the sharp changing of nitrogen diffusion coefficient. They studied different steel grades and found the critical point of nitrogen diffusion had few relations with chromium content. Other researches [135] on the ion-beam nitriding of ASS explained the influence of flux by both free diffusion-sputtering and trapping-detrapping.

Based on these numerical models, Christiansen *et al.* [136, 137] simulated the diffusion of N in austenitic stainless steel and formation of S-phase during gas nitriding. They calculated nitriding potentials with different equilibrium constant $K_{Cr \cdot N}$ and at the value about 0.0061 the simulated profiles would exhibit an abrupt drop and a slowly fading tail. The drop in concentration was explained to be related to the tendency of Cr atoms to have (at least) one N as their nearest neighbour once the solubility is exceeded (short range ordering) and the tail is corresponding to randomly distributed N which is not trapped by Cr. Although this simulation gave well-fitted shape of N profiles in S-phase, quantitatively they overestimated the thickness of S-phase due to the uncertainty of surface concentration.

Many researchers found the activation energy of N diffusion in S-phase [91, 120, 138, 139] was lower than that of normal N diffusion in austenite stainless steel [140, 141]. Rapid diffusion of interstitials in S-phase was concluded by H. Dong [3] as follows. When diffusion occurs in low N austenitic stainless steels, N will be trapped in the trapping sites because of the strong affinity between Cr and N; however, once the expanded austenitic S-phase forms, many trapping sites have been filled and additional coming N atoms can diffuse with little interference from filled trapping sites. And because of the supersaturated interstitials in S-phase, the determination of the activation energy for diffusion of C or N in S-phase requires a more thorough analysis in accordance with the physical chemistry of the system.

Both carburising and nitriding showed abnormal diffusion properties, some models have been proposed to fit the experimental results and realise the mechanism hidden behind the diffusion. The most recognised and widely used model is trapping effects caused by Cr although it is still lack of approval experimental results. However no model in the literature is sufficient to fit experimental data of all carburising and nitriding S-phase processing.

2.3.5 S-phase properties and applications

2.3.5.1 Hardness and toughness

As mentioned in above sections, S-phase is a layer supersaturated with interstitials such as N and C. Hardness of ASS is improved a lot after forming S-phase on the surface. About 1300-1500HV for nitrogen-rich S-phase [142, 143] and 700-1000HV for carbon-rich S-

phase [142-144] have been reported.

Figure 2-7 illustrates the hardness depth profiles of S_C layer (carburised), S_N layer (nitrided) and dual layer S-phase layer (carburised and nitrided) [104].

The nitrogen S-phase shows a higher but a sharp decreasing hardness profile whilst the carbon S-phase has a quite high and gradual change in hardness. The dual treated S-phase compensates the difference in hardness and abrupt gap between S-phase and substrate.

The large hardening effect can be attributed to the structure of S-phase. It is well known that the potent interaction between mobile dislocations and 'tetragonal' strain fields formed by interstitials could harden the martensite [145]. S. Mändl [146] identified the anisometric distortion and strain in the S-phase. Similar to the martensite, the formation of the substitutional-interstitial complex in S-phase with tetragonal symmetry can cause strong interaction between dislocations and non-spherical stress field. So the extremely high hardness of S-phase should be ascribed to both the interstitial supersaturation and the unique structure of S-phase.

It is also apparent that the hardness caused by nitrogen S-phase (S_N) is harder than carbon S-phase (S_C). This could mainly explained by the difference in saturation concentration, as mentioned above that nitrogen S-phase contains about 25at.% N while carbon S-phase retains 12 at.% C. Another reason could be related to the fact that compared with C atoms, N atoms can cause a higher dilation being dissolved in the FCC lattice because of electronic effects and C–Fe bonds being stronger than N–Fe bonds [147]. The hardness

profiles between S_N and S_C also indicates that the load bearing capacity of S_C is better than that of S_N.

Tensile tests of S-phase formed on thin AISI 316 wires(50μm) were conducted by Thaiwatthana *et al.* [130]and yield stress increased after plasma nitriding or carburising, with S_N higher than S_C. But a similar stress-strain curve was found in low temperature carburised specimen compared to the untreated 316 specimen, meanwhile the ductility of S_N deteriorated significantly after S_N formed on AISI 316 wire. Michal *et al.* [148] used 'dog-bone' specimen to carry out tensile tests before and after gas carburising of AISI 316 sheet, and similar curves were recorded and increment of yield stress was reported. However, all their specimens in the tensile contains a very small portion (8-10%) of S-phase comparing to the substrate of AISI316, so the tensile test behaviour was only partially erived from the S-phase.

The ductility or toughness of S_C proved to be better than S_N in the tensile test. It was also reflected in the experimental observation during microhardness testing. Under compressive load, radial cracks could be found at the corners of Vickers indentation in the S_N samples, while at the same circumstances no cracks were observed close to the indentations in the S_C samples [122, 149, 150]. This may relate to the higher quantity of dislocations density and deformation twins found in TEM specimens. The results follows that S_C is more ductile and tough than S_N.

2.3.5.2 Fatigue

The fatigue property of S-phase is important because in some applications stainless steel parts are subjected to cyclic stresses and fatigue may cause the material in failure. Research work by Allen [151] *et al.* put an investigation into the fatigue properties including plain fatigue(PF) and fretting fatigue(FF) of S_N. Rotating bending fatigue test showed that the PF limit of AISI was improved from 390MPa to 480MPa after plasma nitriding for 15hours at 400°C and the FF limit was increased from about 210 to 310MPa. S-phase is more effective in enhancing FF than PF properties. This is probably because the hard S-phase can effectively resist the fretting action and thus minimise the damage. Similar results were found by Ceschini [152] in samples after low temperature carburising at 450°C for 100h. The fatigue limit of AISI 316L could be increased from 366MPa to 512MPa, considerably improved up to 40% compared with that of the untreated material. The fatigue cracks always initiated at the positions near the interface between S-phase and the substrate. It is well known that fatigue cracks normally start at the material surface but also exceptions associated with internal material defects, such as incompatibility of fatigue property of S-phase and untreated austenitic stainless steel. Such subsurface crack initiation is also observed in a plasma nitride AISI 304 austenitic stainless steel [153], shot-peening treated AISI316, AISI316L austenitic stainless steel [154, 155] and low temperature carburising treated AISI 316 [156, 157]. The increase in fatigue properties is expected to be related to the increment of surface hardness by S-phase and large compressive residual stresses introduced by interstitial atoms expanded lattice. Recently Stinvile *et al.* [158] proved the fatigue life of 316L ASS in Low Cycle Fatigue was significantly increased by low temperature plasma nitriding treatment and it was directly

correlated to the residual compressive stress of 2-3GPa deduced in the experiments. The formation of compressive stress inside the S-phase can be easily derived by the bending of a thin foil treated on one side. The internal stress is superimposed to the external load and leads to a reduction of the effective stress in tension. Since only tensile stress produces fatigue cracks and contributes to crack progress, a reduction of the effective stress in tension increases the fatigue life.

2.3.5.3 Wear properties

The wear resistance of S-phase was reported to improve drastically comparing to untreated austenitic stainless steel by many researchers [143, 159-163]. Pacheco *et al.* [164] tested a variety of treated materials by the pin-on-disk tribometer with pressurised water and demonstrated that the wear resistance of low temperature plasma nitriding of AISI 304 stainless steel was over 50-100 times greater than those treated by other methods. An improvement in sliding wear resistance by a factor of up to 20 was found by the formation of S_C layer on AISI 316 stainless steel by *Sun et al.* [106]. These wear tests were performed on a tribo pair of S-phase plane surface vs. steel ball and not very adequate for characterisation of the wear properties of S-phase. Further detailed wear properties of gas carburised AISI 316 were systematically studied by Qu *et al.* [165] using a unidirectional ball sliding on disc tribometer under a load of 5N at speed of 0.1m/s in air at room temperature, 200C and 400C. Both the ball and the disc were variable between untreated (UT) and gas carburised (GC) conditions. Their results showed the wear rate for the GC/GC tribopairs was two magnitudes smaller than the UT/UT pairs at room temperature. With the temperature elevated to 400C, the wear rate for GC/GC increased

but still lower than that of the UT/UT, meanwhile, the coefficient of friction of GC/GC became smaller than UT/UT. Besides the small loads(<10N) carried out on the wear test, Sun and Bell [166] evaluated the wear resistance of S_C at a high load of 1000N under oil lubricated rolling conditions using an Amsler wear tester. They proved that under high load, the wear resistance was good only when the S_C layer was thick (40µm). Thin(15µm) and intermediate(25µm) had little effect on the wear resistance. This is because the maximum Hertzian stress at high loads is located in the soft austenitic below the thin S-phase layer and causes the subsurface deformation and thereafter the rupture of S-phase layer. The load bearing capacity of S-phase is strongly depend on the thickness and although S_C is much better than S_N in this case, thicker layer of S-phase is required for high demanding applications.

Enhancement in wear resistance in Co-Cr [149, 167] and Ni-Cr [168] alloys has also been observed by forming S-phase on the top surface. However, the maximum S-phase layer thickness formed in Co-Cr and Ni-Cr alloys are much thinner than that in austenitic stainless steel. So their load bearing capacities are expected to be much lower than S-phase formed in austenitic stainless steel, therefore the wear resistance of these materials with S-phase will deteriorate if the applied load is increased in wear testing. For instance, it was demonstrated [169] that the wear of the S-phase formed on Inconel 601 alloys increased by about 10 times when the applied load increased from 0.98N to 4.90N. Therefore, it is important to enlarge the thickness of S-phase by all means to ensure the high performance of S-phase during wear resistance. Therefore, the load bearing capacity of the S-phase layers will fail to satisfy the need of some application. Prolonged treatment

could form a thicker diffusion zone, but run the risk of precipitation and a reduction in the corrosion resistance of surface layers. Optimisation of paraequilibrium thermochemical processes is needed to produce a thicker S-phase layer without precipitation within the shortest time. The dual treatment including carburising with nitriding as mentioned in previous section 'hardness and toughness' is a good method to achieve this purpose. Some recent work [170, 171] has demonstrated that changing the minor composition of treated material and hybrid treatment combined carbon and nitrogen could increase the thickness of S-phase layer. Y. Sun *et al.* [107, 172] developed a hybrid plasma surface treatment for austenitic stainless steels, forming a dual layer structure with an extremely hard nitrogen-enriched S phase on top of a hard carbon-enriched S phase.

The hybrid process can significantly improve the corrosion resistance of austenitic steels in 3.0% NaCl and performed much better than individual low temperature nitriding and carburising and better load-bearing capacity as well.

2.3.5.4 Corrosion resistance and corrosion wear resistance

As indicated in the 'origin of S-phase' sections, S-phase retains the corrosion resistance of the base alloy. Many researchers found that the corrosion resistance [4, 159, 173] of both carbon and nitrogen S-phase without precipitates was higher than the substrate. It was well known that beneficial effect could only be obtained when carbon or nitrogen atoms are in solid solution. Once nitride or carbide precipitates of chromium appeared, the corrosion resistance would deteriorate because of chromium depletion in matrix. However, it should be pointed out that the anticorrosion behaviour of S-phase depends

both on the kind of interstitials (C or N) and on the composition and pH values of the solutions used for corrosion tests [174-176].

Corrosion wear resistance of S-phase is also good in some cases. Dearnley *et al.* [177, 178] observed the corrosion wear behaviour of S_N of AISI 316L in electrochemical scratch tests in 3% NaCl solution and bovine serum solution. The results showed S-phase coatings produced a lower sliding contact corrosion current than untreated AISI 316 ASS both in scratching and reciprocation sliding wear. Similar results were reported by Thaiwatthana *et al.* [179] and comparison of S_N and S_C on AISI 316ASS showed that S_N was better in corrosion wear property due to the harder property and better repassivation capacity. The erosion corrosion resistance of S-phase in AISI 316 ASS in a 20 wt.% silica +3.5% NaCl water slurry at 40°C was studied by *Dong et al.* [159] and different erosion corrosion mechanisms were revealed by SEM and synergy between erosion and corrosion is 1.7, 30.0 and 69.4% for the untreated, S_C and S_N respectively. As for Co-Cr alloys, the wear factor of Stellite 21(Co-based alloy) with S-phase formed on the surface in air and in 3.5% NaCl solution can be reduced by 99% and 96%[180].

2.3.5.5 Industrial applications of S-phase

Since the S-phase has outstanding combination of properties, there are many potential applications in industry. It has been mentioned by Bell [181] that the application of S-phase into following fields: marine industry (spindles,ball-valves, butterfly-valves)chemical industry (safety valves) and nuclear industry.

For example, plasma nitriding on AISI 316 has been used as control rod clusters involved in pressurised water reactor for nuclear stations [6, 182]. As shown in Figure 2-8, these rod clusters control assembly consists of thin walled (0.4–1.0 mm) AISI 316 tubes (9.7 mm in diameter and 3.8–4.4 m in length) containing neutron absorbers [6]. The control rod cluster is inserted into the core to moderate the nuclear reaction, and wear occurs due to the sliding contact with the cluster guide tubes and vibration. The S-phase treated instrumentation tubes were installed in nuclear plants before 1998 and more than 90% improvement in wear resistance has been achieved according to the excellent wear resistant property of S-phase.

Another case of application is much more general than the first one. To meet the requirement for corrosion resistance in chloride environments, some highly alloyed super stainless steels have been developed. S-phase hard layered was formed by low temperature gas carburising to ensure a strong vibration resistant grip in the high performance systems [183](see Figure 2-9).

S-phase formed in Ni-based and Co-based alloys could have great potential for aerospace, chemical, nuclear applications; Co-Cr alloys are joint replacement materials for load bearing joint prostheses as hip and knee implants.

Although the S-phase shows a desirable combination of properties, the layer thickness of the S-phase is still much thinner as compared with surface layers formed by conventional equilibrium thermochemical treatments as nitriding and carburising. It is interesting to

develop an optimised hybrid process to form with thicker layers of S-phase and better mechanical performance. After overcoming these technical barriers, applications with S-phase treatment materials would be developed into full capability.

2.4 Metastability of S-Phase

2.4.1 Paraequilibrium and supersaturation

Paraequilibrium is a term proposed by Hultgen in 1947 [184] and subsequently developed by Hillert in 1952 [185] to describe a constrained local equilibrium or a special metastable equilibrium in which mobile components are assumed to be freely redistributed while the less mobile components are assumed to be frozen in place [186].

The concept of paraequilibrium has been frequently used to describe phase transformations and could been introduced into surface engineering field in this case. Under low-temperature carburising and nitriding treatments, the super-saturation of carbon or nitrogen atoms in substitutional alloys is due to paraequibrium in which interstitial atoms diffuses to equilibrate the chemical potential while substitutional solutes are immobile. S-phase can be formed at low temperature by introducing interstitial (e.g. N and C) into austenitic stainless steels (ASS). For example, during low-temperature plasma nitriding of ASS the interstitial atoms can diffuse into a depth of 20-30μm while substitutional atoms (such as Cr) are immobile because of the extra large difference in diffusivity between them. Therefore, the formation of S-phase is not an equilibrium, but metastable equilibrium or paraequilibrium process.

Many researchers [5, 117, 118, 121, 148, 187] studied low-temperature carburization of 316 austenitic stainless steel. The supersaturated carbon dissolved up to 12at.% in the austenite without any precipitation. For nitrogen in S-phase, this maximum N can reach as high as 25 at.% as mentioned above. However, the maximum solid solubility of C in AISI 316 austenitic stainless steel is <0.015at.% at carburising temperature [95]. That means the carbon solubility in S-phase is 800 times larger than the equilibrium state. This massive supersaturation of interstitial atoms in S-phase was accompanied by lattice expansion and large residual stresses. The associated lattice expansion can reach 10% for S_N [188, 189]and less than 3% for S_C. [190, 191]. The residual stresses in gas carburised AISI 316L were reported to be about 2 GPa [117], while in nitride this value could be estimated to be smaller than 7.5GPa [192].

2.4.2 Thermo stability of S-phase

As discussed above, S-phase is a paraequilibrium state with supersaturated solid solution of interstitials as C and N in austenitic stainless steel. It is well known that given favourable conditions, especially thermal, the paraequilibrium would change to more stable state. Research results have demonstrated that S-phase will decomposed into stable phases when isothermally annealed for a long time [193, 194]. TEM observation revealed that S_N formed by plasma nitriding on AISI 316 decomposed into CrN and ferrite with fine lamellar microstructures while S_C changed into $Cr_{23}C_6$ and (Cr,Mo)C with CrN like carbides. And it showed that S_C was more stable than S_N during annealing process. Christiansen *et al.* [195] also investigated the decomposition kinetics under annealing of S-phase formed in AISI 304L and AISI 316L austenitic stainless steels by gas nitriding and it followed that S-

phase formed in AISI 316L was significantly more stable than in AISI 304L. The final decomposition products were also different from each other, with CrN + austenite and CrN + ferrite respectively. Annealing at relatively low temperature would deteriorate the property of S-phase although no precipitate was observed. For example, Ozturk *et al.* [196] annealed S-phase formed by N ion implanted AISI 304 at 400°C for 36 hours and found the lattice expansion was not so large that could sustain the ferromagnetic property of S-phase.

Besides annealing treatment, carburising or nitriding at relative low temperature but with longer time would also change the stability of S-phase. Metastable carbide M_5C_2 (Hägg) and M_7C_3 [5] was formed upon prolonged gas carburising treatment on 316L stainless steel. Hence, the thermo stability of S-phase depends on the type and amount of both the interstitial and substitutional alloying elements. The excellent and unique properties of S-phase strongly rely on the supersaturation of interstitial atoms with no allowance for precipitates to form. Therefore, although S-phase is not stable in thermodynamic point of view, it is necessary to know how to control the use of S-phase under safe conditions during the service life. In addition, currently, little or no information is available on the mechanical stability of S-phase although it is known that some metastable phases in thermodynamics would change into stable phases under mechanical stress conditions. So it is a timely task to investigate the stability of S-phase under both thermal and mechanical conditions.

2.4.3 Deformation induced phase transformations in austenitic stainless steel

The mechanical properties of metastable austenitic stainless steel are strongly affected by the phase transformations caused by deformation. Many researchers have reported that martensitic could form during cold working of austenitic stainless steel [197-200]. After large strain deformation, the microstructures in austenitic stainless steel change and finally affect the mechanical properties. Among which, the evolution of deformation twins and dislocations pileups are most important. ε-martensite with hexagonal close-packed structure was formed along with stacking faults, while α-martensite with body-centered tetragonal nucleation seemed to be associated with dislocation pileups where the stress level was very high [201]. In one hand the stain-hardening effect could increase the strength of austenitic stainless steel greatly and the deformation process was accompanied by martenisite transformation. In the other hand, the formation of ε martensite can soften the stress-strain curves of the stainless steel. Therefore, the phase transformations are complex depending on the deformation processes and strain rates.

Besides martensitic transformation, cold work of austenitic stainless prior to aging could also accelerate the formation of precipitations like $M_{23}C_6$ and M_6C depending on the strain rates and following heat treatments [202]. However, the deformation and stress effects on the S-phase formed on austenitic stainless steel have not been discovered and it is necessary for us to unveil all these puzzles so as to enlarge scientific understanding of the nature of this amazing phase.

2.5 Summary

Although S-phase could greatly improve the mechanical properties of surface of engineering materials, the wider application of the paraequilibrium S-phase is constrained by its metastability.

Research results have demonstrated [5, 193] that prolonged treatment or isothermal annealing would form carbide precipitation and decompose into stable phases, thus leading to significant deterioration in corrosion resistance. Therefore, thermodynamically S-phase is not stable but metastable whilst the incubation time for the decomposition decreases with increasing temperature. So isothermal transformation (TTT) diagrams are essential for the safe use of S-phase and the TTT diagrams of S-phase will depend on many parameters (e.g. type and amount of interstitial and substitutional alloying element).

Currently, little information is available on the mechanical stability of S-phase. It is known that some thermodynamically metastable phases would decompose into stable phases under mechanical stressing. Therefore, it is timely to investigate the metastability of S-phase and increase the stability of paraequilibrium thermodynamically treated ASS, Co-based and Ni-based alloys.

3 Experimental Procedures

3.1 Materials

In this study, two main kinds of austenitic stainless steels were used, AISI 316 austenitic stainless steel (316 ASS) and AISI 316L austenitic stainless steel (316L ASS).

The compositions of these two steels are listed in Tables 3.1-1 and 3.1-2 respectively.

It is shown that their alloys compositions are very close to each other while carbon concentration is a little higher in 316 ASS.

There were two forms of 316 ASS in original, hot-rolled bars with diameter of 25mm and hot-rolled sheet with thickness of 3mm. The 316L ASS was in the form of foil with a thickness of 50μm. The most commonly employed samples were cut from 316ASS bar into 5.5 mm thick disks, using a high precision Struers Accutom-5 cutting machine, fitted with SiC abrasive cutting blades. Then the samples were wet ground into flat surfaces with SiC grinding paper of grit #120. The one face which was to be carburised was ground further up to grit #1200(#240,#400,#800 in steps). Then samples were washed in soap water and then acetone, both in an ultrasonic bath, for 10 minutes.

3.2 Processing

3.2.1 Surface engineering plasma treatment

The low temperature plasma carburising treatment was carried out in a 60kW Klöckner DC plasma vacuum unit as shown in Figure 3.2-1. The instrument is composed of two

main parts, a vacuum chamber and an electric control panel. Between them are mass flow meters (to control the mixture of gas and flow rate of each gas), pressure gauges and thermometer. There are water pipes surround the furnace for cooling and two K-type thermocouples inside the furnace which are protected by ceramic sheaths.

With regard to plasma treatment, it can be generally described as following:

- The chamber is ventilated and lifted up firstly and put all cleaned samples and other installations on the working table. Then dust and particles remaining in the furnace need to be removed by a vacuum cleaner.
- The chamber is lowered and evacuated by a vacuum pump. After the vacuum level reached 1Pa, hydrogen gas (H_2) is fed into the chamber (marks '2' on the gas flow meter) and then turn on the main power to form plasma in the chamber. During heating procedure, the electric power (current and voltage) and gas flow are increased gradually and methane gas (CH_4) is mixed after the temperature gets up to 300°C.
- Adjustment the flow of H_2 and CH_4 to achieve the required composition and finally set all other parameters according to the carburising conditions.
- After the treatment, the electric power is turn off automatically and the chamber is cooled to room temperature by circulated cooling water before it is ventilated and the samples removed.

3.2.2 Carburising treatments under *in situ* tensile stresses

316L ASS foils were cut using a trimmer to a 10mm width and about 100mm length rectangular size. Then the samples were fitted into grips and firmly fixed, one side was hang on a beam of a frame which was illustrated in Figure3.2-2. All frames parts were made from steel and ground to remove any oxidation or scale. Different loads from 500 grams to 4 kilograms (after calculated to stress were 10MPa to 80MPa) were applied on the bottom side of the samples.

The temperatures were measured in two ways: K-type thermocouples inside the furnace and infrared thermometer (Klöckner Ionon GmbH with temperature detecting range from 350°C to 900°C) to compare the temperature between the treating sample and the dummy sample and confirm the temperature of the carburising treatment. The carburising treatments were carried out in an ambient of 400 Pa gas mixtures with 1.5% CH_4 and 98.5% H_2. All other conditions for carburising treatment are listed in Table 3.2-1.

3.2.3 Hot isostatic pressing (HIPping)

HIPping treatment was operated on prior-carburised samples to analyse the stability of S-phase under compressive pressure at elevated temperature. 316 ASS disks cut from rod materials were carburised at 500°C for 10hours in 400 Pa gas mixtures with 1.5% CH_4 and 98.5% H_2.

The EPSI Lab HIP facility (shown in Fig. 3.2-3) contains a HIP unit with maximum operating temperature up to 1450 °C and pressures up to 200 MPa produced by high-pressure argon

gas. This unit consists of a furnace with molybdenum heating elements, a heat shield, a water-cooled pressure vessel and a gas compressor system. The two zone molybdenum furnace (see Fig. 3.2-4) is used to provide the heating, and thermocouples are positioned at the top and bottom of the two hot zones. A computer system is used to monitor the temperature and pressure continuously inside the HIP furnace. Temperature control is within ±3 °C throughout the working zone. The HIPping conditions are listed in Table 3.2-2.

3.2.4 Heat endurance of PC samples under Tensile Stresses

316 ASS sheets (3mm thick) were cut to a conventional 'dog-bone' shape by electric discharge machining, shown in Figure 3.2-5.

All the samples were prepared and cleaned as described above. . Then they were carburised at 500°C for 10 hours in a 400Pa gas mixture of 1.5%CH_4 and 98.5% H_2.

After carburising treatment, the specimens were fixed in a specified rig and fitted into a creep test installation as shown in Figure 3.2-6. In the chamber, samples were heated to the target temperature. Once temperature was stable, tensile loads were added on the back of the installation through a lever in order that the stress applied on the specimen could be magnified by 13 times. The temperatures were measured by using two K-type thermocouples embedded inside the furnace, positioned close to the samples. The extensions of samples were measured by two linear gages. All the information on temperature and extension was recorded simultaneously by the computer once every one second initially and after stabilising, every one minute. The conditions for each test about

temperature and time were listed in Table 3.2-3. After each test cycle, loads were removed and chamber was opened to cool down to room temperature. Then samples were taken out for further characterization.

3.2.5 Reciprocating wear

A reciprocating tribometer (as shown in Figure 3.2-7) was used to evaluate the stability of S-phase under wear strain conditions. 316 ASS disc samples were subjected to plasma carburising treatment at 500°C for 15hrs prior to wear test. Some untreated 316 ASS disc samples were also tested for comparison.

A 12.5 mm WC/Co ball was used as a pin, moved back and forth on the samples' surface under various loads. The sliding stroke was 4 mm, the frequency was 67.2 rpm (1.12 Hz) and the total sliding distance was 258 m.

Wear tests were carried out without and with lubricantion (Mineral oil 'Edwards 45'). The loads for dry-wear, after changed to normal load on the specimen, ranged from 10N to 147N. The loads for lubricated wear tests ranged from 21N to 809N.

The wear volume was calculated by multiplying the area of the wear track with the length of the track. Then the term called wear factor was used to evaluate the wear property of each test.

$$\text{Wear factor} = \frac{\text{Wear volume } (\text{m}^3)}{\text{Load(N)} \times \text{Sliding distance(m)}} \ (\text{m}^2\text{N}^{-1}) \qquad (3.1)$$

3.3 Characterisation techniques

3.3.1 Micro Hardness

Micro hardness was measured by a Mitutoyo MVK-H1 micro-hardness tester with Vickers or Knoop indenters. The load could be varied from 10g to 1kg and a standard sample (EP9716400 with 757.3 $HMV_{0.3}$) was used as calibration before hardness tests each time. The hardness values are the average of at least six measurements and standards BS EN ISO 4545, 6507 were taken as reference for the Knoop and Vickers hardness tests.

3.3.2 X-ray Diffraction (XRD)

A Philips X'Pert diffractometer was used to obtain the X-ray diffraction patterns of samples. Cu radiation with $K_{\alpha 1}$ 1.5406 Å was used and the applied voltage was 40 kV with a 40 mA current. The scan step size was 0.02° in 2θ mode with 1 second for each step. The data was analysed by software X'Pert HighScore version 1.0d(PAN alytical B.V.) with an XRD pattern database.

3.3.3 3D-profilometer

An AMBIOS XP-200 stylus Profilometer was used to measures the surface roughness and wear track. The profilometer is a computerised, high-sensitivity machine that incorporates an optical deflection height measurement mechanism and magneto static force control system. The step heights can be measured precisely from 1nm to 1.2 mm. In stepping mode, 3D-profile images can be reconstructed by each line scan every 2 μm. In the measurement of wear track, 10 mg stylus load was chosen and the scanning speed was taken as 0.03 mm/s.

3.3.4 Atomic Force Microscopy (AFM)

Contact mode atomic force microscopy was conducted in a Digital Instruments Dimension 3100 nanoscope with Veeco NanoScope V.5.12r3 software. The AFM probe was Veeco NP-10 silicon nitride, the radius of the tip was 20nm. The cantilever used was V-shape with a spring constant of 0.12N/m so that it could be deflected by very small forces, and the resonant frequency of the cantilever was 14-26kHz which is high to avoid being susceptible to the vibrational instabilities. After measuring the surface morphology by AFM, the data were treated by a software TrueMap version 5.1.1 (TrueGage).

3.3.5 Glow Discharge Optical Emission Spectroscopy (GDOES)

A Leco GDS-750 QDP unit was used to obtain the composition-depth profiles of carburised samples. In this technique surface atoms were sputtered from the sample and went into the argon plasma, where de-excitation process occurred and each species of particles would emit a characterised spectrum of light from which the quantity of these atoms could be evaluated from the intensity of their specified spectrum. The method and measurement program were calibrated using standard blocks of known composition, according to the instructions of the manufacturer.

The method was also used to sputter the carburised surface and untreated surface of AISI 316 stainless steel. After 10 seconds of sputtering time, the sputtering depth could be estimated from the depth profiles and to reveal the morphology of features of untreated and treated samples.

3.3.6 Scanning Electron Microscopy (SEM)

The morphologies and microstructures of the samples were examined using JEOL 7000 field emission gun SEM. Cross sectional morphologies of plasma carburised samples were cut and mounted in bakelite and wet ground with SiC paper from 240 to 1200 grit and then polished with 6μm diamond pastes. Some samples of the thin foils samples were electro-plated with nickel and erected by a steel clamp (MetPrep Ref 113040) prior to mounting. After polishing, they were etched in a solution consisting of 50%HCl, 25%HNO_3 and 25%H_2O for several seconds. Then the carburised layers were observed under SEM and the thickness of the layers could be measured.

3.3.7 Energy Dispersive X-Ray Spectroscopy (EDX) and Wavelength Dispersive spectrometers (WDS)

The chemical composition of the selected samples were analysed using the EDX by INCA EDX detector and WDS by INCA Wave WD spectrometer associated with the SEM and TEM.

The two methods both use the characteristic X-rays generated from a sample bombarded with electrons to identify the elemental constituents comprising the sample. Both techniques generate a spectrum in which the peaks correspond to specific X-ray lines and the elements can be easily identified. Quantitative data can be obtained by comparing peak heights or areas in the unknown with a standard material. Data collection and analysis with EDS is a relatively quick and simple process because the complete spectrum of energies is acquired simultaneously. While using WDS, the spectrum is acquired sequentially as the full wavelength range is scanned. Therefore it takes longer to acquire a

full spectrum, but the WD technique has much improved resolution compared to EDS. Typical resolution of an ED detector is 70 to 130 eV (depending on the element), whereas peak widths in WD are 2 to 20 eV. The combination of better resolution and the ability to deal with higher count rates allows WDS to detect elements at typically an order of magnitude lower concentration than EDS.

In this study, carbon atoms were quantified by WDS using graphite as calibration sample, the spectrum of which was shown in Figure 3.3-1.

3.3.8 Electron Back Scattered Diffraction (EBSD)

Crystallographic information including orientation maps and phase maps were obtained on a Jeol 7000 FEG SEM fitted with an Oxford Instruments Inca Crystal Mk1 EBSD camera. The mechanism of EBSD could be described as a a stationary electron beam striking a tilted crystalline sample (70 degrees in this case) and the diffracted electrons form a pattern on a fluorescent screen. The pattern is characteristic of the crystal structure and orientation of the sample region from which it was generated. Therefore, the diffraction pattern can be used to measure the crystal orientation and grain boundary mis-orientations, and to identify different phases in the samples. Then the beam is scanned in a grid and the crystal orientation is measured at each point, the resulting map can reveal the constituent grain structure, and orientations.

In this study, crystal map size was set as 512 pixels. The samples for EBSD measurement were ground and polished using the steps mentioned previously, and then were slightly

etched using colloidal silica to obtain a smooth and flat surface. Areas were chosen to ensure the quality of the pattern so that relative good grain mappings were obtained.

3.3.9 Transmission Electron Microscopy (TEM)

Two type of transmission electron microscopes were used in this project: FEI Tecnai F20 Field Emission TEM with Oxford EDX and Gatan PEELS; JEOL 2100 TEM with Oxford Inca EDX.

Conventional TEM specimens were prepared oriented parallel to the surface (planar view). The samples were cut and mechanically thinned from the substrate side to ≈80μm, punched into a round shape with diameter of 3mm and then reduced to ≈20μm by a dimple grinder. Final thinning to electron transparency was accomplished by ion-beam milling in a precision ion polishing system (PIPS) until perforation occurred.

Cross-sectional TEM samples were prepared in a more complicated way. Samples were sectioned into 2 slabs 3mm wide and 1.5mm thick. The slabs were then glued using G-1 epoxy with the treated surface facing each other. Then the two glued slabs were slowly and carefully grinded at both sides down to 200μm. After that the two pieces of thin slabs with surface layer remaining intact were separated and put into a Quanta 3D Filed Emission Gun (FEG) focused ion beam (FIB) miller for further preparation. Prior to milling, tungsten coating was deposited by 5 kV electron-beam firstly and then 30 kV at 0.5 nA ion-beam along the surface of the region from which the sample was to be thinned in order to promote uniform milling and preserve the surface layer. Milling was performed

with low beam currents from 15 nA to 5 nA at 30 kV and final thinning at 1nA to 0.1 nA at 30 kV, finished with a final polish milling at 5 kV 48 pA.

3.3.10 Tensile tests

Tensile tests were carried out on an Instron 5566 (Instron, High Wycombe, UK). Rectangular shape of foil specimens with 50 μm thick, 10 mm wide and 45mm in guage length were used. The tensile speed was 1mm/min. Preload of 1N was applied on the specimen if the specimens were too curved and hard to bend by hand to make straight. At least three samples were prepared for each condition. In some cases, the fracture site happened at the end of guage due to the stress concentration; therefore those testing results were abandoned. Only the fracture sites occurring near the middle of the specimens were accepted. The facture surface was then observed by using JEOL 7000 field emission gun SEM.

3.3.11 Residual stress measurement

The samples for residual stress measurements were plasma carburised disk-sample cut from AISI 316 bars. Both sides of the discs were ground and polished using same method as mentioned previously and then put into the plasma carburising furnace and treated at 450 °C for 10 hours in 400 Pa gas mixtures with 1.5% CH_4 and 98.5% H_2.

Then the samples were measured by the X-ray diffraction $\sin^2\psi$ method using a Bruker diffractometer equipped with Diffrac^{plus} Stress software in the University of Sheffield. The stress software package consists of two parts, Edstress and Stress. From these, Edstress

program was used to define the stress-specific part of the hardware set-up and the measurement parameters. The major parameters defined are; 2θ start and stop, 2θ step size, exposure time on each 2θ step, number of azimuth angle φ and tilt angles ψ ranged from -45° to 45° depending upon the diffractometer used. Whereas, Stress program was utilised for stress components and stress tensors calculation on the basis of raw data obtained by Edstress program [203]. Bruker's stress program is also provided with: calculation settings for absorption correction (eliminating the influence of the irradiated area and the diffraction geometry on the measured intensity distribution), backgrounds (eliminates scattered intensity not distributing to the diffraction line), PL correction (eliminates the dependence of scattered and diffracted intensity from the diffraction angle theta), smooth (to reduce the effect of counting statistics) and $K_{\alpha 2}$ (eliminates the scattered intensity due to the $K_{\alpha 2}$ radiation of the X-ray tube from the measured intensity distribution).

The residual strain (both direct, and shear) was derived from the slope of the elliptical fit between the fractional change of the plane spacing (i.e. strain $\varepsilon_{\psi\phi}$) and $Sin^2\psi$, as shown in Figure 3.3-2.

Then according to Hooke's law, a reformulated equation for stress and strain tensor component is expressed as following [204]:

$$\varepsilon_{ij} = \frac{1+v}{E}\sigma_{ij} - \delta_{ij}\frac{v}{E}\sum_k \sigma_{kk} \qquad (3.2)$$

where, *E* is Young's Modulus and ν is Poisson's ration of the material and δ_{ij} is Dirac delta function. Therefore, by conversing measured strain values into stress values, the residual stresses are obtained. It is noteworthy that several factors can influence the measured residual stress by using $\sin^2\psi$ method: sample height which needs to be levelling to the same flat surface; surface roughness also is important to ensure the proper reflection signal at each ψ angles; meanwhile, the microstructures of the sample, i.e. texture, grain size and phase structures can also arise the difficulty in residual stress measurement. Therefore, it is important to have an overview of your sample and make a good preparation before conducting a measurement. Further detailed information can be found in a practice guide given by Fitzpatrick *et al.* [205].

4 Experimental Results

4.1 PC treatment on 316L ASS foils without stress

4.1.1 Surface layer structure

After plasma carburising (PC), the originally straight 316L stainless steel foils were bent into a curved shape, an example of which is shown in Fig. 4.1-1. The 50 μm thick 316L ASS foil was too thin to provide any constraint to the expansion of surface layers caused by plasma carburising; therefore, it was inevitably deformed under the action of residual stresses.

Cross sectional samples were cut and prepared for SEM observations; the detailed procedure was described in Section 3.3. Figure 4.1-2 shows the cross sectional SEM microstructure of plasma carburised at 450°C for 10 hours ('PC450 10h') after etching. The S-phase is identified as bright layers at both sides of the foil, at the surface. The substrate of austenitic stainless steel was greatly etched; whereas the S-phase layer resisted the chemical attack evidenced by its featureless appearance. The thickness of S-phase layer was measured to be about 12μm.

For longer carburising treatments at the same 450°C temperature, the thickness of carburised layer was increased. As shown in Figure 4.1-3, the 450°C/ 10h carburised layer was measured to be about 17μm. Some features like grain boundaries and slip bands were revealed after etching. However, the S-phase layer was still much better in etching resistance comparing to the 316L ASS substrate.

Further prolonged carburising treatment at 450°C for 30hours ('PC450 30h') produced a totally different microstructures. The microstructure after etching was illustrated in Figure 4.1-4(a) and the bright layer which was previously obvious no longer existed. Instead, some needle like morphology was observed from the surface (see 4.1-4b for detail). Meanwhile, the grain boundaries were more pronounced after etching.

4.1.2 Carbon concentrations of the surface layer

Carbon concentrations absorbed in PC treated 316L ASS were detected by WDS. As shown in Figure 4.1-5, the general carbon contents of S-phase was about 13 at.%, where three profiles converged at the 5 μm position. Although the high value at the near surface (about 23 at.%) was still questionable due to the reliability of this method, the results were still comparable. The depth of carburised layer was consistent to that measured by SEM. Generally, the carbon concentrations were increased with the prolonging time of PC treatment.

As will be shown in the next section, XRD analysis demonstrated that the sample 'PC450 30h' contained precipitates of Fe_5C_2 and $Cr_{23}C_6$. Therefore, the carbon concentration could reach a range between 20.7at.% and 28.6at.% if the surface layer was densely populated with these carbides or even a very thin compound layer was formed. Although the precipitates were too fine to be identified under SEM, the measured carbon concentration was the average value of the carbides and S-phase matrix. The shape of the carbon depth

profiles shown in Figure 4.1-5 still represented the diffusion process of carbon during the PC treatment. The carbon levels increased with the treatment time, and the corrosion properties of S-phase deteriorated according to the SEM image after etching (see Figure 4.1-4a&b).

4.1.3 Surface phase identification

XRD characterisation was carried out on the PC treated 316L ASS foils. The XRD profile of original sample foil and sample 'PC450 10h' are shown in Figure 4.1-6. The original peaks belonged to austenitic phase (γ) and were marked as $\gamma_{(111)}$ to $\gamma_{(222)}$, the subscript denoted different diffractive plane. After PC treatment at 450°C for 10 hours (PC450 10h), all peaks were shifted to left side, corresponding to the expansion of the lattice parameters. The peaks were marked as $S_{(111)}$ to $S_{(222)}$ representing S-phase, there were no peaks of carbides besides S-phase after this PC treating condition for 316L stainless foil.

Importantly, XRD results (Figure 4.1-7) revealed the phase evolution of the surface on 316L ASS with PC duration. One obvious change was the extent of peaks shift to left side. It was clear that the 'PC450 10h' sample had the largest peak shift amongst all the three samples. It represented that in the 'PC450 10h' sample, the solubility of carbon atoms was highest due to the effect of supersaturation without precipitation; meanwhile, the other two samples began to form precipitates with the elongation of treatment time and the carbon remained in the state of solid solution decreased. When the carbides precipitated from S-phase, the carbon atoms in solution state decreased. Therefore, although the carbon concentration measured by GDS was highest for 'PC450 30h', the carbon in the

FCC interstitials decreased with the precipitation process. The measured carbon concentration was the average value of carbides and S-phase matrix.

Another change was the occurrence of precipitation peaks. Minor peaks of Fe_5C_2 phase which probably contains Cr element as well like $(Fe,Cr)_5C_2$ was detectable on sample 'PC450 20h' while no sign of precipitates could be observed in 'PC450 10h'. 'PC450 30h' had strong evidence of precipitates for many small peaks, which could be identified as Fe_5C_2 and $Cr_{23}C_6$. However, these precipitates could not be revealed by SEM images and the only evidence reviewed was relatively poor resistance to etching in 'PC450 30h' (see Figure 4.1-4a&b).

The typical S-phase formed on AISI 316L ASS foil after 450°C for 10hours ('PC450 10h') was observed using TEM. Microstructure and SAD pattern of the S-phase were shown in Figure 4.1-8. The selected area was a triple junction of S-phase grains and contained twins ,dislocation lines and dislocation loops in the S-phase which was commensurate with the high stress state of S-phase caused by the supersaturation of carbon in the austenitic substrate. The SAD pattern indexing found that the structure of S-phase remained FCC structure and no precipitation was found although both the α and β angles of the TEM specimen holder had been tilted sequentially and the whole area scrutinised for any possible occurrence of precipitations especially in those positions near the grain boundaries and twin boundaries. So the results proved that precipitation-free S-phase formed on the AISI 316L ASS foil after plasma carburising treatment at 450°C for 10hours.

The XRD results revealed that the top surface of plasma carburised AISI 316L foil for 30hours could have Hägg carbides (Fe_5C_2) and chromium carbides ($Cr_{23}C_6$). EBSD mapping was used to identify twin boundaries, grain orientations and different phase structures of this sample and the mapping of cross sectional sample was shown in Figure 4.1-9. It can be seen that the S-phase kept substrate FCC structure such that the interface between the S-phase layer and the substrate cannot be identified. Mapping also indicated possible positions of the precipitates mentioned above (see black colour in Figure 4.1-9a), which are mostly in the places from the surface and near the grain boundaries. However, because of the small quantity and the fine size of the precipitates, it is difficult to identify the phases.

Further investigation was carried out on the phases of precipitates in sample 'PC450 30h' by TEM observations. The sample was cross sectional prepared by FIB and the XTEM microstructure and corresponding SAD patterns are shown in Figures 4.1-10 and 4.1-11. It can be seen that precipitates formed in S-phase were in needle shapes and growth inward from surface. Indexing of selected area diffraction (SAD) patterns taken from these needles revealed a carbide structure of χ-F_5C_2 (Reference code: 00-020-0508). It was also found that the Hägg phase posses a preferred orientation to S-phase matrix as evidenced in Figure 4.1-10(b,c), which is

$$[323]_{\mathrm{S-phase}} \,//\, [125]_{\chi-\mathrm{Fe5C2}}$$

$$(\bar{1}31)_{\mathrm{S-phase}} \,//\, (3\bar{4}1)_{\chi-\mathrm{Fe5C2}}$$

Beside the needle shaped Hägg carbides, plenty of deformation twins were observed, as indicated in Figure 4.1-11, in the S-Phase area close to the surface and this was confirmed by taking SAD patterns from those plates and the indexing of them revealed the S-phase patterns. One evidence is shown in Figure 4.1-11c, where [031] FCC pattern with S-phase d-spacing was indentified.

4.1.4 Hardness and tensile strength

The Knoop micro hardness profiles of these PC treated samples were shown in Figure 4.1-12. It can be seen that the surface of 316L foils can be effectively hardened by plasma carburising. The trend of hardness demonstrated that the strengthening effect was increased with treatment time from sample 'PC450 10h' to 'PC450 20h'. By comparing these two profiles, it was apparent that the hardness values of 'PC450 20h' were higher than that of 'PC450 10h' (with the max value 960 $H_{k0.01}$ to 870 $H_{k0.01}$) and the thickness of hardened layer was also increased by the treatment time. However, the sample 'PC450 30' illustrated a different trend of hardness distribution. The maximum hardness value was as high as 'PC450 10h' but much lower than that of 'PC450 20h', the hardness in the centre of the cross section was as high as that of 'PC450 20h'.

Tensile tests were carried out on an untreated 316L ASS sample and samples after carburising treatments of different durations. The results are illustrated in Figure 4.1-13. It is apparent that the original 316L foil had yield strength (YS) of about 280MPa and ultimate tensile strength (UTS) of about 460MPa. The tensile curve exhibited a typical ductile property of 316L stainless steel, the elongation of which was 12% from the tensile

test. After plasma carburising, all the samples exhibited higher tensile strengths. For example, the UTS of PC450 10h samples was increased to about 660MPa and the maximum tensile strength was obtained in the sample carburised at 450°C for 20hours with the tensile strength about 920MPa. Further prolonged carburising treatment on sample until 30hours led to the reduced UTS of 600MPa. The tensile curves also proved that samples significantly lost their ductility after the carburising treatments. Interestingly, the 'PC450 30h' sample showed slippery stepping curves after tensile stress exceeded UTS.

After tensile test, necking was apparent and the thickness of the specimen was reduced from 50µm to about 10µm. Typical ductile fracture morphology of untreated 316L foil was presented in Figure 4.1-14. Wavy features together with some dimples had been observed in the fracture surface and are typical and normally observed after a ductile fracture tensile test.

The tensile fracture feature of plasma carburised AISI 316L foil 'PC450 10h' is illustrated in Figure 4.1-15a. There were two clearly different types of fracture surfaces. One was the brittle fracture which came from the S-phase case; the other was from the remaining ductile austenitic substrate. River patterns could be observed in the S-phase layer. A magnified image (see Figure 4.1-15b) revealed the cleavage facets and shearing bands accompanying the fracture behaviour. Equiaxed dimples formed in the centre of the specimen, indicative of ductile fracture of the substrate (Fig. 4.1-15a). Clearly, the tensile fracture morphologyof the S-phase layer differed greatly from that of the austenitic substrate. The formation of the S-phase transformed the austenitic stainless steel from

very ductile to quite brittle, increasing the strength and reducing the ductility.

The sample 'PC450°C 20h' exhibited the highest tensile strength value among all the specimens tested. The morphology of fracture surface is illustrated in Figure 4.1-16. There were dimples and shear bands as observed in the previous samples; however, the fracture seemed to be aligned 45° in angles to the tensile direction and fewer equiaxed dimples remained comparing the fracture of 'PC450 10h'.

Prolonged carburising treatment of AISI 316L foil till 30 hours showed a step behaviour for stress-strain curve and it was also reflected in the fracture morphology (see Figures 4.1-17a) as a 'zig-zag' feature. A crack appeared behind the present top cleavage(Figure 4.1-17b) and they were torn apart during tensile test. Cleavages and the cleavage facets revealed the facture type of this sample could be intergranular in nature. Very few dimples remained in the tensile fracture and brittle fracture morphology like river patterns(Figure 4.1-17a) and shearing bands were abundant in the SEM image.

4.2 PC treatment on 316L ASS foils under tensile stresses

4.2.1 Surface layer structure

Cross-section SEM microstructures of 450°C 10h carburised samples under different tensile stresses are shown in Figure 4.2-1. After etching in 50%HCl + 25%HNO_3 +25%H_2O solutions for 12 s, four samples showed significant different layer structures in terms of surface layer thickness and resistance to the acid attack. It was shown that after carburising treatment, all samples formed a surface layer on both side of the thin foils.

After etching, the austenitic substrate in the middle revealed grain boundaries and other etching features while the surface layers showed a bright and featureless character, indicating a better resistance to the etching attack than the substrate. The thicknesses of the layers increased with the applied tensile stress during PC treatments as can be seen in Figure 4.2-1. Another noticeable change in the microstructure was that some needle like features (see Figure 4.2-2e for a clear view) had formed at the outermost surfaces when the applied tensile stress reached 40MPa and it was still more apparent for sample PC450 80MPa.

It was noteworthy that the two surface layers overlapped each other in the sample 'PC450 80MPa' and some etching pits were observed in the overlap area. Further EDX analysis revealed that inside those voids, high contents of Ti and Al were detected, as shown in Figure 4.2-2 and the quantified results were listed in Table 4.2-1. The particle remaining in the voids after etching contained about 4.46 wt.% Ti while those places outside the voids revealed undetectable amounts of Ti. It is believed therefore that these regions which were less resistant to the etching solution used comprised accumulated trace elements of Ti and Al, possibly from inclusions.

4.2.2 Surface phase identification and composition

XRD patterns of 316L samples before and after plasma carburising treatments under tensile stress from 0MPa to 80MPa are shown in Figure 4.2-3. It can be seen that typical S-phase peaks, FCC structured and shifted to the left side of the austenite peaks, were identified for all plasma carburised samples, which were marked as S(111), S(200), etc.

Comparison of the S-phase peak intensities and positions of carburised samples with and without *in situ* stress shows that the sample carburised with 20MPa tensile stress produced an intensity increase and left-shift of the S-phase peaks. However, when the tensile stress increased to 40 and 80MPa, the S-phase peaks are broader than the 0MPa S-phase peaks and shifted to the right side of the 0MPa S-phase peaks. Meanwhile, a minor peak corresponding to the spacing distance d=0.202nm was detected for these two samples, indicating possible presence of a small quantity of precipitates.

Cross sectional TEM observation on specimen PC450 40MPa revealed that the surface layer mainly consisted of an S-phase layer, as evidenced by the SAD patterns from the layer which shows an fcc structure pattern (Figures 4.2-4 a,b) with the lattice constant (0.369 nm) similar to the that detected by the XRD analysis. A few areas with fine lamellar precipitates were found near the outermost surface layer along S-phase grain and twin boundaries (Figure 4.2-4 and Figure 4.2-5). On indexing of the SAD patterns taken from the areas of precipitation, two kinds of carbides and α-Feprecipitated from the S-phase were observed (Figure 4.2-4c, Figure 4.2-5).

As can be seen in Figure 4.2-4 c, one of the carbides is CrN-like CrC, which possesses a similar crystal structure and lattice constant to CrN. When this thin plate carbide precipitated from S-phase, C and Cr were depleted from adjacent areas of the S-phase, thus leading to the formation of thin plates of α-Fe. After the precipitation of CrC and α-Fe, the original S-phase transformed to γ-Fe with low content of carbon (γ_C). As can be seen in Fig 4.2-4c, three phases with a preferred orientation of:

$[110]_{CrC}//[110]_{\gamma c\text{-}Fe}//[111]_{\alpha\text{-}Fe}$ and

$(002)_{CrC}//(002)_{\gamma c\text{-}Fe}//(1\text{-}10)_{\alpha\text{-}Fe}$.

A similar phenomenon was observed by Li et al. [189] in plasma carburised austenitic stainless steel during annealing. The second kind of carbide identified is $Cr_{23}C_6$ and the diffraction patterns are in fine discontinues rings, as can be seen in Figure 4.2-5. It is believed that this $Cr_{23}C_6$ was transformed from metastable CrC-like carbide under favourable thermodynamic conditions. Clearly, precipitation of carbides occurred in 450°C/10h plasma carburised 316L samples when the applied tensile stress researched 40MPa. However, the amount of the precipitates was very small such that only minor peaks were appeared in the XRD pattern (Fig. 4.2-3)

Figure 4.2-6 showed the TEM focused beam energy dispersive X-ray spectra of the S-phase area at the very edge of surface (a) and 6 μm below the surface (b). The very fine beam of about 6nm allowed much better special resolution comparing to normal SEM EDX analysis. The quantitative results were summarised in Table 4.2-2 and Table 4.2-3. The carbon concentration of the S-phase near the surface and 6μm below the surface was 11.53 and 8.05 at.%, respectively. The value is very close to the typical results given in the literature measured using various different analytical methods [5, 95]. So the supersaturated carbon in S-phase in plasma carburised AISI 316L foil could reach as high as about 12at.% at the surface and gradually decreased to about 8at.% at a distance of 6 μm below the surface.

4.2.3 Tensile strength and hardness

Tensile stress-strain curves of carburised AISI 316L at 450°C for 10hours under different tensile stresses (0MPa, 20MPa and 40MPa) are shown in Figure 4.2-7 and an untreated AISI 316L tensile curve is included for comparison. The ultimate tensile strengths (UTS) of all carburised samples are increased by 5-20% as compared to that of the untreated sample. With higher applied tensile stress during carburising, there was a decrease in the measured UTS.

Figures 4.2-8 (a),(b) revealed the fracture morphology of the 450°C/10 treated sample under 20MPa tensile stress. Like the 450°C/10 treated sample without applied stress (Figure 4.1-14), the fracture surface of the 450°C/10 treated sample under 20MPa tensile stress had a sandwich structure: brittle fracture cases at both surfaces with a ductile fracture band in the middle. Elongated dimples (Figure 4.2-8b) were formed and large area connecting the dimples and shearing bands have a typical pattern of 'tongue' (Figure 4.2-8b) which suggests the specimen became more brittle after the carburising treatment under 20MPa tensile stress.

Further increasing the tensile stress during the 450°C/10 plasma carburising treatment significantly reduced the thickness of the ductile fracture band with dimples in the middle (Figure 4.2-9), which suggests that the amount of remaining austenitic substrate decreased. Therefore, the treated AISI 316L foil became more brittle and cracks were formed in the side surfaces as shown in Figure 4.2-9.

Cross-section micro hardness profiles of the thin foils plasma carburised under different *in situ* tensile stresses are illustrated in Figure 4.2-10. It was revealed that the outermost surface possesses the highest hardness of $900H_{k0.01}$ and the values decreased towards the interface between the substrate and the surface layers for the PC450 0MPa and PC450 20MPa samples. For the PC450 40MPa and 80MPa samples, because the side S-phase surface layers met and overlapped each other, the centre area hardness is also increased from the substrate of 300 $H_{k0.01}$ to 550 $H_{k0.01}$.

4.3 Effect of temperature and pressure on S-phase

In order to study the effect of compressive stresses and temperature on the stability of S-phase, a serial of HIPping treatments were carried out on 500°C/10h plasma carburised samples. The parameters chosen for plasma carburising are traditionally used for bulk 316 stainless steel to form S-phase without precipitation.

4.3.1 Surface layer structures

As shown in Figure 4.3-1, the cross sectional image of the 500°C/10h plasma carburised sample after etching in HCl/ HNO_3 solution Is characterised by a bright top layer of approximately 20 μm in thickness. This surface layer resisted the attack of the etching solution and remained featureless; however, the austenitic substrate was less resistant to the etching solution, revealing grain boundaries and twin boundaries. XDR analysis (Fig. 4.3-6) confirmed that the 500°C/10h plasma carburised surface consisted of a single S-phase without any other phases.

In order to investigate the effect of combined temperature and pressure, the prior-carburised samples (Fig. 4.3-1) were subjected to HIPping treatments. In addition, some samples were also heat treated (HT) using the same thermal cycle of the HIPping treatments in order to separately study the effect of pressure.

Figure 4.3-2(a) shows the sample after heat treatment at 525°C for 10 hours. Comparing with the microstructure of top S-phase layer in the un-heat-treated (or as-plasma carburised sample) condition (Figure 4.3-1), it is apparent that the heat treated S-phase layer showed some features absent in the un-heat-treated sample; several black curves were revealed by the etching solution and some black spots were observed in the top S-phase layer as well. Under same temperature and time with 180MPa isostatic compressive stress, the counterpart by HIPping treatment was shown in Figure 4.3-2b. After etching, except for some black spots at the very surface, the S-phase layer was almost as bright as that of the as-carburised sample (Fig, 4.3-1). Therefore, it implies that no precipitation occurred in the many body of the S-phase during the HIPping treatment.

When the temperature rose to 550°C, and the dwell time was reduced to 5 hours, the effect was very similar to that produced by the heat treatment at 525°C for 10 hours. It can be deducted by comparing Figure 4.3-2(c) with Figure 4.3-2(d) that the compressive stress applied by HIPping depressed the occurrence of black etching features in the S-phase layer, i.e. reduced the possibility of precipitation in the S-phase.. It is noteworthy that increase in the heat treatment time or temperature can reduce the stability of the S-phase and promote the formation of precipitates. However, the compressive stress was

found to be effective in restraining the precipitation process.

Figure 4.3-2(e) illustrates the cross sectional image of the 500°C/10h PC treated sample after heat treatment at 575°C for 1 hour. The S-phase layer was much better in resistance to etching solution comparing to 'HT525 10h' and 'HT550 5h'. However, it might be near the precipitating threshold because small black spots and shallow lines existed in some places. As for the HIPping treated sample with the same thermal cycle (i.e. at 575°C for 1hour), it was clear (see Figure 4.3-2f) that the HIPped S-phase layer was almost the same as as-PCed S-phase implying that no precipitation might occur.

However, the sample HIPped for 2 hours, which is shown in Fig. 4.3-5, was clearly etched. The features revealed grain boundaries, twin boundaries and slip bands. Some areas also appeared black.

At 600°C, the heating effect on the precipitating process was very significant. As shown in Figure 4.3-2g, the top S-phase layer was severely etched revealing black lines along the grain boundaries. HIPping at 600°C for 1hour had a positive influence on retarding the precipitation process. It could be seen in Figure 4.3-2h that the etching lines were not as deep as those in Figure 4.3-2g.

It is generally believed that the black etching lines in S-phase which originally revealed no features are the sign of early precipitation; it caused Cr segregation and became less resistance to the etching solution. As shown in Figure 4.3-3, EDX line scan briefly indicated the segregation tendency of Cr. Another line scan (see Figure 4.3.4) revealed a very thin

oxide layer formed on the top of S-phase for nearly all the heated and HIPped samples largely because of the impurity of argon gas used.

Although the compressive stresses during HIPping can restrain the precipitation process as observed in Figure 4.3-2, it is not omnipotent in depressing the thermodynamic process. The influence is not profound when the treatment temperature increased largely, for example 600°C as shown in Figure 4.3-2h; or when the treatment time extended appropriately, for example 2hours at 575°C as shown in Figure 4.3-5.

4.3.2 Surface layer phase changes

XRD analysis was used to identify the evolution of phase structures of the surface layers of the as-plasma carburised, heat treated and HIPped samples. Figure 4.3-6 showed XRD charts of untreated and PC treated 316 samples. It was easily to identify the S-phase in the as-carburised samples as mentioned in previous sections and by other researchers [2, 106].From the XRD analysis, there were no precipitates or oxides on the top of surface layer after plasma carburising treatment.

Figure 4.3-7 depicts the XRD charts of the HT525 10h and HIP525 10h samples. It is interesting to notice that ferrite (α-Fe) peaks appeared in the sample 'HT525 10h'. The formation of ferrite during high-temperature annealing of S-phase was also observed by Li [206]. As has been discussed in Chapter 2, the S-phase is metastable. If chromium segregates in some phases and then ferrite could become stable, which will be discussed in detail in the next chapter. Therefore, the XRD results gave evidence on the possible

occurrence of precipitates, which is supported by etching images (Figs. 4.3-2 & 4.3-3). However, there were no appreciable peaks of any carbide. This could be related to the relatively low sensitivity of XRD measurement and very limited quantity of precipitates such that no adequate reflection intensity from the carbides could be collected. Another possibility could be that the carbides formed at this stage are meta-stable and not chemically restricted to a known structures and compositions (i.e. non-stoichiometry). Instead, oxide peaks were easily identified as Fe_4O_3, and the HIPped samples showed a stronger intensity in the reflection of the oxides as compared with the heat treated (HT) samples.

The XRD charts for 550 °C treated samples are very similar to that of 525°C treated samples. Figure 4.3-8 clearly illustrated that ferrite existed in the 'HT550 5h' sample. Figure 4.3-9 shows the XRD charts of the 'HT575 1h' sample and it can be seen that in addition to Fe_4O_3, Fe_2O_3 oxide was also formed on the HT sample. However, no appreciable peaks of Fe_2O_3 could be identified on the HIPped sample. It seems that HIPping can delay the formation of Fe_2O_3. No obvious carbide peaks were discovered in these samples. Figure 4.3-10 shows the XRD charts of 600°C heat treated and HIPped PC treated samples. The oxides types were different for HT and HIPping treatments, similar to 575°C treated samples.

Further SEM/FIB and TEM analysis was carried out on two samples: 'HT525 10h' and 'HIP525 10h'. The morphology of the top surface and cross-section image for these two samples were revealed in Figure 4.3-11a, b and c, d respectively. It is clearly showing that

a multi-grain oxide layer (EDX evidenced high oxygen) was formed on both samples while grains are denser and larger for 'HIP525 10h'than for 'HT52510h'. However, the sample'HIP525 10h' developed thicker oxide layer(3.06μm) than that of 'HT52510h'(0.3μm).

Figure 4.3-12 shows BF and DF XTEM microstructures and corresponding SAD patterns for 'HIP525 10h'. It revealed that except for the twin bands, no sign of precipitates are within the sample surface and indexing of all the SAD patterns taken from the sample identified an FCC structure with spots diffusion and elongation, an indication of high residue stress and pre-decomposition stage of the microstructure. However, for sample 'HT525 10h', a top layer of about 0.5 μm showed fine precipitates as evidence by the sharp diffraction rings superimposed with FCC spots pattern (see Figure 4.3-13). Indexing of the patterns, identified a CrN like (in terms of the crystal constant) precipitate, CrC (early precipitation form which was also observed previously in section 4.2), and ferrite under this condition. The TEM results agreed well with the XRD analysis and explained that the minor peaks ($2\theta \approx 44.82°$) in XRD are contributed to these two phases of precipitates. Therefore, it is obvious that the compressive stress applied by HIP facility restrains the precipitation in S-phase at same heat conditions.

4.3.3 Changes of surface layer composition

The depth distribution of the composition of the surface layer after heat treatment and HIPping was analysed by GDS. Figure 4.3-14 shows typical depth profiles of elements in as-carburised 316ASS samples. All important elements in the sample were detected using

GDS method and quantified accordinglystudy the composition changes after different HIPping and heat treatments. The carbon depth profiles of all theses samples formed during the diffusion processes are most valuable.

Figure 4.3-15 shows the carbon depth profile of 'PC ASS', 'HT525 10h' and 'HIP525 10h' samples. It can be seen from the GDS results that the carbon concentration near the surface of 'PC ASS' sample is above 6.5 at.%. The trend of carbon depth profiles revealed that the maximum carbon content near the surface was significantly reduced but the thickness of the surface case was increased after HIPping and HT treatments due to inward diffusion of carbon during these treatments. However, it can be deducted by comparing the carbon depth profiles in the 'HT525 10h' and 'HT 525 10h' samples that the compressive stress applied by HIPping treatment retarded the diffusion of carbon atoms from both the carburised surface cases towards the centre substrate. Consequently, the 'HIP525 10h' sample had a high carbon quantity in the top surface case of about 25 microns but a shallow carbon penetration into the substrate.

Similar phenomenon was observed in Figures 4.3-16, 4.3-17 and 4.3-18 for 550, 575 and 600°C post-treated samples, respectively. All the results reached an agreement that the compressive stress did retard the diffusion of carbon in PC treated 316ASS samples at elevated temperature. This is further supported by the effect of compressive stress levels on the diffusion of carbon at 575°C for 1 hour. As shown in Figure 4.3-17, the carbon depth profile of the 90MPa HIPPed sample ('HIP575 90MPa 1h') was located in-between those of the 0MPa ('HT575 1h') and 180MPa ('HIP575 180MPa 1h') treated samples.

4.3.4 Evolution of surface hardness

Hardness depth profiles were measured by performing Knoop indents on the cross sectional samples. The results were illustrated in Figures 4.3-19, 4.3-20, 4.3-21 and 4.3-22. By comparing these profiles, the following two observations can be made.

Firstly, compared with the as-carburised samples, the hardness of the post-treated samples is generally lower in the near surface areas but higher in the subsurface areas. This implies that diffusion of carbon from the as-carburised surface towards the core may have occurred. This is fully supported by the GDS measured carbon depth profiles shown in Figures 4.3-12 to 15. Secondly, although the difference in some cases is not significant, the HIPping treated samples exhibited slightly higher hardness values than that of correspondingly heat treated samples at the near surface areas. This is in line with the carbon depth distribution in HT and HIPped treated samples (Figs 4.3-15 to 18). Again, this demonstrated that the compressive stress applied during HIPping could slow down the inward diffusion of carbon.

4.4 Effect of tensile stresses on the annealing of carburised 316ASS

4.4.1 Stability of S-phase at elevated temperature under tensile stresses

4.4.1.1 Change of surface layer structure

The carburised layers formed on 316ASS after annealing at different temperatures and under various stresses were observed in cross sectional specimen cutting from the original ‘dog-bone’ sample. Figure 4.4-1a shows the typical S-phase morphology formed on 500°C /10h plasma carburised316ASS. It can be seen that after etching the S-phase

formed on the surface can be easily identified as a featureless layer with thickness about 20 μm.

After annealing at 400°C for 150hours under tensile stresses of 0, 100 and 200MPa, the morphologies of the S-phase layer were illustrated in Figures 4.4-1b, Figure 4.4-1c and Figure 4.4-1d, respectively. Comparing them with Figure 4.4-1a, the thickness of the carburised layer increased with the stress, up to about 23μm for 400 200MPa. However, the effect of stress was not very obvious due to the relative low temperature for annealing at 400°C.

When the temperature was raised to 450°C (as shown in Figures 4.4-1e-g), the carburised layer extended further till about 30μm due to the more active diffusion of carbon. At the top surface, oxide scales could be found and the oxide scale shown in Figure 4.4-1g was thicker than that of Figure 4.4-1e, which meant that the tensile stress promoted the diffusion of oxygen into carburised layer.

The morphology of carburised layer also changed and more etching features were revealed. As shown in Figure 4.4-1f and Figure 4.4-1g, slip bands were observed in the carburised layer, especially in the grains near the surface (see Figure 4.4-1k for magnified view). While for 450°C annealed samples with no applied tensile stress, no such slip bands could be observed in Figure 4.4-1e. More slipping bands were formed under the tensile stress at temperatures above 450°C. The deformation of the sample under tensile tress caused creep and the main morphology was characterised by aggregated slip bands.

Figures 4.4-1h-j came from specimens studied under the highest temperature,500°C. The carburised layers were expanded to about 50μm according to the etching morphologies. Similarly slip bands were found in the top layers. In addition, it was also found that the grain boundaries in the S-phase were preferentially etched (see Figure 4.4-1l for magnified view). Oxide scales also existed at the top surface (Figure 4.4-1h). By contrast, the carburised layer did not show much etching feature after annealing at 500°C for 100hours without tensile stress.

4.4.1.2 Surface layer phase evolution

The XRD charts of carburised 316ASS after annealing at 400°C, 450°C and 500°C under tensile stress were grouped and shown in Fig. 4.4-2, Fig. 4.4-3 and Fig. 4.4-4, respectively. Typical S-phase peaks were shown as 'PC ASS' in each XRD profiles for comparison, which were characterised by left shift of all the original austenitic peaks caused by supersaturation of carbon in austenitic stainless steel. After annealed at elevated temperatures ranging from 400 to 500°C under different levels of tensile stresses, these shifts decreased because of redistribution of carbon. The lattice expansion of S-phase could be calculated by the positions of each peak.

As shown in Figure 4.4-5, by Nelson-Riley plots, the lattice constant of S-phase and its evolution over temperature and pressure could be measured. By extrapolating the fitting linear curve to zero point, it could be obtained that the lattice constant of original 316ASS was about 0.3596 nm and the lattice was expanded to 0.3691 nm after carburising treatment. From the plots, it also could be known that all the other carburised enduring

heat and stress had a lattice constant between these two values. With the increment of heating temperature, the expansion of lattice decreased, therefore it is important to control the using temperature of S-phase. For example, under 400 °C, although the annealing time is 150 hours, the lattice expansion of which is larger than 450 °C for a shorter period of annealing (100hours). Because the property of S-phase is strongly depended on the extent of expanded austenite lattice structure, it is crucial to control the using temperature, especially for long time service. The Nelson-Riley plots also revealed that the tensile stress applied on the sample decreased the lattice expansion by comparing the results at 450 °C. It means that the tensile stress is favourable for the diffusion of carbon atoms in the solid solution states.

Another phase change in the XRD patterns that could be clearly observed was the occurrence of iron oxides, Fe_2O_3 and Fe_3O_4 in stoichiometry but the oxides might contain some other alloying elements like Cr and Ni. No sign of precipitates were detected by the XRD machine used on samples that had been treated at elevated temperature up to 500°C for 100 hours.

4.4.1.3 Composition changes

To study the carbon distributions in these annealed samples with or without tensile stress, WDS analysis was carried out to detect the carbon concentrations along the depth of carburised layer.

The results were shown in Figure 4.4-6. From these profiles, the carbon concentration at the top surface of plasma carburised 316ASS was detected to be 3.8 wt.% and then decreased to 0.8wt.% at 5 m depth. Although detecting carbon concentration by WDS differed from other methods and not very accurate in measuring elements at low quantity, it was still relatively comparable. Carbon was dissipated to about 0.75wt.% after 100hours' enduring at 500 °C. The carbon diffusion distance was increased with the temperature although the maximum carbon concentration decreased.

The carbon profiles agreed well with the SEM images in order to evaluate the thickness of the carburised layer. For example, the carburised layer for creep at 500°C had a thickness of about 50μm and the carbon profile showed higher carbon concentration in sample of 500°C. The WDS analysis gave evidence about the accelerating dissipation of carbon atoms under the effect of tensile stress at elevated temperatures (see 450 °C samples for comparison). Although the lattice expansion obtained from XRD results had already proved that the supersaturation of carbon in the carburised layer had reduced largely after long time enduring at elevated temperature, the carbon profiles showed directly the reduction in carbon comparing to the S-phase.

4.4.1.4 Hardness and strengthening mechanism

In order to investigate the influence of annealing and tensile stress on the mechanical properties of plasma carburised samples, micro hardness depth profiles across the cross section of the surface cases were also measured for all annealed samples.

The hardness of as-carburised case at a depth of 5μm is about 770HV0.025, which gradually decreased with the depth. As shown in Figure 4.4-7, following annealing at 400 °C for 150h, the hardness of the annealed samples decreased but the thickness of the hardened case was increased to about 40 μm. It is noted that the applied tensile stress can, to a lager extent, reduce the reduction in hardness during the 400 °C/150h annealing. For 450 °C/100h annealed samples, similar trend was also observed (Figure 4.4-8) although the stress effect was not so significant. The '450 200MPa' sample began to show a sigmoid trend in hardness distribution, which increased first then decreased.

More significant effect of applied tensile stress was observed for 500 °C/100h annealed samples. The sigmoid tendency was much more obvious in Figure 4.4-9 for samples treated at 500 °C under 200 MPa. The hardness was even as high as the as-carburised sample at the depth of 20 μm. Since the carbon concentration was reduced at elevated annealing temperature, the strengthening effect might be related to the deformation caused by the applied tensile stress.

To understand the hardening mechanism of the sample annealed at 500°C for 100 hours under a tensile stress of 200MPa, the microstructure was examined by TEM. Figure 4.4-10 presents the conventional TEM bright-field images of the specimen. High density of mechanical twins were observed, which is common for deformation microstructure of metals with low stacking fault energy (SFE<20mJ/m^2 for 316 stainless steel). The macro-twin fringes with a scale of 0.5 μm could be observed in Figure 4.4-10a at the both sides of a grain boundary, which is in good agreement with the SEM morphology shown in

Figure 4.4-1. More close examination under a higher magnification revealed nano-twins with a finer scale of about 10nm(Figure 4.4-10b) in the structure. The corresponding selected area diffraction pattern indicated that the nano twins patterns are along the $(1\bar{1}0)$ zone (Fig. 4.4-10c). Figure 4.4-11 depicts two types of twins intercepted with each other, which could contribute to the strengthening effect observed in Figure 4.4-9. Careful TEM observations did not find any precipitates in the surface or along grain boundaries.

Figure 4.3-12 shows the elongation of samples with time (i.e. creep) that had been recorded during the creep tests. Because the sample was subjected to a tensile stress for 100 hours, there would be some creep effect on the materials. Especially at elevated temperature and under 200 MPa tensile stress, the elongation of the specimen was about 0.157 mm in a total gauge length of 31.75 mm, which led to a plastic strain of 0.5% for the sample. At moderate temperatures, for example, the elongation of the PC 450 200MPa sample was only 0.05mm. Comparing to all other samples, the PC500 200MPa sample had the greatest creep; the large deformation caused a high density of crystal defects (such as twins), which would interact with carbon in the S-phase layer.

4.4.2 Oxidation of S-phase under tensile stress at elevated temperature

4.4.2.1 Microstructures

EDX line scans were performed in the cross sectional samples of PC 500 0MPa and PC 500 200MPa. The results were shown in Figure 4.4-13 and Figure 4.4-14, respectively. It can be seen from Figure 4.4-13 that the top layer shown in Figure 4.4-13a is rich in chromium and oxygen and the interface between the top layer and the subsurface is lean in iron. XRD

analysis revealed that two types of oxides, Fe_3O_4 and Fe_2O_3, were formed on the top of carburised layer after long time annealing at elevated temperature in air (Figure 4.4-4). Therefore, it is reasonable to deduct that the top layer shown in Figure 4.4-13a was most probably consisted of two oxide sub layers. It is well known that Fe_3O_4 contains a higher Fe content than Fe_2O_3, and therefore the outside oxide sublayer could be dominated by Fe_3O_4 and the inner side oxide sub layer may contain Fe_2O_3. It can be estimated from the EDX depth profiles in Figure 4.4-13 that the oxide layer of PC 500 0MPa was composed of about 0.5 m thick Fe_3O_4 and 0.5 μm thick Fe_2O_3.

As shown in Figure 4.4-14a, the PC 500 200MPa sample contained a thicker oxide layer. Similarly, based on the XRD (Fig. 4.4-4) and EDX analyses, this surface oxide layer could be divided into two sub layers: Fe_3O_4 (about 1.0 μm) and Fe_2O_3 (about 0.8 μm). As a result, the ratio of Fe_3O_4 over Fe_2O_3 was larger in PC 500 200MPa than that in PC 500 0MPa. Therefore, it can be summarised based on the XRD and EDX results that the tensile stress applied during annealing in air could enhance the oxidation and especially increase the amount of Fe_3O_4 which normally formed at the outside layer.

Another interesting phenomenon observed by SEM (Figure 4.4-14a) is that the oxide intrusion behaviour into the substrate was different for these two samples with and without tensile stress. The yellow line showed in Figure 4.4-14b represented the interface between the oxide layer and metal substrate; however, oxide in both samples grew into the substrate at some points probably due to the surface roughness of the sample. The depth of oxide growth into the substrate was less than 1 μm for the 500 0Mpa sample

(without tensile stress) whilst the PC 500 200MPa sample (with 200MPa tensile stress) had some deeper intrusion larger than 2 μm.

Cross sectional TEM morphology of the oxide layer formed on the PC 500 200MPa sample is shown in Figure 4.4-15. It can be see that the single oxide layer shown in SEM micrograph (Figure 4.4-14a) actually contained two oxide sub layers with different contrast under TEM. The SAD analysis revealed that the outer layer was mainly Fe_3O_4 whilst the inner layer consisted of a mixture of Fe_3O_4 and Fe_2O_3.

The composition of these oxide layers was detected by EDS with a fine beam of about 3 nm and the results are listed in Table 4.4-1. It can be seen that the dense nanocrystalline Fe_3O_4 layer actually contained 7.55 at% chromium and so it should be $(Fe,Cr)_3O_4$. According to crystallography, Fe_3O_4 and $FeCr_2O_4$ have the same group Fd3m with very close lattice constants a= 0.8396 nm for Fe_3O_4 and 0.8379 nm for $FeCr_2O_4$. The partial replacement of Fe^{3+} with Cr^{3+} is believed to increase the oxidation resistance.

The Inner oxide layer consists of nano particles of Fe_2O_3 embedded in the matrix of $(Fe,Cr)_3O_4$, and the effect of tensile stress on the particles size is compared in Figure 4.4-16. As shown in Figure 4.4-16b, the oxide particles distributed in the 500 200MPa sample (Fig. 4.4-16b) are more uniform and smaller (about 25 nm) than the oxide particles (about 40 nm) in the zero stressed 500 0MPa sample (Figure 4.4-16a).

Figure 4.4-17 shows a typical Fe_2O_3 particle embedded in the Fe_3O_4 matrix and its high resolution morphology is given in Figure4.4-18 with the incident beam parallel to the

$[\bar{2}\,21]$ direction. The lattice image can be taken as being constructed with (102) and (110) planes with crystal lattice spacing of 0.366 nm and 0.249 nm respectively. They are slightly smaller than standard value of the corresponding lattice spacing for R-3c Fe_2O_3 but larger than the standard values from Cr_2O_3 of same R-3C group. The EDS composition analysis also proved that it contained 15.55at% chromium.

After understanding the microstructure of oxides formed on S-phase after elevated temperature exposure, it is of importance to study the oxidation behaviour of normal 316 stainless so as to be taken as a reference. Similar procedure was carried out on the AISI 316 stainless steel samples without carburising treatment. For simplicity, oxidation conditions were set at typical 500 °C for 100 hours with and without 200 MPa tensile stress. Then the samples were characterised by XRD and SEM and TEM to analyse the oxide layer.

Figure 4.4-19 shows the XRD patterns of annealed AISI 316 ASS at 500 °C for 100 hours in air with 200MPa tensile stress and with no stress. The XRD charts revealed small peaks of minor oxide layer of Cr_2O_3, and the intensity of the oxide peaks was slightly stronger from the annealed sample under 200MPa tensile stress than from the zero stress annealed sample.

The oxide layer was also characterised by SEM EDX line scan of cross sectional samples. As illustrated in Figure 4.4-20, the oxide layer formed on untreated 316 ASS is quite thin (about 50nm) comparing with those (1000-2000nm) formed on S-phase layer. . The signal

of oxygen was obviously strong showing the presence of the oxide layer and the chromium level was attained at a high level which means the oxides composition could be mainly chromium oxide. The sample treated at 500 °C without tensile stress was also analysed by cross sectional SEM, however, attempt to acquire a line scan was not successful because of the even thinner oxide layer and was outside the limit of the SEM capability. A cross sectional TEM specimen was prepared in order to compensate.

As shown in Figure 4.4-21a, the oxide layer under TEM as appeared to be amorphous with a bright contrast beneath the black protective layer of tungsten. The magnified morphology (Fig. 4.4-21b) showed that the thickness of this oxide layer was about 15nm. Therefore, it is clear that the applied tensile stress is beneficial for thickening the oxide layer formed on both S-phase and normal 316 stainless steel. At the temperature of 500°C, after 100hours, the oxide layer formed on S-phase was much thicker than that formed on the untreated 316ASS. Under 200MPa tensile the thickness was about 1.8 μm for S-phase and about 50nm for normal 316ASS; under zero stress the oxide layer was 1 μm for S-phase and about 15nm for 316ASS.

4.4.2.2 Mechanical properties

The mechanical properties of the oxide layers formed on untreated and PC treated 316ASS samples were measured by nano-indention.

Figure 4.4-22 shows the multiple load-unload curves performed by nano indentation on oxide layer formed on untreated and PC treated 316ASS under 200MPa tensile stress. The

load capacity was not good and the curves were inconsistent for all four different positions. Therefore, the oxide layer formed under 200MPa tensile stress failed to achieve uniform load bearing capacity (arrows showing initiate of layer crack).

Regarding to the oxide layer formed without tensile stress, the results are shown in Figure 4.4-23. All tested points displayed similar curves and showed consistency in load bearing until maximum load was applied. The hardness profiles revealed that the hardness gradient was smaller on the PC treated samples than on the untreated one. In other words, the oxide layer formed on the PC treated sample matched well with the substrate, and therefore it is assumed to avoid crack when subjected to application with compressive stresses.

4.5 S-phase under reciprocating wear

Reciprocating sliding wear tests were conducted on plasma carburised 316ASS samples to study the stability of S-phase under different loads sliding against a WC ball in air without lubrication (Section 4.5.1) and with oil lubrication (Section 4.5.2). For the purpose of comparison, untreated 316ASS samples were also tested under the same conditions.

4.5.1 Dry Sliding Wear

4.5.1.1 Wear factor

The wear factor of PC and untreated 316ASS samples under unlubricated conditions was calculated according to Equation 3.1 in Chapter 3 and the results are summarised in Figure 4.5-1. It can be seen that in the unlubricated wear conditions, the wear factor for both

untreated and plasma carburised samples increased with the increase of applied load; then, a sudden jump in the wear factor was observed at the load of about 40N and 120N for the untreated and plasma carburised materials, respectively .

It is also obvious that plasma carburising greatly enhanced the wear resistance of 316ASS. For example, under 21N load, the wear factor of the untreated 316ASSis 3.02×10^{-13} m^2N^{-1} while that of the PC treated sample is only 1.64×10^{-15} m^2N^{-1}, with a dramatic decrease of about 184 times.

4.5.1.2 Wear track analysis

Figure 4.5-2 depicts the wear track formed in of 21N untreated 316ASS during reciprocating sliding under 21N in air. Figure 4.5-2a revealed severe sliding wear as characterised by deep and wide ploughs with many cracks perpendicular to the sliding direction in the wear track. It is of interest to find that the wear track surface showed typical ‘thin-ice’ failure features normally observed in coated material although the material was not surface treated.

Close examination also revealed white small particles (Figure 4.5-2b), in the wear track. The wear track was rough and had many bumps and craters. To analysis the remaining in the wear track, EDX spectrums were taken from several typical positions, as shown in Figure 4.5-3. The quantified results are listed in Table 4.5-1. It was clearly identified that the main composition of these humps were oxides with iron and chromium. Spectrum 1 was lack of oxygen and rich in chromium comparing to others. Both the large parts of the

bumps (spectrum 3) and discrete isle (spectrum 2), even the very fragile particles (spectrum 4) showed similar compositions containing 20-30 wt% oxygen. Therefore, oxides formed on the contact area during the wear process on 316 ASS sample due to the high flash temperature and contact with oxygen in the air. Under the effect of high contact stress, these oxides layer cracked because of the unmatchable strength of the plastically deformed substrate and the brittle hard oxide layer. The oxides were cracked into small pieces and particles and removed by the sliding movement. For example, Position of spectrum 1 was the place where the oxides were just broken and removed, thus forming a crater into the S-phase layer.

Another supporting evidence is that high tungsten content was detected from the humps (Spectrums 2-4) in the wear track; however, very low content of tungsten was identified in the crater (Spectrum 1). This is because the tungsten carbide ball contacted the stainless steel surface during the sliding wear and a small amount of W was transferred onto the counterface. Therefore, the adhesive wear mechanism might have contributed to the wear process. In addition, the oxidation process also played a role in the wear process. However, the wear process of the untreated 316 stainless steel should have been predominated by severe sliding wear as evidenced by the large plastic deformation/ploughing.

Figure 4.5-4 shows the wear track formed in PC 316ASS under the same wear conditions. Apparently, the morphology of the wear track was relative smooth and different from that of untreated one (Fig. 4.5-2a), where bumps could hardly be found in the wear track.

Instead, parallel shallow grooves along the sliding directions were observed. These features are the evidence of abrasive wear. Further EDX analysis on these features (Figure 4.5-5) gave different compositions (listed in Table 4.5-2) with that of untreated samples. The oxygen level is lower which means less oxygen was introduced when sliding wear took place. This could be aroused by the decrease of flash heat transferred to the surface due to minor plastic deformation and material transfer as well as relatively smooth wear track surfaces. Accordingly, the tungsten level in the wear track was also lower in the PC treated sample than in the untreated one.

Meanwhile, few loose particles of isles of oxides could be found in the wear track. This phenomenon could be explained by the fact that the hard oxide layer could be mechanically supported by the PC treatment enhanced substrate, causing the whole surface to become more wear resistant. Therefore, S-phase enhanced the austenitic stainless steel and thus changed the wear mechanism: mild abrasive wear was dominant over adhesive wear. Besides, oxides formed on the top surface gained stronger support from the beneath layer of S-phase than just austenitic substrate. Therefore, oxidation wear dominated the wear process of PC treated austenitic stainless steel.

However, when the applied load exceeded 120N severe sliding wear also occurred to the PC treated austenitic stainless steel. The wear track appeared similar to the one formed in the untreated materials (Fig. 4.5-2) dominated by severe ploughing. This is largely because when the applied load was above a critical load (120N in this study) ‘thin ice’ effect would also take place. Without firm mechanical support, the oxide films formed

would be damaged and removed rapidly as observed in the sliding wear of untreated austenitic stainless steel.

4.5.1.3 EBSD analysis

EBSD analysis of cross sectional samples from both untreated and PC treated 316ASS revealed the phase evolution during the wear process. Martensite was found to be formed during wear (see Figure 4.5-6 for denotation of each phase and orientation). However, the phases of surface layer were not simply martensite because of the oxidation. Dry wear effect on untreated 316ASS sample caused the surface to transform from FCC structure to BCT martensite as shown in Figure 4.5-7. It also denoted that the FCC substrate formed several sub-grain orientations due to the severe plastic deformation.

Figure 4.5-8 shows the EBSD results of wear on PC treated sample under 95N. It is noticeable that the overall top S-phase layer remained unchanged, no sub-orientations and martensites. However, phase transformation may have occurred at the very surface of the S-phase case. Beneath the S-phase layer, the austenitic structure was unstable and formed martensite and more sub-grain orientations were observed. Meanwhile, the interface between the S-phase case and the substrate austenitic phase was apparent in the EBSD orientation map.

4.5.2 Oil Lubricated Sliding Wear

4.5.2.1 Wear factor

Reciprocating wear tests with lubricants were also performed on untreated and PC treated 316ASS samples. Mineral oil was used as lubricant and different loads were applied on the samples to study the wear mechanism and stability of S-phase.

After tests, the wear tracks were measured and all wear factors were calculated and illustrated in Figure 4.5-9. The lubricating effect was obvious if the wear factor curves were compared with that shown in Figure 4.5-1 for unlubricated wear. For untreated material, the rapid increase in wear factor occurred at around 150N, which is significantly higher than that observed in unlubricated wear. The wear factor during the stable stage reduced from about 300 to 2 $\times 10^{-13}$ m^2N^{-1}, representing a factor of 150 times reduction in wear factor.

For PC treated S-phase, the increase in wear factor with the applied load was very slow and no sudden change in wear factor was observed until 900N. The average wear factor was about 1-1.5 $\times 10^{-13}$ m^2N^{-1}, which is at least 200 times lower than that for untreated material tested under the same conditions.

4.5.2.2 Wear track analysis

Figure 4.5-10 shows the wear track formed in untreated 316 ASS by sliding against a ball WC under 56N and oil lubricated conditions. It can be seen that adhesive wear still existed but with less ploughing and material transfer. No sign of oxide particles were found in the

track and there were some adhesive craters along with many fine parallel marks on the surface of wear track. The compositions of these features as shown in Figure 4.5-11 were probed by EDX and the results were listed in Table 4.5-3. It is demonstrated that the oxygen level is much lower than that of a dry wear and tungsten level was also lower. This means that the extent of adhesive wear was reduced by oil lubrication. However, carbon is higher which could be introduced by the oil when local heat may produce some carbon on the surface.

Figure 4.5-12 illustrates the SEM image wear track formed in PC 316ASS by sliding against a ball WC under 214N and oil lubricated conditions. Clearly, the morphology of the wear track was different from the wear track in untreated material. Abrasive wear marks were clearly observable. The EDX analysis (Figure 4.5-13 &Table 4.5-4) of the wear track revealed similar compositions to the untreated one, but with even lower oxygen level.

Wear track of PC treated samples under higher load revealed similar morphology as shown in Figures 4.5-14a (529N) and b(739N). Therefore, the wear mechanism should be similar under variation of applied loads within this range.

4.5.2.3 EBSD analysis

EBSD results in Figure 4.5-15 showed that no martensite or sub orientation happened in the S-phase layer or substrate under the load of 95N. The interface between the S-phase and the substrate austenite was not clear. Therefore, under low load, the wear process did not change the S-phase structure or the austenitic substrates beneath.

From the wear factor curves, it is noteworthy that the value attained a plateau after the load exceeded the 599N. Therefore it is necessary to analyse what happened to the structures under that high load and even further. As schemed in Figure 4.5-16, two EBSD positions were chosen from the cross section of each sample after wear under 599N and 739N.

When the load increased to 599N (Figure 4.5-17a), martensite was transformed from the substrate austenite under the contact area. It is believed that the stress status changed from very high compressive stress right beneath the contact position to minor tensile stress at the bump side. From EBSD analysis, it was demonstrated that martensite formed in the austenitic substrates under S-phase. However, the bump side formed much less amount of martensite and the S-phase is stable under this high load.

Further increase the applied load to 739 N(see Figure 4.5-18), the amount of martensite formed in the original austenite substrate under the contact position increased as expected. However, the S-phase layer still showed no changes under this load. The abundant marteniste formed under the S-phase can strengthen the substrate and lead to the decrease of wear factor. Martensite was also found at the bump side, which means that the martensite formed not only under compressive stress.

A common phenomenon was observed in the EBSD images of above all, that is the identification of interface of S-phase and austenitic substrate. When the load was low (for example 95N) , the interface was hard to be identified form the orientation map (in Fig.

4.5-15b). When the load increased, the plastic deformation also increased and the interface became clear (Figs 4.5-17 & 18). As generally believed, S-phase is formed by diffusion of interstitial atoms; therefore the composition is continuous across the interface and also the crystalline structure is the same FCC as the substrate. Interestingly, the action to severe deformation of S-phase is totally different from the substrate.

4.6 Residual compressive stress in S-phase and surface deformation

A sample carburised at 450°C for 10hours forming S-phase layer on the 316ASS substrate uniformly is shown in Figure 4.6-1. The carbon taken in the layer was characterised by GDS. The maximum carbon concentration could be estimated above 2 wt.% from Figure 4.6-2.

The residual stress in this PC treated sample was measured by the $\sin^2 \psi$ method using the diffracted peak S(222) at 2θ=92.877°(Figure 4.6-3). The diffraction peak S(222) typically belonged to S-phase which was shifted left side from the diffraction peak γ(222) of original austenite phase. This high-angle diffraction peak was chosen to ensure higher sensitivity to strain. For residual stress tensor evaluation, measurements were carried out at five ψ angles, (-18°,-9°,0°,9°,18°) with φ angle at 0°. The peak intensity of each ψ angle and the peak after correction (peaks beneath the high ones) by the software were shown in Figure 4.6-4. The fitting results were illustrated in Figure 4.6-5. After stress calculation, the residual stress in the S-phase formed at the top surface was evaluated to be -2208(+/-172) MPa for the normal stress and 132(+/-16) MPa for the shear stress. Such a large residual stress could be accompanied by deformation of morphology.

The sputtering effect in GDOES by collision of argon iron to the surface could remove the surface layer gradually with a fixed diminishing rate. It was interesting to observe the surface morphology after sputtering for a very short period of time. Figure 4.6-6 revealed the SEM image of the polished AISI 316ASS after sputtering for 10 seconds, in accordance to the removal of surface layer roughly about 0.2 μm. The morphology showed some feature of twin and persistent slip bands.

However, when sputtering procedure was carried out in plasma carburised AISI 316ASS, the situation changed greatly (see Figure 4.6-7). Much more abundant of persistent slip bands could be observed in the scope. Due to the angles between slip bands in various grains, the grain boundaries were clearly illustrated as well as each twin boundary. Magnified SEM image in Figure 4.6-8 revealed that the slip bands had a spacing distance about 1 μm and varied between different grains due to the orientation. Glide steps could also been observed across the main persistent slip bands. By comparing these different morphologies of untreated and plasma carburised AISI 316ASS, it is known that the surface deformation was large in S-phase corresponding with 2.2GPa compressive residual stress.

EDX analyses were taken from two different positions: extrusion and intrusion, which was shown in Figure 4.6-9. The spectrum from the extrusion spot showed slightly higher carbon intensity than that of the intrusion spot. Although it was less evidential to say that the extrusion part had higher carbon concentration than the intrusion counterparts originally, but it could be estimated that the extrusion of persistent slip bands were

formed due to the surface deformation caused by carburising treatment. And the ion beam of GDS cleaned the loose deposit (formed during PC) on the surface and revealed the extrusive tomography clearly.

Figure 4.6-10 shows a 3D topological image taken by AFM from the as-plasma carburised 316ASS sample. Before carburising treatment, the sample was polished using progressively finer grades of diamond paste and finally slighted etched using colloidal silica to finish it to a smooth and flat surface and also diminish the residual stress which could caused by polishing.

Then after plasma carburising at 450°C for 10 hours, the surface was detected by AFM with tapping mode. The position was chosen at the position where the persistent slip bands occurred. Cross sectional height profile was take from the topological image and illustrated in Figure 4.6-10(b). It was interesting to find that the interval of slip bands was 1.5 μm and the maximum height of the extrusion was about 450nm.

However, the extrusion obviously came from the slip bands of the surface layer. Generally speaking, the slip bands were caused by the deformation of the surface layer. As measured by XRD residual stress test, the compressive stress was about 2.2 GPa as an average of the top X-ray penetration layer. It was an extreme high tress which could arouse deformation of the surface layer. Evidence could be found in previous sections of this chapter, when plasma carburised treatment was carried out on the 316L stainless foils, the shape of the sample was curved from straight shape. In this bulk sample, the shape

deformation of the surface layer was constrained by the substrate and as a consequence, the deformation was allowed in slip bands so that from the surface, persistent slip bands could be observed.

5 Discussion

5.1 Effect of tensile stresses on the formation of S-phase during carburising treatment on 316L ASS

The experimental results had clearly demonstrated that different outcomes were achieved by PC treatment with 316L ASS foils with different *in situ* tensile stresses. In this section, the influences of tensile stresses on the S-phase were separated into two subsections and discussed as follows.

5.1.1 Effect on the diffusion of carbon atoms

It is generally believed that the PC treatment is a diffusion process, which is to introduce carbon atoms into the interstitial positions of austenitic substrate. The fundamental equation to describe the diffusion process is Fick's second law [207]:

$$\frac{\partial C}{\partial t} = \frac{\partial}{\partial x}\left(D\frac{\partial C}{\partial x}\right) \quad (5.1\text{-}1)$$

where x is the diffusion distance (m), C is the concentration of diffusion species, t is the diffusion time (s) and D is the diffusion coefficient (m^2/s).

Assuming the diffusion coefficient D is independent of concentration (in the special case of a constant diffusion coefficient), the Fick's second law could be written as follows:

$$\frac{\partial C}{\partial t} = D\frac{\partial^2 C}{\partial x^2} \quad (5.1\text{-}2)$$

This second-order partial differential equation may be solved for various boundary conditions. One case of a boundary condition is semi-infinite, when the concentration of the diffusing species A is held constant at the surface of material B which is being diffused through and is semi-infinite in extent. Assume that the initial concentration of species A throughout the semi-infinite calculation is C_0 and the concentration of A at the surface is raised to C_s and maintained at that value for time t.

Then the solution of Fick's Law is [208]:

$$\frac{C_x - C_0}{C_s - C_0} = 1 - \mathrm{erf}\left(\frac{x}{2\sqrt{Dt}}\right) \quad (5.1\text{-}3)$$

where C_x is the concentration of the diffusion atom A at location x after time t and erf is the error function which is defined as follows:

$$\mathrm{erf}(x) = \frac{2}{\sqrt{\pi}} \int_0^x \exp\left(-y^2\right) dy \quad (5.1\text{-}4)$$

For a given $C_x = C_1$ (C_1 is defined as the concentration of diffusion species at the interface between the diffusion zone and the substrate), it can be deduced that

$$\frac{C_1 - C_0}{C_s - C_0} = const \rightarrow \left(\frac{x}{2\sqrt{Dt}}\right) = const \quad (5.1\text{-}5)$$

Therefore,

$$x^2 = kDt \tag{5.1-6}$$

where k is a constant

If t=constant for each diffusion process,

$$x^2 = k'D = k'D_0 \exp\left(-\frac{Q}{RT}\right) \tag{5.1-7}$$

In which k' is another constant, D_0 is independent of temperature and Q is the activation energy, T is the absolute temperature and R is a gas constant.

$$\ln(x^2) = ln(k'D_0) - \frac{Q}{RT} \tag{5.1-8}$$

Therefore,

$$\frac{d(lnx^2)}{d(\frac{1}{T})} = -\frac{Q}{R} \tag{5.1-9}$$

Therefore, in the graph of $\ln(x^2)$ against 1/T, the activation energy of diffusion could be evaluated from the slope of the linear relationship.

It is noteworthy that the semi-infinite diffusion model describing the carburising treatment is not always accurate in every circumstance. Especially in the case of very thin foil when in the core part of sample the carbon profiles from two end sides overlapped each other, the carbon source is believed to be placed at both sides, therefore the accurate initial and boundary conditions for a thin foil(with a thickness h) diffusion model should be:

$$\begin{cases} C(x,0) = C_0 \\ C(0,t) = C_s \\ \frac{\partial C(\frac{h}{2},t)}{\partial x} = 0 \end{cases} \qquad (5.1\text{-}10)$$

In this case, the solution is not as simple as the semi-infinite case. However, at low temperature and short period of treating time, the two carburised layers are still too thin to overlap each other. Therefore, it is appropriate to use the semi-infinite model to simplify the diffusion solution and deduce the diffusion parameters easily. In the case of PC treatment of 316L ASS 50 μm thick foil, 450 °C/10h produces a thin layer which satisfies the semi-infinite conditions mentioned above. But it definitely cannot apply to 450 °C/20h PC treated samples, and boundary conditions of 5.1-10 should be considered instead. In the following discussion, carburised samples below 450 °C for 10hours were used to use the semi-infinite model.

In order to evaluate the influence of tensile stress on the diffusion process, especially an

important parameter like activation energy, it is necessary to know the diffusion depths achieved through different treatment temperatures. Figure 5.1-1 shows SEM microstructures of carburised layers obtained from three different treatment temperatures (400, 425 and 450°C), with and without 40 MPa *in situ* tensile stress.

The surface layer thickness measured from the cross-sections of the carburised samples is summarised in Figure 5.1-2. It can be seen that the thickness of the surface treated layers increased with treatment temperature irrespective of the application of *in situ* tensile stress. It is also clear that when treated at the same temperatures the applied *in situ* tensile stress can significantly increase the thickness of the surface treated layers. It is of interest to note that the deviation of layer thickness from a straight line relationship is larger for the *in situ* stressed samples than for the stress-free samples.

According to the slope of the linear lines, the diffusion activation energy of carbon was estimated to be 142.76(±1.41) kJ/mol with no tensile stress and 133.91(±2.12) kJ/mol with 40MPa tensile stress. Therefore, the *in situ* 40 MPa tensile stress decreased the diffusion activation energy by about 9kJ/mol. This means that tensile stresses applied to the sample during plasma carburising make the diffusion process faster.

During the carburising treatment, carbon atoms were introduced into the substrate austenitic structure as interstitials. A large amount of supersaturated carbon in S-phase (above 12 at.%) increased the lattice constant of austenite and a very high level of compressive stress was reached in the S-phase layer. Hence, applied *in situ* tensile stress

may have a positive effect on the system by partially cancelling the compressive stress associated with the formation of the S-phase layer, thus benefiting the process of carbon diffusion.

5.1.2 Effect on the precipitation

The effect of tensile stress proved to be favourable for increasing the thickness of S-phase. However, when the stress exceeded 40 MPa, fine precipitates appeared near the surface. At the early stage of S-phase decomposition, metastable CrN-like CrC precipitated from the expanded S-phase. Meanwhile, $M_{23}C_6$ was found along grain boundaries near the surface (Figure 4.2-5). The decomposition of S-phase can be deemed as non-continuous precipitation. The products of decomposition prefer to nucleate at the grain boundaries or near the surface and then grow inwards. Limited by the low diffusion coefficient of substitutional alloying atoms at the carburising temperature (e.g. the diffusion coefficient of Cr is only 10^{-21} m^2/s [209]), these precipitates exhibit nanoscale lamellar structures.

With the precipitation of carbides, the lattice expansion of S-phase is decreased. Figure 5.1-4 shows the lattice constant of S-phase as a function of increasing applied tensile stress obtained from XRD (311) diffraction. It can be seen from the curve that the lattice constant first increased with applying 20 MPa tensile stress before an abrupt drop at 40 MPa which agrees well with the precipitation observed in the specimen treated at that stress condition.

The effect of applied *in situ* tensile stress on the precipitation of $M_{23}C_6$ (M denotes

substitutional atoms such as Fe, Cr, Ni) from supersaturated S-phase may be evaluated from the thermodynamic standpoint. The Gibbs free energy of $M_{23}C_6$ can be written as follows:

$$G^{M_{23}C_6} = \Delta G^{M_{23}C_6} + 23G_M^{\alpha} + 6G_C^{G} \quad (5.1\text{-}11)$$

where, $\Delta G^{M_{23}C_6}$ is the formation energy of $M_{23}C_6$, G_M^{α} and G_C^{G} is the Gibbs free energy of ferrite and graphite respectively.

When $M_{23}C_6$ is formed from the original austenitic phase γ (which is supersaturated with carbon atoms), the austenitic phase γ_1 (which contains carbon atoms in solution at its equilibrium state) remains in the phase structure. The driving force ΔG_N of $\gamma \rightarrow M_{23}C_6 + \gamma_1$ can be expressed by:

$$\Delta G_N^{\gamma \rightarrow M_{23}C_6+\gamma_1} = \frac{1}{6} x_{M_{23}C_6} G^{M_{23}C_6} - G^{\gamma}|_{x_\gamma} - \left(x_{M_{23}C_6} - x_\gamma\right) \frac{dG^{\gamma}}{dx}|_{x_\gamma} \quad (5.1\text{-}12)$$

here, x is the mole fraction of carbon in each phase denoted by its subscripts. The thermodynamic derivations and the physical meanings of the parameters can similarly refer to the literature [210]:

$$G^{\gamma} = x_\gamma\left(G_C^{G} + RTlna_C^{\gamma}\right) + \left(1 - x_\gamma\right)(G_M^{\gamma} + RTlna_M^{\gamma}) \quad (5.1\text{-}13)$$

$$\frac{dG^{\gamma}}{dx}|_{x_{\gamma}} = G_C^G - G_M^{\gamma} + RTln\frac{a_C^{\gamma}}{a_M^{\gamma}}|_{x_{\gamma}} \quad (5.1\text{-}14)$$

Substitute equations (5.1-13) and (5.1-14) into (5.1-12), it can be derived as follows:

$$\Delta G_N^{\gamma\to M_{23}C_6+\gamma_1} = \frac{1}{6}x_{M_{23}C_6}\left(G^{M_{23}C_6} - 6G_C^G - 23G_M^{\alpha} - 6RTlna_C^{\gamma}\right) + \left(1 - x_{M_{23}C_6}\right)(\Delta G_M^{\gamma\to\alpha} - RTlna_M^{\gamma}) \quad (5.1\text{-}15)$$

The driving force of γ → α was given by [211, 212]:

$$\Delta G_N^{\gamma\to\alpha} = \Delta G_M^{\gamma\to\alpha} - RT\ln\alpha_M^{\gamma} \quad (5.1\text{-}16)$$

Accordingly,

$$\Delta G_M^{\gamma\to\alpha} = 141\sum x_i\left(\Delta T_M^i - \Delta T_{NM}^i\right) + \Delta G_{Fe}^{\gamma\to\alpha} \quad (5.1\text{-}17)$$

where x_i is the mole fraction of each element i, ΔT_M^i and ΔT_{NM}^i are Zener parameters and can be found in references [213, 214] and listed in Table 5.1-1.

$$\Delta G_{Fe}^{\gamma\to\alpha} = 20853.06 - 466.35T' - 0.0046304T'^2 + 71.147T'\ln T' \quad (5.1\text{-}18)$$

$$T' = T - 100 \sum x_i \Delta T_M^i \quad (5.1\text{-}19)$$

The Gibbs free energy and thermodynamic parameters are taken from CALPHAD by Lee [215].

The activity coefficient can be calculated according to [210]:

$$\ln \alpha_M^\gamma = \left\{ \ln \left[\frac{(1 - Z_\gamma x_c^\gamma)}{1 - x_c^\gamma} \right] \right\} / (Z_\gamma - 1) \quad (5.1\text{-}20)$$

where $Z_\gamma = 14 - 12 \exp(-1250/RT)$ (5.1-21)

R is the gas constant.

Suppose the $\gamma \rightarrow M_{23}C_6 + \gamma_1$ transformation follows the steady state nucleation rate equation [216, 217]:

$$J_S^* = C \cdot D \cdot exp\left(-\frac{\Delta G^*}{kT}\right) \quad (5.1\text{-}22)$$

where J_S^* is the flux of the diffusing material, C is the concentration and ΔG^* is the energy barrier for diffusion; k is the Boltzmann constant and T is the absolute temperature.

According to the model proposed by Feder and Lange [218, 219], the incubation time τ for

a new nuclei forming on the substrate surface is expressed in the equation, which represents the time required for forming a single layer of second phase β on the surface of substrate :

$$\tau = \frac{8kT\gamma a^4}{V_\beta^2(\Delta g_v + w)^2 D\chi_\beta} \quad (5.1\text{-}23)$$

where γ is the interfacial energy, a is the lattice constant, V_β is the molar volume, Δg_v is the free energy change per unit volume for nucleation and w the sum of the dilatational and shear strain energies and k the Boltzmann constant. D is the diffusion coefficient of the faster diffusing element and χ_β is the carbon atom fraction in austenite. The carbon diffusion coefficient D in AISI 316L was taken from the experimental results given by Agarwala [220],

$$D = 1.9 \times 10^{-5} \exp\left(\frac{-156482}{RT}\right) m^2/s \quad (5.1\text{-}24)$$

If all the equations above are rearranged and and the incubation time for $M_{23}C_6$ formation from carbon-supersaturated austenite is calculated for three different carbon concentrations (0.15, 1.5 and 15 at.%), with, for simplicity, M as Cr, the temperature-time chart of $Cr_{23}C_6$ is shown in Figure 5.1-5. Compared to experimental results from literature

[202], the simulated incubation time is a little shorter. However, it is reasonable that the very early stages of $Cr_{23}C_6$ precipitation are undetectable by XRD, and for the further growth of $Cr_{23}C_6$, which is controlled by the diffusion of Cr and retarded for longer time due to the low diffusion coefficient mentioned above. This simulation confirms that the S-phase is not stable at elevated temperatures. The S-phase formed in austenitic stainless steel, if not decarburised, can undergo no decomposition for years at temperatures below 200°C. However, the decarburisation process is not avoidable at temperatures >350°C (D_C>$10^{-18}$$m^2$/s).

Considering the effect of *in situ* stress, the strain energy caused by 40 MPa tensile stress is small (1%) as compared to the energy of phase transformation, so its contribution could be neglected. Therefore the main factor which influences the incubation time will be the diffusion activation energy. As discussed above, the activation energy is decreased by about 9 kJ/mol under 40 MPa applied tensile stress. It is reasonable to assume that the incubation time is inversely proportion to the diffusion coefficient. Hence, the ratio of incubation time with (τ_s) and without (τ) tensile stress can be expressed as:

$$\frac{\tau_S}{\tau} \cong \frac{D}{D_S} = \exp\left(-\frac{\Delta Q}{RT}\right) \qquad (5.1\text{-}25)$$

here, ΔQ is the deficiency of activation energy caused by external stress. The results are illustrated in Figure 5.1-6 and it can be seen that the applied tensile stresses decrease the

incubation time for $Cr_{23}C_6$ precipitating from S-phase. For example, at 450°C, the incubation time will be reduced by about 75% with 40 MPa stress (ΔQ = 9kJ/mol).

Therefore, it is demonstrated by thermodynamic calculations that the tensile stress applied on the samples during plasma carburising can stimulate the carbon diffusion and increase the thickness of S-phase. Meanwhile, the precipitation process is also accelerated by *in situ* tensile stress.

5.2 Stress effect on the stability of S-phase at elevated temperature

The stability of S-phase is of great importance both from a scientific aspect and industrial applications. The paraequilibrium state of the expanded austenite with supersaturated carbon or nitrogen interstitials can change to stable states. As previous researchers discovered (see section 2.4.3), more stable phases of carbides or nitrides replaced the phase of supersaturated interstitials when annealing at elevated temperatures for a certain period of time. And the different products of the decomposition processing of S-phase (e.g. $Cr_{23}C_6$, (Cr,Mo)C, CrN and ferrite) depend on the substrate (basic compositions of austenitic stainless steel) , processing (carburising or nitriding) and subsequent annealing conditions (temperature and time).

The use of S-phase under stress conditions is very common in industrial applications (e.g. valves, hydro tubes and bearing components). However, the stability of S-phase under stress has not been investigated by previous researchers. In this chapter, the effect of two different conditions of stress will be discussed based on the experimental results reported

in Sections 4.3 & 4.4.

5.2.1 Effect of isostatic compressive stress

The isostatic compressive stress is applied to the carburised 316 ASS by hot isostatic pressing (HIPping). By comparing the carbon profiles of specimen after annealing with and without compressive stress (Figures. 4.3-15, 16, 17 & 18), it is obvious that the compressive stresses do suppress the diffusion of carbon atoms at every combination of temperature and time. This is evidenced by the fact that the carbon concentration in the near surface (about 15-20 μm) layer is higher but the total carbon diffusion depth is shallower for samples annealed under compressive stresses (i.e. HIP) than for samples annealed under zero stress (i.e. HT) at the same temperature ranging from 525-600°C. This effect is enhanced by the increase in the compressive stress applied (see Figure 4.3-17).

To understand the effect of compressive stress on the diffusion of carbon analytically, annealing treatments under both compressive stress and zero stress at three temperatures (550°C, 575°C and 600°C) for same treatment time (1 hour) were carried out on as-carburised samples. The GDS results showing the carbon profiles were compared in Figure 5.2-1 for zero stress and Figure 5.2-2 for 180 MPa compressive stress respectively. The carbon profile of original carburised sample was illustrated in the previous section and again in Fig. 5.2-3 for reference.

The quantity of carbon detected by GDS is in relatively good accuracy and here the

thicknesses of the S-phase are determined roughly by the carbon profiles where the carbon concentration gradually decreased to a plateau of low value. However, the depth of S-phase cannot be just determined by the carbon profiles. With the combination of SEM results of cross sectional samples after etching, it is much more reasonable to determine the critical point of the interface of S-phase and the substrates. However, unlike the processing of diffusion equation for PC treatments as discussed in Section 5.1, it is impossible to deduce the diffusion parameters from the final thickness of carburised layer. This is because the final thickness of the S-phase layer depends on the thickness of as-carburised layer and the inward diffusion during HIPping and heat treatments. For the problem of stability of S-phase after exposure to elevated temperature, it is a diffusion process with limited source of carbon which is introduced by previous PC treatment. The situation is complicated comparing with the jPC treatment along, when the source of carbon is considered unlimited and the concentration is fixed in the carburising atmosphere.

In order to solve the problem of carbon diffusion in the study and then analyse the stability of S-phase under thermo and stress conditions, it is necessary to review the diffusion equation.

$$\frac{\partial C}{\partial t} = D\frac{\partial^2 C}{\partial x^2} \qquad (5.2\text{-}1)$$

The equation describing the diffusion process is based on one assumption that the

diffusion coefficient is unchanged with the concentration. Then the equation can be simplified and solved according to different boundary conditions and assumptions.

First of all, the general initial boundary conditions for the differentiation equation of this kind are shown as following:

$$C(x,0) = \begin{cases} f(x), & (x_1, x_2) \\ 0, & (-\infty, x_1); (x_2, +\infty) \end{cases} \quad (5.2\text{-}2)$$

It means that at the initial state (t=0), the diffusion elements are constrained in the range from x_1 to x_2; outside this range the concentration is deemed to be zero.

In the case a solution for the stability of S-phase, the distribution function *f*(x) is assumed to be the carbon profile of PC ASS prior to all the HIPping and annealing treatments. As shown in Fig. 5.2-3, the carbon atoms dissolved in the specimen after plasma carburising treatments are constrained in the surface case within a depth of about 40 μm. Therefore, the specified parameters x_1 and x_2 are zero and 40 μm, respectively.

One solution of the diffusional equation with the initial states mentioned above is written as [221]:

$$C(x,t) = \frac{1}{2\sqrt{\pi D t}} \int_{x_1}^{x_2} f(\xi)\, e^{-\frac{(\xi - x)^2}{4Dt}} d\xi \quad (5.2\text{-}3)$$

However, it is still in a complicated form and difficult to solve by using currently known experimental parameters. Therefore, a further assumption is needed to simplify the solution.

If the diffusion elements initially congregated near the zero position and within a narrow range, which means the source of the diffusion element are constrained in a small area rather than a continuous distribution over the long range the solution can be simplified to be:

$$C(x,t) = \frac{Q}{2\sqrt{\pi Dt}} e^{-\frac{x^2}{4Dt}} \qquad (5.2\text{-}4)$$

Here, Q is the quantity of diffusion element per unit area. In the practical application of this case, Q is the integration of Fig. 5.2-3 in the range of highest carbon concentration to the value discussed. The assumption made here is reasonable for analysing this problem because S-phase is supersaturated in carbon atoms (above 12at.%) at the outermost surface. Therefore the carbon atoms congregate mostly within the outer thin layer and induce inward diffusion to the substrate.

In order to easily evaluate the diffusion coefficient of carbon by exposure to different temperatures, the concentrations at zero point are considered for analyses. Simply and

mathematically, by choosing x=0 in equation 5.2-4, the exponential component is degenerated to 1 and it can be written as:

$$C(0,t) = \frac{Q}{2\sqrt{\pi D t}} \qquad (5.2\text{-}5)$$

In the case of 1 hour exposure at elevated temperature, all other parameters of the equation are known to calculate the value of D. The results are listed in Table 5.2-1.

Hereby the diffusion coefficients for all conditions are calculated. By comparing the results, it is apparent that the diffusion coefficient increases with temperature from 550°C to 600°C regardless of stress, i.e. with or without compressive stresses.

Meanwhile, the diffusion coefficient of carbon during HIPping under an isostatic compressive stress of 180 MPa is smaller than that of stress-free-counterpart at different temperatures of 550 °C, 575 °C and 600 °C. Although the diffusion process can be approxmately evaluated by the final thickness of the carbon rich layer shown in Figures 4.3-15 to Figure 4.3-18, it is now much more precise to know the effect of compressive stress and thermal effect by comparing their corresponding diffusion coefficients.

Furthermore, if the diffusion coefficient is temperature dependent with the Arrhenius equation:

$$D = D_0 e^{-\frac{Q}{RT}} \quad (5.2\text{-}6)$$

with parameters having the usual meaning: Q is the activation energy for carbon diffusion in the austenitic stainless steel, R is the gas constant and T is the absolute temperature.

To estimate the activation energy of carbon diffusion during annealing, InD is plotted against 1/T (Figure 5.2-4) and the activation energy for heat treatment without stress and HIPping under 180 MPa compressive stresses is evaluated to be about 125.1 and 157.1 kJ/mol, respectively. The activation energy of HIPped samples under 180 MPa compressive stress is about 32kJ/mol higher than that of heat treated samples at zero stress. As discussed in Section 5.1.1, inward diffusion of carbon during the formation of S-phase caused lattice expansion and the resulting residual compressive stress. Therefore, the applied tensile stress during the formation of S-phase can promote the diffusion of carbon and consequently reduce the activation energy. On the other hand, the compressive stress during the HIPping would retard the inward diffusion of carbon in S-phase. It is then predictable that the compressive stress is favourable in suppressing the precipitation in S-phase according to the model proposed in Section 5.1.1.

It is noteworthy that the activation energy (which is 125.1 kJ/mol) obtained from annealing of S-phase without compressive stress is smaller than that (which is 142.8kJ/mol) obtained from S-phase formation without applied stress (see Section 5.1.1). Firstly, this difference could be explained partially by the fact that these two values of activation energy for carbon diffusion were calculated from different temperature ranges:

400-450 °C for S-phase formation and 550-600°C for annealing. Secondly, as discussed in Section 2.3.3, S-phase has a high density of defects (stacking faults, dislocation, slip lines and deformation twins). Therefore, it is easier for carbon diffusion in S-phase with a high density of defects during annealing than in original austenite with limited defects during the formation of S-phase.

5.2.2 Effect of uniaxial tensile stress

In industrial applications, the uniaxial tensile stress is also a very common stress status for structural components. Therefore the stability of S-phase under tensile stresses is essential to be known as a part of the stress-thermal performances.

The general finding from Section 5.1 is that the tensile stress favours the diffusion of carbon and precipitation during the formation of S-phase. Therefore, at elevated temperature higher than 500 °C, the tensile stress is believed to accelerate the precipitation and produce degradation of S-phase. Moderate temperatures are chosen in the study to avoid the significant precipitation and test the stability of S-phase and the behaviour during long exposures to heat and tensile stress.

As shown in Fig. 4.4-5, the lattice parameter of the expanded austenite in the S-phase layers was obtained by the Nelson-Riey plot obtained from all the X-ray diffraction. There exists a tendency that with increasing temperature and tensile stress, the lattice parameter $a_{(hkl)}$ becomes smaller and approaches the untreated state. Therefore, the solubility of carbon in the S-phase is decreased by increasing the temperature and tensile

stress. This implies that the tensile stress does accelerate the carbon diffusion overall in the S-phase during the heat exposure period.

Since the sample size is not available for GDS tests, it is not feasible to conduct diffusion calculations in this case. Another complication for the experiments is the atmosphere: all samples for this part of tests are subjected into the surrounding of air without sealing facilities. Therefore, the oxidation is severe and can obviously influence the carbon diffusion by decarburisation at the surface. Although indirectly, the carbon concentrations can still be estimated in the solution from the previous XRD analysis and it agrees with the results of previous discussion.

The hardness profiles are influenced by two main factors; firstly, there is the level of carbon saturation (solid solution strengthening), the higher the carbon absorbed, the higher hardness it exhibits. Of course the precipitation process can also influence the hardness, but it is excluded in this case because no precipitates were found by any methods in these samples.

To explain the strengthening phenomenon in Figure 4.4-9, it is necessary to understand the basic theories of strengthening. The solid solution strengthening mechanism is considered as one of the most important strengthening mechanism because of the high level of alloying elements in the treated layer, for example S-phase with supersaturated carbon atoms. The mechanism involves the imposed lattice strains due to the elastic distortions of the lattice; therefore the movement of dislocations is restricted. This

explained the high hardness of S-phase comparing to the untreated austenite. When treated at a high temperature, the carbon concentration decreased and then the solid solution strengthening effect is diminished and the hardness dropped (see Figure 4.4-9 '500 0MPa').

The second strengthening effect is the working-hardening mechanism. During deformation, the grains are broken up by dense dislocation walls (called geometrically necessary boundaries) into domains/cell blocks, which possess different combinations of operative slip systems [222]. Because of the accumulation of grain boundary or misfit dislocations generated by the numerous slip systems, the misorientations increase rapidly. Absorption of dislocations to grain boundaries and grain sliding all contribute to the increase in misorientations [223]. These dislocations distribute inhomogeneously in the subgrain boundaries and they do not relax easily due to the relatively low deformation temperature (<0.5 Tm, melting point). The severe deformation in austenitic stainless steel can produce high dislocation density and then form sub-structure or cell wall.

Therefore, the 'sigmoid' trend in hardness (see Figure 4.4-9 '500 200MPa' ,the hardness initially increases, reaches a high level and then decreases) can be explained by the working-hardening mechanism. As revealed by TEM results, the 'PC500 200MPa' sample contains a higher density of nanotwins which can intercept each other.

The recorded elongation profiles (Fig. 4.4-12) of samples also implied that the 'PC500 200MPa' sample produced the largest strain change after the exposure to stress at several

temperatures. Therefore, the creep process must be considered in an explanation of hardening effect. High creep strength is usually attained by alloying with Nb, Ti and V, followed by suitable heat treatments to produce the nanosized carbides containing these alloying elements. In this study, it is noteworthy that plasma carburised 316ASS has a higher hardness than the substrate after creep at 500 °C for 100 hours at 200 MPa. With no obvious precipitation, the S-phase subjected to tensile strength can form a structure of intercepting nanotwins that exhibits a relative high hardness. This effect may lead to another way of manufacturing new materials i.e. increased creep strength austenitic stainless steel, especially with enhanced creep strength of the surface layer.

5.3 S-phase under wear

As has been revealed in Section 4.5, the S-phase formed on 316 ASS greatly enhanced the wear resistance of stainless steel. Both in unlubricated (in air) and in oil lubricated conditions, the wear factor of 316 ASS decreased by about one hundred times. In addition, interesting phase transformation was observed during wear of untreated and PC treated 316ASS.

5.3.1 Phase transitions under wear

As reported in Section 4.5, phase transformation occurred during the wear of untreated (Figure 4.5-7) and PC treated (Figure 4.5-8, 17 & 18) 316ASS, which in turn will affect their wear behaviour.

The untreated 316SS is easy to form martensite as shown in Fig. 4.5-7 at the load of 21N.

Such transformation also observed in the substrate of PC treated 316SS and the fraction of martensite increases with the load during wear tests (Figures 4.5-17 vs 18).

The phase transformation from austenite to martensite observed in this study can be attributed to the fact that austenitic stainless steels in face centred cubic (FCC) phases, γ are metastable. Therefore, a modest plastic strain can trigger a rapid martensitic transformation to the body-centred cubic (BCC) phase, α'.

This phase transformation has also been observed by other researchers and such transformation also depends on the chemical composition of austenitic stainless steels [224, 225]. For example, martensitic transformation under stress can easily take place in 304 ASS because it contains relatively small amounts of austenite stabilising Ni (8-10wt.%) and significant amounts of ferrite stabilising Cr (18-20wt.%) solutes. On the other hand, such behaviour does not appear in 310 ASS because it contains higher content of Ni (>19wt.%) and is therefore much more stable in the austenitic phase. Type 316ASS has an intermediate composition between these two steels, giving intermediate behaviour, which means phase transformation can occur for 316ASS in wear under sufficiently arduous conditions.

As shown in Figure 4.5-8, a very thin surface layer of original S-phase layer was transferred into martensite under 95N in unlubricated conditions. However, almost no martensite was formed in the main S-phase layer although martensite was observed below the S-phase layer. This indicates that the stability of S-phase was better than untreated austenite.

The transformation of superficial S-phase case into martensite could be attributed to combined mechanical and thermal effects during reciprocating sliding in air. This is supported by the fact that no martensite was observed in the wear track formed in S-phase layer under lubricated conditions. This is largely because the tangential friction force was much lower in oil lubricated wear than in dry wear, thus leading to significantly reduced surface shear stress; in addition, reduced friction and oil can effectively reduce flashing temperature at the real contact areas. Hence, it is reasonable to deduce that combined mechanical shear stress and thermal heat may have promoted the S-phase to martensite transformation.

5.3.2 Wear mechanisms

It is well known that the wear behaviour can be influenced by many reasons. The study of sliding wear of austenitic stainless steel has proved that the influence of phase transitions is identified as one of these reasons [224, 225] .

As shown in Figure 4.5-1, the wear factor of untreated 316ASS is much higher than that of PC treated material under the same reciprocating wear conditions. This could be attributed to the hardness difference between S-phase and austenite. As shown in Figures 4.5-2 & 4, abrasive wear and oxidation wear occurred to untreated and PC treated 316ASS. It is known that the abrasive wear resistance of a material mainly depends on its hardness relative to that of the counterface; oxidation wear is also related, to some extent, to the hardness of the substrate material which supports the surface oxide film formed during the wear process.

It is known from Figures 4.1-12 that the surface hardness of carbon S-phase formed in 316ASS by plasma carburising can reach about 900HV while the hardness of the substrate is below 300HV. However, as evidenced by the EBSD mapping in Figure 4.5-7, a surface layer of about 20 μm in the untreated 316ASS was transferred into martensite during wear. This may to some extent enhance the hardness of the untreated material since it is well-known that martensite is harder than austenite. However, it should be indicated that the hardness of martensite mainly depends on its carbon content and 316ASS contains a very low level of carbon (<0.15at%) and therefore the martensite transferred from austenite in 316ASS should be harder than the austenite substrate but much lower than the carbon S-phase formed by PC treatment. Consequently, much severe wear is expected to the untreated material than to the PC treated S-phase case.

It is also of great interest to find that many cracks both parallel and perpendicular to the sliding direction were found at the bottom of the wear track formed in untreated material during reciprocating sliding wear under 21N (Figure 4.5-2). These cracks look similar to the cracks formed during scratch of thin coatings on a soft substrate with good bonding. This could be explained by the formation tribo-interaction induced martensite on the surface, which is harder than the austenite substrate as discussed above.

The formation of such surface martensite case may, to some extent, reduce the wear of 316ASS under a low load due to its higher hardness in relative to austenite. However, further increase of load will cause severe damage to the martensite case, thus forming so-called ‘thin-ice’ effect normally observed in hard coating-soft substrate systems. Once the

surface martensite case was broken and removed as wear debris, very severe wear would be expected because the relatively hard martesite wear debris could act as abrasives entrapped in the wear track. This is supported by the observation that dramatic increase in wear factor started to the untreated 316ASS when the applied load was above 40N (Figure 4.5-1).

On the other hand, the wear factor of the PC treated S-phase case is more than 10 times lower than that of the untreated material when tested under 21N. As evidenced in Figures 4.5-4 and 5, the PC treated material is dominated by oxidative wear with very mild abrasive wear. The S-phase layer is much stronger than the trobo-induced martensite in the untreated material and therefore the tribo-induced surface oxide layer can be effective supported by the strong S-phase case. Some cracks were observed in the wear track formed in the S-phase case. This has also been observed by other researchers [226] in oxidative wear because of the difference in physical and mechanical properties between the tribo-formed oxide layer and the metallic substrate.

In addition to the formation of tribo-induced oxide films, as shown in Figure 4.5-8, a thin surface layer was transferred into martensite during reciprocating wear of PC treated S-phase under 95N. This is mainly due to its metastable nature and combined mechanical and thermal actions (see Section 5.3.1).

Unlike the martensite formed during reciprocating wear of untreated material, the tribo-induced martensite should contain a high amount of carbon because it was formed from

the carbon S-phase. As discussed before, the hardness of martensite is a functional of its carbon content and hence a high surface hardness is expected although it is not so hard as the S-phase. In addition, this relatively hard martensite is still mechanically supported by the strong S-phase subsurface. Accordingly, very low wear factor could be expected for the PC treated material.

It has been shown in Figure 4.5-1, the wear factor increased almost linearly with the applied load before a sudden jump took place at a critical load of 120N. This implies that under such a high load, the S-phase case may have collapsed when its thickness was significantly reduced to below a minimum value due to wear.

The above mechanism is supported by the wear behaviour of S-phase case under oil lubricated conditions. As can be seen from Figure 4.5-9, the wear factor of the PC treated S-phase is very low. This is mainly because of the following three factors: (1) the tangent force and thus surface shear stress was significantly reduced by oil lubrication. This can not only move the maximum shear stress from surface to the subsurface but also reduce the amplitude of the stress; (2) no S-phase-to-martensite transformation occurred up to a load of 739N under oil lubricated conditions (Figure 4.5-18) largely due to the reduced surface shear stress and/or surface flashing temperature; (3) martensitic transformation occurred beneath the S-phase case (Figures 4.5-17 & 18), which can effectively support the surface S-phase case. Therefore, it could be concluded that it is this gradient layer structure that have contributed to the very low wear factor for the PC treated S-phase under oil lubricated conditions.

5.4 Residual Stress and Lattice Expansion of S-phase

The experimental results presented in the preceding chapters clearly revealed that S-phase formed on AISI 316L stainless steel foils and 316 stainless steel sheet and bulk material at relatively low temperature for certain treatment times (less than 20 hours 450 °C at and 10 hours at 500 °C). The carbon content in the carburised layers can reach about 12 at.% (about 2.84wt.% respectively) according to the literature (see Section 2.4.2 'paraequilibrium and supersaturation'). In this work, the S-phase formed was characterised by different methods, and the carbon concentrations are in reasonable agreement despite of the sensitivity and capability of different techniques (2.73wt.% by EDX of XTEM,3.8wt.% by WDS, 2.5wt.% by GDS).

Clearly, the concentration of carbon atoms has already far exceed that of the solid solubility in 316 stainless steel which is only about 0.015 at.%. Through XRD and TEM, it has been revealed that S-phase is free of precipitates even though such high number of carbon atoms is distributed in the interstitial sites. It is well known that the supersaturation of S-phase is unstable or metastable and will change to the stable phases with some additional energy. As has been proved in this study, both tensile stress applied on the samples and prolonged treatment to 30 hours at 450 °C plasma carburising treatment will precipitate carbides, such as Fe_5C_2 or $Cr_{23}C_6$. Once the precipitation has occurred, the carbon saturated in S-phase will decrease and the lattice expansion also becomes smaller.

From the measured peak positions of XRD results, the lattice parameter a_{hkl} can be calculated and these data are plotted against $Cos\theta \cdot Cot\theta$. For ideal crystalline structures with no distortion, the plot will give a straight line and the intercept with the vertical axis is the true lattice parameter a_0. Figure 5.4-1 shows such a plot for the untreated, and plasma carburised 316L stainless foils at 450°C for 10hours, 20hours and 30hours. From the plot, it is obvious to notice that the plot of untreated 316L sample was a straight line with an intercept of 3.59632(+/- 0.00027)Å. However, the plots from samples after carburising reveal large scatters for which it is difficult to draw a straight line passing through all these points. This suggests that distortion or imperfection happened in the S-phase in 316L stainless steel. With prolonged treatment time, the lattice expansion decreased, especially for the peak (200). This can be explained by the stress relief resulting when precipitation occurred and the supersaturated S-phase decomposed

The peak deviation of S-phase, which has been investigated and discussed by Sun *et al*. [227], is probably caused by the formation of stacking faults and high compressive residual stresses resulting in a highly distorted and disordered fcc structure. It may be observed from Figure 5.4-1 that for different treatments the difference is much larger between a_{200} than between a_{111}. It is also of interest to note that for the bulk material, after carburising, the peak shift of (200) usually is larger than that of (111) (see Figure 5.4-2); however, for the carburised 50 μm thick foils, the peak shift of (200) usually is smaller than that of (111) (see Figure 5.4-1). This is mainly because the residual compressive stress formed in thin foil should be much smaller than that formed in bulk material.

For simplicity, sample ‘PC 0MPa’ is taken out to be analysed by using the same method as used by Sun *et al.* [227, 228]. As proposed by theses authors, there are three different mechanisms by which to modify the lattice constants of the S-phase: the saturation of carbon, residual stress and defects like stacking faults.

This can be expressed as Equation

$$\Delta a = \Delta a_{SS} + \Delta a_{RS} + \Delta a_{SF} \quad (5.4\text{-}1)$$

The subscript ‘SS’ represents solid solution, ’RS’ means residual stress and ‘SF’ corresponds to stacking fault.

When large amount of carbon diffuses into the sample and forms S-phase during carburising, the lattice of surface structure is expanded. However, as discussed in the literature review (Chapter 2) , researchers find that the structure of S-phase was not changed. Therefore, the absorbed carbon atoms in the fcc structure should result in a uniform expansion rather than distortion of the lattice constant. So that the intrinsic source of different peak shifts from XRD analysis could be mainly attributed to the residual stress and stacking fault.

Due to the supersaturation in the S-phase and the constraints of the substrate, the residual level is very high in the S-phase. As measured by some researchers [192] in nitrided or carburised samples, the value of compressive residual stress in the surface layer can reach several GPa depending on the treating conditions. In the study of this

project, for reference, AISI 316 bulk stainless steel was also carburised at 450 °C 10hours same as the AISI 316L foil. The Nelson-Riley plots are shown in Figure 5.4-2. It can be evaluated the lattice constant of untreated 316 stainless steel is 3.59726(+/-0.0025) Å which is very similar to that of the 316L stainless steel.

The residual stress was measured by XRD analysis using $\sin^2\psi$ method and approximately 2.2GPa of compressive normal stress was calculated by the software. The change in the lattice parameter, as proposed by Wagner [229] can be defined by

$$\Delta a_{hkl} = a_0 (S_1)_{hkl} \sigma \qquad (5.4\text{-}2)$$

where $(S_1)_{hkl}$ is the elastic constant and is listed in Table5.4-1 for austenitic stainless steel. Then the expansion of lattice constants caused by residual stress could be estimated and the results (Δa_{RS}) are shown in Table 5.4-2

In addition to the contribution of the residual stress to the diffraction peak shift, the high density of defects such as stacking faults also play roles in the incompatible shifts of XRD peaks. According to the theories of Paterson [102] and Warren [230], if stacking faults are present in the material, then the change in lattice parameter Δa_{hkl}, which depends on the indices of reflection (*hkl*), is related to stacking fault probability(SFP) α by the following Equation:

$$\Delta a_{hkl} = a_0 G_{hkl} \alpha \qquad (5.4\text{-}3)$$

where G_{hkl} is the stacking fault parameter, values of which are listed in Table 5.4-1.

By fitting the data obtained from experiments, an estimated value of stacking fault probability α of 0.022 is used to get the optimised calculation. Such a SFP value is reasonable for carburised AISI 316ASS because a value about 0.03 was proposed by T.Christiansen [105] in their nitride S-phase structure. However, the SFP is two times increased from untreated ASS by the dissolution of carbon atoms or nitrogen atoms [231]. All the calculated values of the change of lattice constant caused by three different ways are listed in Table 5.4-2.

From the results, it is known that the largest deviation of calculated values comparing with the measured values comes from the deflection of (200).This can be explained in that the residual stress is not homogeneous in each crystalline plane. In the calculation of this model, the residual stress obtained from (222) crystalline plane is assumed to be equal everywhere within the penetration depth of X-ray. However, the actual situation could be deviated from this, especially for the (200) direction along which the carbon atoms may diffuse faster than the other direction. Therefore, the residual stress in the (200) could be different from the other plane and when the surface layer is constrained by the substrate, the residual stress is correspondingly larger. Meanwhile, it is explained why the XRD peak shifts of the PC treated foil samples are different from bulk ones. Owning to their nearly free constraint from the substrate during carburising, the stress can be easily relieved and the residual stress after treatments can be both positive and negative, therefore, the Nelson-Riley plots are different from those of the bulk samples. It is supposed and

confirmed in experiments [105] that the totally stress-free PC treated sample (powders) shows exact results with the fitting models mentioned above.

In general, the lattice expansion of S-phase can be summarised in these ways. One contribution is the solid solution; it expands the lattice constant by occupying the interstitial positions and enlarges the volume of cell. Another important factor is the residual stress which can be explained by elastic models. Normally in the PC treated bulk stainless steels, the residual compressive stress is as large as several GPa. Besides these two factors, the existence of stacking faults can cause the disturbance of the XRD peak positions and therefore influence the measurement of lattice expansion by XRD method.

6 Conclusions

The evidence produced throughout this project and the discussion presented in the last chapter can be summarised as follows:

Part I – Effect of *in situ* applied stress on S-phase formation

1. Plasma carburising of 316L foil at 450 °C for 10-20 hours can form a single S-phase layer on the both sides of the foil. Long-time (≥30h) plasma carburising at 450 °C led to the decomposition of S-phase and formation of needle-like Fe_5C_2 precipitates.
2. Applied tensile stresses in the range of 20-80MPa can promote the formation of S-phase during plasma carburising of 316L foils at temperatures ranging from 400-450°C. The thickness of the S-phase layers almost doubled when a tensile stress of 80 MPa was applied during 450 °C /10 h plasma carburising of 316L.
3. The calculated activation energy for carbon diffusion in 316L was reduced from 142.76 kJ/mol to 133.91 kJ/mol when a tensile stress of 40 MPa was applied during plasma carburising at temperatures ranging from 400 to 450 °C for 10 h.
4. When the applied tensile stress exceeded a value of 40 MPa, carbides including metastable CrC and $Cr_{23}C_6$ precipitated from the S-phase. A very fine lamellar structure consisting mainly of $Cr_{23}C_6$ and α-Fe was found near the surface.
5. Thermodynamic simulation-based results agreed well with the experimental results in the way that the tensile stress affected the formation and stability of the S-phase. Applied tensile stress can reduce the incubation time of $Cr_{23}C_6$

precipitation from the saturated austenitic phase.

6. The *in situ* application of 20M Pa tensile stress during 450 °C/10 h plasma carburising of 316L thin foils can increase the S-phase thickness without causing the formation of precipitates and loss of tensile strength.
7. The tensile strength of 316L ASS foil increased by forming S-phase cases on the both sides of the foil with a maximum tensile strength of 920 MPa for 450 °C/20 h plasma carburised foils. The tensile strength was reduced by the formation of Fe_5C_2 precipitates.
8. The tensile fracture surfaces of plasma carburised 316L foils revealed brittle feature of S-phase cases on both sides and ductile fracture in the central austenitic substrate.

Part II – Thermo-mechanical stability of S-phase

9. Exposing carburised S-phase to elevated temperature for a period of time (i.e. 525 °C for 10 h, 550 °C for 5 h, 575 °C for 2 h and 600 °C for 1 h) led to the decomposition of the surface of S-phase case into CrC and α-Fe.
10. Applying isostatic compressive stress by HIPping can maintain the stability of carburised S-phase formed on 316 ASS at elevated temperature by depressing its decomposition and precipitation, as compared to stress-free counterparts.
11. Compressive stress retarded the carbon diffusion at elevated temperature and the activation energy for carbon diffusion increased from 125.1 kJ/mol for stress-free annealing to 157.1 kJ/mol when applying 180 MPa isostatic compressive stress during annealing.
12. The applied compressive stress during HIPping of carburised S-phase at high-

temperature can impede the reduction of the hardness of the S-phase case.

13. Application of tensile stress can accelerate the carbon diffusion, increase the thickness of carburised case but reduce the carbon supersaturation of S-phase during annealing of as-carburised samples at temperatures ranging from 400-500 °C.
14. When tensile stressed at 400 °C for 150 h, the microstructure features of the carbon S-phase was not affected by the stress levels up to 200 MPa; but the thickness of the S-phase layer increased marginally.
15. When tensile stressed at 450 and 500°C for 100MPa or above, the corrosion resistance of the carbon S-phase layers was slightly reduced as evidenced by the dark colour and deep etched grain boundaries.
16. The application of a tensile stress during annealing of S-phase layer at 500°C for 100 h can retard the deduction of its hardness. This is believed to be related to the increased micro- and nano-twins and early stage precipitation of carbides in the S-phase.

Part III – Properties and behaviour of S-phase

17. Multi-layered Fe_2O_3 and Fe_3O_4 oxides were formed on the top of S-phase after annealing at elevated temperature in air. The formed oxide layer is much thicker on S-phase than on untreated 316 ASS.
18. Tensile stress promotes the growth of oxides formed on both S-phase and untreated 316 ASS during annealing in air. The oxide layer formed on the S-phase had better load capacity than that on untreated 316 ASS.
19. The reciprocating sliding wear of 316ASS under unlubricated and oil lubricated

conditions can be significantly reduced by forming carbon S-phase during low-temperature plasma carburising.

20. Under unlubricated conditions, the wear changed from severe sliding wear for untreated 316ASS to mild oxidation wear for carbon S-phase mainly because of increased surface hardness.
21. The severe sliding wear of untreated 316ASS under unlubricated conditions could be attributed to the collapse of *in situ* formed relatively high hardness martensite on the surface due to its weak soft austenite substrate and thus low load bearing capacity.
22. A very thin surface layer of S-phase case and the austenite substrate beneath the S-phase case were transformed to martensite owing to the tribo-action during unlubricated reciprocating sliding wear.
23. The low wear factor of S-phase during unlubricated reciprocating sliding wear could be attributed to the strong support to the surface oxide layer formed in the wear track from the S-phase and martensite underneath.
24. Carbon S-phase formed in 316ASS by low-temperature plasma carburising is stable under lubricated sliding wear conditions up to a very high load of 739N.
25. The quantity of transformed martensite beneath S-phase in the substrates austenite increased with increasing the applied load, which can increase the load bearing capacity of S-phase case and proved to be good design of stress-gradient surface engineering.
26. The large residual compressive stress existed in carburised S-phase and was measured to be 2.2 GPa while the shear stress was relative low about 132 MPa.

7 Future Work

The present project contributed to the understanding of the effect of stress on the formation and stability of carburised S-phase on austenitic stainless steel. Evidence was produced on the mechanisms of metastability and phase transformation of S-phase under different stress conditions including isostatic compressive stress, uniaxial tensile stress and wear. From the results obtained in this project, following topics are suggested as future studies:

1. Optimise the procedure of PC treatments under *in situ* tensile stress for real scale industrial components to increase the thickness of S-phase on their surfaces. It can be realised through detailed stress analysis in samples and control of other treatment parameters such as temperatures and time.
2. Develop three-dimensional maps to show the thermo-mechanical stability of S-phase under combined thermal and mechanical actions.
3. Study the relationship of residual stress evolution and stability of carbon S-phase by conducting *in situ* residual stress measurements at elevated temperatures.

8 References

1. Lo KH, Shek CH, Lai JKL. Recent developments in stainless steels Materials Science and Engineering: R: Reports. 2009; 65:39-104
2. Zhang ZL, Bell T. Structure and corrosion resistance of plasma nitrided stainless steel. Surface Engineering. 1985; 1:131-6.
3. Dong H. S-phase surface engineering of Fe-Cr,Co-Cr and Ni-Cr alloys. International Materials Reviews. 2010; 55:65-98.
4. Li CX, Bell T. Corrosion properties of active screen plasma nitrided 316 austenitic stainless steel. Corrosion Science. 2004; 46:1527-47.
5. Ernst F, Cao Y, Michal GM, Heuer AH. Carbide precipitation in austenitic stainless steel carburized at low temperature. Acta Materialia. 2007; 55:1895–906.
6. Lebrun JP, Poirier L, Hertz D, Lincot C. Environmentally friendly low temperature plasma processing of stainless steel components for nuclear industry Surface Engineering. 2002; 18:423-8.
7. Baddoo NR. Stainless steel in construction: A review of research, applications, challenges and opportunities. Journal of Constructional Steel Research. 2008; 64:1199-206.
8. Streicher MA. Stainless steel: past,present and future. . The metallurgical evolution of stainless steel. London: The Metals Society; 1979. p. 442-75.
9. A non-rusting steel. New York Times. 1915 31 January
10. Carlisle RP. Scientific American Inventions and Discoveries: John Wiley and Sons; 2004.
11. ThyssenKrupp Nirosta history. [cited 2010 10 August]; Available from: www.thyssenkrupp-nirosta.de/History.
12. Bhadeshia H, Honeycombe R. Steels: microstructure and properties. 3rd ed. London: Butterworth-Heinemann; 2006.
13. Monypenny JHG. Stainless Iron and Steel. 3rd ed. London: Chapman &Hall LTD.; 1951.
14. Okamoto G. Passivenext termprevious termfilmnext term of 18-8 previous termstainlessnext term steel structure and its function. Corrosion Science. 1973; 13(6):471-89.
15. [cited 2011 Sept. 30]; Available from: http://www.calphad.com/iron-carbon.html.
16. Pryce L, Andrews KW. Practical estimation of composition balance in ferrite content in stainless steels. JISI. 1960; 195:415-7.
17. Peckner D, Bernstein IM. Handbook of stainless steels1977.
18. Monypenny JHG. Stainless Iron and Steel. London: Chapman & Hall LTD.; 1951.
19. Cortie MB, Pollak H. Embrittlement and aging at 475 °C in an experimental ferriticnext termprevious termstainlessnext termprevious termsteelnext term containing 38 wt.% chromium. Material Science and Engineering A. 1995; 199(2):153-63.
20. Eichelman GH, Hull FC. The effects of composition on the temperature of spontaneous transformation of austenite to martensite in 18-8 type stainless steels. Trans ASM. 1953; 45:77-95.

21. Monkman FC, Cuff FG, Grant NJ. Computation of Ms for stainless steels. Metal Progress. 1957; 71:94.
22. Remy L, Pineau A. Observation of stacked layers of twins and epsilon martensite in a deformed austenitic stainless-steel. Metallurgical Transactions. 1974; 5:963-5.
23. Abrassart F. Stress-induced gamma-alpha' martensitic transformation in 2 carbon stainless-steels - application to trip steels. Metallurgical Transactions. 1973; 4:2205.
24. T.HChen, Weng KL, Yang JR. The effect of high-temperature exposure on the microstructural stability and toughness property in a 2205 duplex stainless steel. Material Science and Engineering A. 2002; 338(1-2):259-70.
25. Shek CH, Wong KW, Lai JKL. Review of temperature indicators and the use of previous termduplexnext termprevious termstainlessnext termprevious termsteelsnext term for life assessment. Materials Science and Engineering: R: Reports. 1997; 19(5-6):153-200.
26. Singhal LK, Martin JW. Growth of M23C6 carbide on incoherent twin boundaries in austenite. Acta Metallurgica. 1967; 15:1603.
27. Howell PR, Bee JV, Honeycombe RWK. Crystallography of the austenite-ferrite-carbide transformation in Fe-Cr-C alloys. Metallurgical Transactions A-Physical Metallurgy and Materials Science. 1979; 10:1213-22.
28. Goldsmith HJ. The structure of carbides in alloy steels .1. General steel. Journal of the Iron and Steel Institute. 1948; 160:345-62.
29. Ricks RA, Howell PR, Honeycombe RWK. Effect of Ni on the decomposition of austenite in Fe-Cu alloys. Metallurgical and Materials Transactions A. 1979; 10:1049.
30. Wasnik DN, Dey GK, Kain V, Samajdar I. Precipitation stages in a 316L austenitic stainless steel. Scripta Materialia. 2003; 49:135-41.
31. Terada M, Saiki M, Costa I, Padilha AF. Microstructure and intergranular corrosion of the austenitic stainless steel. J Nucl Mater. 2006; 358:40.
32. Turnbull A, Francis PE, Ryan MP, Orkney LP, Griffiths AJ, Hawkins B. A novel approach to characterizing the corrosion resistance of super duplex stainless steel welds. Corrosion. 2002; 58:1039-48.
33. IARC Monographs on the Evaluation of Carcinogenic Risks to Humans: Surgical Implants and Other Feorign Bodies. Lyon1999. p. 65.
34. Sumita M, Hanawa T, Teoh SH. Development of nitrogen-containing nickel-free austenitic stainless steels for metallic biomaterials-review. Material Science and Engineering C. 2004; 24:753-60.
35. Sieurin H, Sandstrom R, Westin EM. Fracture toughness of the lean duplex stainless steel LDX 2101 Metallurgical and Materials Transactions A. 2006; 37:2975-81.
36. Fini M, Aldini NN, Torricelli P, Giavaresi G, Borsari V, Lenger H, et al. A new austenitic stainless steel with negligible nickel content: an in vitro and in vivo comparative investigation Biomaterials. 2003; 24:4929-39.
37. Montanaro L, Cerellati M, Campoccia D, Arciola CR. Promising in vitro performances of a new nickel-free stainless steel Journal of Materials: Materials in Medicine. 2006; 17:267-75.
38. Reclaru L, Luthy H, Ziegenhagen R, Eschler PY, Blatter A. Anisotropy of nickel release and corrosion in austenitic stainless steels. Acta Biomaterialia.

2008; 4:680-5.
39. Reclaru L, Ziegenhagen R, Eschler PY, Blatter A, Lemaitre J. Comparative corrosion study of "Ni-free" austenitic stainless steels in view of medical applications Acta Biomaterialia. 2006; 2:433-44.
40. Gavriljuk VG, Tyshchenko AI, Razumov ON, Petrov YN, Shanina BD, Berns H. Corrosion-resistant analogue of Hadfield steel. Material Science and Engineering A. 2006; 420:47-54.
41. Walter MJ. Stainless steel for medical implants. Advanced Materials & Processes. 2006:22-4.
42. Miura R, Nakajima H. In: Clark AF, Reed RP, editors. Advances in Cryogenic Engineering. New York: Plenum Press; 1986. p. 245-52.
43. Yuan Z, Dai Q, Cheng X, Chen K, Xu W. Impact properties of high-nitrogen austenitic stainless steels. Material Science and Engineering A. 2008; 475:202-6.
44. Fu R, Zheng Y, Ren Y. Mechanical properties of 32Mn-7Cr-0.6Mo-0.3N austenitic steel for cryogenic applications Journal of Materials Engineering and Performance. 2001; 10:456-9.
45. http://www.china001.com/show_hdr.php?xname=PPDDMV0&dname=A887B41&xpos=15. [cited 2011 10 March].
46. Makin WE, Troy WC. The Heat Treatment of the Chromium-Carbon Stainless Steel. Annual Meeting of American Society for Metals1941. p. 34.
47. Mordyuk BN, Prokopenko GI, Vasylyev MA, Iefimov MO. Effect of structure evolution induced by ultrasonic peening on the corrosion behavior of AISI-321 stainless steel. Materials Science and Engineering A. 2007; 458:253-61.
48. Wang T, Yu J, Dong B. Surface nanocrystallization induced by shot peening and its effect on corrosion resistance of 1Cr18Ni9Ti stainless steel. Surface & Coatings Technology. 2006; 200:4777-81.
49. Liu G, Lu J, Lu K. Surface nanocrystallization of 316L stainless steel induced by ultrasonic shot peening. Material Science and Engineering A. 2000; 286:91-5.
50. Lu K, Lu J. Surface nanocrystallization (SNC) of metallic materials-presentation of the concept behind a new approach. Journal of Materials Science and Technology. 1999; 15:193-7.
51. Roland T, Retraint D, Lu K, Lu J. Fatigue life improvement through surface nanostructuring of stainless steel by means of surface mechanical attrition treatment Scripta Materialia. 2006; 54:1949-54.
52. Zhang HW, Hei ZK, Liu G, Lu J, Lu K. Formation of nanostructured surface layer on AISI 304 stainless steel by means of surface mechanical attrition treatment. Acta Materialia. 2003; 51:1871-81.
53. Chen XH, Lu J, Lu L, Lu K. Tensile properties of a nanocrystalline 316L austenitic stainless steel Scripta Materialia. 2005; 52:1039-44.
54. Lu K, Lu J. Nanostructured surface layer on metallic materials induced by surface mechanical attrition treatment Material Science and Engineering A. 2004; 375-377:38-45.
55. Yu B, Davis EM, Hodges RS, Irvin RT, Li DY. Surface nanocrystallization of stainless steel for reduced biofilm adherence. Nanotechnology. 2008; 19:335101.
56. Wang XY, Li DY. Mechanical and electrochemical behavior of nanocrystalline surface of 304 stainless steel Electrochimica Acta. 2002; 47:3939-47.
57. Akgun OV, Inal OT. Laser surface melting and alloying of type 304L stainless steel .2. Corrosion and wear resistance properties. Journal of Materials Science.

1995; 30:6105-12.
58. Kwok CT, Man HC, Cheng FT. Cavitation erosion and pitting corrosion of laser surface melted stainless steels. Surface & Coatings Technology. 1998; 99:295-304.
59. Kumar S, Banerjee MK. Improvement of intergranular corrosion resistance of type 316 stainless steel by laser surface melting Surface Engineering. 2001; 17:483-9.
60. Conde A, Garcia I, Damborenea JJd. Fitting corrosion of 304 stainless steel after laser surface melting in argon and nitrogen atmospheres Corrosion Science. 2001; 43:817-28.
61. Chong PH, Liu Z, Wang XY, Skeldon P. Pitting corrosion behaviour of large area laser surface treated 304L stainless-steel. Thin Solid Films. 2004; 453-454:388-93.
62. Tsay LW, Liu YC, Lin D-Y, Young MC. The use of laser surface-annealed treatment to retard fatigue crack growth of austenitic stainless steel Material Science and Engineering A. 2004; 384:177-83.
63. Shiue RK, Chang CT, Young MC. The effect of residual thermal stresses on the fatigue crack growth of laser-surface-annealed AISI 304 stainless steel: Part I: computer simulation Material Science and Engineering A. 2004; 364:101-8.
64. Tassin C, Laroude F, Pons M, Lelait L. Improvement of the wear resistance of 316L stainless steel by laser surface alloying. Surface & Coatings Technology. 1996; 80:207-10.
65. Kwok CT, Cheng FT, Man HC. Laser surface modification of UNS S31603 stainless steel using NiCrSiB alloy for enhancing cavitation erosion resistance. Surface & Coatings Technology. 1998; 107:31-40.
66. Majumdar JD, Manna I. Laser surface alloying of AISI 304-stainless steel with molybdenum for improvement in pitting and erosion-corrosion resistance. Material Science and Engineering A. 1999; 267:50-9.
67. Lo KH, Cheng FT, Kwok CT, Man HC. Improvement of cavitation erosion resistance of AISI 316 stainless steel by laser surface alloying using fine WC powder Surface & Coatings Technology. 2003; 165:258-67.
68. Abenojar J, Velasco F, Torralba JM, Bas JA, Calero JA, Marce R. Reinforcing 316L stainless steel with intermetallic and carbide particles Material Science and Engineering A. 2002; 335:1-5.
69. Di MG, Cuppari V, Souza RM, Sinatora A. Effect of hard second phase on cavitation erosion of FeCrNiC alloys Wear. 2005; 258:596-603.
70. Peyre P, Scherpereel X, Berthe L, Carboni C, Fabbro R, Beranger G, et al. Surface modifications induced in 316L steel by laser peening and shot-peening. Influence on pitting corrosion resistance Material Science and Engineering A. 2000; 280:294-302.
71. Lo KH, Cheng FT, Man HC. Laser transformation hardening of AISI 440C martensitic stainless steel for higher cavitation erosion resistance Surface & Coatings Technology. 2003; 173:96-104.
72. Kwok CT, Man HC, Cheng FT. Cavitation erosion and pitting corrosion behaviour of laser surface-melted martensitic stainless steel UNSS42000 Surface & Coatings Technology. 2000; 126:238-55.
73. Yue TM, Yu JK, Man HC. The effect of excimer laser surface treatment on pitting corrosion resistance of 316LS stainless steel. Surface & Coatings

Technology. 2001; 137:65-71.
74. Grube WL. Heat Treating. ASM Handbook: ASM International; 1991. p. 1012.
75. Mattox DM. Vacuum Deposition, Reactive Evaporation and Gas Evaporation. ASM Handbook, Surface Engineering: ASM International; 1994. p. 1039.
76. Redmer R. Physical properties of dense, low-temperature plasmas. Physics Reports. 1997; 282:35-157.
77. Hanak JJ. Plasma potential gradient in dc positive column and its effect on the deposition and photovoltaic performance of a-Si:H films. Journal of Non-Crystalline Solids. 1985; 77-78:773-6.
78. Hotta S, Tawada Y, Okamoto H, Hamakawa Y. Effect of the substrate potential on the incorporation manner of hydrogen and impurity in alpha-Si-H films. JOURNAL DE PHYSIQUE 1981; 42:631-4.
79. Townsend JS, McCallum SP. Electrical properties of neon. Philosophical Magazine. 1928; 6:857-78.
80. Rutscher A, Ch Wilke. Investigation of very long faraday dark space. Vacuum. 1976; 26:212.
81. Liberman MA, Lichtenberg AJ. Principles of Plasma Discharges and Materials Processing. New Jersey: John Wieley & Sons; 2005.
82. Thornton A. Influence of apparatus geometry and deposition conditions on the structure and topography of thick sputtered coatings. J Vac Sci Technol. 1978; 15:171.
83. Tominaga K, Ao T, Sato Y, Mori I, Kusaka K, Hanabusa T. Magnetic field dependence of AlN film properties in dc planar magnetron sputtering with opposed targets Vacuum. 1998; 51:549-53.
84. Mattox DM. The Low-Pressure Plasma Processing Environment. Handbook of Physical Vapor Deposition (PVD) Processing: William Andrew 1998. p. 237-87.
85. Staines AM, Bell T. Technological importance of plasma-induced nitrided and carburized layers on steel. Thin Solid Films. 1981; 86:201-11.
86. Ichii K, Fujimura K, Takase T. Technology Report of Kansai University. 1986; 27:135-44.
87. Leyland A, Lewis DB, Stevensom PR, Matthews A. Low temperature plasma diffusion treatment of stainless steels for improved wear resistance. Surface and Coatings Technology. 1993; 62:608-17.
88. Marchev K, Cooper CV, Blucher JT, B.C.Giessen. Conditions for the formation of a martensitic single-phase compound layer in ion-nitrided 316L austenitic stainless steel. Surface and Coatings Technology. 1998; 99:225-8.
89. Lebrun JP, inventor European Patent EP 10001812002 02-01-2002.
90. Bell T, Sun Y, inventors; European Patent EP10001812002 02-01.
91. Williamson DL, Ozturk O, Wei R, Wilbur PJ. Metastable phase formation and enhanced diffusion in f.c.c. alloys under high dose, high flux nitrogen implantation at high and low ion energies Surface and Coatings Technology. 1994; 65:15-23.
92. Samandi M, Shedden BA, Smith DI, Collins GA, Hutchings R, Tendys J. Microstructure, corrosion and tribological behaviour of plasma immersion ion-implanted austenitic stainless steel Surface and Coatings Technology. 1993; 59:261-6
93. Blawert C, Kalvelage H, Mordike BL, Collins GA, Short KT, Jirásková Y, et al. Nitrogen and carbon expanded austenite produced by PI3 Surface and Coatings

Technology. 2001; 136:181-7.
94. Tahara M, Senbokuya H, Kitano K, inventors; US Patent 5564831996.
95. Cao Y, Ernst F, Michal GM. Colossal carbon supersaturation in austenitic stainless steels carburized at low temperature Acta Materialia. 2003; 51:4171-81.
96. Dahm KL, Dearnley PA. S-phase coatings produced by unbalanced magnetron sputtering. Surface Engineering. 1996; 12:61-7.
97. Li XY, Habibi N, Bell T, Dong H. Microstructural characterisation of a plasma carburised low carbon Co–Cr alloy. Surface Engineering. 2007; 23:45-51.
98. Nishimoto A, Ichii K, Nakao K, Takai M, Akamatsu K. Thermochemical Surface Engineering of Stainless Steels. 2000:289-307.
99. Yasumaru N. In: Bell T, Akamatsu K, editors. Stainless Steel 2000: Thermochemical Surface Engineering of Stainless Steels London: The Institute of Materials; 2000. p. 229-45.
100. Singh V, Marchev K, Cooper CV, Meletis EI. Intensified plasma-assisted nitriding of AISI 316L stainless steel. Surface and Coatings Technology. 2002; 160:249-58.
101. Blawert C, Weisheit A, Mordike BL, Knoop RM. Plasma immersion ion implantation of stainless steel: austenitic stainless steel in comparison to austenitic-ferritic stainless steel. Surface & Coatings Technology. 1996; 85:15-27.
102. Paterson MS. X‐ray diffraction by face‐centered cubic crystals with deformation faults Journal of Applied Physics. 1952; 23:805-11.
103. Warren BE. X-ray diffraction: Addison-Wesley; 1969.
104. Christiansen T, Somers MAJ. Low temperature gaseous nitriding and carburising of stainless steel. Surface Engineering. 2005; 21:445-55.
105. T. Christiansen, Somers MAJ. On the crystallographic structure of S-phase. Scripta Materialia. 2004; 50:35–7.
106. Sun Y, Li X, Bell T. Low temperature plasma carburising of austenitic stainless steels for improved wear and corrosion resistance. Surface Engineering. 1999; 15:49-54.
107. Sun Y, Li X, Bell T. Structural characteristics of low temperature plasma carburised austenitic stainless steel. Materials Science and Technology. 1999; 15:1171-8.
108. Bell T. Current status of supersaturated surface engineered S-phase materials. Key Engineering Materials. 2008; 373-374:289-95.
109. Gavriljuk VG, Berns H. High nitrogen steel-structure, properties,manufacturing,applications. Berlin: Springer; 1999.
110. Williamson DL, Davis JA, Wilbur PJ. Effect of austenitic stainless steel composition on low-energy, high-flux,nitrogen ion beam processing. Surface and Coatings Technology. 1998; 103–104:178–84.
111. Riviere JP, Cahoreau M, Meheust P. Chemical bonding of nitrogen in low energy high flux implanted austenitic stainless steel. Journal of Applied Physics. 2002; 91:6361-6.
112. Daham KL, Betts AJ, Dearnley PA. In: Sudarshan TS, Jeandin M, editors. Surface modification technology XXI. OH: ASM International; 2007. p. 519-26.
113. Shanker P, Sundararaman D, Ranganathan S. Clustering and ordering of nitrogen in nuclear grade 316LN austenitic stainless steel. J Nucl Mater. 1998; 254:1-8.

114. Murayama M, Hono K, Hirukawa H, Ohmura T, MAtsuoka S. The combined effect of molybdenum and nitrogen on the fatigued microstructure of 316 type austenitic stainless steel Scripta Materialia. 1999; 41:467-73.
115. Oddershede J, Christiansen TL, Stahl K, Somers MAJ. EXAFS investigation of low temperature nitrided stainless steel. Journal of Materials Science. 2008; 43:5358-67.
116. Makishi T, Nakata K. Thermochemical Surface Engineering of Stainless Steel. 2000:133-48.
117. Heuer AH, Ernst F, Kahn H, Avishai A, Michal GM, Pitchure DJ, et al. Interstitial defects in 316L austenitic stainless steel containing ‘‘colossal’’ carbon concentrations: An internal friction study. Scripta Materialia. 2007; 56:1067–70.
118. Michal GM, Ernst F, Heuer AH. Carbon Paraequilibrium in Austenitic Stainless Steel. Metallurgical and Materials Transactions A. 2006; 37a:1819-24.
119. Sun Y, Bell T, Kolosvary Z, Flis J. In: T.Bell, Akamatsu K, editors. Stainless steel 2000: thermochemical surface engineering of stainless steel. London: The Institute of Materials; 2001. p. 65-81.
120. Tsujikawa M, Noguchi S, Yamauchi N, Ueda N, Sone T. Effect of molybdenum on hardness of low-temperature plasma carburized austenitic stainless steel. Surface and Coatings Technology. 2007; 201:5102–7.
121. Ernst F, Cao Y, Michal GM. Carbides in low-temperature-carburized stainless steels. Acta Materialia. 2004; 52:1469–77.
122. Buhagiar J, Li XY, Dong H. Formation and microstructural characterisation of S-phase layers in Ni-free austenitic stainless steels by low-temperature plasma surface alloying. Surface & Coatings Technology. 2009; 204:330-45.
123. Tsujikawa M, Egawa M, Ueda N, Okamato A, Sone T, Nakata K. Effect of molybdenum and copper on S-phase layer thickness of low-temperature carburized austenitic stainless steel. Surface & Coatings Technology. 2008; 202:5488-92.
124. Lutz J, Gerlach JW, Mändl S. PIII nitriding of fcc-alloys containing Ni and Cr. Physica Status Solidi (a). 2008; 205A:980-4.
125. Shang S, Bottger AJ, Steenvoorden MP, Craje MWJ. Hyperfine interactions in hexagonal e-Fe6Ny phase investigated by Mossbauer spectroscopy and ab initio calculations. Acta Materialia. 2006; 54:2407–17.
126. Shang SL, Bottger AJ, Liu ZK. The influence of interstitial distribution on phase stability and properties of hexagonal ε-Fe6Cx, ε-Fe6Ny and ε-Fe6CxNy phases: A first-principles calculation. Acta Materialia. 2008; 56:719-25.
127. Duman E, Acet M, Hülser T, Wassermann EF, Rellinghaus B, Itié JP, et al. Large spontaneous magnetostrictive softening below the Curie temperature of Fe3C Invar particles. Journal of Applied Physics. 2004; 96:5668.
128. Gajbhiye NS, Bhattacharyya S. Magnetic properties of ε-Fe3N–GaN core–shell nanowires. Nanotechnology 2005; 16:2012-9.
129. Marchev K, Hidalgo R, Landis M, Vallerio R, Cooper CV, B.C.Giessen. The metastable m phase layer on ion-nitrided austenitic stainless steels: Part 2: crystal structure and observation of its two-directional orientational anisotropy. Surface & Coatings Technology. 1999; 112:67-70.
130. Thaiwatthana S, Li XY, H.Dong, T.Bell. Comparison studies on properties of nitrogen and carbon S phase on low temperature plasma alloyed AISI 316

stainless steel. Surface Engineering. 2002; 18:433-7.
131. Sun Y, Bell T. A Numerical Model of Plasma Nitriding of Low Alloy Steels. Material Science and Engineering A. 1997; A 224:33-47.
132. Parascandola S, Moller W, Williamson DL. The nitrogen transport in austenitic stainless steel at moderate temperatures. Applied Physics Letters. 2000; 76:2194-6.
133. Mandl S, Rauschenbach B. Concentration dependent nitrogen diffusion coefficient in expanded austenite formed by ion implantation. Journal of Applied Physics. 2002; 91:9737-42.
134. Mandl S, Scholzea F, Neumanna H, Rauschenbach B. Nitrogen diffusivity in expanded austenite. Surface and Coatings Technology. 2003; 174 –175:1191–5.
135. Abrasonis G, Rivière JP, Templier C, Pranevièius L, Barradas NP. Flux effect on the ion-beam nitriding of austenitic stainless-steel AISI 304L. Journal of Applied Physics. 2005; 97:124906.
136. Christiansen T, Dahl KV, Somers MAJ. Simulation of nitrogen concentration depth profiles in low temperature nitrided stainless steel. Defect and Diffusion Forum. 2006; 258-260:378-83.
137. Christiansen T, Dahl KV, Somers MAJ. Nitrogen diffusion and nitrogen depth profiles in expanded austenite: experimental assessment, numerical simulation and role of stress. Materials Science and Technology. 2008; 24:159-67.
138. Esfandiari M, Dong H. Plasma surface engineering of precipitation hardening stainless steels. Surface Engineering. 2006; 22:86-92.
139. Fewell MP, Priest JM, Baldwin MJ, Collins GA, Short KT. Short KT. Nitriding at low temperature. Surface & Coatings Technology. 2000; 131:284-90.
140. Grieveson P, Turkdogan ET. Trans Metall Soc AIME 1964; 230:407.
141. Hirvonen J, Anttila A. Annealing behavior of implanted nitrogen in AISI 316 stainless-steel. Applied Physics Letters. 1985; 46:835-6.
142. Cheng Z, Li CX, Dong H, Bell T. Low temperature plasma nitrocarburising of AISI 316 austenitic stainless steel. Surface and Coatings Technology 2005; 191:195-200.
143. Thaiwatthana S, Li XY, H.Dong, T.Bell. Mechanical and chemical properties of low temperature plasma surface alloyed 316 austenitic stainless steel. Surface Engineering 2002; 18:140-4.
144. Lewis DB, Leyland A, Stevenson PR, Cawley J, Matthews A. Metallurgical study of low-temperature plasma carbon diffusion treatments for stainless steels. Surface and Coatings Technology. 1993; 60:416-23.
145. Cohen M. Trans TMS-AIME. 1962; 224:638-57.
146. Mändl S, Rauschenbach B. Anisotropic strain in nitrided austenitic stainless steel. Journal of Applied Physics. 2000; 88:3323-9.
147. Ledbetter HM, Austin MW. Dilation of an fcc Fe-Cr-Ni alloy by interstitial carbon and nitrogen. Materials Science and Technology. 1987; 3:101-4.
148. Michal GM, Ernst F, Kahn H, Cao Y, Oba F, Agarwal N, et al. Carbon supersaturation due to paraequilibrium carburization: Stainless steels with greatly improved mechanical properties. Acta Materialia. 2006; 54:1597–606.
149. Chen J, Dong H. Corrosion and Corrosion-Wear Behaviour of Plasma Carburised Stellite 21 CoCr Alloy. Tribology - Materials, Surfaces & Interfaces. 2009; 3:24-30.
150. Menthe E, Bulak A, Olfe J, Zimmermann A, Rie K-T. Improvement of the

mechanical properties of austenitic stainless steel after plasa nitriding. Surface & Coatings Technology. 2000; 133-134:259-63.
151. Allen C, Li CX, Bell T, Sun Y. The effect of fretting on the fatigue behaviour of plasma nitrided stainless steels. Wear. 2003; 254:1106-12.
152. Ceschini L, Minak G. Fatigue behaviour of low temperature carburised AISI 316L austenitic stainless steel. Surface & Coatings Technology. 2008; 202:1778-84.
153. Raman SGS, Jayaprakash M. Influence of Plasma Nitriding on Plain Fatigue and Fretting Fatigue Behaviour of AISI 304 Austenitic Stainless Steel. Surface & Coatings Technology. 2007; 201:5906-11.
154. Masaki K, Ochi Y, Ishii E. Fatigue properties of hard shot-peened SUS316L - Behaviors of hardness distribution, residual stress distribution and fatigue cracks during the fatigue process Materials Science Research International. 1998; 4:200.
155. Masaki K, Ochi Y, Matsumura T. Initiation and propagation behaviour of fatigue cracks in hard-shot peened Type 316L steel in high cycle fatigue. Fatigue & Fracture of Engineering Materials & Structures. 2004; 27:1137-45.
156. Tokaji K, Kohyama K, Akita M. Fatigue behaviour and fracture mechanism of a 316 stainless steel hardened by carburizing International Journal of Fatigue. 2004; 26:543-51.
157. Akita M, Tokaji K. Effect of carburizing on notch fatigue behaviour in AISI 316 austenitic stainless steel Surface & Coatings Technology. 2006; 200:6073-8.
158. Stinville JC, Villechaise P, Templier C, Riviere JR, Drouet M. Plasma nitriding of 316L austenitic stainless steel: Experimental investigation of fatigue lif and surface evolution. Surface & Coatings Technology. 2010; 204:1947-51.
159. Dong H, Qi PY, Li XY, Llewellyn RJ. Improving the erosion–corrosion resistance of AISI 316 austenitic stainless steel by low-temperature plasma surface alloying with N and C. Materials Science and Engineering A. 2006; 431:137–45.
160. Li CX, Bell T. Sliding wear properties of active screen plasma nitrided 316 austenitic stainless steel. Wear. 2004; 256:1144-52.
161. Sun Y, Bell T. Dry sliding wear resistance of low temperature plasma carburised austenitic stainless steel. Wear. 2002; 253:689–93.
162. Sun Y, Bell T. Sliding wear characteristics of low temperature plasma nitrided 316 austenitic stainless steel. Wear. 1998; 218:34-42.
163. Saklakoglu N, Saklakoglu IE, Short KT, Collins GA. Tribological behavior of PIII treated AISI 316 L austenitic stainless steel against UHMWPE counterface. Wear. 2006; 261:264-8.
164. O.Pacheco, D.Hertz, J.P.Lebrun, H.Michel. Ionitriding of Austenitic Stainless Steels. International Conference on Carburizing and Nitriding with atmospheres; Cleveland: ASM; 1995. p. 269-74.
165. Qu J, Blau PJ, Jolly BC. Tribological properties of stainless steels treated by colossal carbon supersaturation. Wear. 2007; 263:719-26.
166. Sun Y, Bell T. Effect of layer thickness on the rolling-sliding wear behavior of low-temperature plasma-carburized austenitic stainless steel Tribology Letters 2002; 13:29-34.
167. Habibi N. Low-temperature plasma surface engineering of medical grade Co-Cr alloys [PhD thesis]. Birmingham, UK: The University of Birmingham; 2008.

168. Singh V, Meleti EI. Synthesis, characterization and properties of intensified plasma-assisted nitrided superalloy Inconel 718. Surface & Coatings Technology. 2006; 201:1093-101.
169. Dahm KL, Short KT, Collins GA. Characterisation of nitrogen-bearing surface layers on Ni-base superalloys. Wear. 2007; 263:625-8.
170. Tsujikawa M, Yoshida D, Yamauchi N, Ueda N, Sone T, Tanaka S. Surface material design of 316 stainless steel by combination of low temperature carburizing and nitriding. Surface and Coatings Technology. 2005; 200:507- 11.
171. Y.Sun. Effect of carbon addition on low-temperature plasma nitriding characteristics of austenitic stainless steel Vacuum. 2006; 81:114-9.
172. Sun Y. Hybrid plasma surface alloying of austenitic stainless steels with nitrogen and carbon.Materials Science and Engineering A 2005; 404:124-9.
173. Lei KM, Zhu XM. In vitro corrosion resistance of plasma source ion nitrided austenitic stainless steels. Biomaterials. 2001; 22:641-7.
174. Gontijo LC, Machado R, Kuri SE, Casteletti LC, Nascente PAP. Corrosion resistance of the layers formed on the surface of plasma-nitrided AISI 304L steel. Thin Solid Films. 2006; 515:1093-6.
175. Flis J, Kucznska M. Effect of low-temperature plasma nitriding on corrosion of 304L stainless steel in sulfate and chloride solutions. J Electrochem Soc. 2004; 151:B573-B80.
176. Song YS, Lee JH, Lee KH, Lee DY. Corrosion properties of N-doped austenitic stainless steel films prepared by IBAD. Surface & Coatings Technology. 2005; 195:227-33.
177. Dearnley PA, Pina CGF, Fisher J. Assessment of S-phase coated medical grade stainless steel (Ortron 90) for use in the human joint replacement corrosion-wear environment. J Phys D. 2008; 41D:105305.
178. Dearnley PA, Aldrich-Smith G. Corrosion-wear mechanisms of hard coated austenitic 316L stainless steels. Wear. 2004; 256:491-9.
179. Thaiwatthana S, Li XY, Dong H, Bell T. Corrosion wear behaviour of low temperature plasma alloyed 316 austenitic stainless steel. Surface Engineering. 2003; 19(3):211-6.
180. Chen J, Li XY, Bell T, Dong H. Improving the wear properties of Stellite 21 alloy by plasma surface alloying with carbon and nitrogen. Wear. 2008; 264:157-65.
181. Bell T. Surface engineering of austenitic stainless steel. Surface Engineering. 2002; 18:415-22.
182. Lebrum JP, Poirier L, Hertz D, Lincot C. In: Bell T, Akamatsu K, editors. Stainless steel 2000: thermochemical surface engineering of stainless steel; London: The Institute of Materials; 2001. p. 361-75.
183. Swagelok. http://www.swagelok.com/fittings/tube_fittings/tube_fitting_innovation.htm. 2010 [21 July, 2010].
184. Hultgren A. Isothermal transformation of austenite. Transactions of American Society for Metals. 1947; 39:915-1005.
185. Hillert M. Jernkontorets Annaler. 1952; 136:25-37.
186. M. Hillert PE. Phase Diagrams and Phase Transformation. Cambridge: Cambridge University Press; 1998.
187. Agarwal N, Kahn H, Avishai A, Michal G, Ernst F, Heuer AH. Enhanced fatigue

resistance in 316L austenitic stainless steel due to low-temperature paraequilibrium carburization. Acta Materialia. 2007; 55:5572–80.
188. El-Rahman AMA, El-Hossary FM, Fitz T, Negm NZ, Prokert F, Pham MT, et al. Effect of N2 to C2H2 ratio on r.f. plasma surface treatment of austenitic stainless steelSurface & Coatings Technology. 2004; 183:268-74.
189. Sun Y, Haruman E. Effect of carbon addition on low-temperature plasma nitriding characteristics of austenitic stainless steel. Vacuum. 2006; 81:114–9.
190. Borgioli F, Fossati A, Galvanetto E, Bacci T. Glow-discharge nitriding of AISI 316L austenitic stainless steel: influence of treatment temperatureSurface & Coatings Technology. 2005; 200:2474-80.
191. Farrell K, Specht ED, Panf J, Walker LR, Rar A, Mayotte JR. Characterization of a carburized surface layer on an austenitic stainless steel. J Nucl Mater. 2005; 343:123-33.
192. Christiansen TL, Hummelshϕj TS, Somers MAJ. Expanded austenite, crystallography and residual stress. Surface Engineering. 2010; 26:242-7.
193. Li XY, S.Thaiwatthana, Dong H. Thermal stability of carbon S phase in 316 stainless steel.Surface Engineering. 2002; 18:448-52.
194. Li XY, Sun Y, Bell T. The stability of the nitrogen S-phase in austenitic stainless steel Z Metallkd. 1999; 90:901-7.
195. Christiansen T, Somers MAJ. Decomposition kinetics of expanded austenite with high nitrogen contents. Z Metallkd. 2006; 97:79-88.
196. Orhan Ozturk DLW. Thermal stability of the high-N solid-solution layer on stainless steel. Surface and Coatings Technology. 2002; 158 –159:288–94.
197. Tamura I. Deformation-induced martensitic transformation and transformation-induced plasticity in steels. Metal science. 1982; 16:245-53
198. Nakada N, Ito H, Matsuoka Y, Tsuchiyama T, Takaki S. Deformation-induced martensitic transformation behavior in cold-rolled and cold-drawn type 316 stainless steels. Acta Materialia. 2010; 58:895-903
199. Talonen J, Hänninen H. Formation of shear bands and strain-induced martensite during plastic deformation of metastable austenitic stainless steels Acta Materialia. 2007; 55:6108-18
200. Datta K, Delhez R, Bronsveld PM, Beyer J, Geijselaers HJM, Post J. A low-temperature study to examine the role of ε-martensite during strain-induced transformations in metastable austenitic stainless steels Acta Materialia. 2009; 57:3321-6
201. Byun TS, Hashimoto N, Farrell K. Temperature dependence of strain hardening and plastic instability behaviors in austenitic stainless steels. Acta Materialia. 2004; 52:3889-99
202. B.Weiss, Stickler R. Phase instabilities during high temperature exposure of 316 austenitic stainless steel. Metallurgical Transactions. 1972; 3:851-66.
203. Khan RHU. Characteristics and Stress State of Plasma Electrolytic Oxidation Coatings: The University of Sheffield; 2008.
204. Birkholz M, Fewster PF, Genzel C. Thin film analysis by X-ray scattering. Germany: Wiley-VCH; 2006.
205. Fitzpatrick ME, Fry AT, Holdway P, Kandil FA, Shackleton J, Suominen L. Determination of Residual Stresses by X-ray Diffraction – Issue 2. Teddington, Middlesex, United Kingdom: National Physical Laboratory2005.
206. Li XY. Characterisation of low-temperature plasma nitrided austenitic stainless

steels: University of Birmingham; 1999.
207. Barrer RM. Diffusion in and through Solids: Cambridge University Press; 1951.
208. Shewmon PG. Diffusion in Solids: Mc Graw-Hill Press; 1963.
209. Bowen AW, Leak GM. SOLUTE DIFFUSION IN ALPHA-IRON AND GAMMA-IRON. Metall Trans. 1970; 1:1695.
210. Hsu TY, Mou YW. Thermodynamics of the banitic transformation in Fe-C alloys. Acta Metall. 1984; 32:1469-81.
211. Zhang L, Zhang CB, Wang YM, Liu XH, Wang GD. Cellular automation model to simulate nucleation and growth of ferrite grains for low-carbon steels. Journal of Materials Research. 2002; 17:2251-9.
212. Zhang L, Zhang CB, Wang YM, Wang SQ, Ye HQ. A cellular automation investigation of the transformation from austenite to ferrite during continuous cooling. Acta Materialia. 2003; 51:5519-27.
213. Zener C. Impact of magnetism upon metallurgy. Journal of Metals, Transactions AIME. 1955; 203:619-30.
214. Aaronson HI, Domian HA, Pound GM. Thermodynamics of the austenite - proeutectoid ferrite transformation II, Fe-C-X alloys. Trans Metall Soc AIME. 1966; 236:768-81.
215. Bycong-Joo Lee. On the stability of Cr carbides. CALPHAD. 1992; 16:121-49.
216. Hsu TY. Theory and Modeling of phase transformations under stress in steel. Transactions of Materials and Heat Treatment 2004; 25(5):1-7.
217. Hsu TY. additivity hypothesis and effects of stress on phase transformations in steel. Current Opinion in Solid State and Materials Science. 2005; 9:256-68.
218. Feder J, Russell KC, Pound GM. Homogeneous nucleation and growth of droplets in vapours. Adv Phys. 1966; 15:111-78.
219. Lange WF, III, Enomoto M, Aaronson HI. The kinetics of ferrite nucleation at austenite grain boundaries in Fe-C alloys. Metallurgical Transactions A. 1988; 19A:427-40.
220. Agarwala RP, Naik MC, Anand MS, Paul AR. Diffusion of Carbon in Stainless Steels. J Nucl Mater. 1970; 36(1):41-&.
221. Crank J. The Mathematics of Diffusion: Clarendon Press; 1956.
222. Lo KH, Shek CH, Lai JKL. Recent developments in stainless steels. Materials Science and Engineering: R: Reports. 2009; 65(4-6):39-104.
223. Belyakov A, Sakai T, Miura H, Tsuzaki K. Grain refinement in copper under large strain deformation. Philosophical Magazine A. 2001; 81 2629.
224. Hsu KL, Ahn TM, Rigney DA. Friction, wear and microstructure of unlubricated austenitic stainless steels. Wear. 1980; 60:13-37.
225. Yang ZY, Naylor MGS, Rigney DA. Sliding wear of 304 and 310 stainless steels. Wear. 1985; 105:73-86.
226. Farias MCM, Souza RM, Sinatora A, Tanaka DK. The influence of applied load, sliding velocity and martensitic transformation on the unlubricated sliding wear of austenitic stainless steels. Wear. 2007; 263(1-6):773-81.
227. SUN Y, LI XY, BELL T. X-ray diffraction characterisation of low temperature plasma nitrided austenitic stainless steels. Journal of Materials Science. 1999; 34:4793 – 802.
228. Chen J. Plasma Surface Alloying of CoCr Alloys to Combat Wear: University of Birmingham; 2007.
229. Wagner CNJ, Boisseau JP, Aqua EN. X-ray diffraction of plastically deformed

copper. Trans Met Soc AIME. 1965; 233:1280-6.
230. Warren BE. X-ray studies of deformed metals. Progress in Metal Physics. 1959; 8:147.
231. Yakubtsov IA, Ariapour A, Perovic DD. Effect of nitrogen on stacking fault energy of f.c.c. iron-based alloys. Acta Materialia. 1999; 47(4):1271-9

Tables

Table 2-1 The chemical compositions (at.%) of typical commercial austenitic stainless steels [12]

AISI type	Composition (at %)						
Element	301	302	304	310	316	321	347
C	0.72 max	0.38 max	0.38 max	1.20 max	0.38 max	0.38 max	0.38 max
N	0.12	0.12	0.12	0.12	0.12	0.12	0.12
Cr	17-19	18-20	19-21	26-28	17-19	17-19	17-19
Ni	6-8	8-10	8-12	19-22	9-14	9-12	9-13
Mo					1-2		
Ti						5x %C	
Nb							10x %C
Mn	1.50	1.50	1.50	1.50	1.50	1.50	1.50

Table 3.1-1 The chemical composition of AISI 316 stainless steel sheet (at. %)

C	Cr	Ni	Mo	Mn	Si	P	S	Cu	N	Fe
0.23	18.35	10.32	1.18	1.62	0.94	<0.05	0.01	0.35	0.29	Balance

Table 3.1-2 The chemical composition of AISI 316L stainless steel foil (at. %)

C	Cr	Ni	Mo	Mn	Si	P	S	Cu	N	Co	Al	Fe
0.15	18.76	10.65	1.10	1.61	0.98	<0.05	0.01	0.35	0.24	0.19	0.21	Balance

Table 3.2-1 The conditions for plasma carburising under *in situ* tensile stress

Code	Temperature (°C)	Stress in situ (MPa)	Treatment Time (h)
PC 450 0 MPa	450	0	10
PC 450 20 MPa	450	20	10
PC 450 40 MPa	450	40	10
PC450 80 MPa	450	80	10
PC400 0 MPa	400	0	10
PC400 40 MPa	400	40	10
PC425 0 MPa	425	0	10
PC425 40 MPa	425	40	10

Table 3.2-2 The experimental conditions for HIPping carbon S-phase

Samples Code	Temperature (°C)	Pressure (MPa)	Enduring Time (h)
PC ASS	0	0	0
HIP 525 10h	525	180	10
HIP 550 5h	550	180	5
HIP 575 1h(HIP 180MPa 1h)	575	180	1
HIP 575 2h	575	180	2
HIP 90MPa 1h	575	90	1
HIP 600 1h	600	180	1
HIP 600 0.5h	600	180	0.5
HIP 550 1h	550	180	1

Table 3.2-3 The experimental conditions for annealing carbon S-phase under tensile stress (i.e. creeping)

Samples Code	Temperature (°C)	Tensile Stress (MPa)	Enduring Time (h)
PC ASS	0	0	0
400 0MPa	400	0	150
400 100MPa	400	100	150
400 200MPa	400	200	150
450 0MPa	450	0	100
450 100MPa	450	100	100
450 200MPa	450	200	100
500 0MPa	500	0	100
500 100MPa	500	100	100
500 200MPa	500	200	100

Table 4.2-1 The chemical composition of voids formed after etching in Sample 'PC45080MPa'

Element	Spectrum 1		Spectrum 7	
	Weight %		Weight %	
C	2.6	±0.59	5.21	±0.57
O	0.7	±0.30	0.83	±0.46
Al	0.6	±0.08		
Si	0.2	±0.07	0.84	±0.11
S	0.4	±0.09	0.78	±0.11
Cl	0.7	±0.09		
Ti	4.5	±0.17		
Cr	18.3	±0.32	16.88	±0.27
Mn	1.9	±0.23	1.37	±0.19
Fe	60.1	±0.59	61.86	±0.60
Ni	10.0	±0.35	12.24	±0.33

Table 4.2-2 TEM/EDX analysis of the S-phase near the surface

Element	Weight %	Weight % Sigma (±)	Atomic %
C	2.7	0.29	11.53
Si	0.7	0.05	1.34
Cr	15.9	0.14	15.57
Mn	1.5	0.08	1.41
Fe	63.1	0.30	57.50
Ni	12.3	0.14	10.68
Mo	3.7	0.25	1.97

Table 4.2-3 TEM /EDX analysis of the S-phase 6μm below the surface

Element	Weight %	Weight % Sigma (±)	Atomic %
C	1.8	0.16	8.05
Si	0.6	0.03	1.12
Cr	16.0	0.10	16.15
Mn	1.6	0.06	1.50
Fe	62.8	0.20	59.24
Ni	12.9	0.10	11.57
Mo	4.3	0.18	2.37

Table 4.4-1 EDX results from different oxide layers

Element	Atomic %			
	Fe_3O_4	Fe_2O_3	Substrate	Fe_2O_3 in substrate
O	50.57	50.0	4.98	54.74
Cr	7.55	15.6	19.93	6.3
Mn	0.68	1.2	1.47	0.6
Fe	33.90	26.4	60.32	27.51
Ni	2.25	1.7	7.83	1.25

Table 4.5-1 Chemical compositions (wt. %) measured by EDX in the wear track of UT 316ASS tested in air at a load of 21N

	C	O	Si	Cr	Mn	Fe	Co	Ni	Mo	W
Spectrum 1	2.30	5.33	0.39	15.51	1.51	60.36	0.66	10.54	2.33	1.07
Spectrum 2	1.93	20.29		10.39	0.94	37.51	1.19	6.39	1.32	20.04
Spectrum 3	2.00	30.29		8.21	0.69	31.10	1.28	5.26	1.11	20.06
Spectrum 4	3.80	26.45		9.87	0.92	36.41	0.94	6.22	1.41	13.99

Table 4.5-2 Chemical compositions (wt.%) measured by EDX in the wear track of PC 316ASS tested in air at a load of 21N

	C	O	Cr	Mn	Fe	Co	Ni	Mo	W
Spectrum 1	2.52	15.54	13.20	1.17	47.17	0.70	8.78	2.09	8.74
Spectrum 2	2.11	12.75	13.92	1.46	50.36	0.69	9.36	1.89	7.45
Spectrum 3	2.48	14.55	13.34	1.48	48.31	0.48	8.89	1.78	8.70
Spectrum 4	2.86	16.67	12.75	1.17	46.07	0.59	8.58	1.88	9.43

Table 4.5-3 Chemical compositions (wt.%) measured by EDX in the wear track of UT 316ASS tested in oil at a load of 56N

	C	O	Si	Cr	Mn	Fe	Co	Ni	Mo	W
Spectrum 1	16.80	4.90	0.30	12.23	1.46	51.96	0.27	8.28	3.22	0.59
Spectrum 2	16.94	2.31	0.15	12.73	0.68	54.87	0.52	8.75	2.78	0.26
Spectrum 3	18.46	6.00	0.21	12.31	1.28	49.71	0.35	8.82	2.67	0.19
Spectrum 4	19.85	5.51	0.34	12.71	0.99	49.26	0.40	8.10	2.85	

Table 4.5-4 Chemical compositions (wt. %) measured by EDX in the wear track of PC 316ASS tested in oil at a load of 214N

	C	O	Si	Cr	Mn	Fe	Co	Ni	Mo	W
Spectrum 1	6.31	0.10	0.31	15.73	1.92	62.78	0.12	10.02	2.35	0.37
Spectrum 2	13.40	1.47	1.88	13.93	1.18	56.17	0.63	9.51	1.83	
Spectrum 3	9.56	0.11	0.22	15.45	1.75	60.17	0.36	10.13	1.79	0.43

Table 5.1-1 ΔT_M and ΔT_{NM} parameters for alloying elements [213,214]

Alloying Elements	°C per wt pct x		°C per at. pct x	
	ΔT_M	ΔT_{NM}	ΔT_M	ΔT_{NM}
Cr	-20	-19	-19	-18
Mn	-38	-40	-37.5	-39.5
Ni	-5.5	-17	-6	-18
Co	18	15	19.5	16
Mo	-15	-10	-26	-17
Al	17	30	8	15
Cu	-4	-10	4.5	-11.5
Si	-6	0	-3	0

Tables 5.2-1 Calculated diffusion coefficient of carbon from GDS profiles at different heat treatment conditions

Conditions	HT5501h	HT5751h	HT600 1h	HIP5501h	HIP5751h	HIP6001h
Diffusion coefficient ($\times 10^{-15} m^2/s$)	5.4436	5.6470	9.3876	2.0317	3.6175	7.5804

Table 5.4-1 Elastic constant values and fault parameters for various reflections of austenitic stainless steel [230]

hkl	$(S_1)_{hkl}$ $(10^{-6}MPa^{-1})$	G_{hkl}
111	-0.96	-0.0345
200	-2.55	+0.0689
220	-1.36	-0.0345
311	-1.80	+0.0125
222	-0.96	+0.0172

Table 5.4-2 Calculated values lattice distortion caused by three ways comparing with measured value for carburised bulk AISI316

hkl	Δa_{RS} (Å)	Δa_{SF} (Å)	Δa_{SS} (Å)	Δa calculated (Å)	Δa measured (Å)	Relative Error (%)
111	0.007677	-0.00628	0.083	0.090846	0.09067	0.2
200	0.023504	0.012541	0.083	0.107021	0.12534	14.6
220	0.011634	-0.00628	0.083	0.09489	0.09027	5.1
311	0.016065	0.002275	0.083	0.099418	0.10761	7.6
222	0.007677	0.003131	0.083	0.090846	0.08685	4.6

Figures

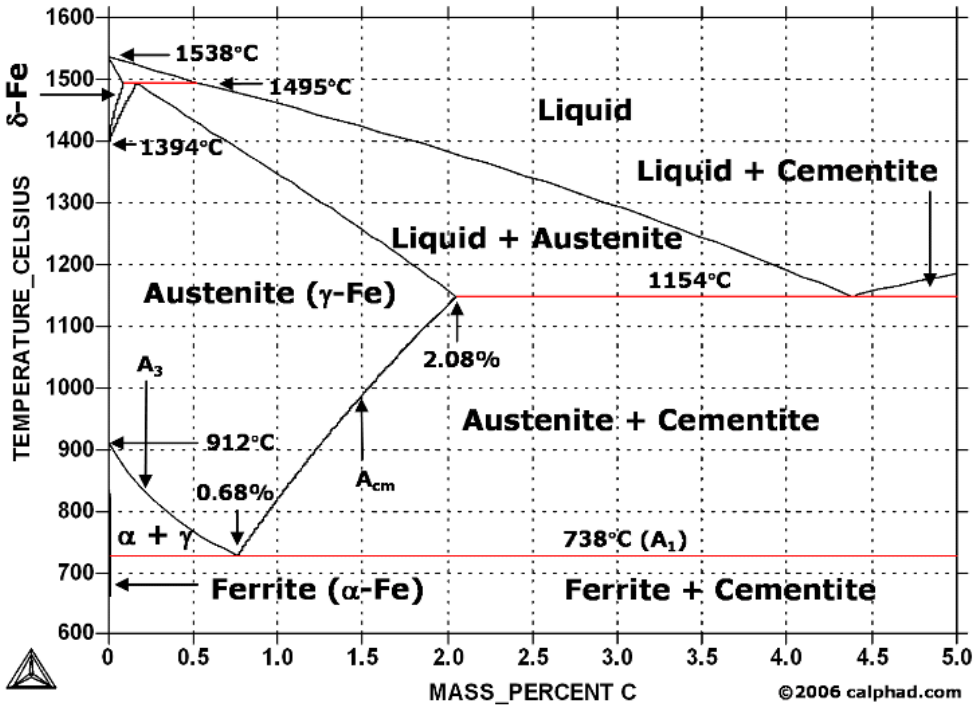

Figure 2-1 Fe-C phase diagram [15]

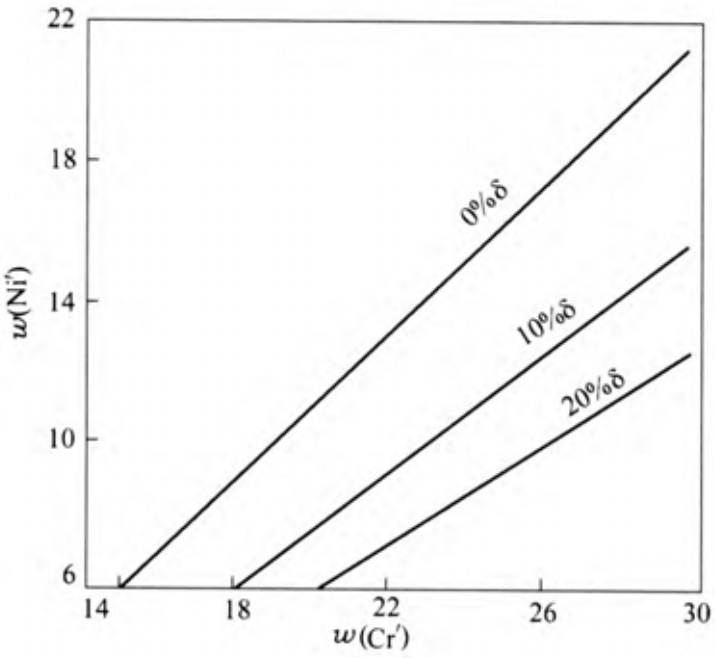

Figure 2-2 The equilibrium phase diagram for stainless steels of ferrite and austenite as a function of the chromium and nickel equivalents [16]

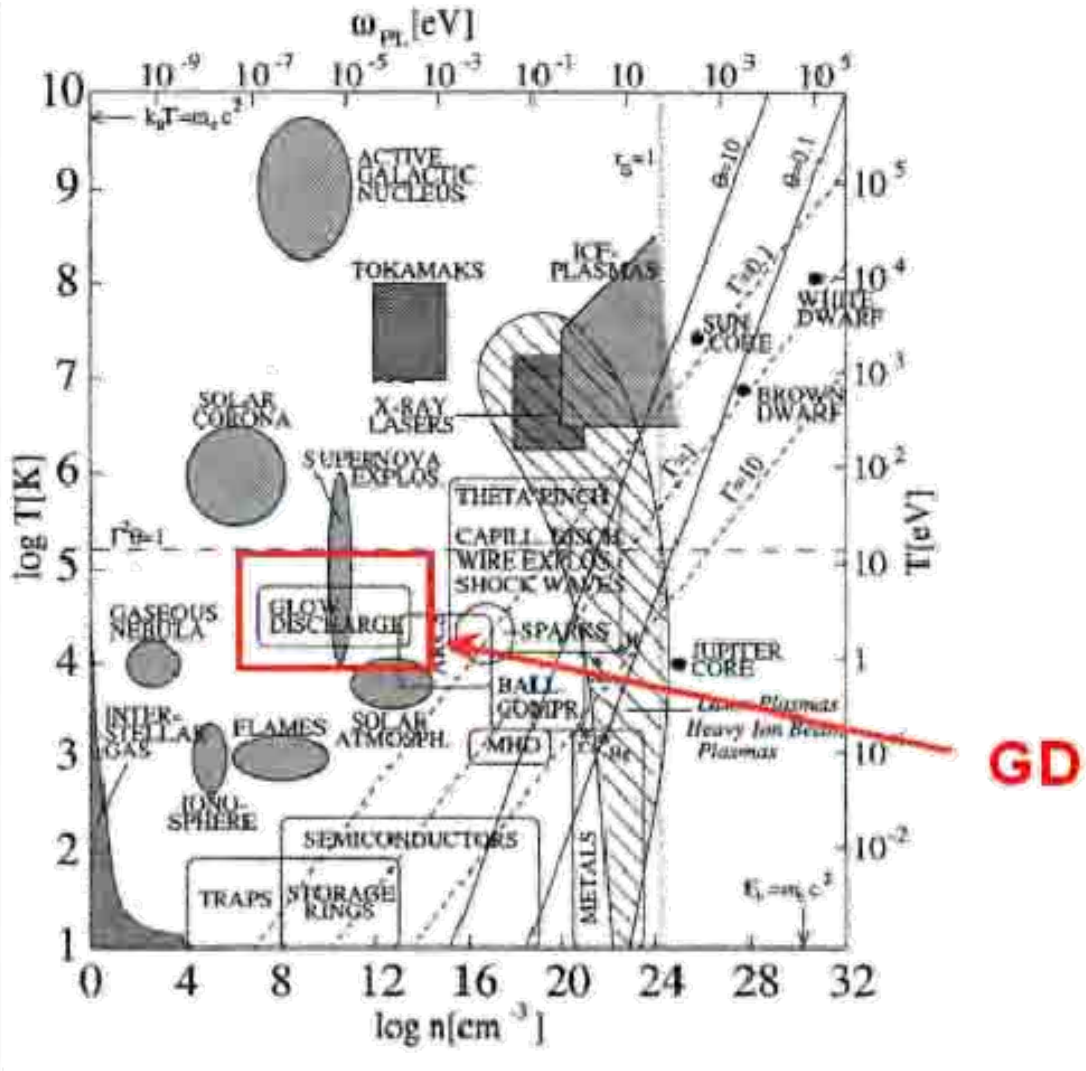

Figure 2-3 Schematics of different types of plasma [76]

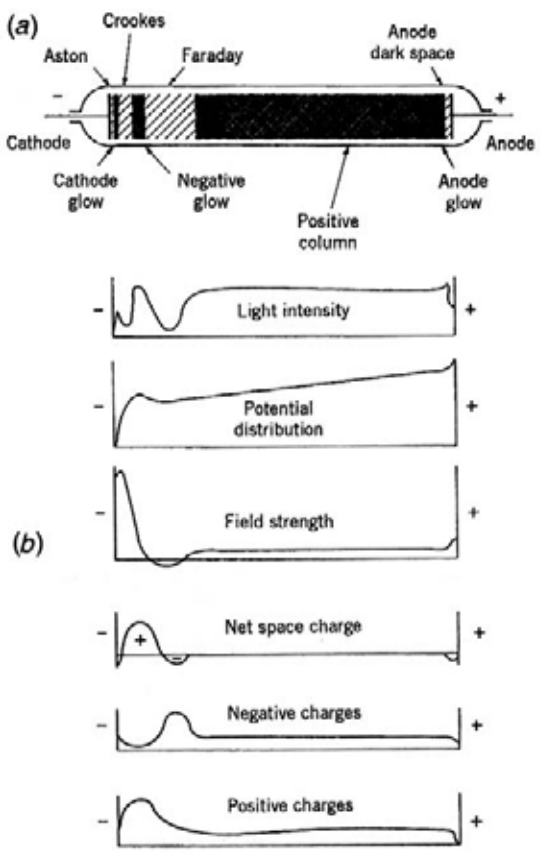

Figure 2-4 (a) Illustrates showing different region of direct current (DC) glow discharge; (b) corresponding parameters [77]

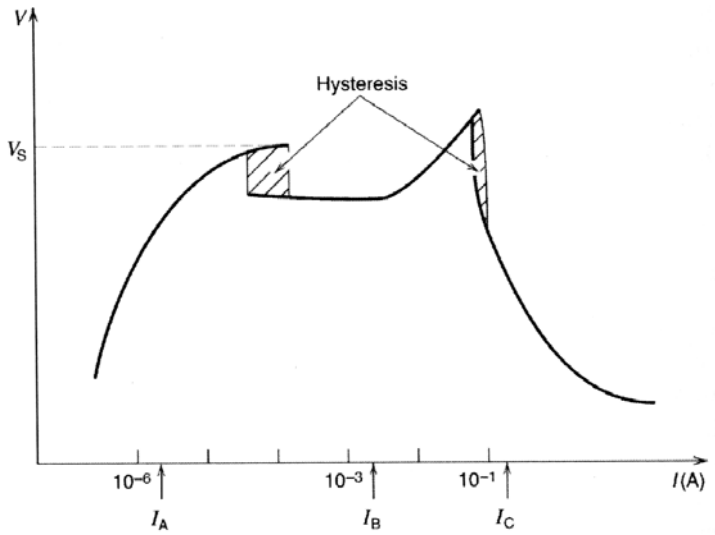

Figure 2-5 Typical voltage-current characteristic of a DC discharge [81]

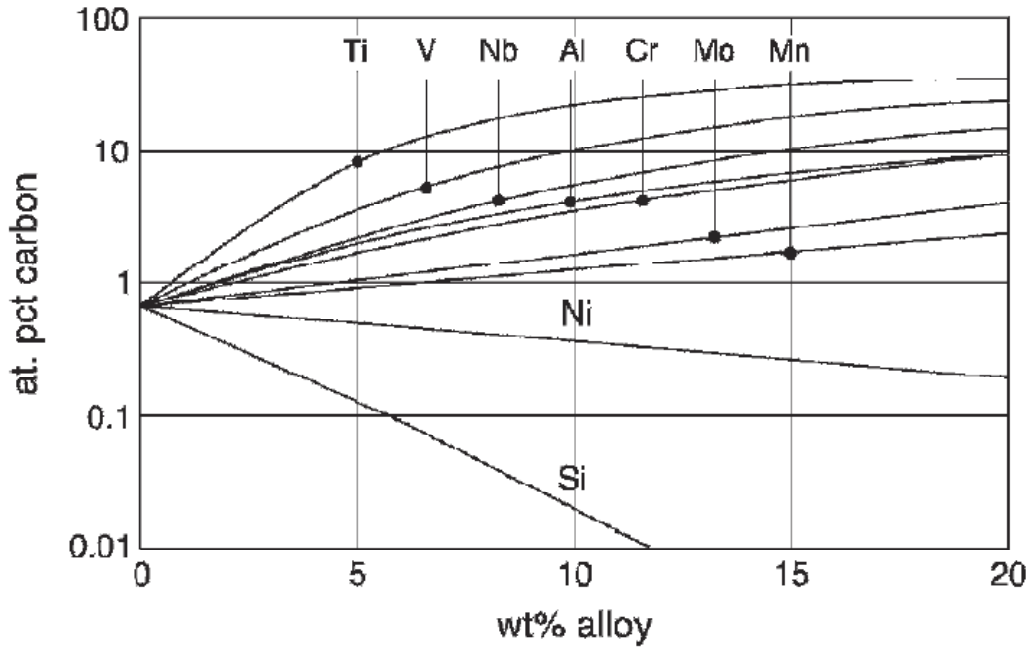

Figure 2-6 Carbon solubility in Fe-based austenitic alloys at 477 °C as a function of ternary alloy additions under paraequilibrium conditions [118]

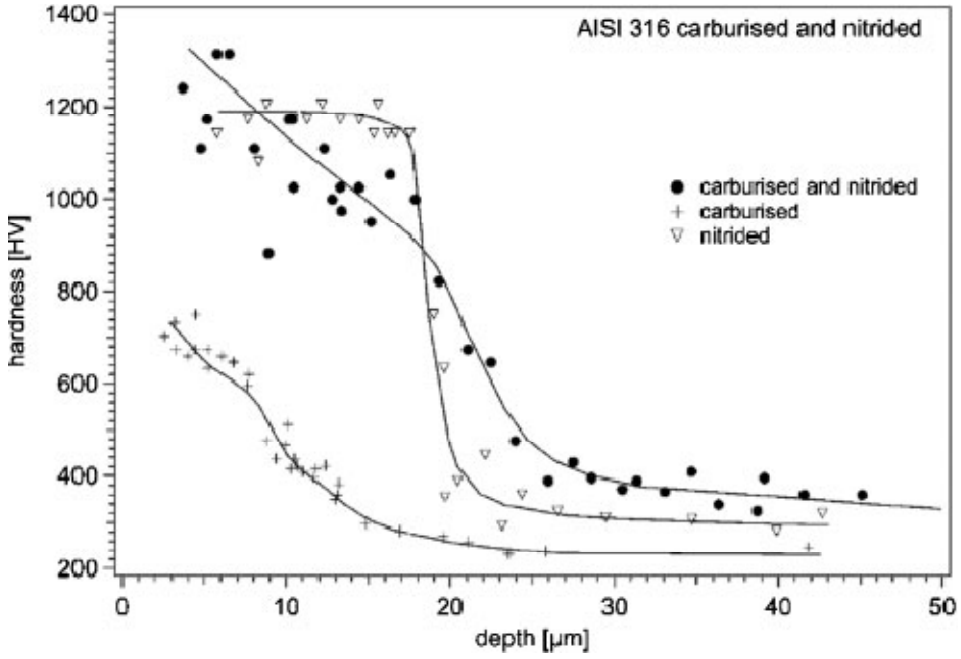

Figure 2-7 Hardness depth profiles of S-phase layers with different interstitials [104]

Figure 2-8 Plasma treatment of control rod cluster of AISI 316 tubes for nuclear reactor [6]

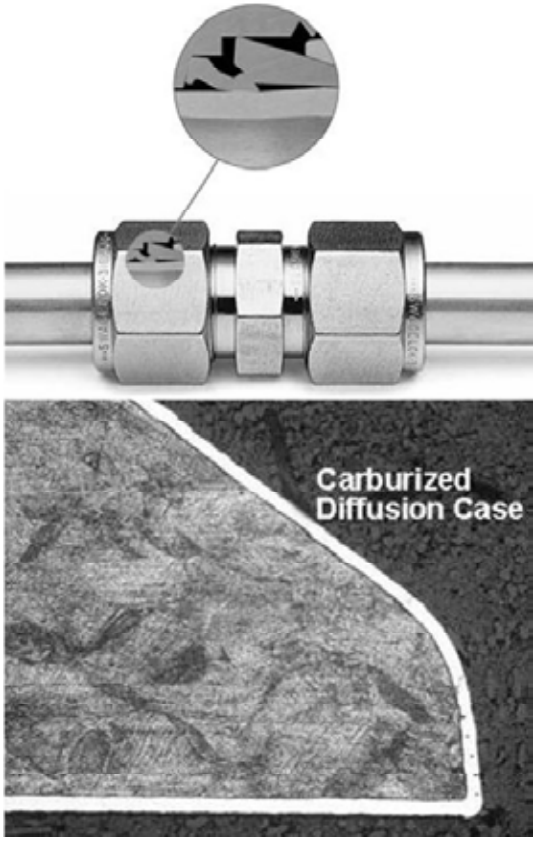

Figure 2-9 Gas carburised S-phase on grip components [183]

Figure 3.2-1 The 40kW Klöchner Ionon Gmbh plasma unit at the University of Birmingham DC plasma vacuum unit

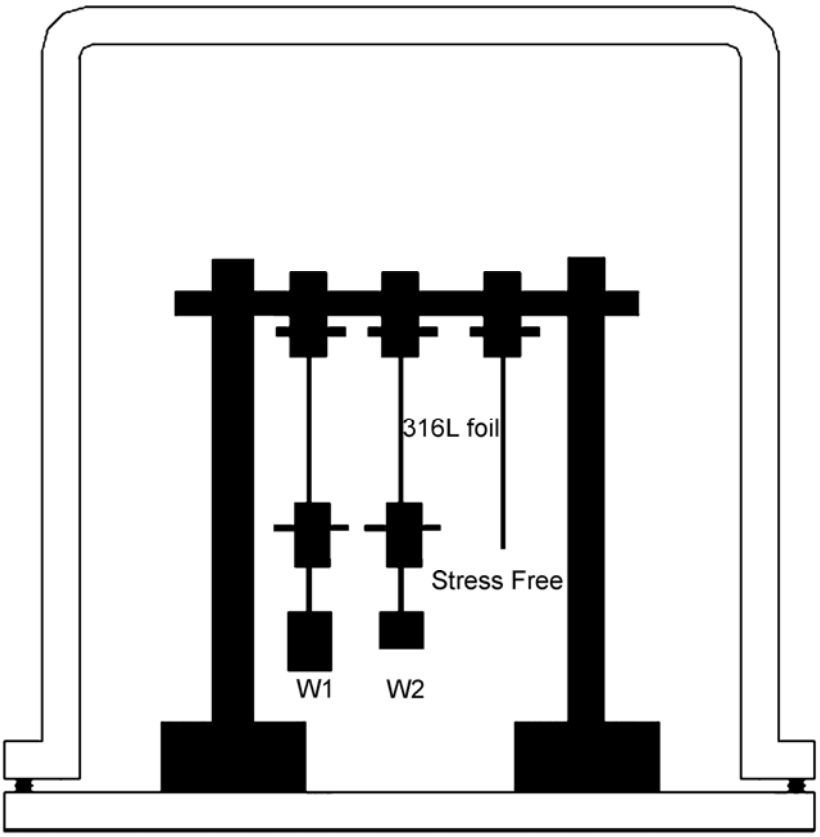

Figure 3.2-2 The schematic diagram of the set-up of plasma carburising with in-situ tensile stress

Figure 3.2-3 The EPSI Lab HIP facility at the University of Birmingham

Figure 3.2-4 The molybdenum furnace of HIP facility at the University of Birmingham

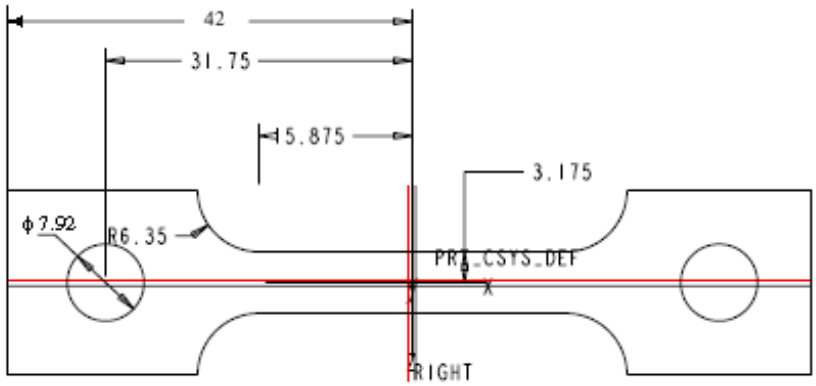

Fig 3.2-5 Schematic drawing of dog-bone specimen for creep experiments (unit: mm)

Figure 3.2-6 Installations for experiments of annealing of carburised 316ASS under tensile stresses

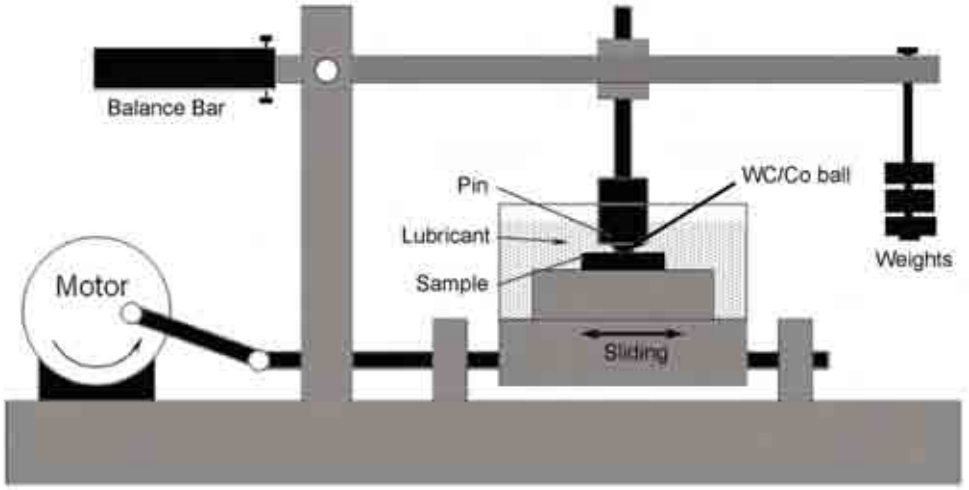

Figure 3.2-7 Schematic diagram of the reciprocating tribometer

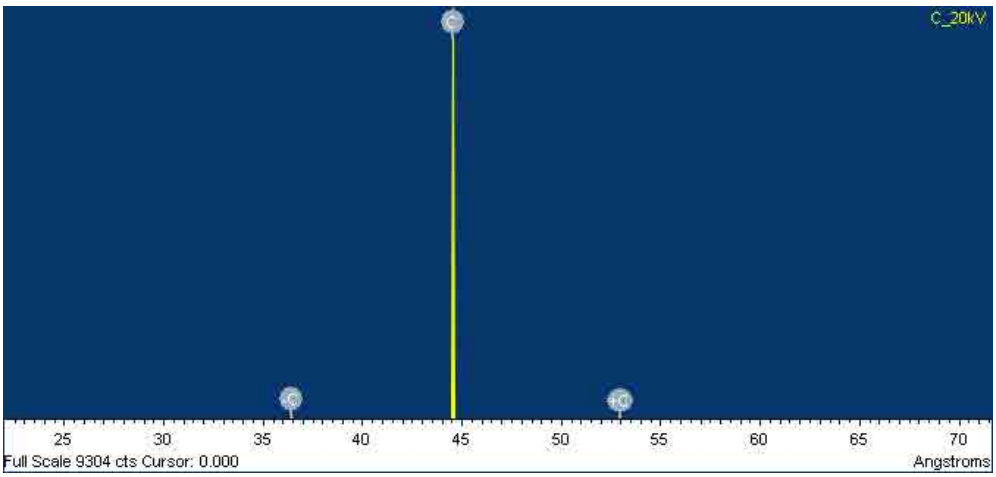

Figure 3.3-1 WDS spectrum of graphite for the calibration of carbon

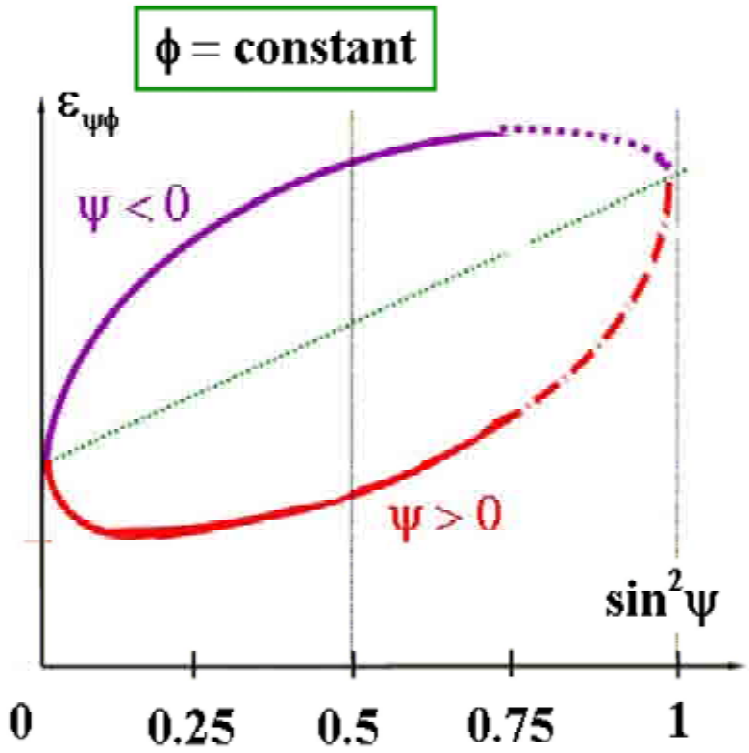

Figure 3.3-2 Schematic showing elliptical fit of $\varepsilon_{\psi\phi}$ versus $\sin^2\psi$ [203]

Figure 4.1-1 The picture of 316L foil specimen after plasma carburising

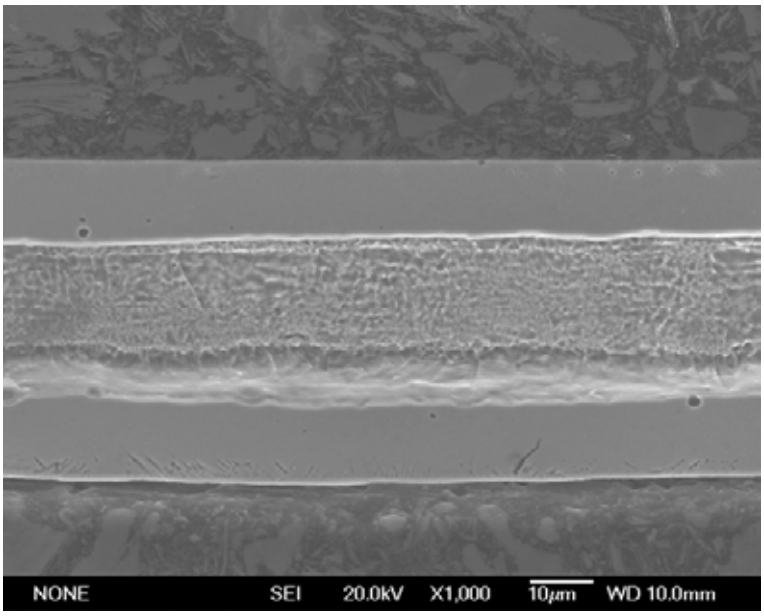

Figure 4.1-2 A cross sectional SEM image of PC450 10h treated 316L foil specimen

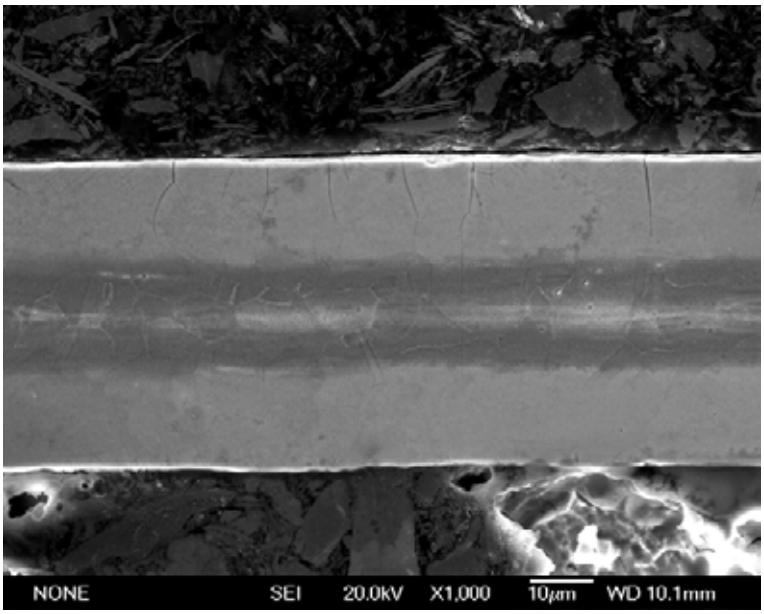

Figure 4.1-3 A cross sectional SEM image of PC450 20h treated 316L foil specimen

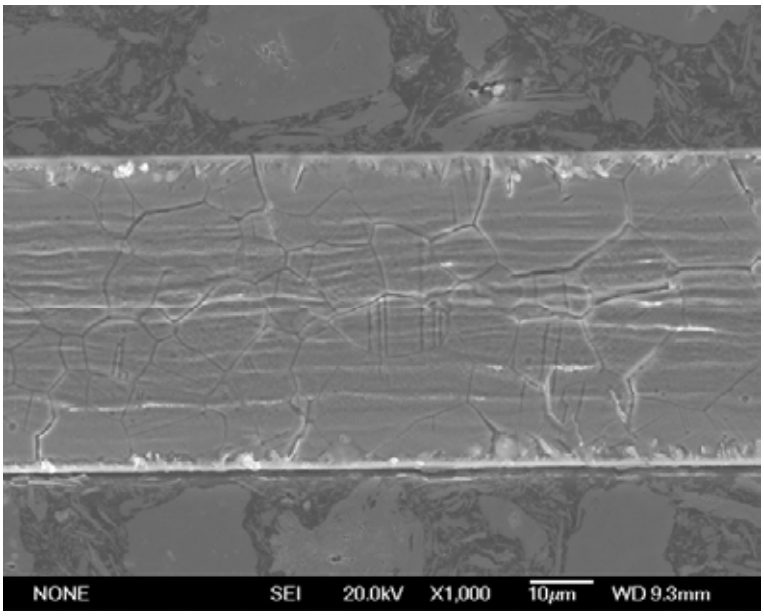

(a)

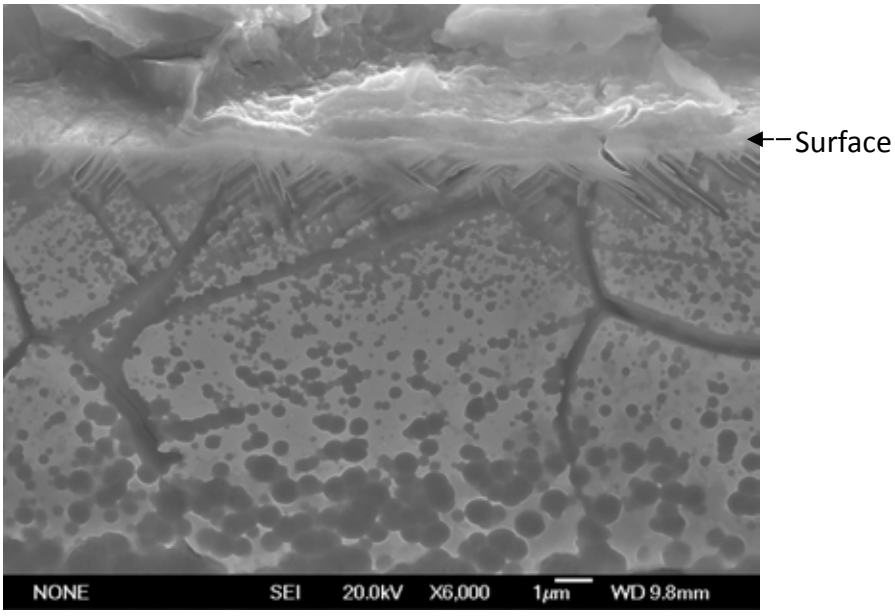

(b)

Figure 4.1-4 (a) Cross sectional SEM image of PC450 30h treated 316L foil specimen; (b) Magnified image of the needle like morphology growing from the surface.

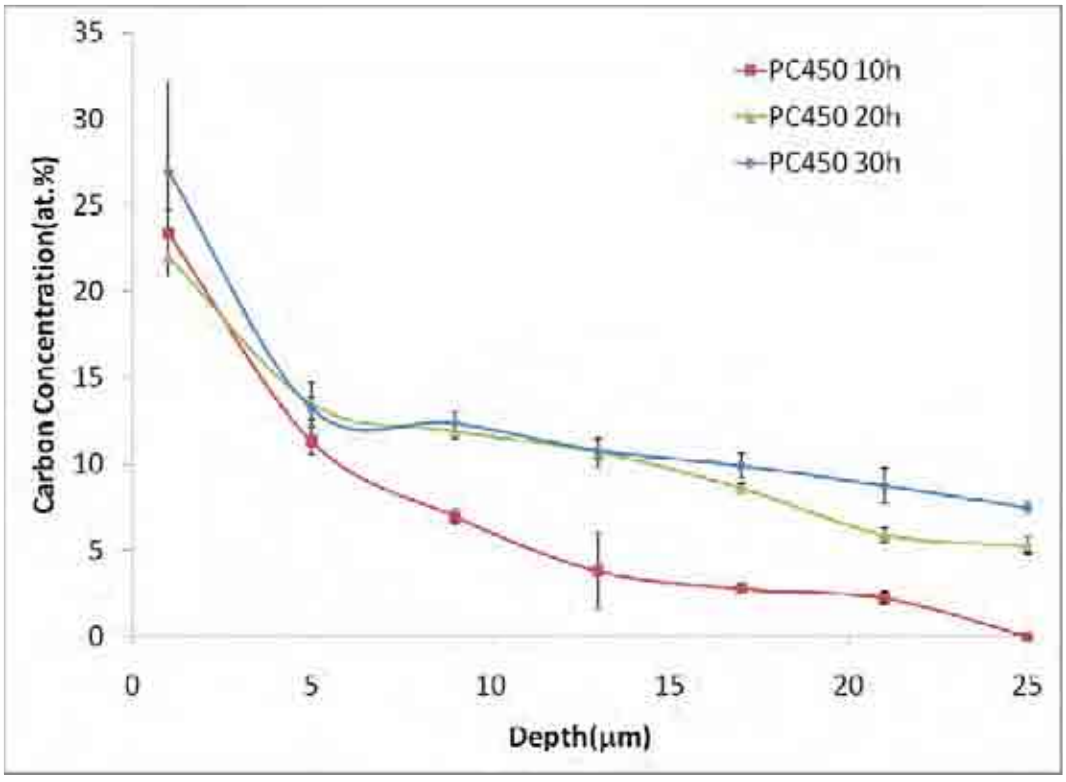

Figure 4.1-5 Carbon profiles of PC450 10h, 20h and 30h treated 316L foils measured by WDS

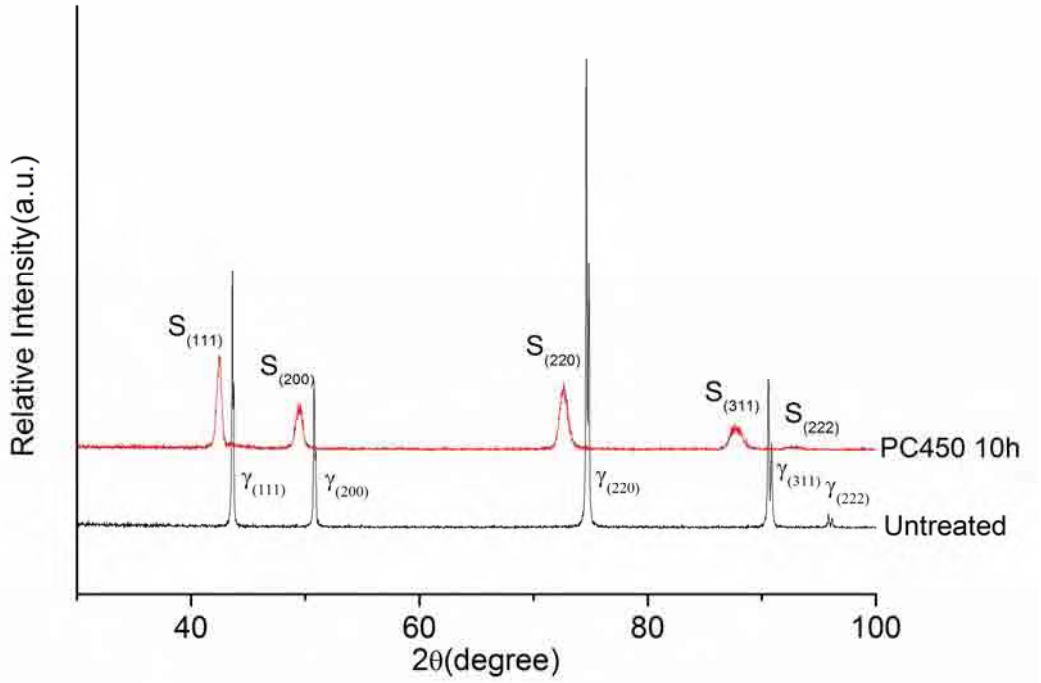

Figure 4.1-6 XRD patterns of untreated and PC450 10h treated 316L foils (the peak splitting in the untreated condition is due to the improper filtering of kα2 in the XRD machine)

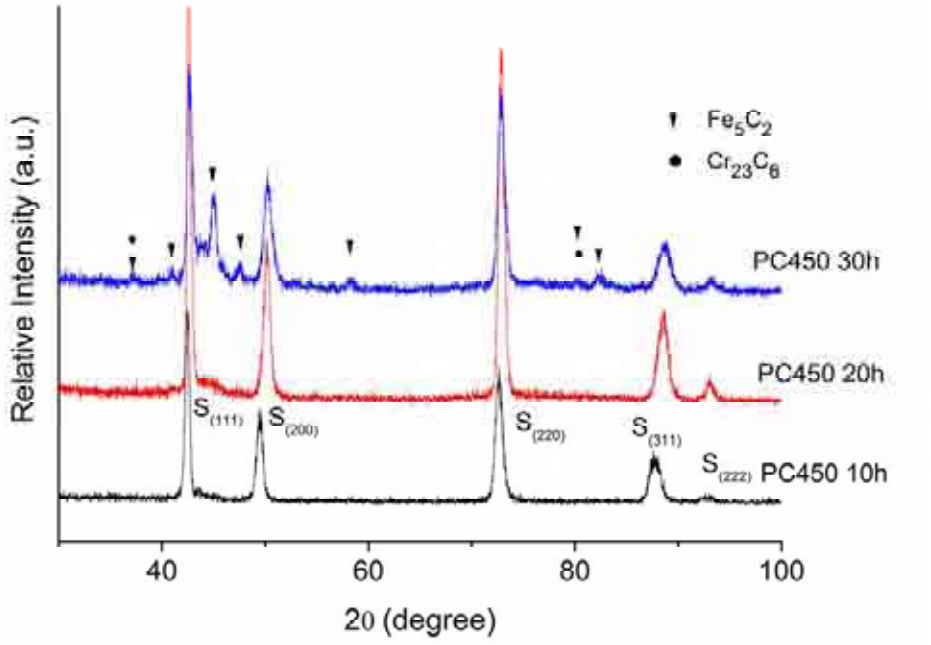

Figure 4.1-7 XRD patterns of PC450 10h, 20h and 30h treated 316L foil

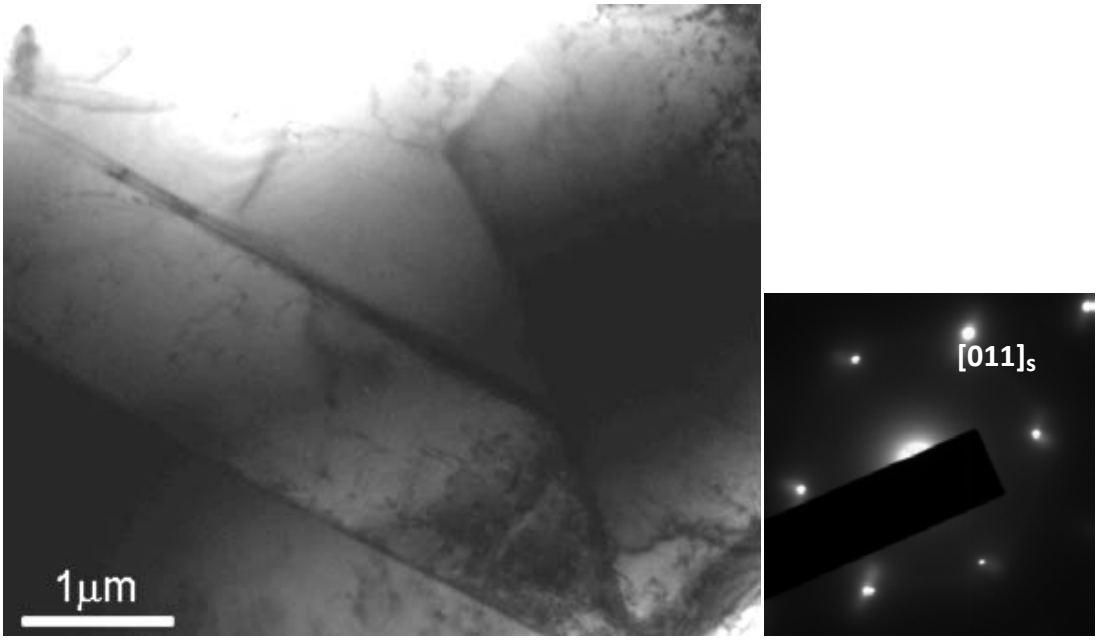

(a) (b)

Figure 4.1-8 TEM characterisation of Sample 'PC450 10h': (a) Typical TEM S-phase microstructure of Sample 'PC450 10h'; (b) FCC patterns of S-Phase, b=[011]s

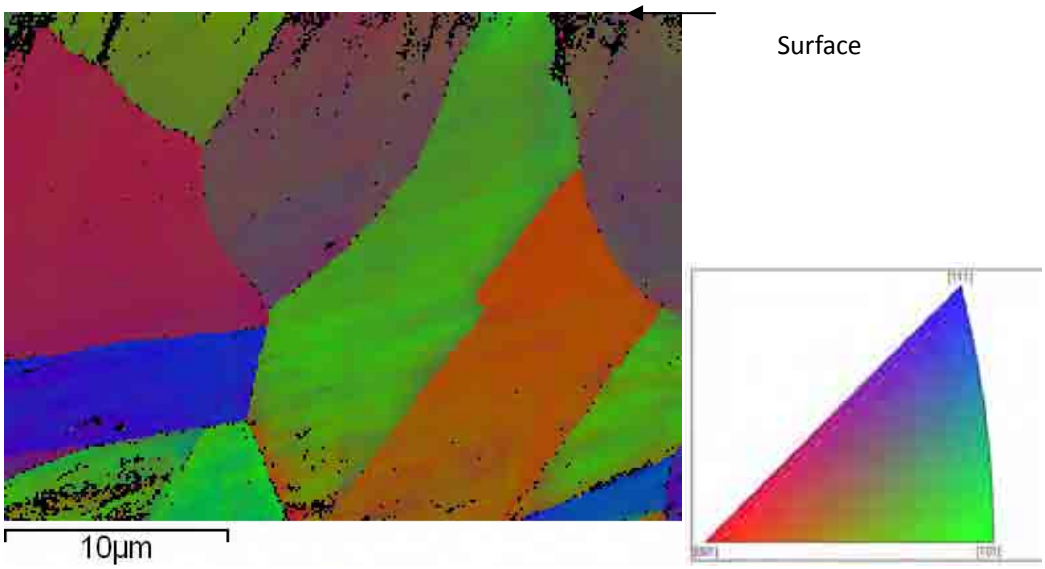

(a) (b)

Figure 4.1-9 EBSD analysis of Sample 'PC450 30h': (a) orientation mapping of austenitic phase (gamma) and (b) colour key for orientations

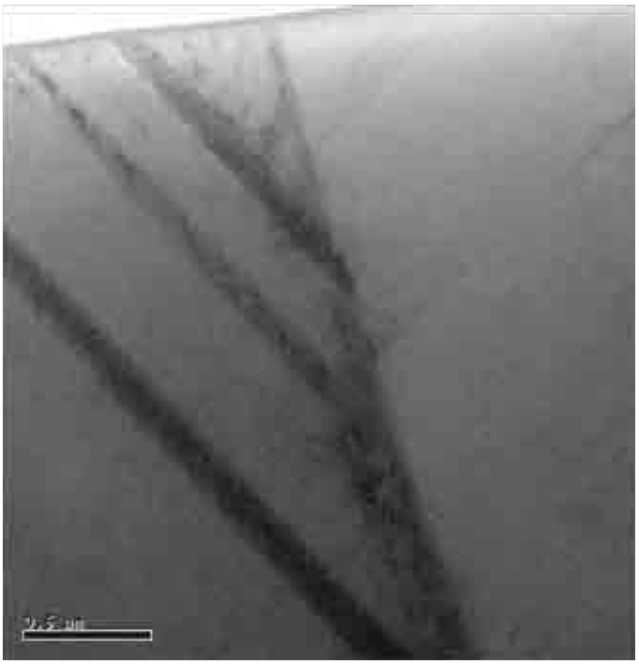

(a)

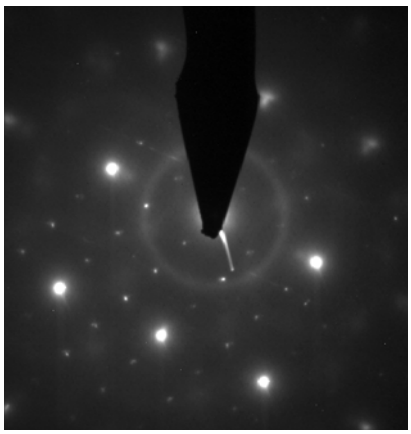

(b)

(c)

$[323]_{\mathrm{S-phase}}$ // $[125]_{\chi-\mathrm{Fe5C2}}$

$(\bar{1}31)_{\mathrm{S-phase}}$ // $(3\bar{4}1)_{\chi-\mathrm{Fe5C2}}$

(d)

Figure 4.1-10 Cross-sectional TEM results of Sample 'PC450-30h': a) microstructure and b) and SAD patterns showing needles of χ-Fe_5C_2 on S-phase; c) index of SAD patterns of b) and interpretation of orientation relationships

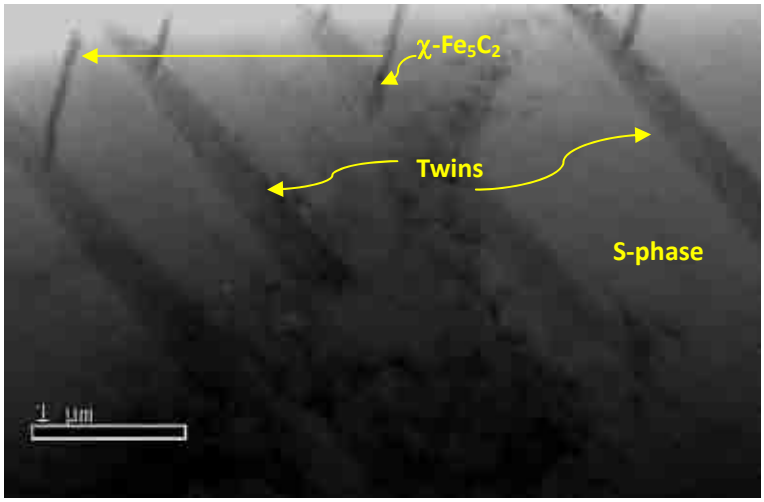

(a)

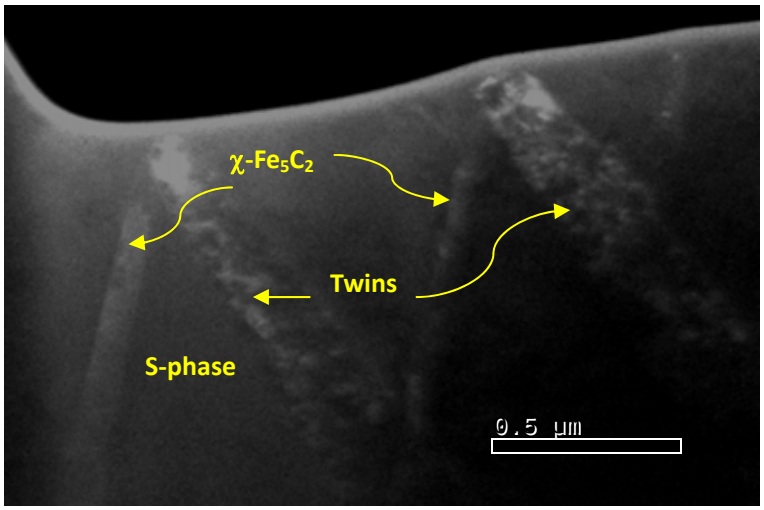

(b)

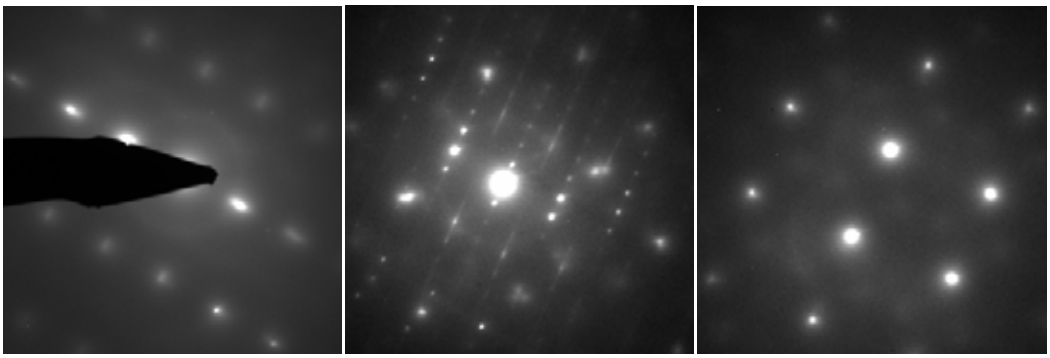

(c) (d) (e)

Figure 4.1-11 Cross sectional TEM characteristics of Sample 'PC450-30h' (a) bright field microstructure, (b) dark field microstructures and SAD patterns taken from(c) bands of twins, [013]FCC; (d) needles of χ-Fe_5C_2, [012]and (e) S-phase matrix,[323]FCC

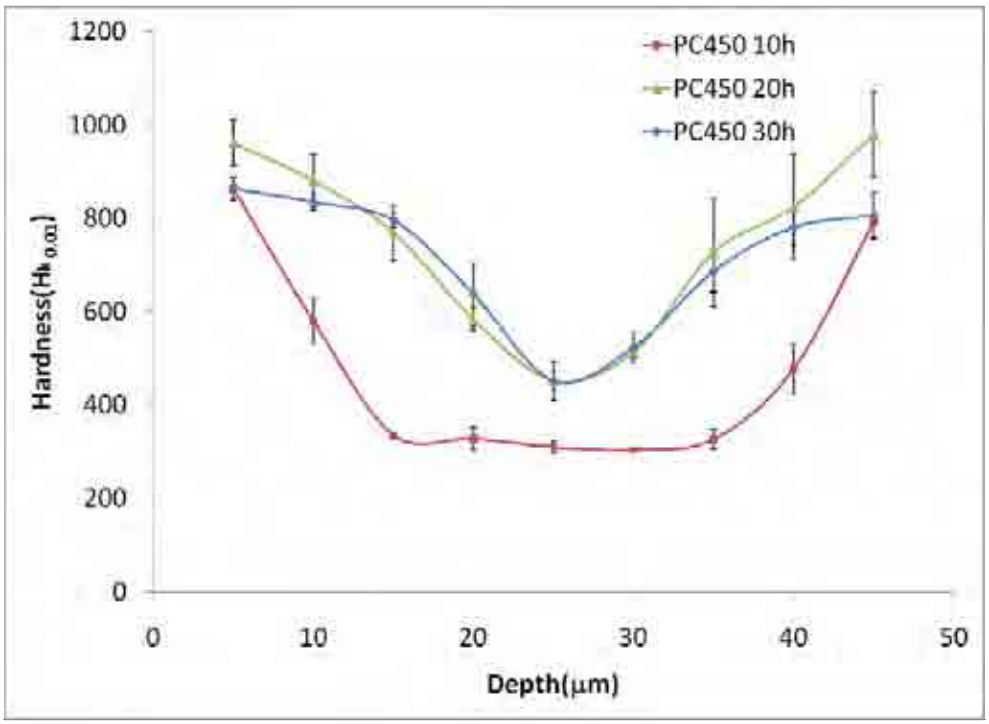

Figure 4.1-12 Micro hardness profiles across PC450 10h, 20h and 30h treated 316L foils

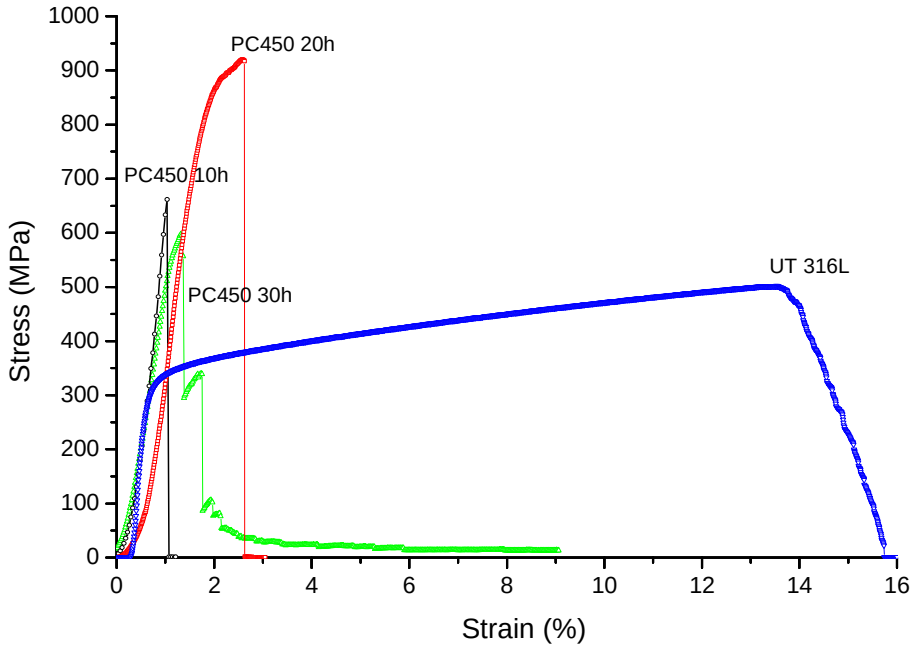

Figure 4.1-13 Tensile curves for untreated (UT316L) and PC450 10h,20h and 30h treated 316L foils

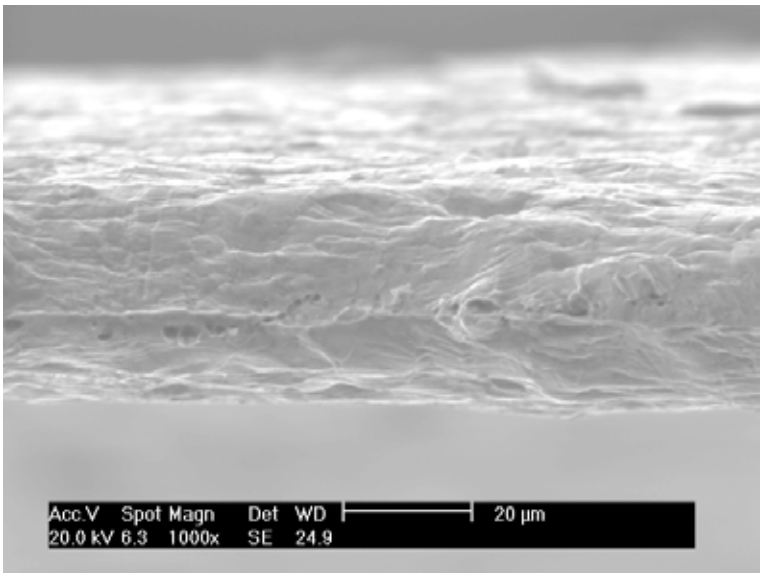

Figure 4.1-14 Fracture morphology of UT 316L foil after tensile test

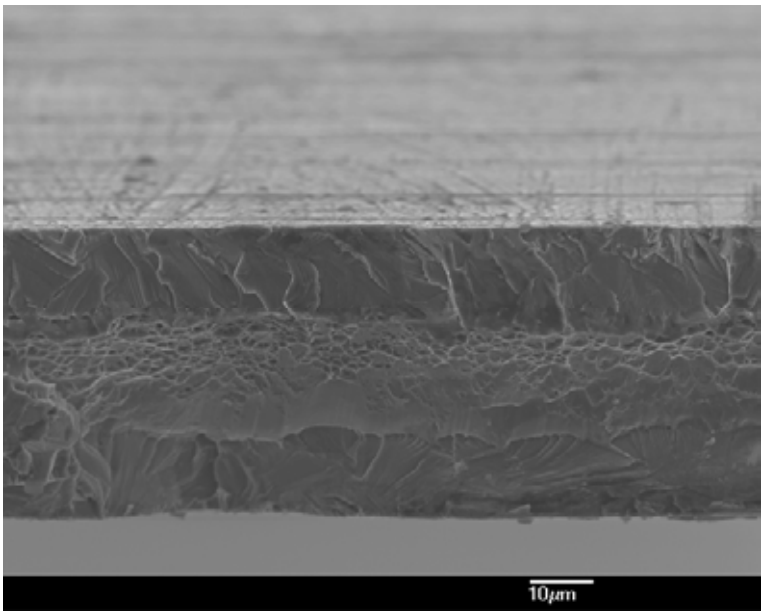

(a)

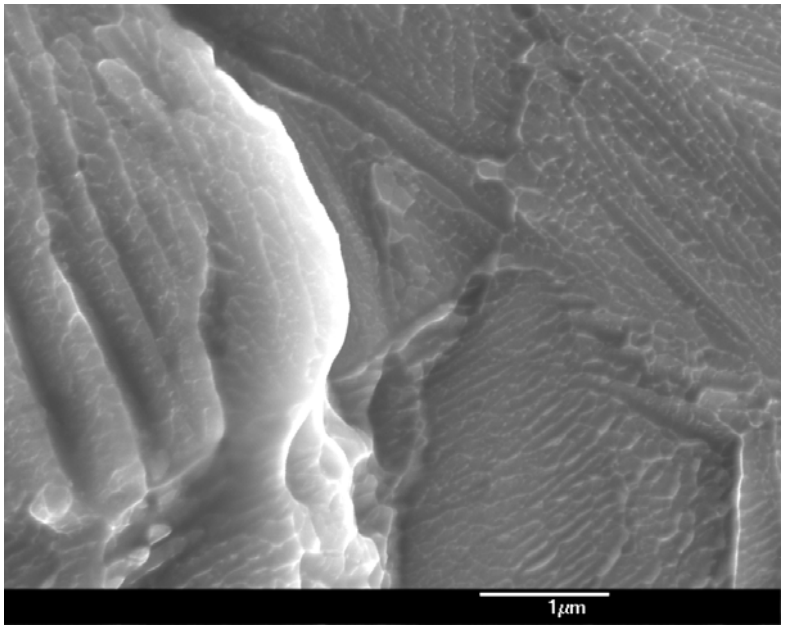

(b)

Figure 4.1-15 (a) Fracture morphology of PC450 10h treated 316L foil after tensile test; (b) cleavage facets in S-phase

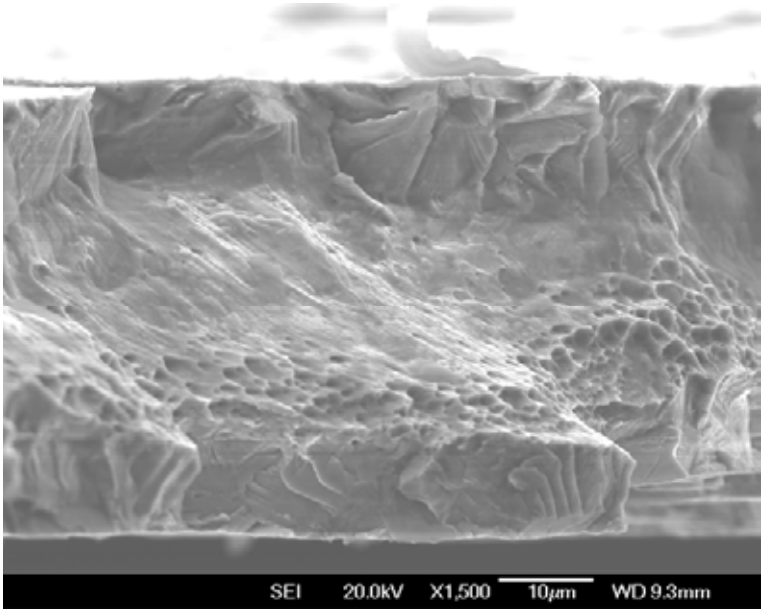

Figure 4.1-16 Fracture morphology of PC450 20h treated 316L foil after tensile test

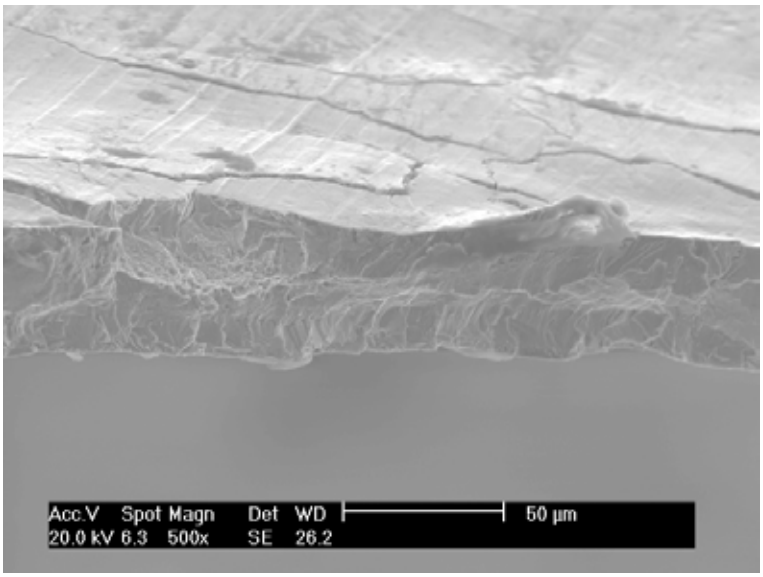

(a)

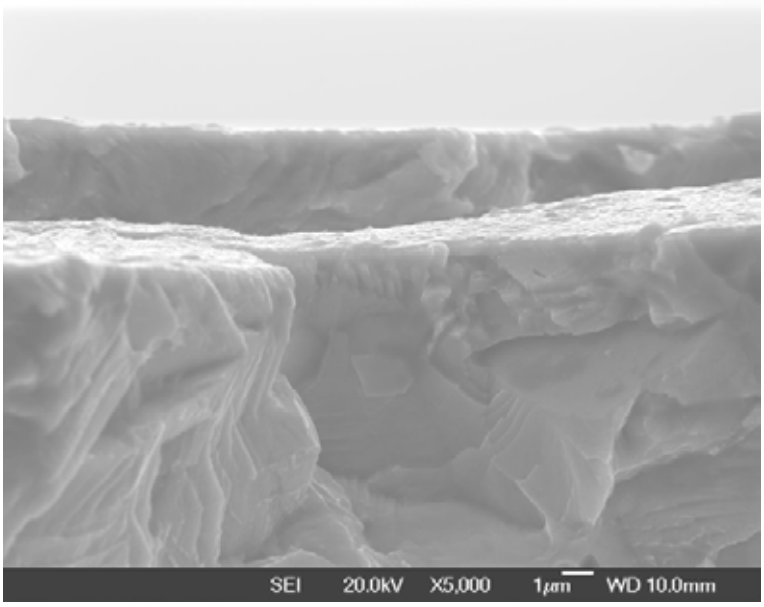

(b)

Figure 4.1-17 (a) Fracture morphology of PC450 30h treated 316L foil after tensile test; (b) magnified tearing feature

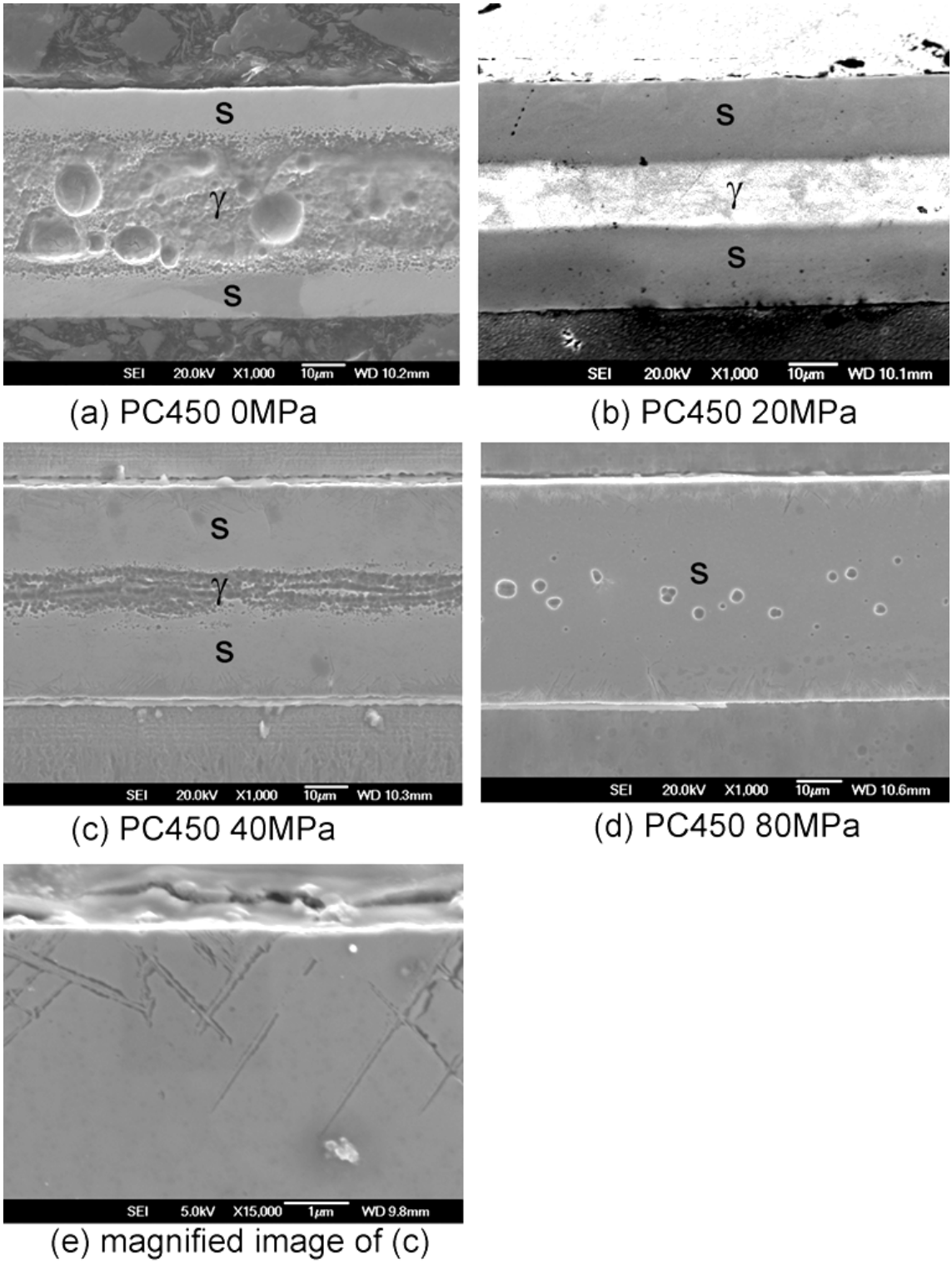

Figure 4.2-1 Cross sectional SEM micrographs of etched 316L foils after 450°C 10h carburising under a tensile stress of 0MPa, 20MPa and 40MPa

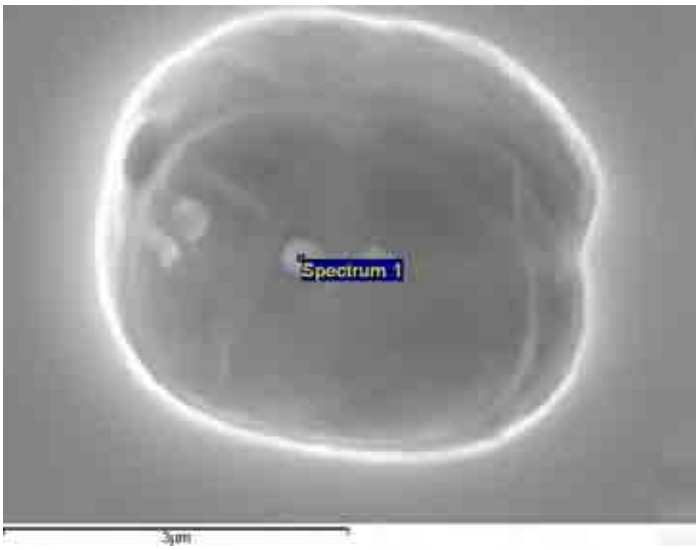

(a)

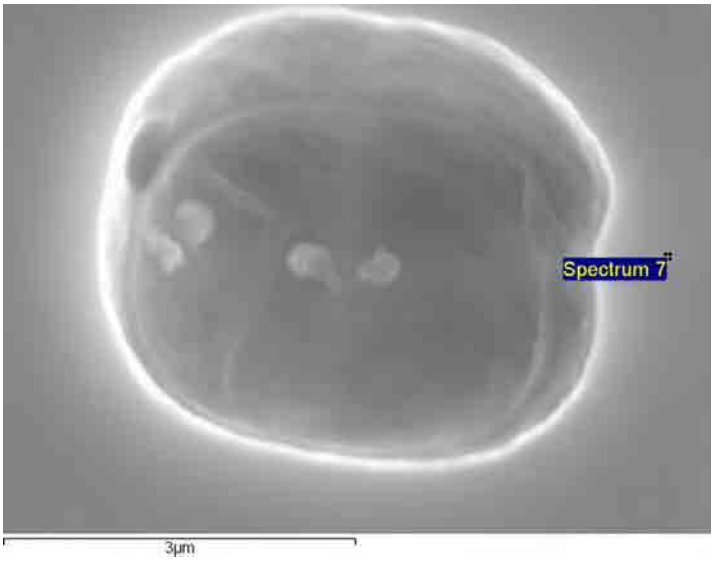

(b)

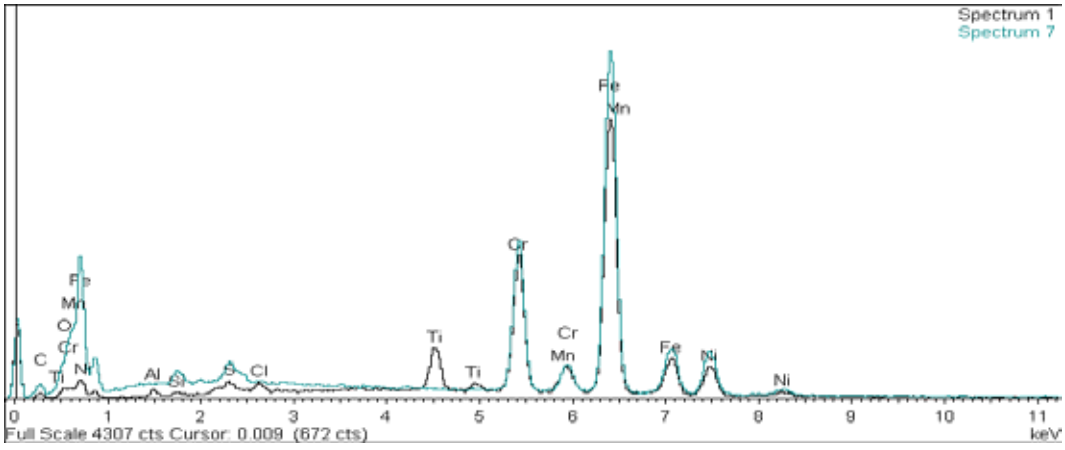

(c)

Figure 4.2-2 EDX analysis of voids formed after etching in 'PC450 80MPa' (a) on the particle remaining in the void; (b) outside the void; (c) spectrums of a & b

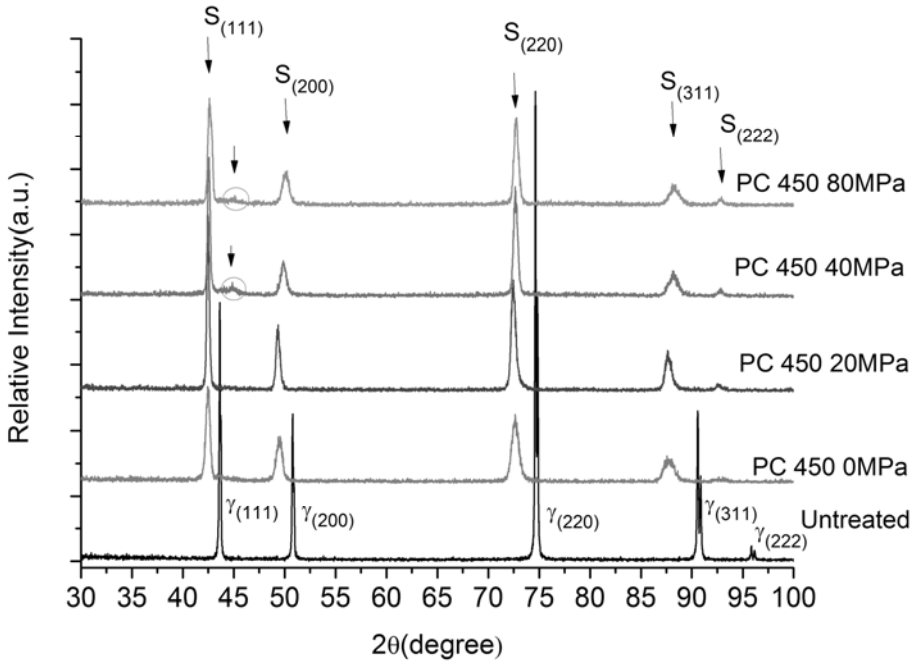

Figure 4.2-3 XRD patterns of 316L foils untreated and plasma carburised under different *in-situ* tensile stress levels

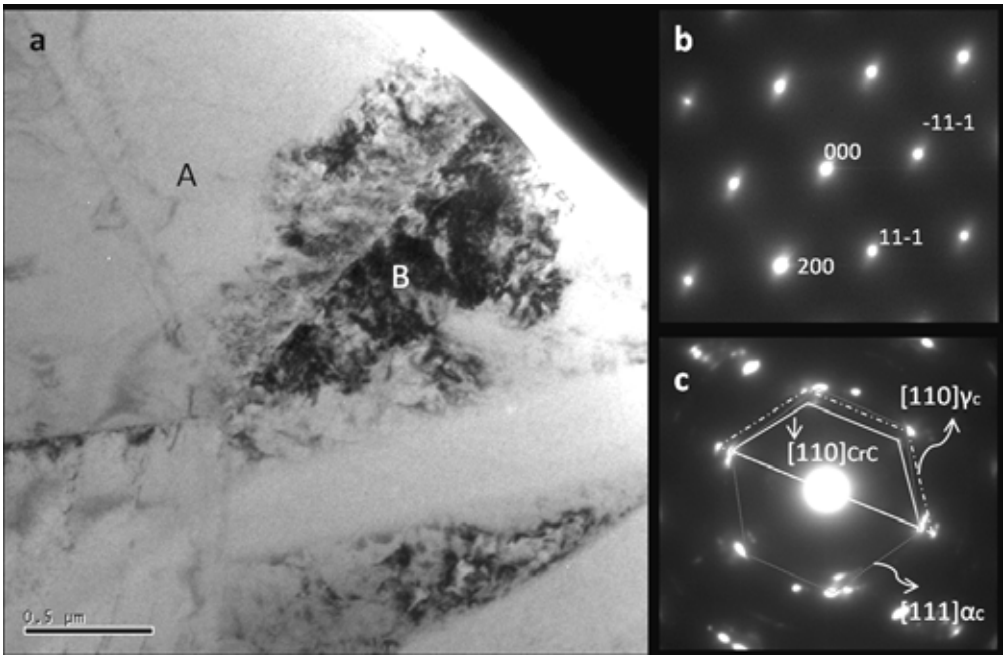

Figure 4.2-4 Cross sectional TEM characteristics of Sample 'PC450 40MPa': (a) microstructure and corresponding SAD patterns, (b) area of S-phase (indicated by A) and (c) precipitates (indicated by B).

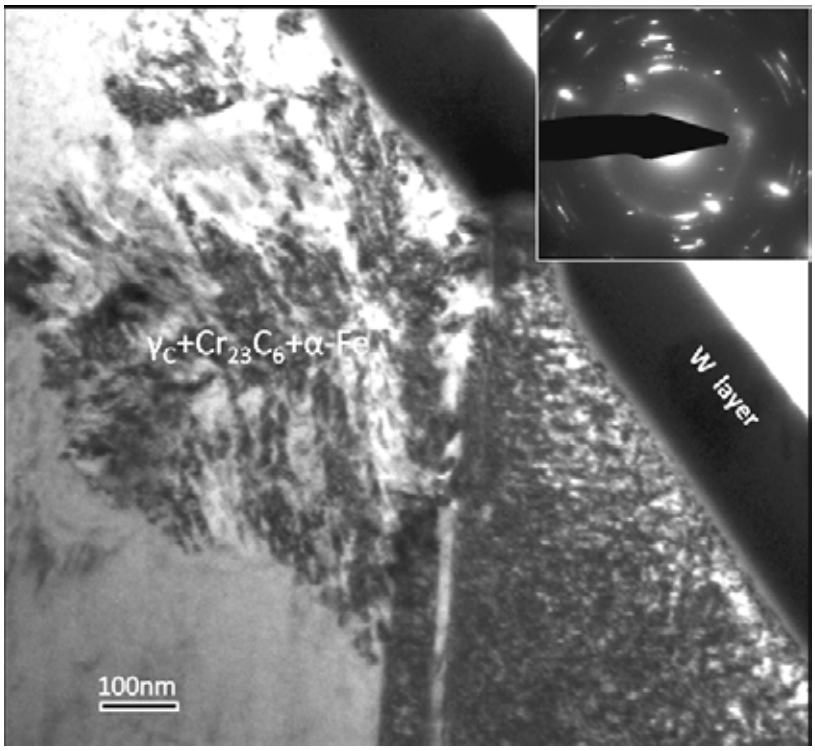

Figure 4.2-5 Cross sectional TEM microstructure and corresponding SAD pattern showing fine plates of γ_C+$Cr_{23}C_6$+α-Fe.

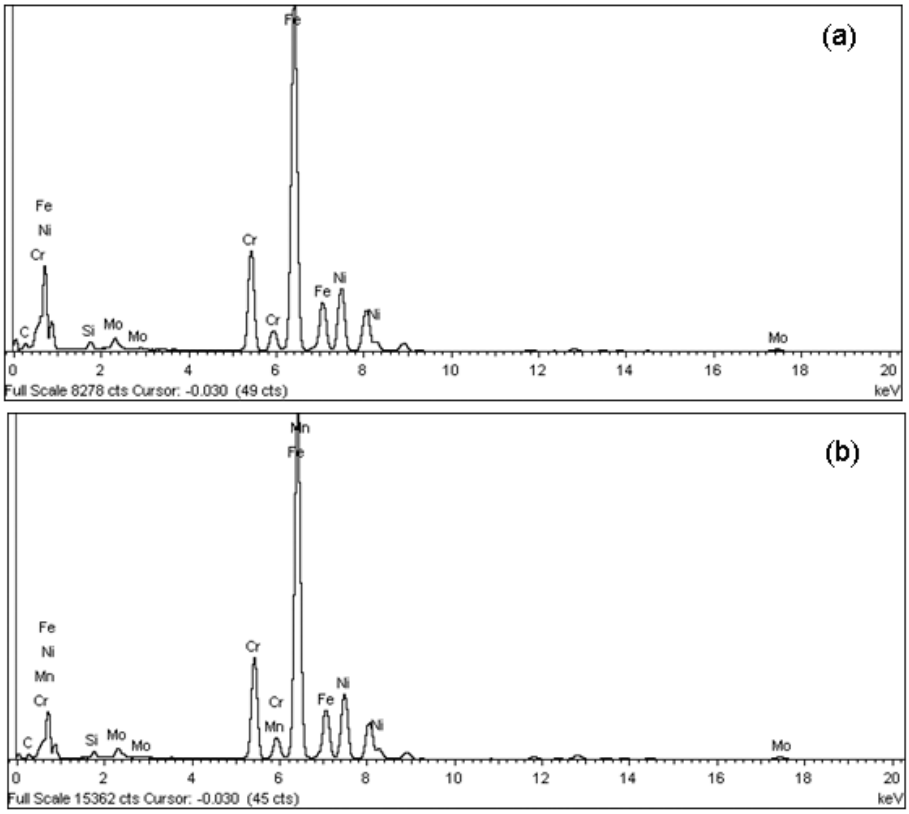

Figure 4.2-6 EDX spectra from S-phase (a) near the surface and (b) 6 μm below the surface

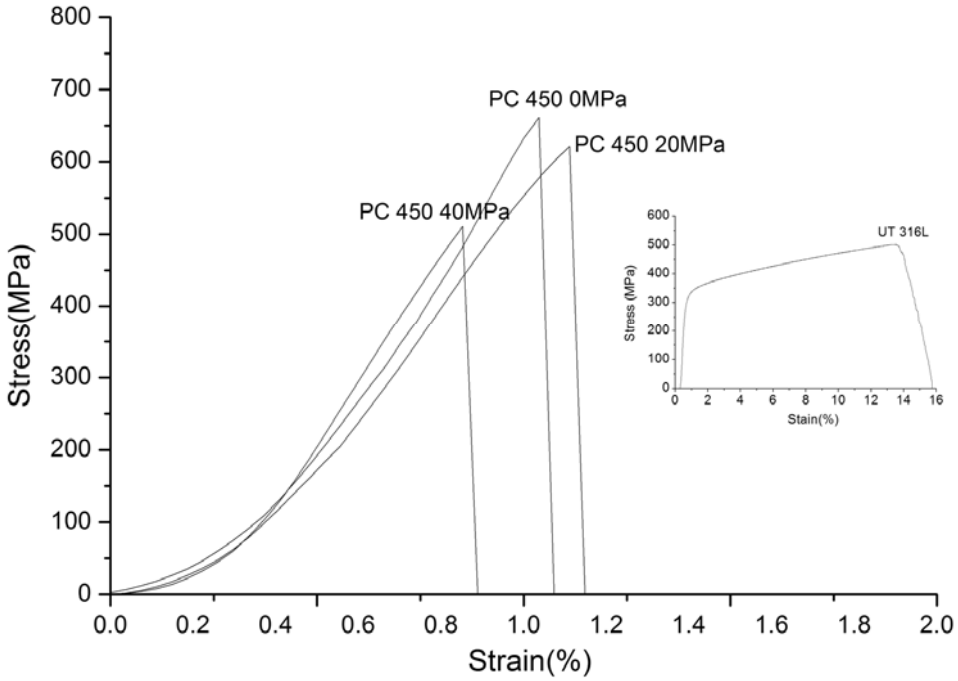

Figure 4.2-7 Stress - stain behaviour of as-received and carburised AISI 316L at 450°C for 10hours under different tensile stress levels (0MPa, 20MPa and 40MPa)

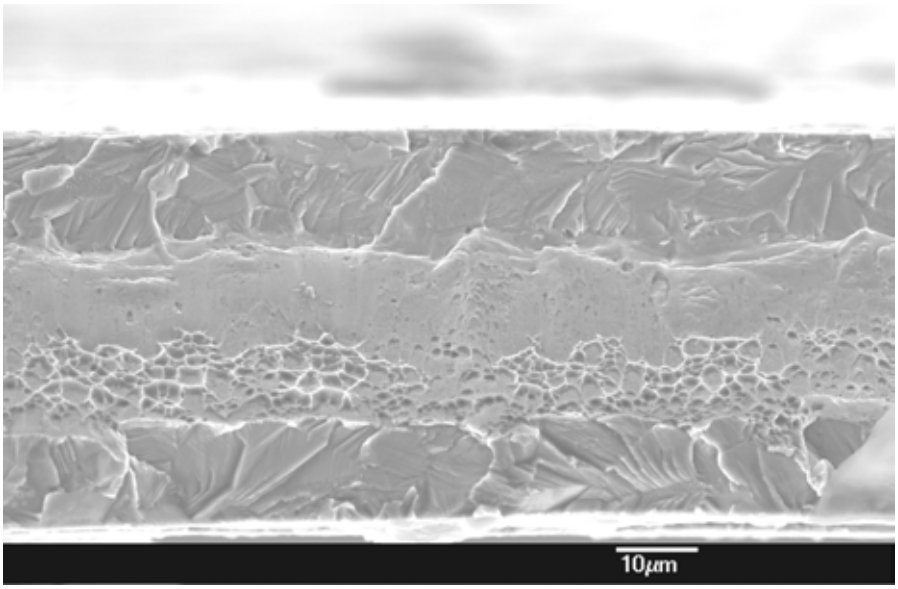

(a)

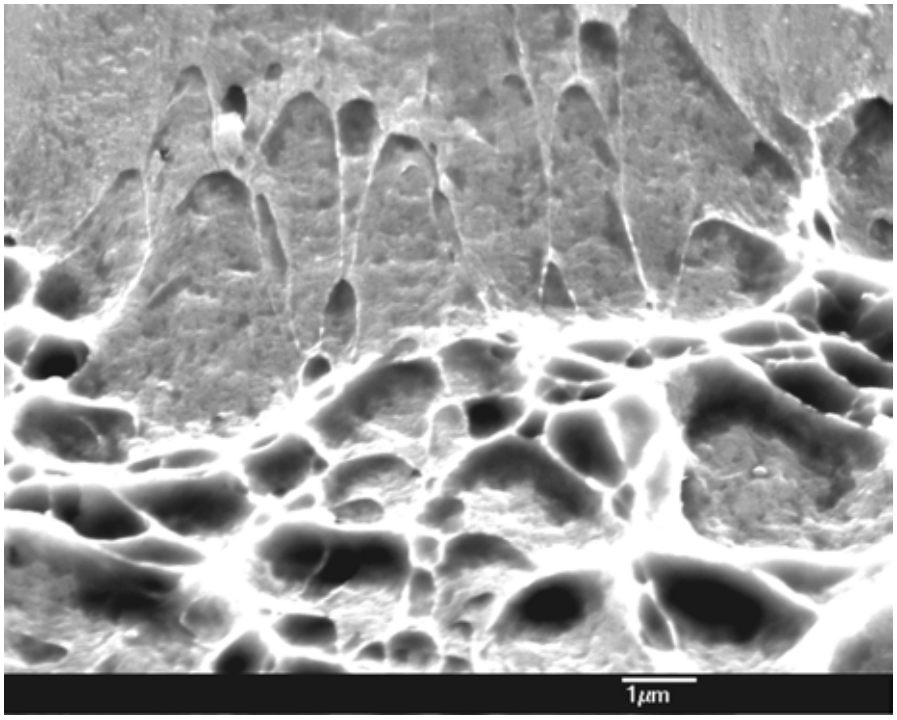

(b)

Figure 4.2-8 (a) Fracture morphology of Sample 'PC450 20MPa' after tensile test (a) low magnification and (b) high magnification in the fractured zone

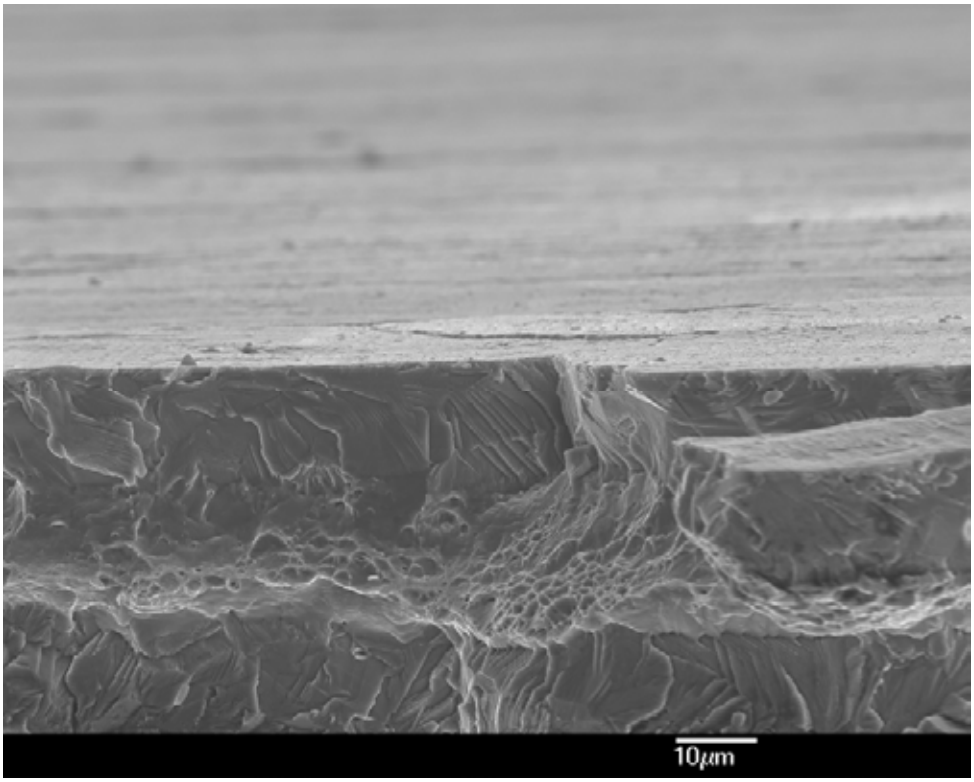

Figure 4.2-9 Fracture morphology of PC450 40MPa after tensile test

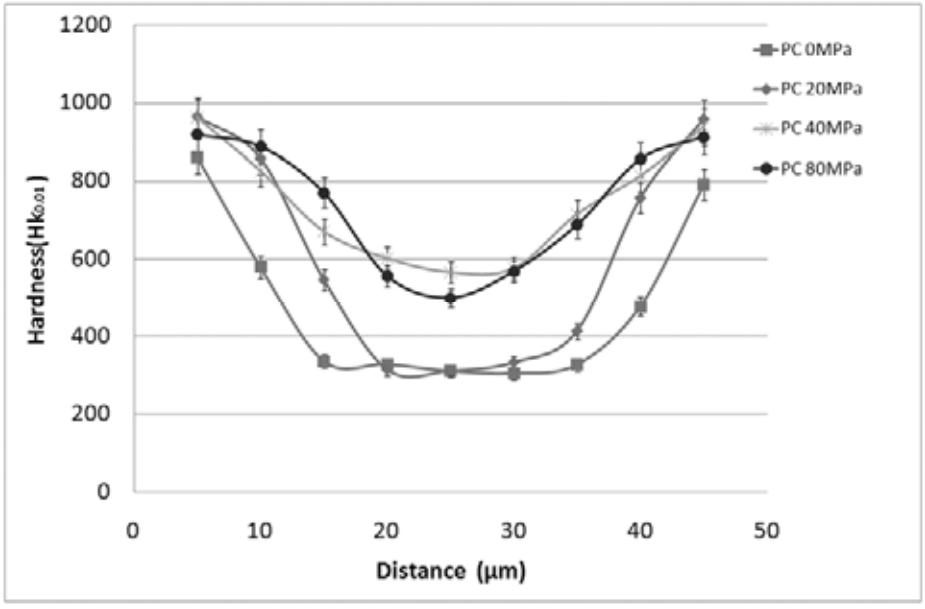

Figure 4.2-10 Micro hardness profiles across the thin foils carburised under different *in situ* tensile stress levels

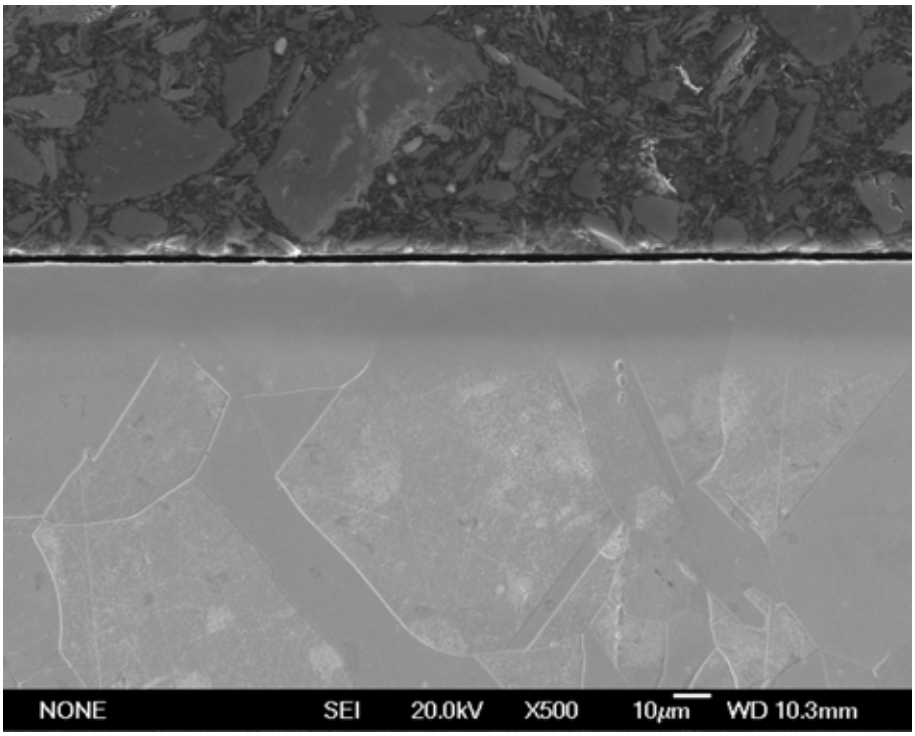

Figure 4.3-1 A cross sectional SEM image of carburised 316ASS bulk

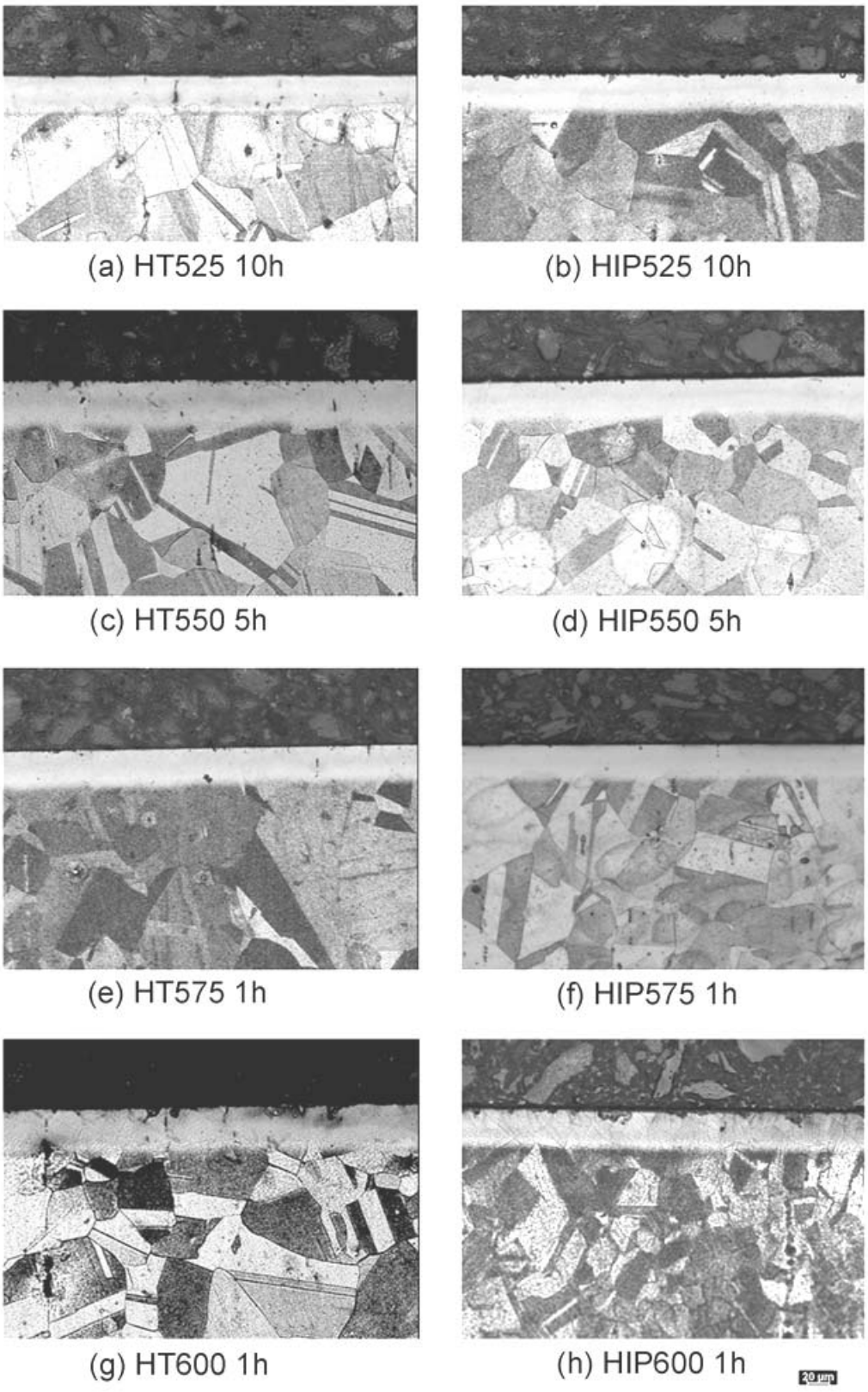

Figure 4.3-2 Cross sectional optical microstructures of samples after various HT and HIP treatments

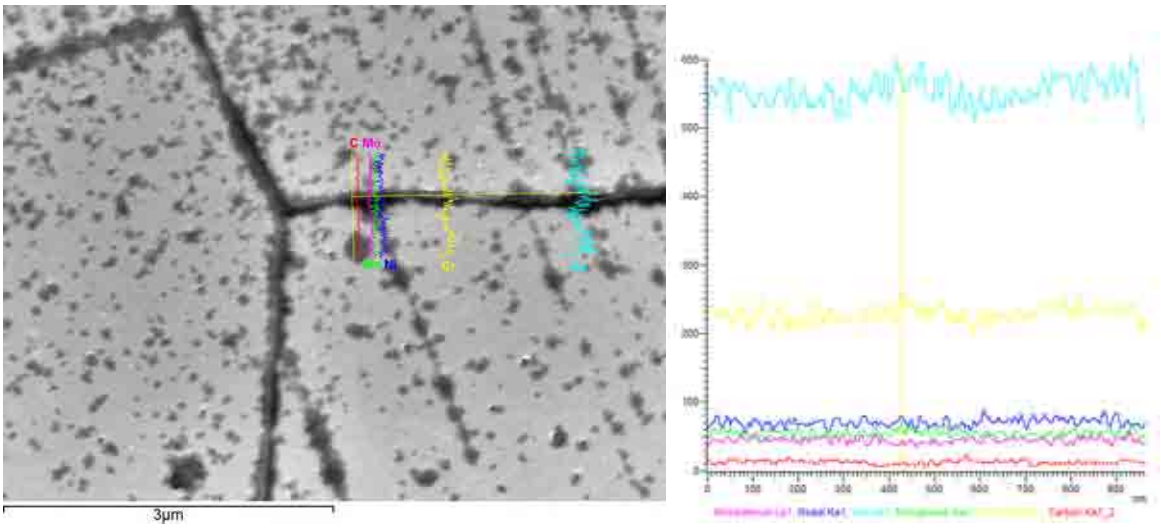

Figure 4.3-3 (a) SEM micrograph of the etched grain boundary in the S-phase layer of Sample ‘HT 600 1h’ and (b) the corresponding EDX line scan results

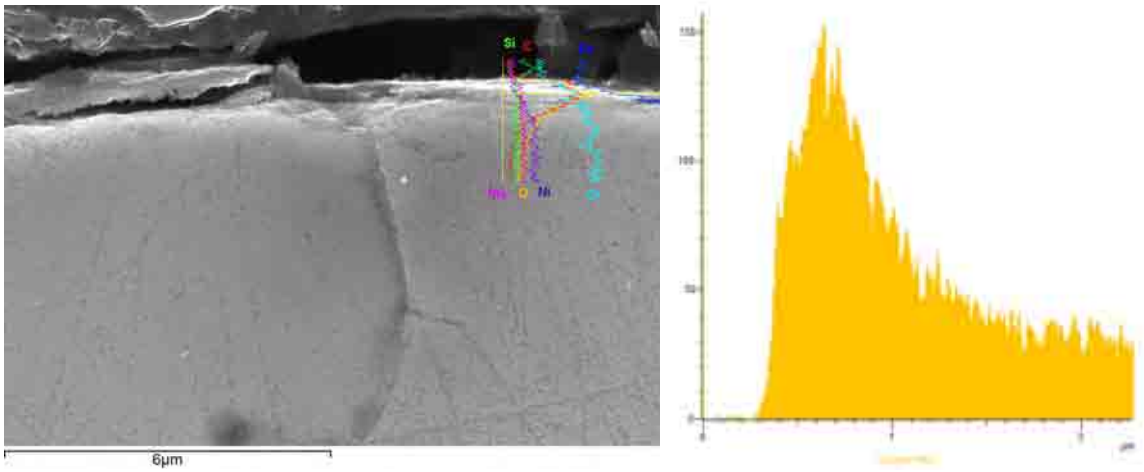

Figure 4.3.4 (a) SEM micrograph of the oxide layer formed on the top of S-phase in Sample ‘HT525 10h’ (oxygen in yellow) and (b) the corresponding EDX line scan results

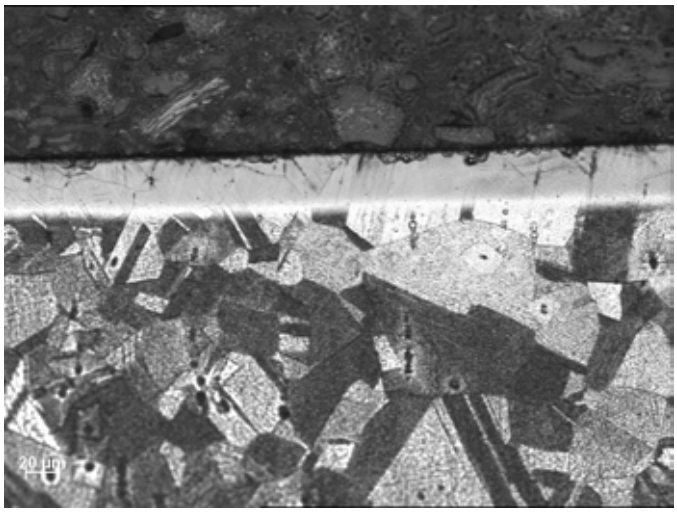

Figure 4.3-5 A cross sectional optical image of HIP575 2h

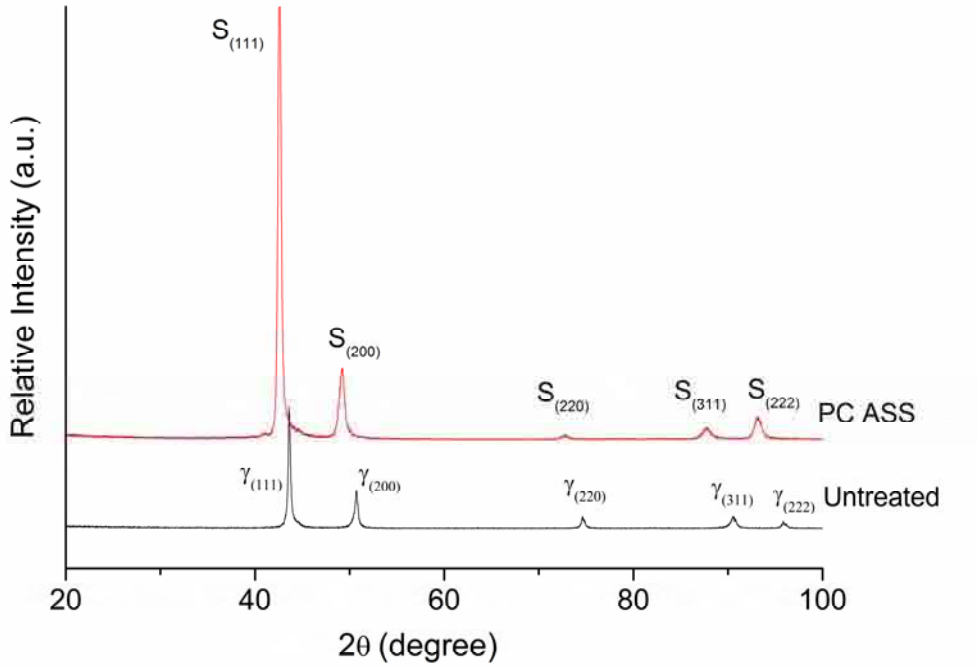

Figure 4.3-6 XRD patterns of untreated and carburised (500°C/ 10hrs) 316ASS samples

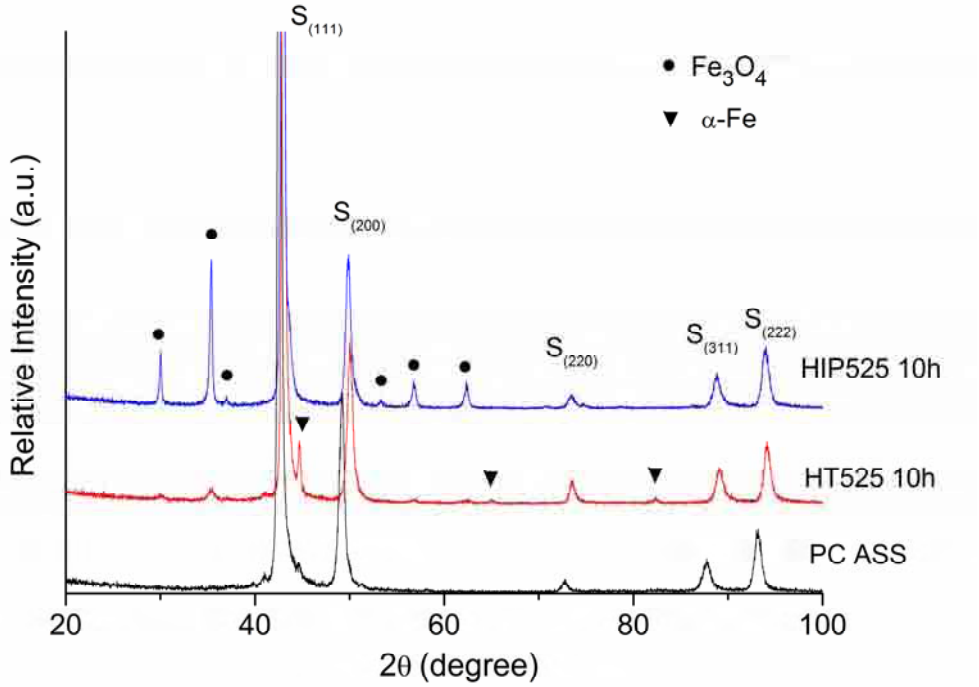

Figure 4.3-7 XRD patterns of HT525 10h and HIP525 10h (180 MPa) on carburised 316ASS samples

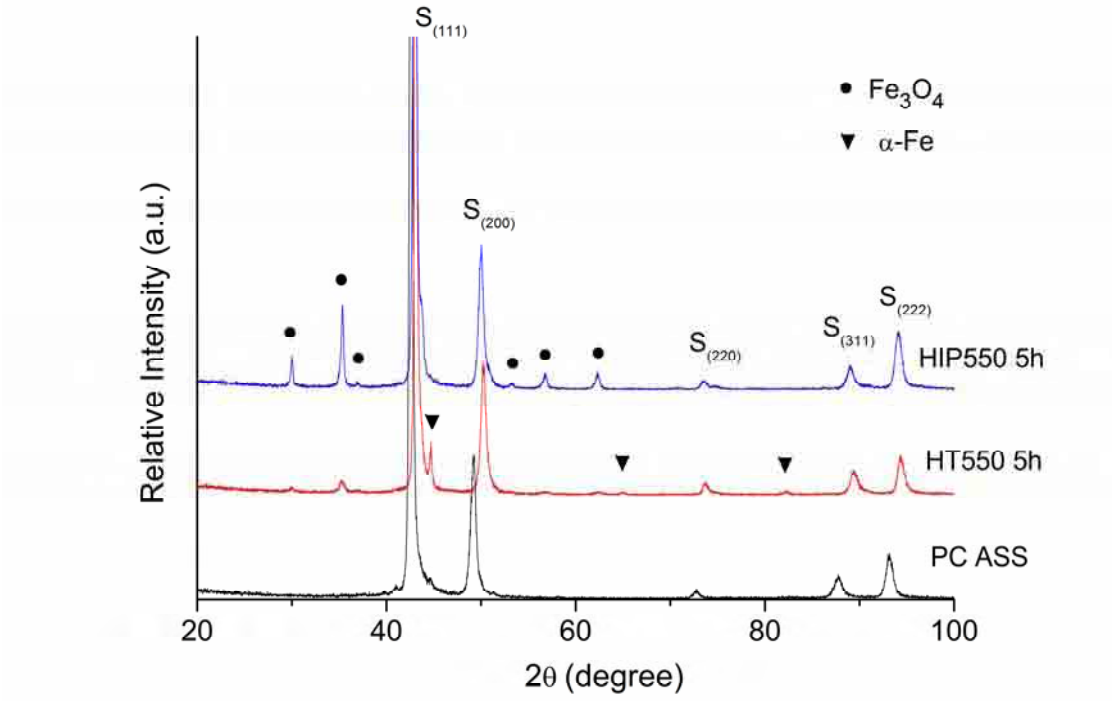

Figure 4.3-8 XRD patterns of HT550 5h and HIP550 5h (180 MPa) on carburised 316ASS samples

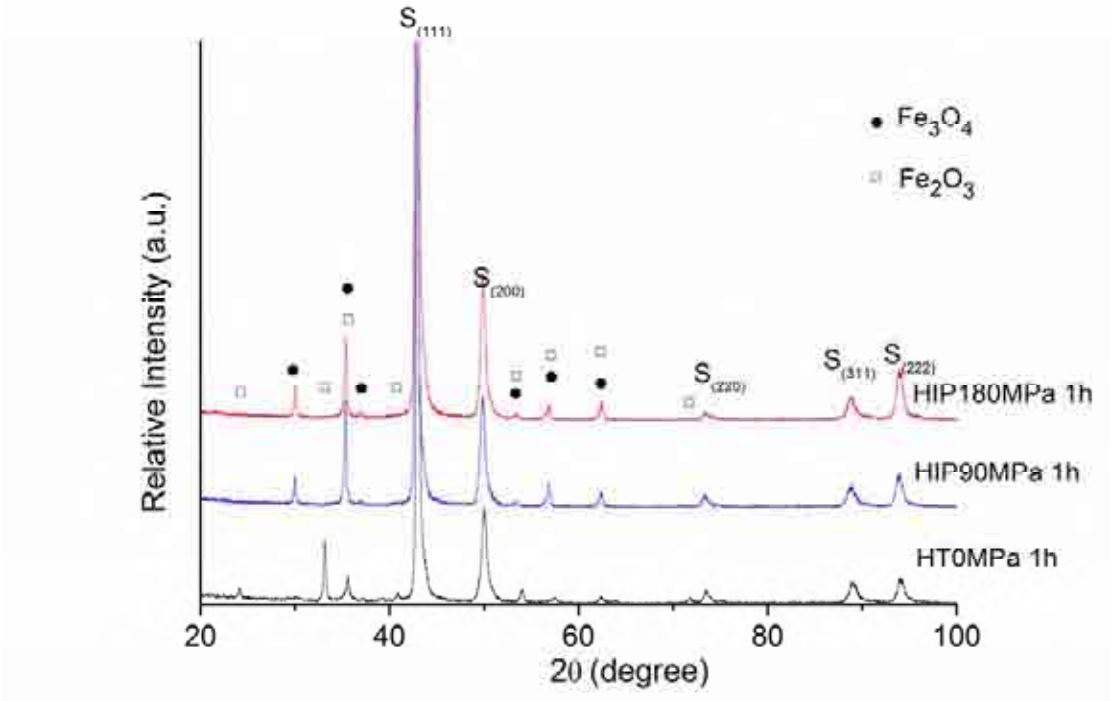

Figure 4.3-9 XRD patterns of carburised 316ASS samples with heat treatment at 575°C for 1hour ('HT0MPa 1h') and HIPping for 1h under 90 MPa and 180 MPa compressive stresses (Sample 'HIP90MPa 1h' and Sample 'HIP180MPa 1h')

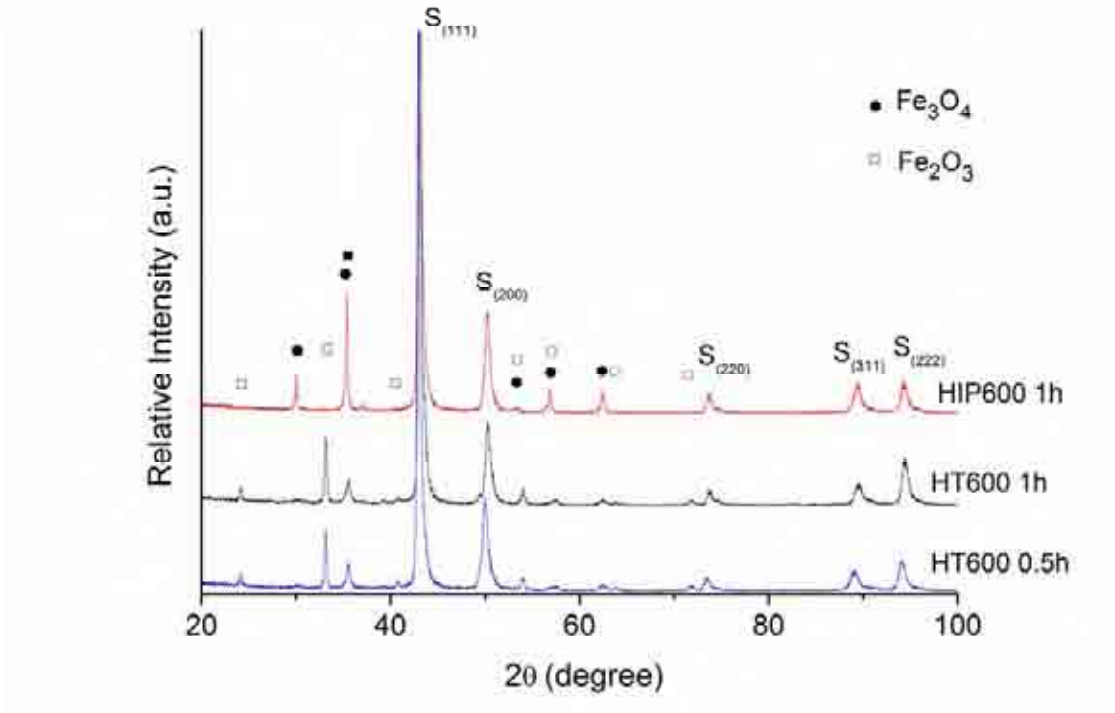

Figure 4.3-10 XRD patterns of carburised samples with heat treatment at 600°C for 0.5, 1 hour and HIPping for 1hour

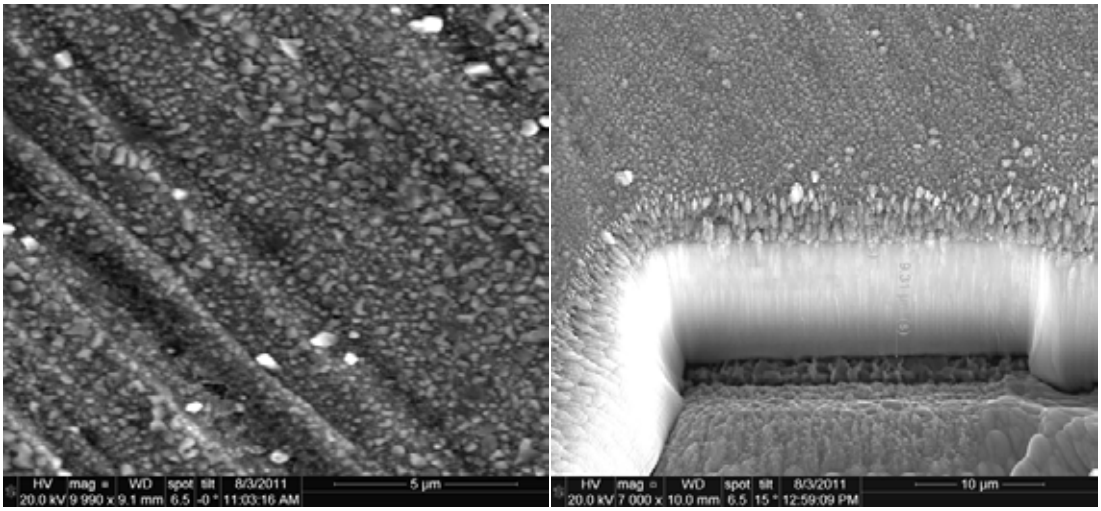

(a) (b)

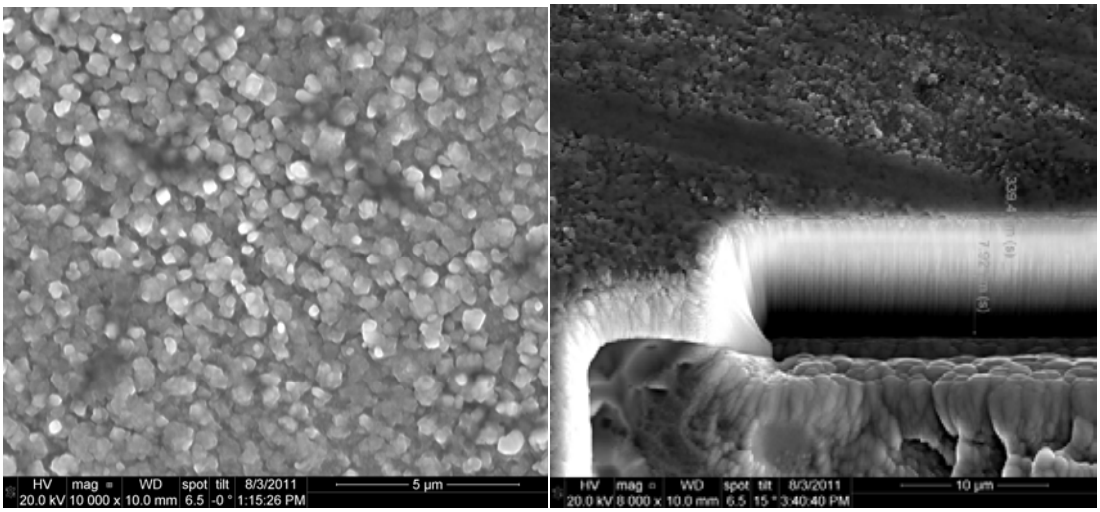

(c) (d)

Figure 4.3-11 SEM surface morphology and corresponding cross-sectional microstructures (sectioned by FIB) for Sample ‘HT525 10h’ (a& b); and Sample ‘HIP525 10h’ (c& d) respectively

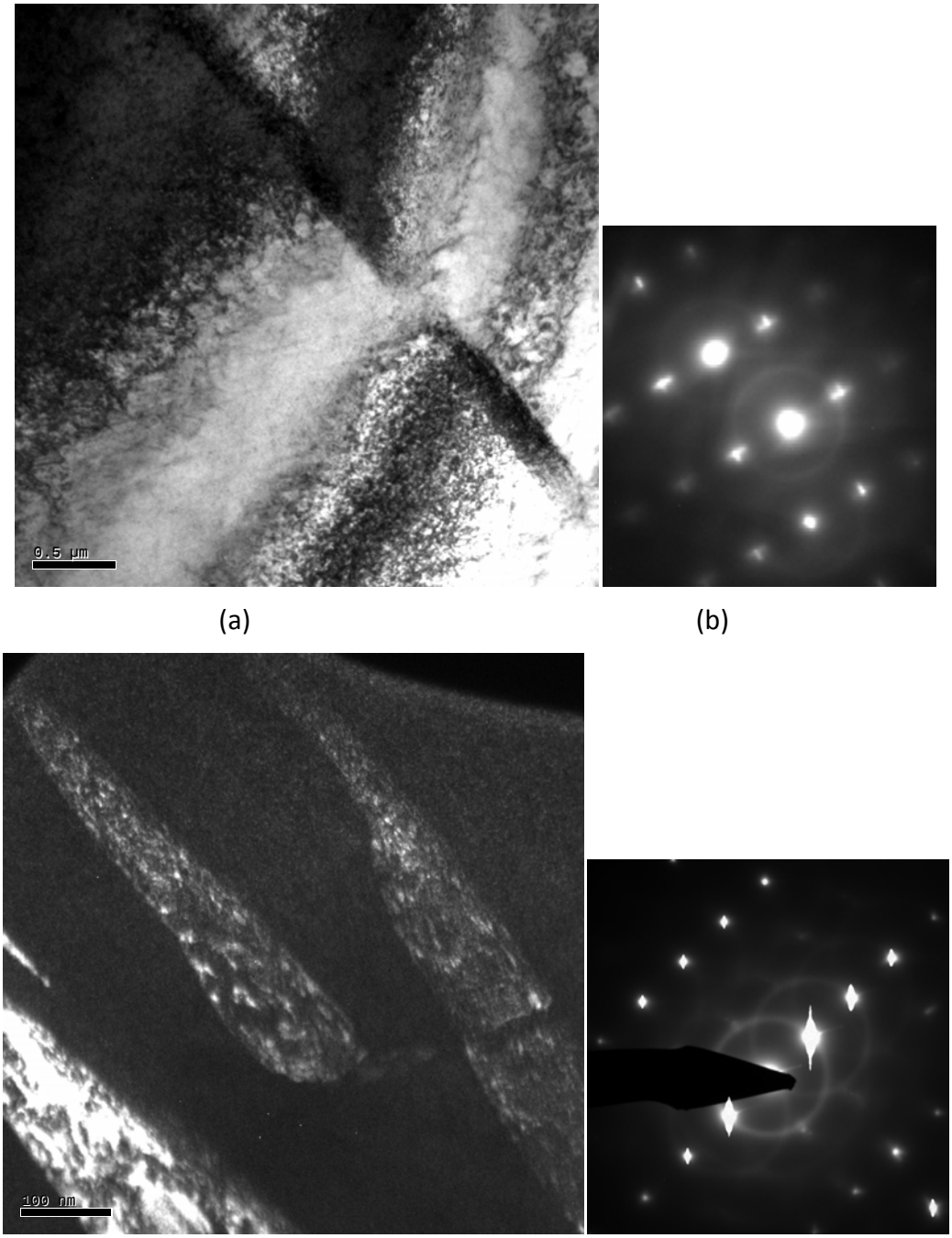

Figure 4.3-12 TEM microstructure and SAD patterns taken from S-phase layer for Sample 'HIP525 10h'. (a) BF microstructure and (c) diffraction pattern of b=[013]; (b) DF microstructure and (d) corresponding SAD pattern, b=123, of twin bands in S-phase

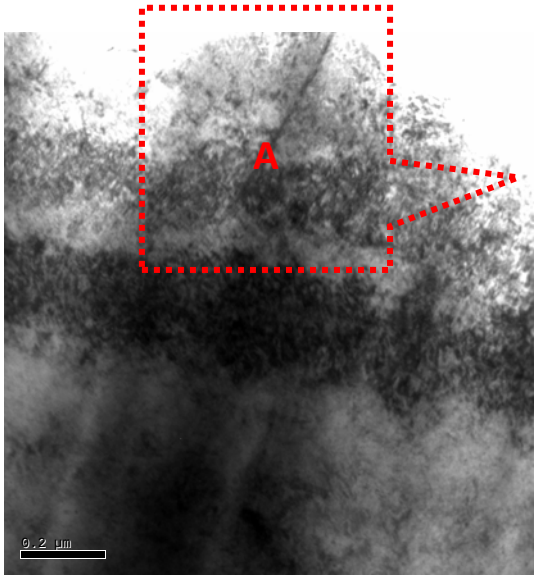

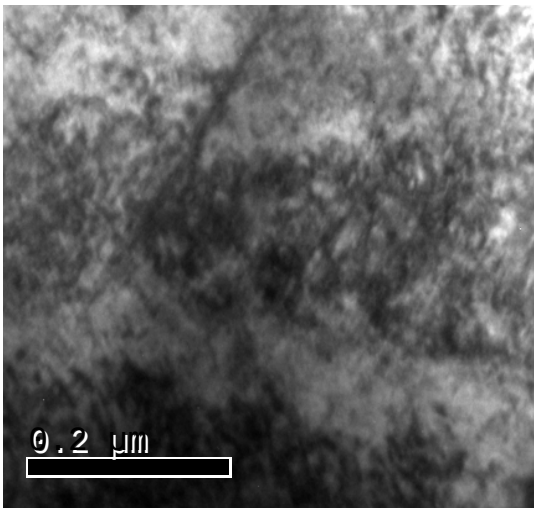

(a)

(b)

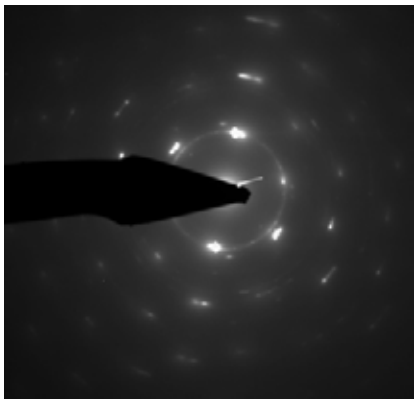

(c)

Rings/spots	d-spacing	HKL		
		CrC	γ-Fe	α-Fe
1	2.38	111		
2	2.07	200	111	
3	2.04			110
4	1.80		200	
5	1.49	220		200
6	1.28	311	220	
7	1.17	222		211
8	1.09		311	
9	1.05	400		

(d)

Figure 4.3-13 TEM microstructures and SAD patterns taken from S-phase layer of Sample 'HT525 10h'. (a)&(b) BF microstructures and (c) diffraction pattern from area A, showing carbide and a-Fe transformed from S-phase, indexed in table (d).

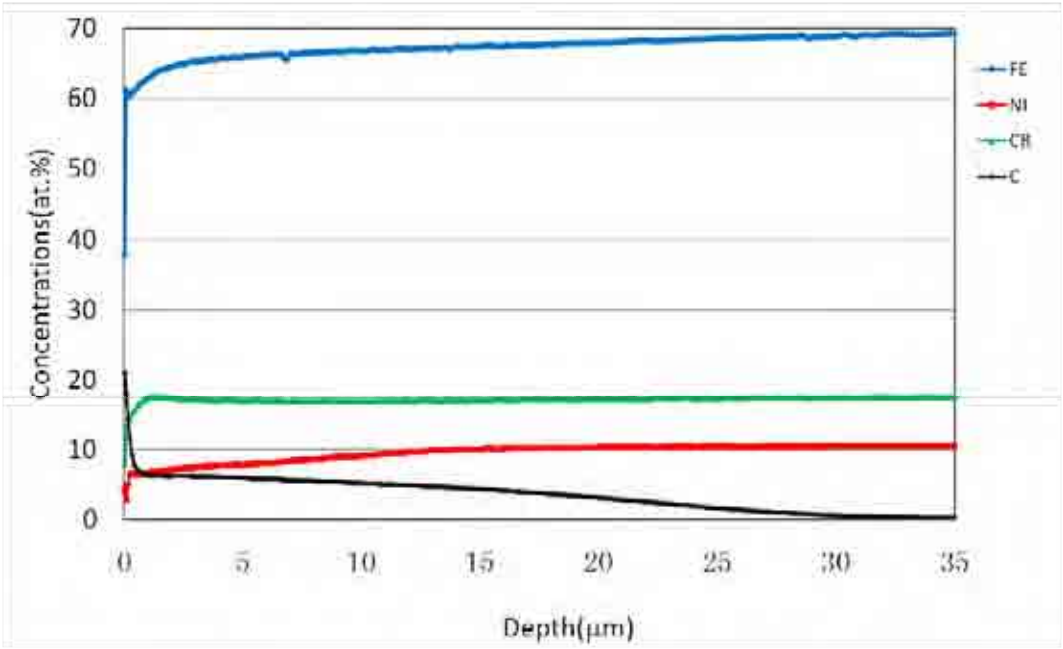

Figure 4.3-14 GDS elemental profiles of carburised 316 ASS (500°C/10hrs)

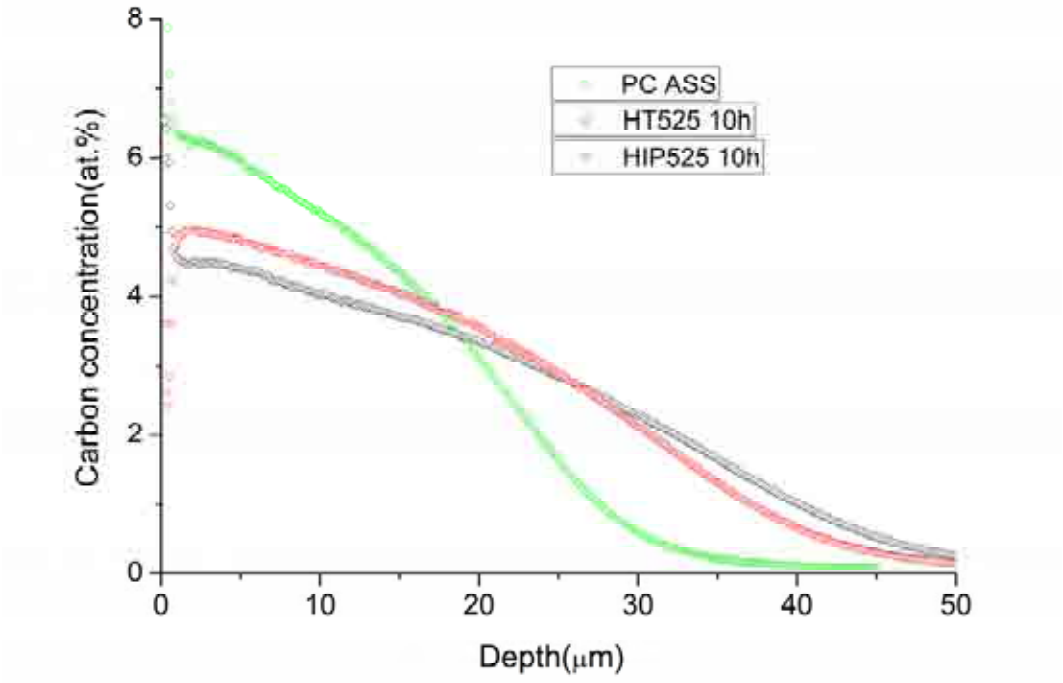

Figure 4.3-15 GDS carbon profiles of Sample 'PC ASS', 'HT525 10h' and 'HIP525 10h' (180MPa)

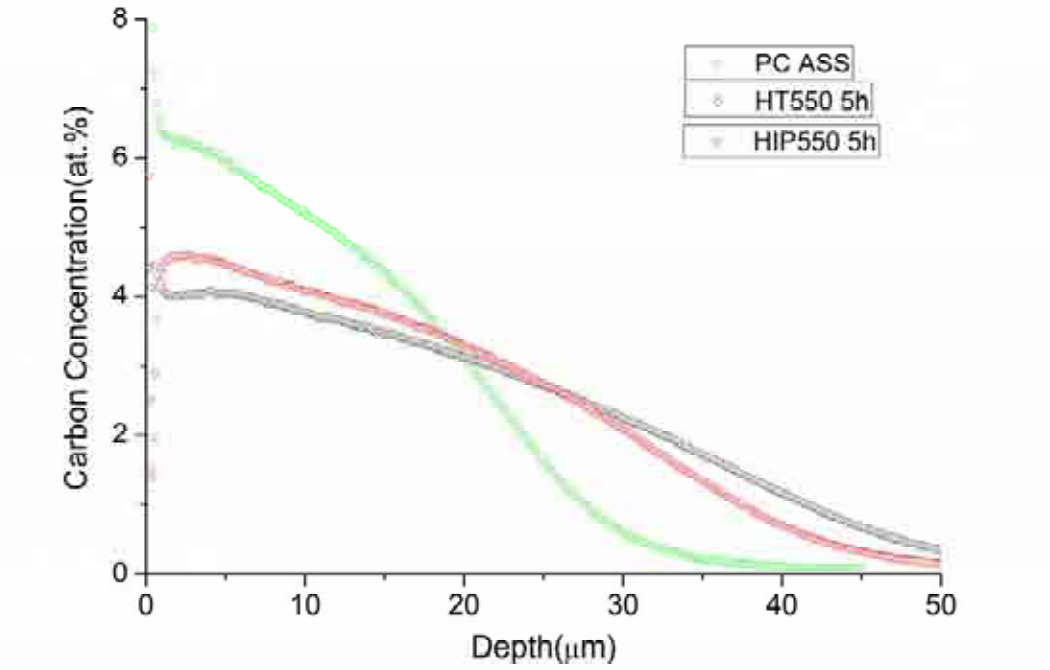

Figure 4.3-16 GDS carbon profiles of Sample 'PC ASS', 'HT550 5h' and 'HIP550 5h' (180MPa) GDS

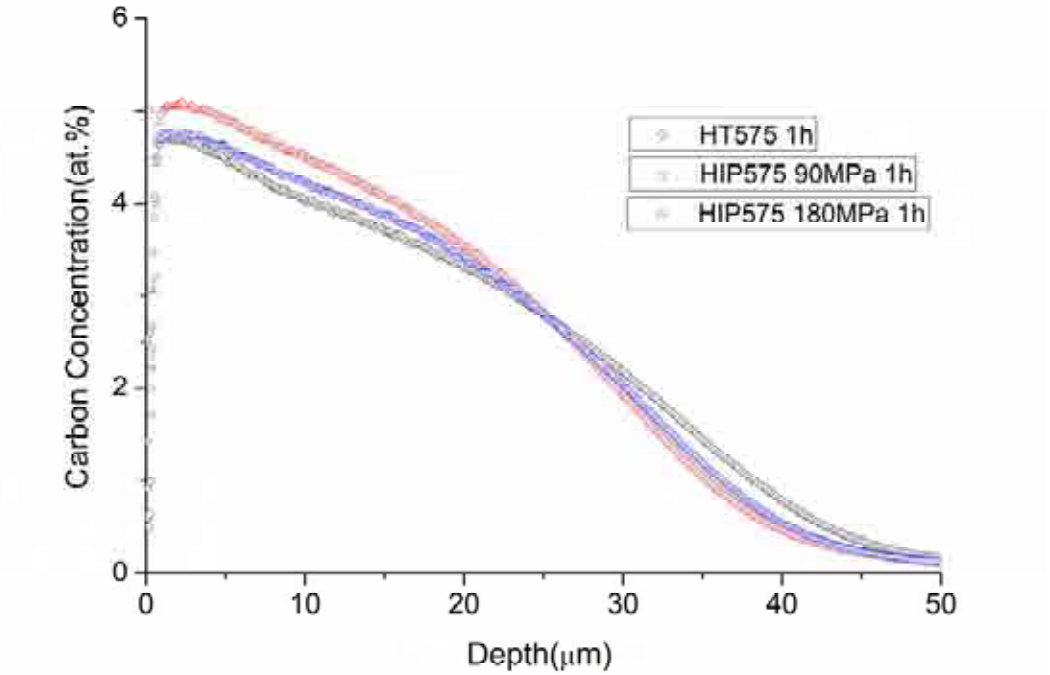

Figure 4.3-17 GDS carbon profiles of Sample 'HT575 1h', 'HIP575 180MPa 1h' and 'HIP575 90MPa 1h'

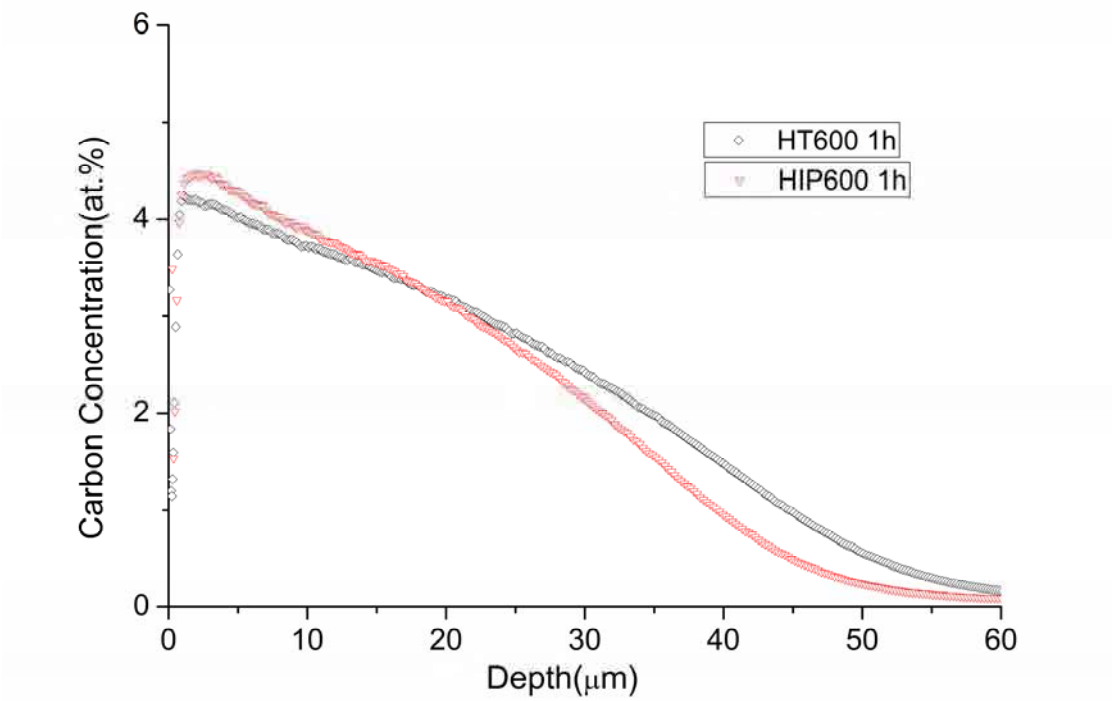

Figure 4.3-18 GDS carbon profiles of Sample 'HT600 1h' and 'HIP600 1h' (180MPa)

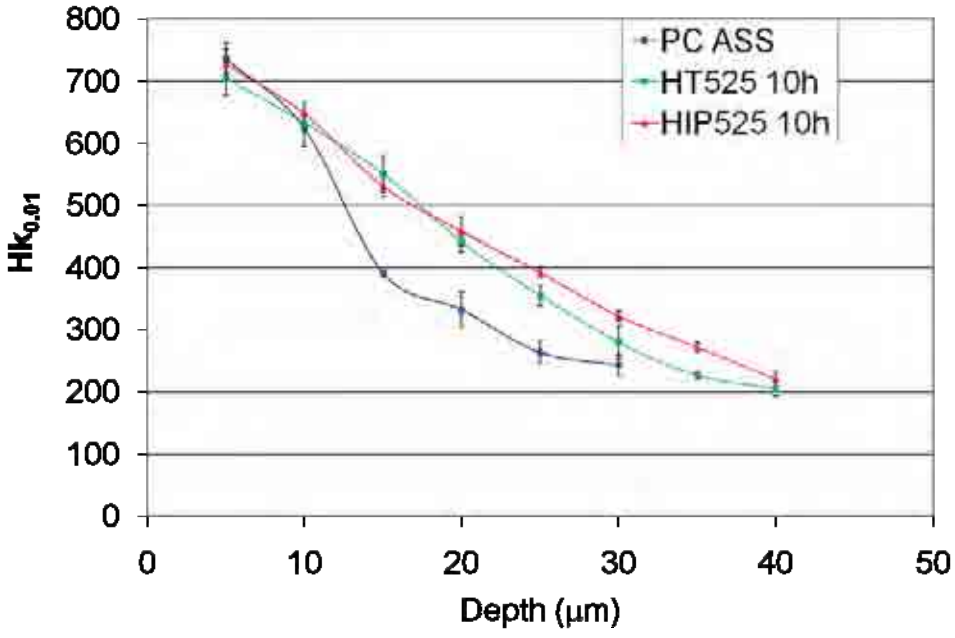

Figure 4.3-19 Micro hardness profiles of Sample 'PC ASS', 'HT525 10h' and 'HIP525 10h' (180MPa)

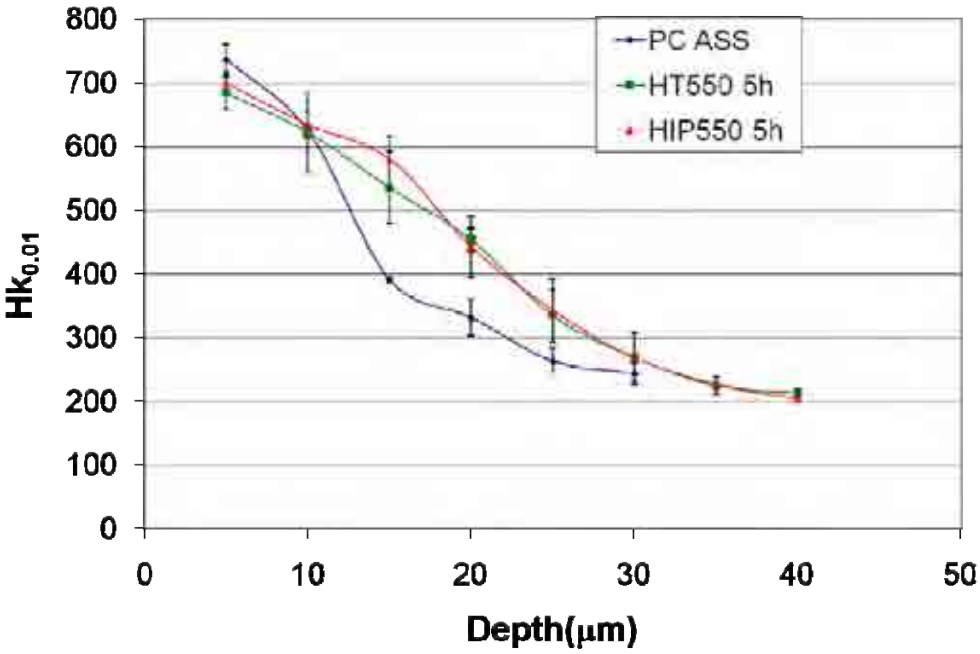

Figure 4.3-20 Micro hardness profiles of Sample 'PC ASS', 'HT550 5h' and 'HIP550 5h' (180MPa)

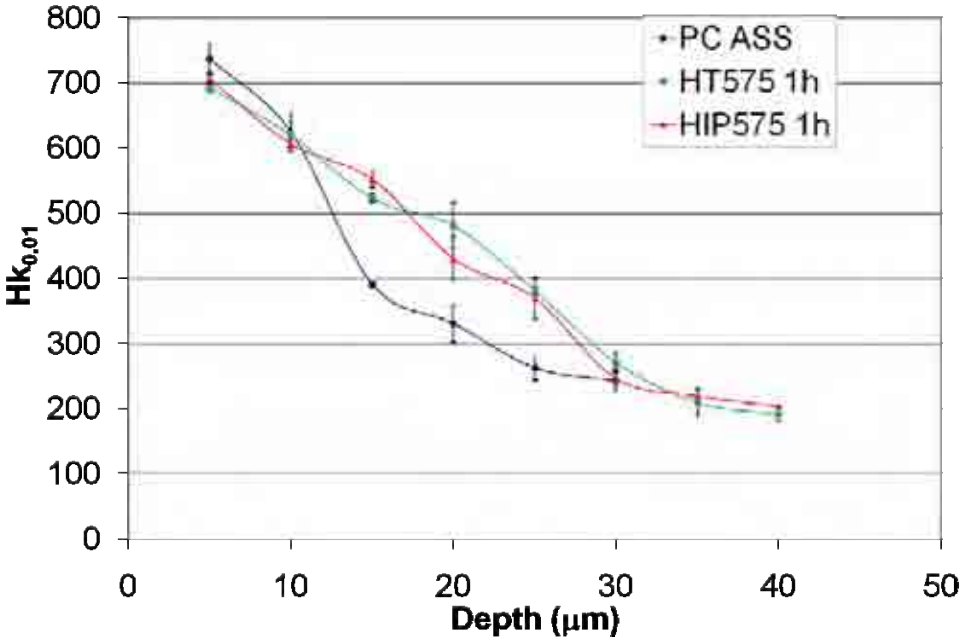

Figure 4.3-21 Micro hardness profiles of Sample 'PC ASS', 'HT575 1h' and 'HIP575 1h' (180MPa)

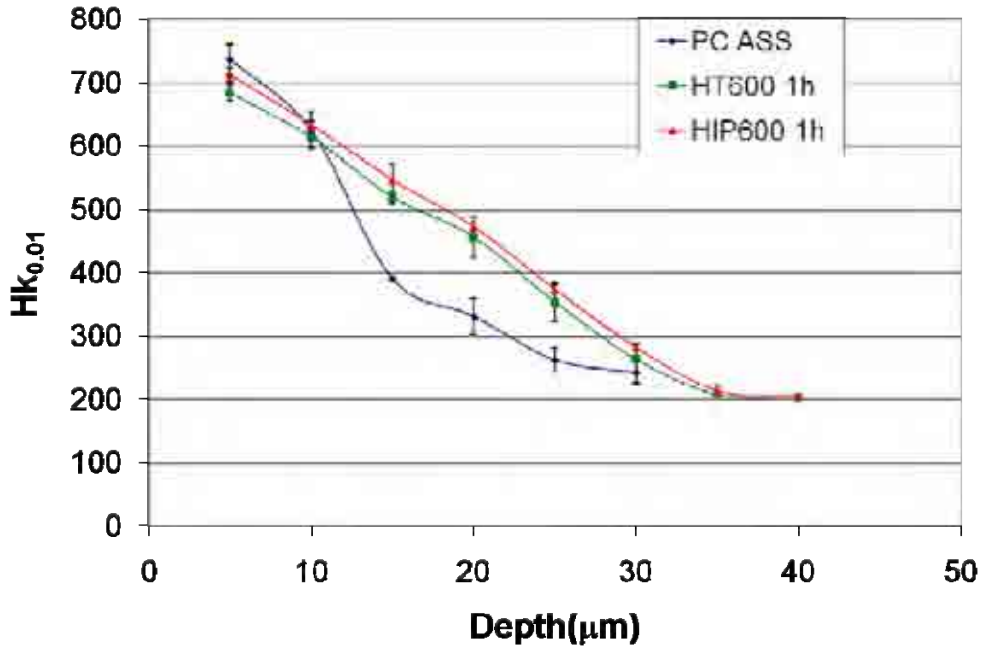

Figure 4.3-22 Micro hardness profile of 'PC ASS', 'HT600 1h' and 'HIP600 1h'(180MPa)

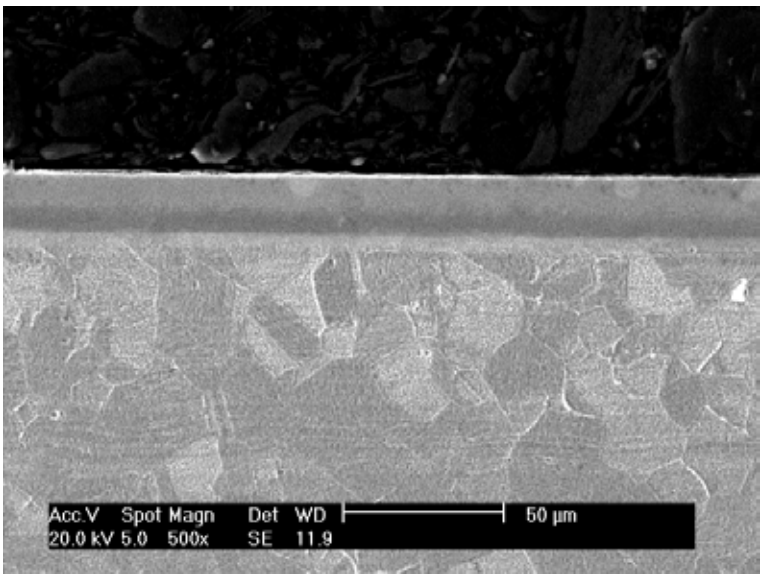

(a) PC ASS

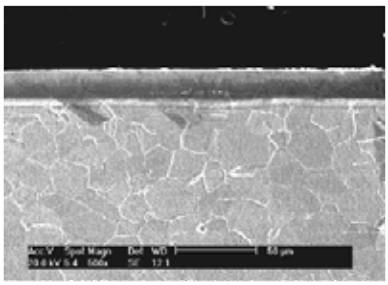

(b) 400 0MPa

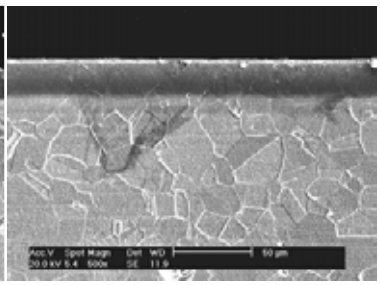

(c) 400 100MPa

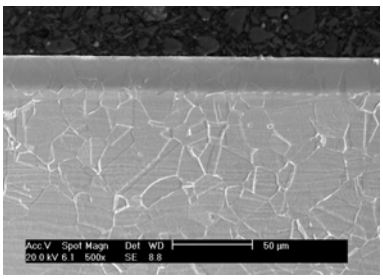

(d) 400 200MPa

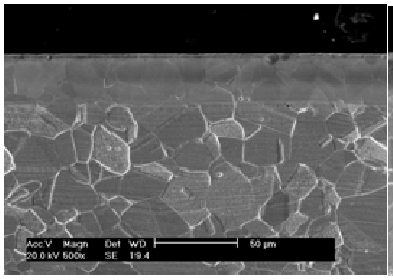

(e) 450 0MPa

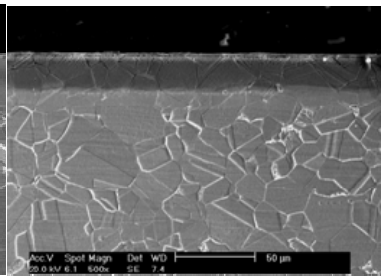

(f) 450 100MPa

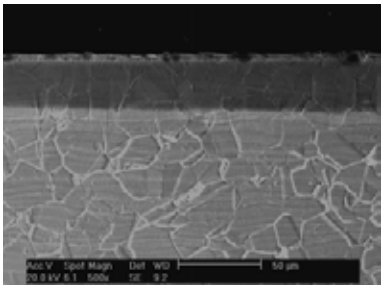

(g) 450 200MPa

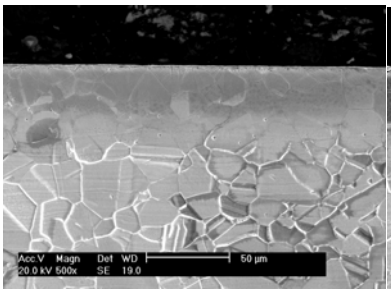

(h) 500 0MPa

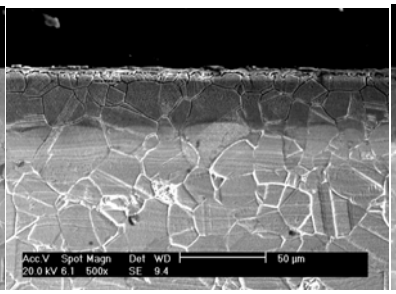

(i) 500 100MPa

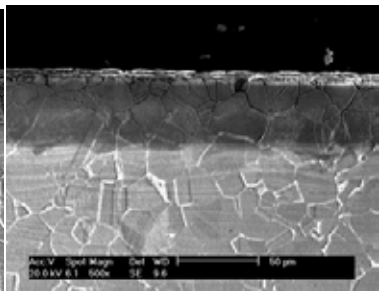

(j) 500 200MPa

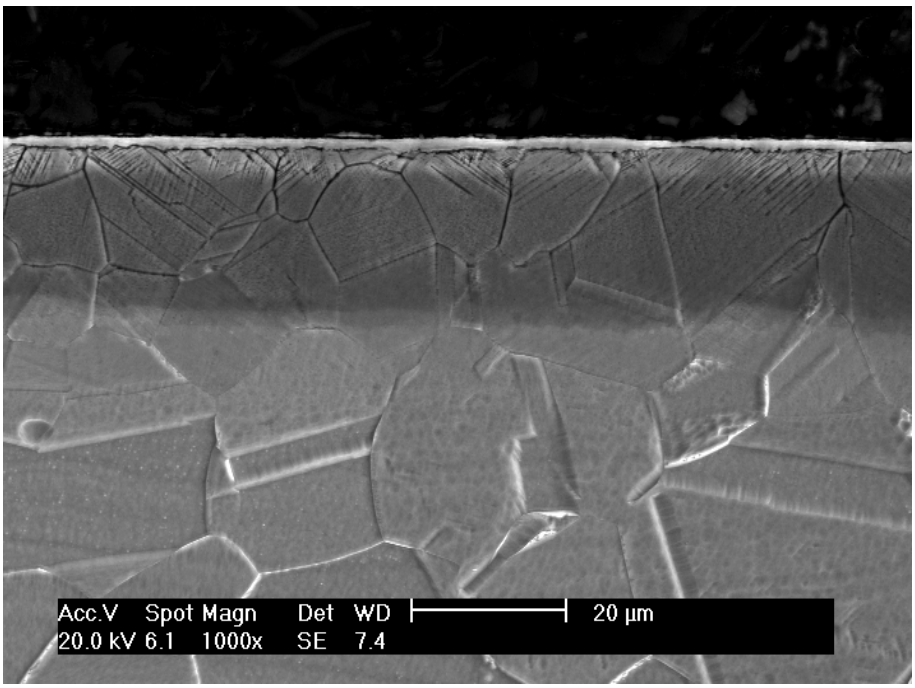

(k) 450 100MPa (magnified)

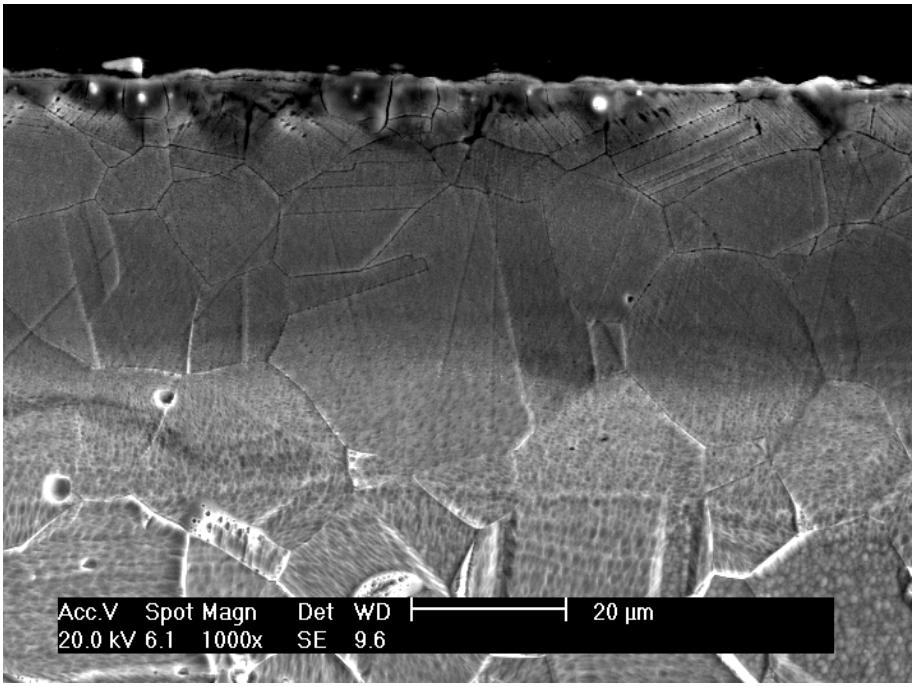

(l) 500 200MPa (magnified)

Figure 4.4-1 SEM morphologies of carburised 316 ASS (a) and after enduring under stress and temperature (b)-(j); (k),(l) magnified images showing etching features in S-phase

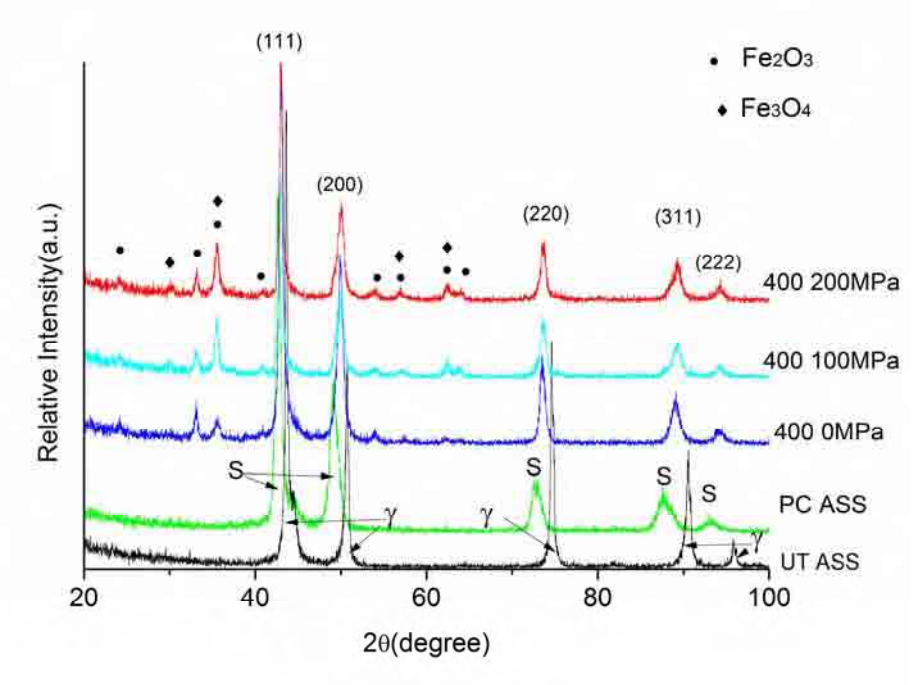

Figure 4.4-2 XRD patterns of PC treated 316ASS and after annealing for 150hours at 400°C under 0,100 and 200MPa tensile stresses

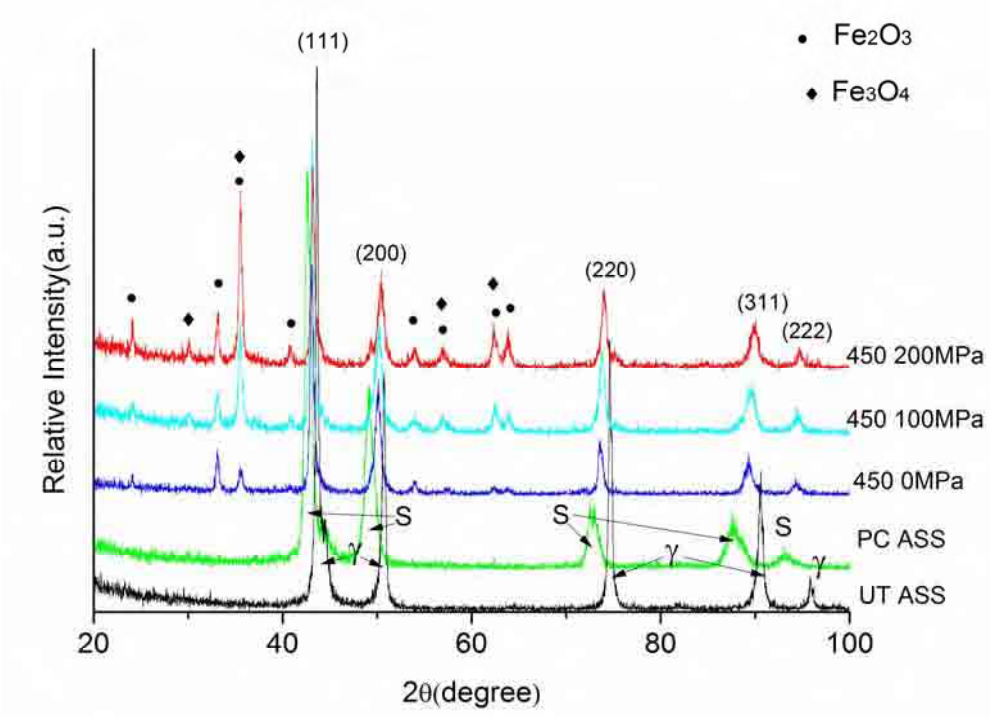

Figure 4.4-3 XRD patterns of PC treated 316ASS and after annealing for 100hours at 450°C under 0,100 and 200MPa tensile stresses

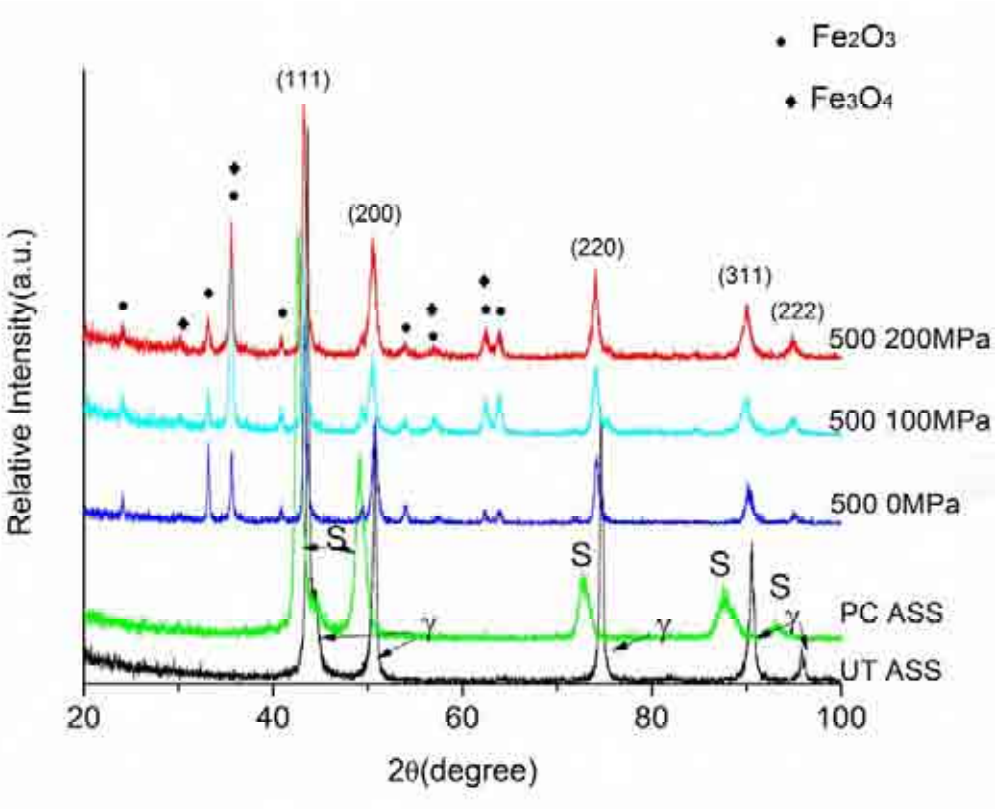

Figure 4.4-4 XRD patterns of PC treated 316ASS and after annealing for 100hours at 500°C under 0,100 and 200MPa tensile stresses

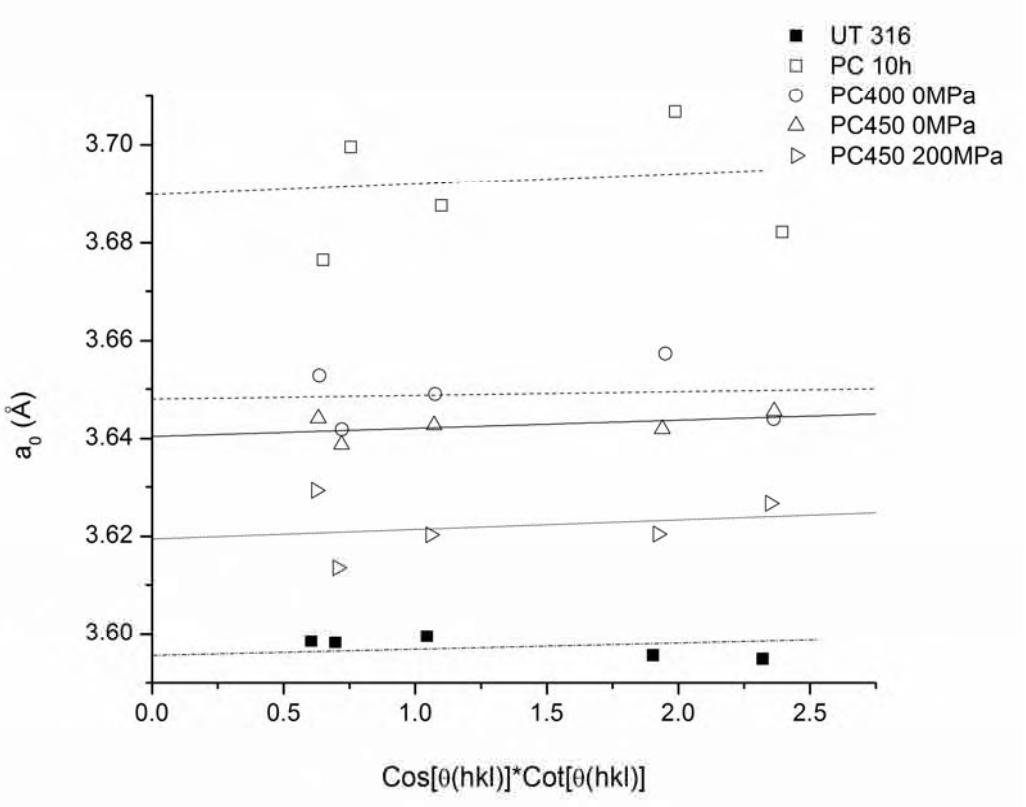

Figure 4.4-5 Nelson-Riley plots and fitting curves for measuring the lattice expansion of S-phase

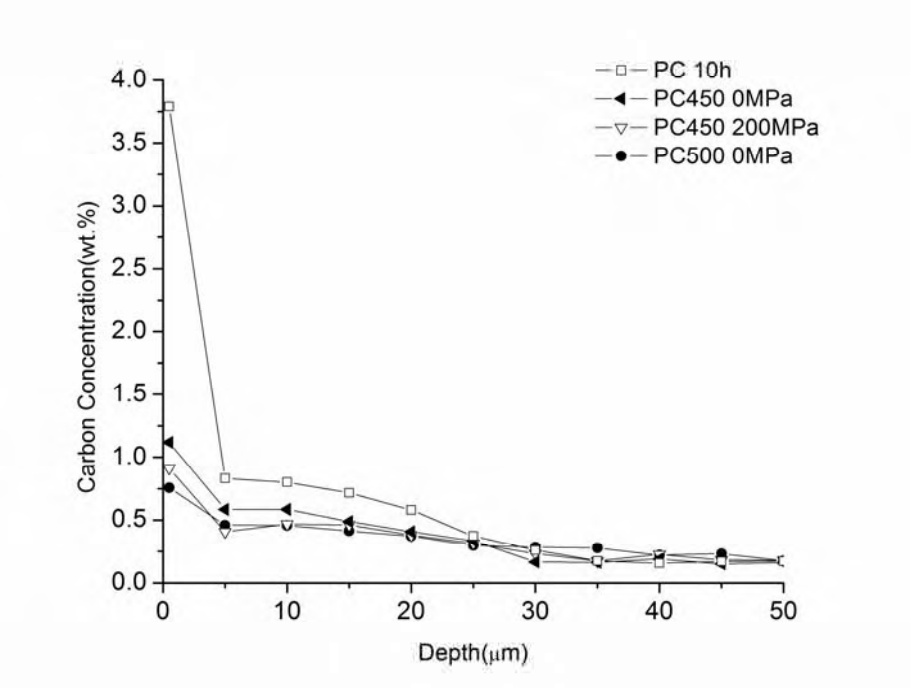

Figure 4.4-6 Carbon profiles along the cross sectional samples of just plasma carburised and after annealing under different tensile stresses for 100 hours

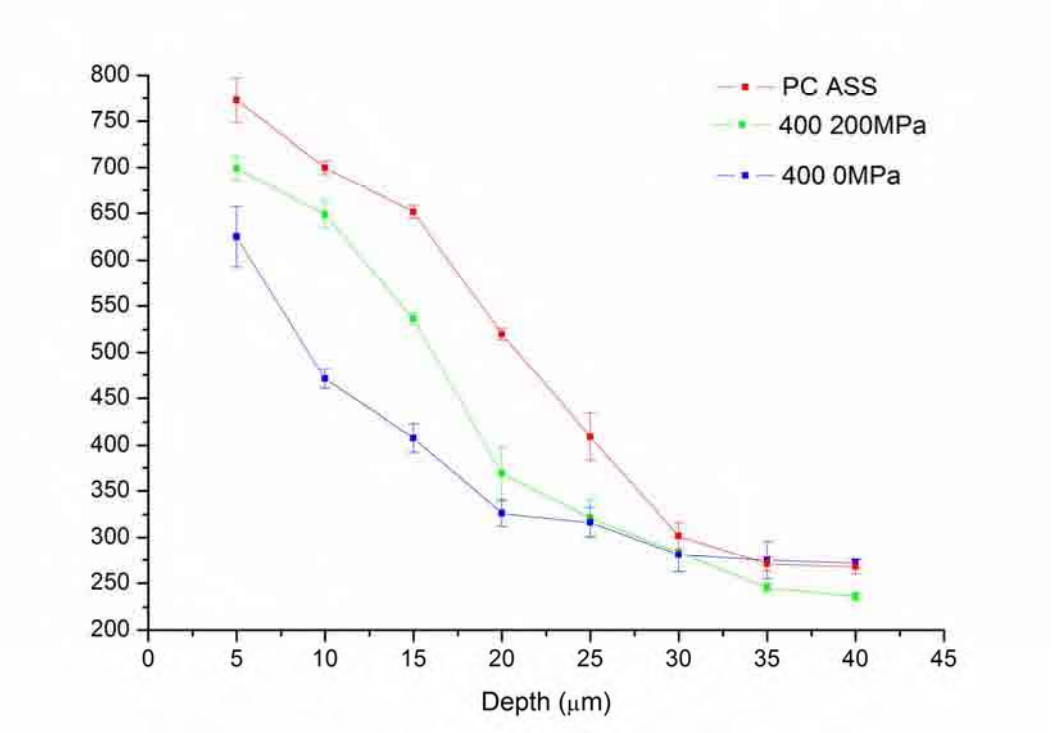

Figure 4.4-7 Effect of tensile stress on the hardness profiles along the cross sectional samples after 400°C/ 150 hours annealing

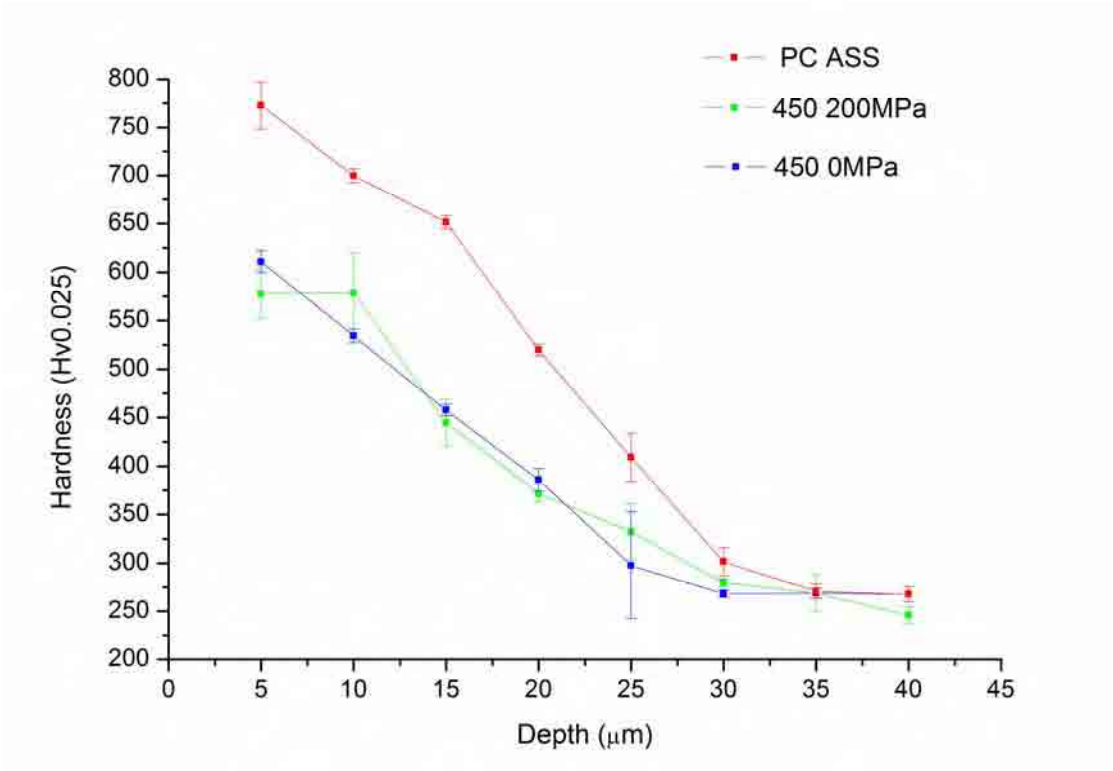

Figure 4.4-8 Effect of tensile stress on the hardness profiles along the cross sectional samples after 450°C/ 100 hours annealing

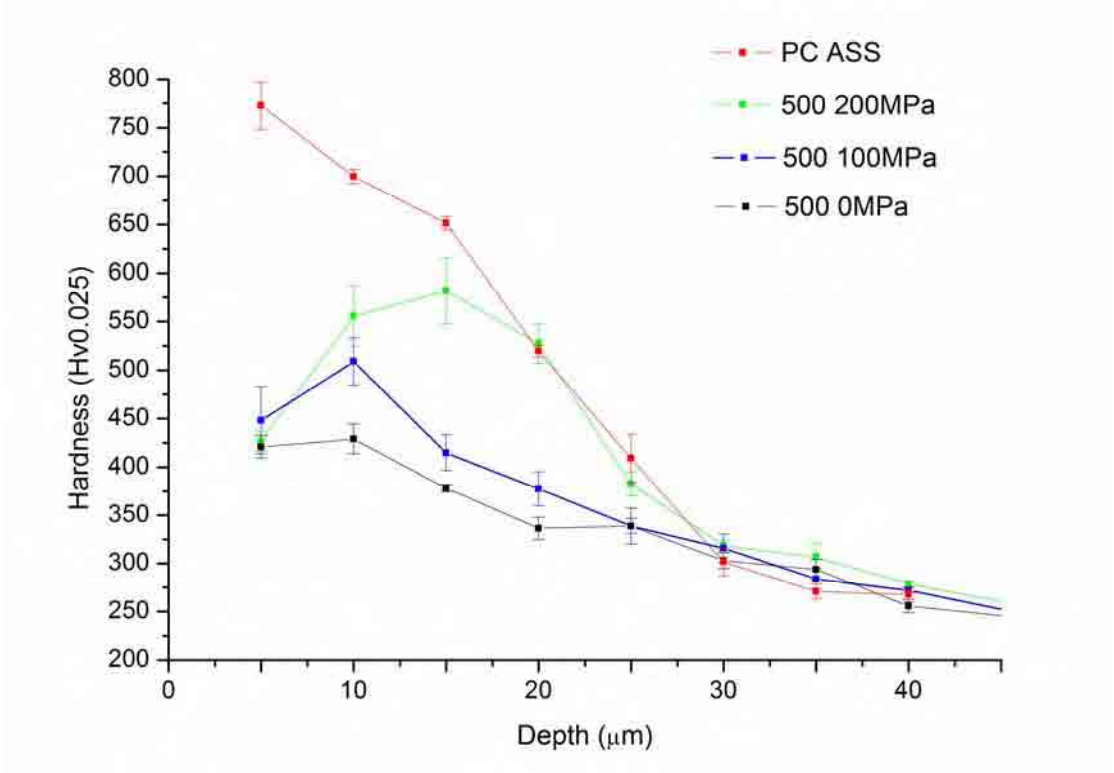

Figure 4.4-9 Effect of tensile stress on the hardness profiles along the cross sectional samples after 500°C/ 100 hours annealing

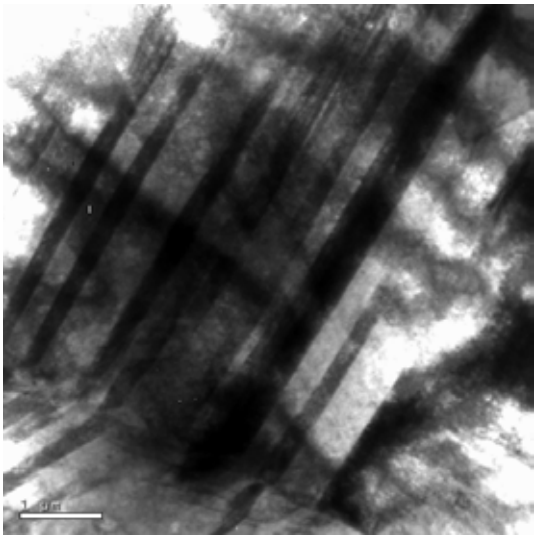

(a)

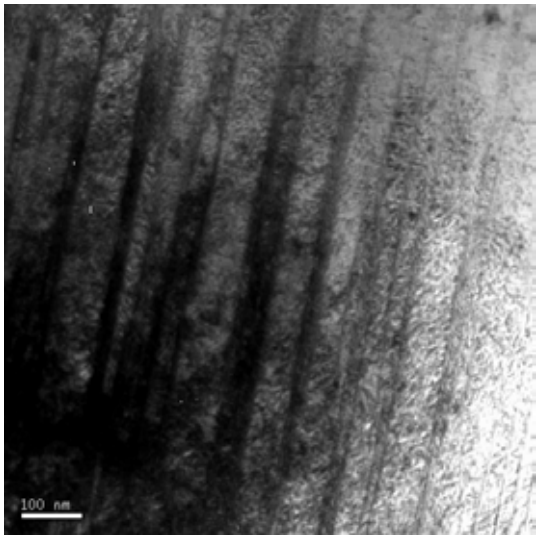

(b)

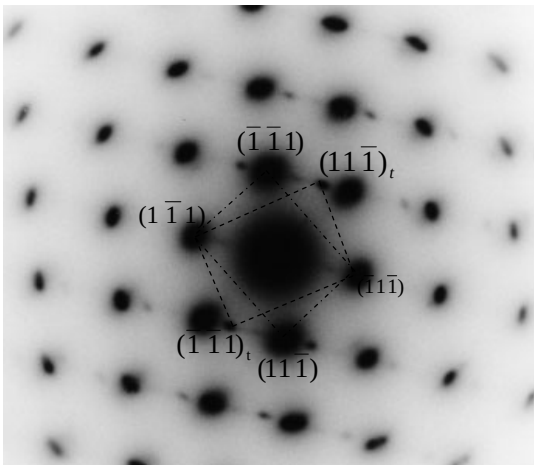

(c)

Figure 4.4-10 Conventional TEM bright field microscopy of sample‘500 200MPa’ (a) macro twining (b)nanotwining (c)SAD pattern from (b) showing$[1\bar{1}0]$ twining

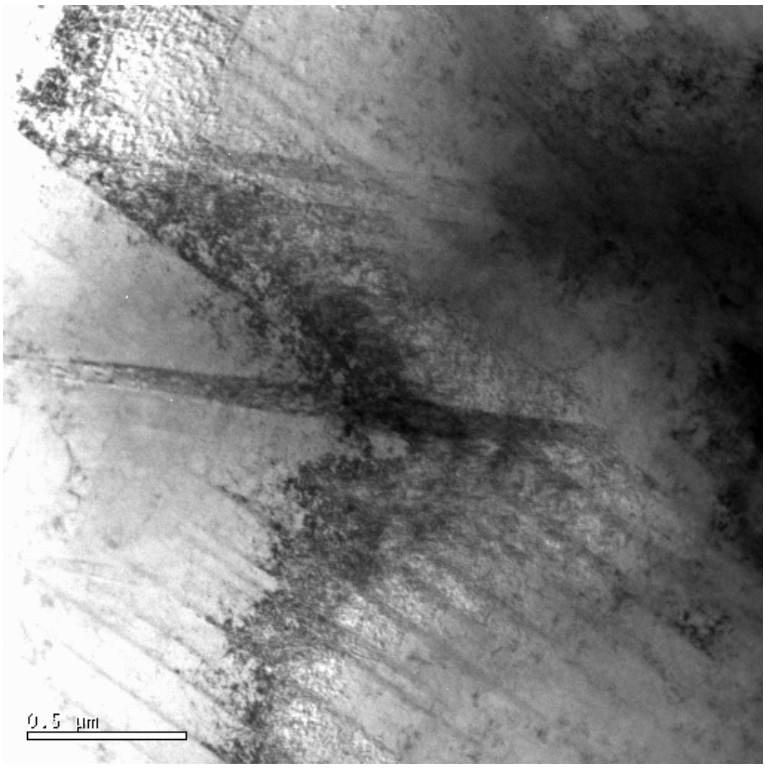

Figure 4.4-11 Twining intercepting with each other of sample‘500 200MPa’

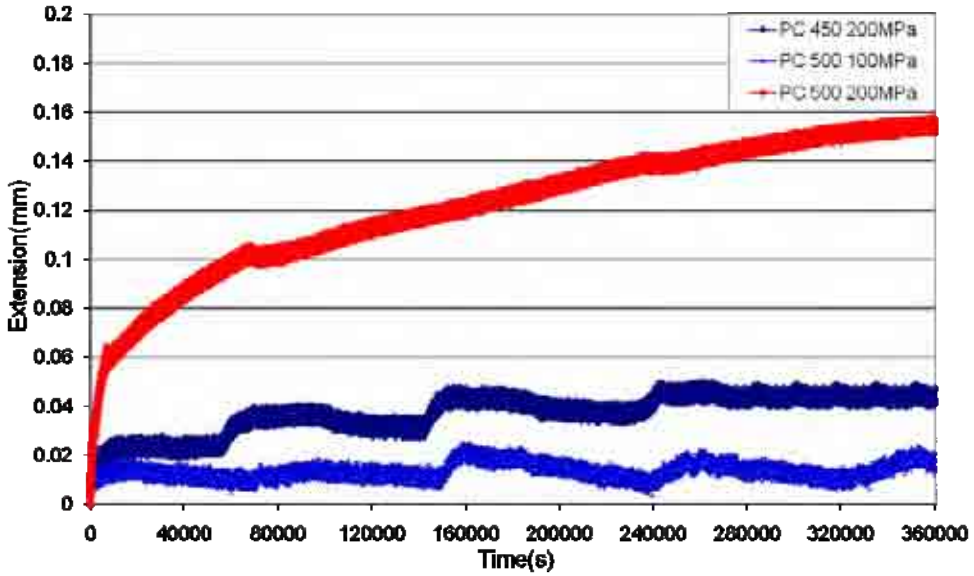

Figure 4.4-12 Elongation of samples with time at elevated temperature under tensile load

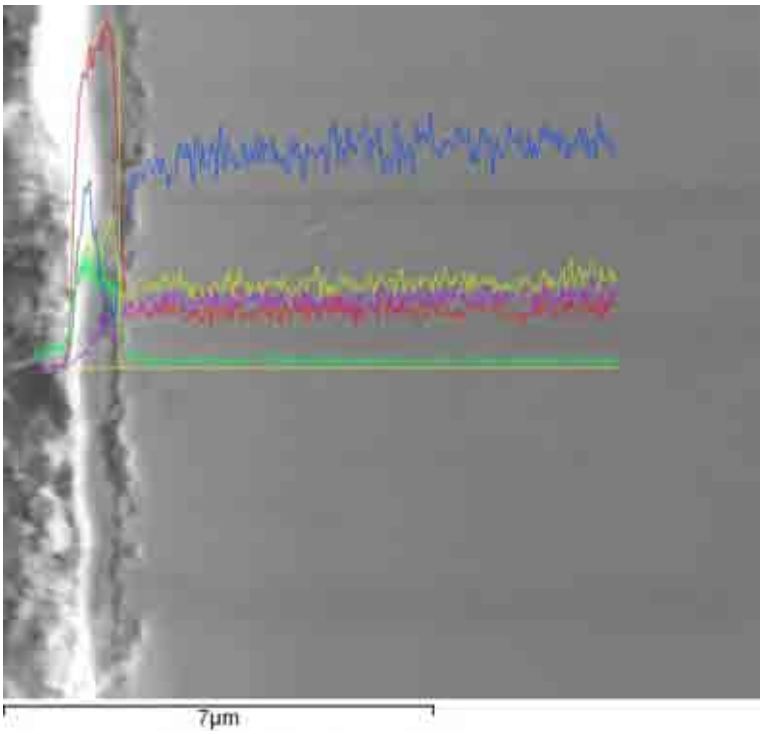

(a)

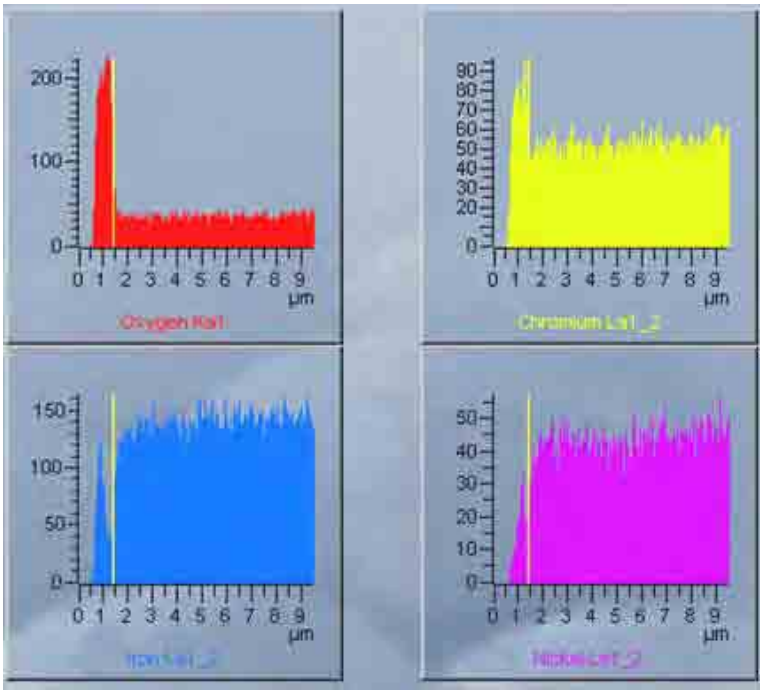

(b)

Figure 4.4-13 Cross sectional SEM line scan results of Sample ‘500 0MPa’

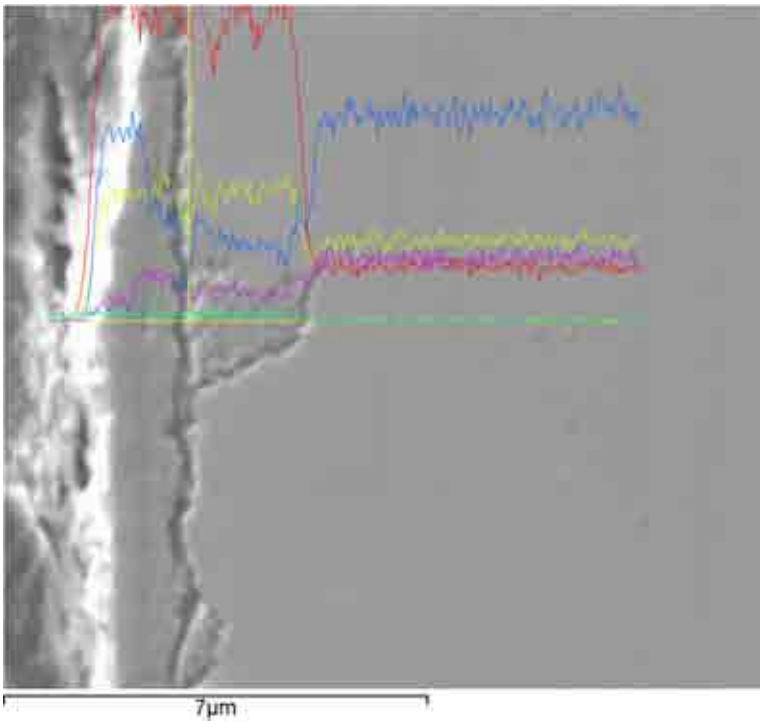

(a)

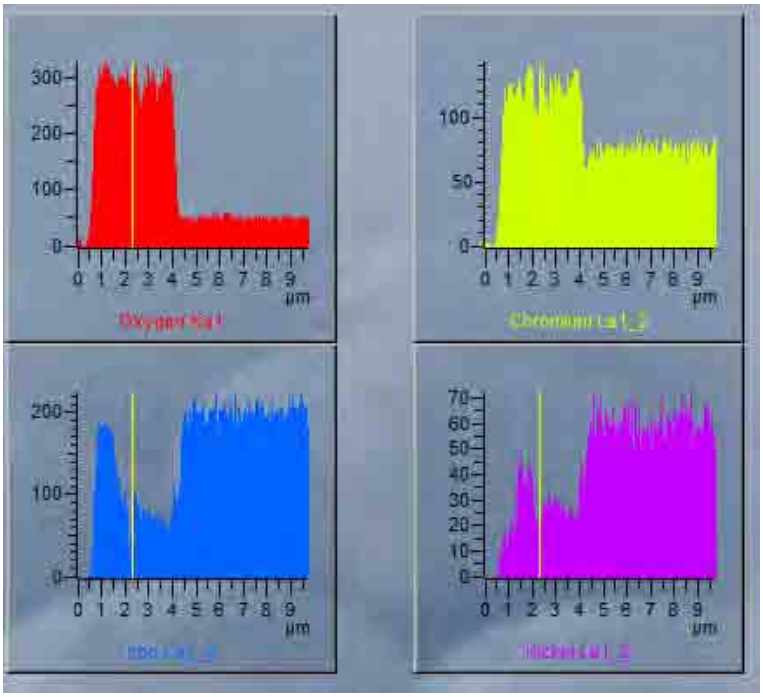

(b)

Figure 4.4-14 Cross sectional SEM line scan results of Sample ‘500 200MPa’

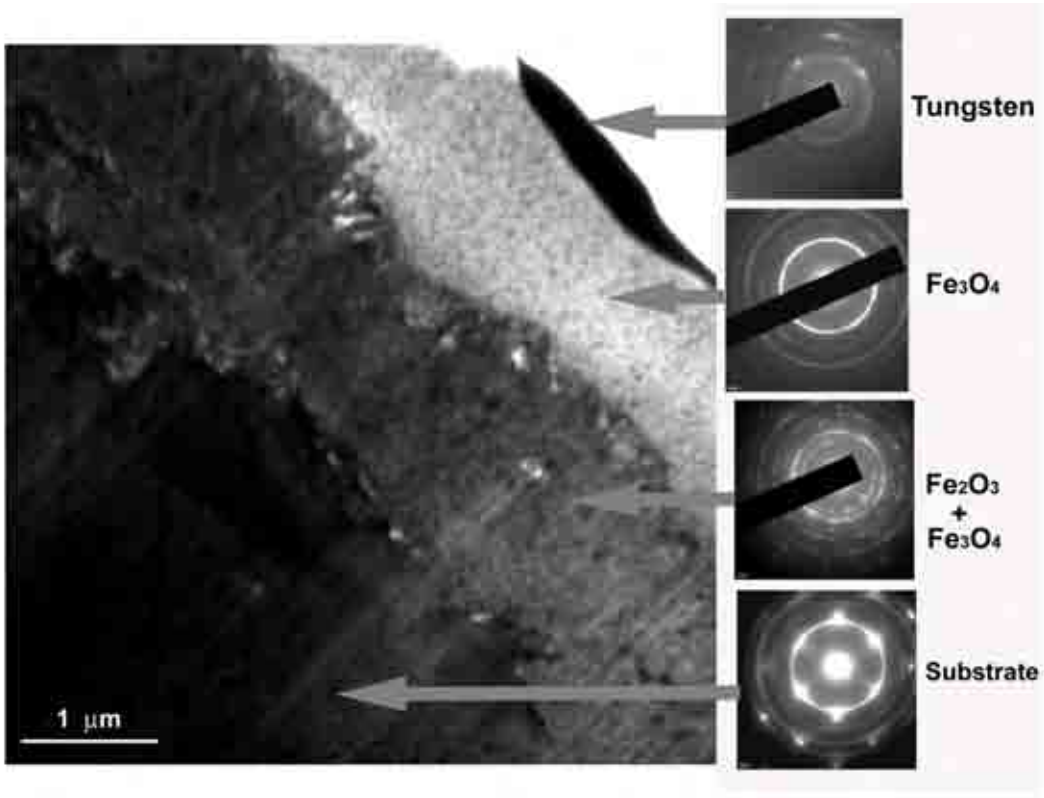

Figure 4.4-15 Cross sectional TEM of oxides layer on Sample '500 200MPa'

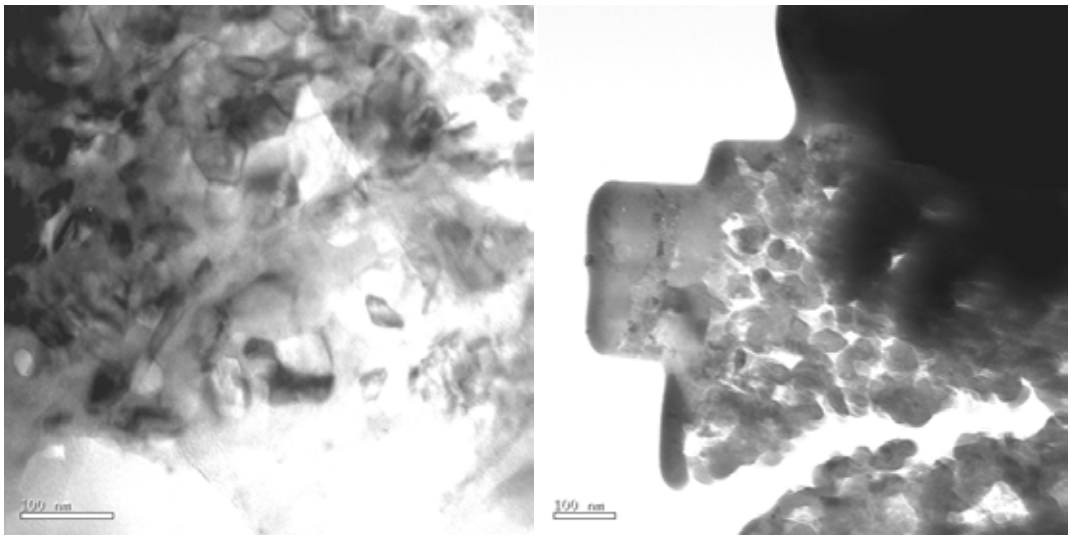

(a) (b)

Figure 4.4-16 Nano particles of $(FeCr)_2O_3$ in oxides layer at 500°C: (a) without tensile stress and (b)with tensile stress 200MPa

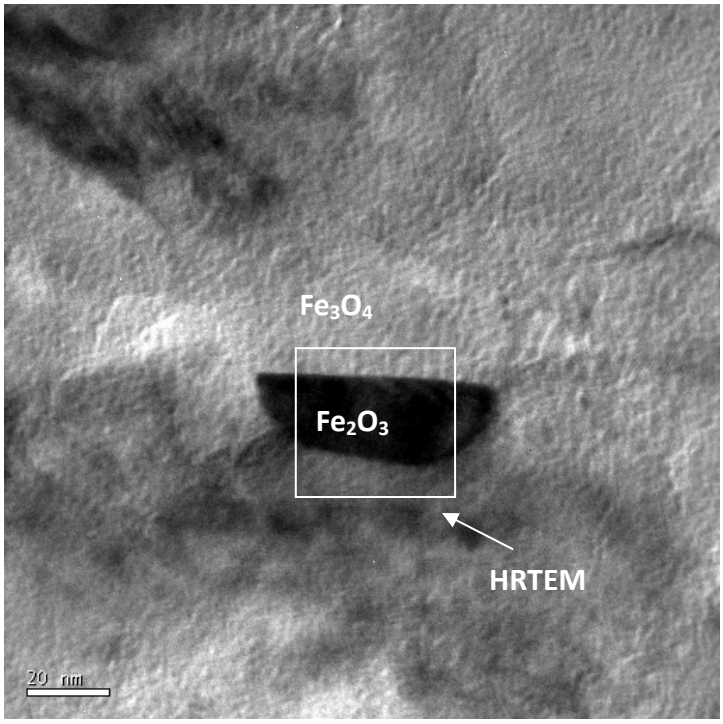

Figure 4.4-17 Nano sized Fe_2O_3 grown into the Fe_3O_4 layer of Sample '500 0MPa'

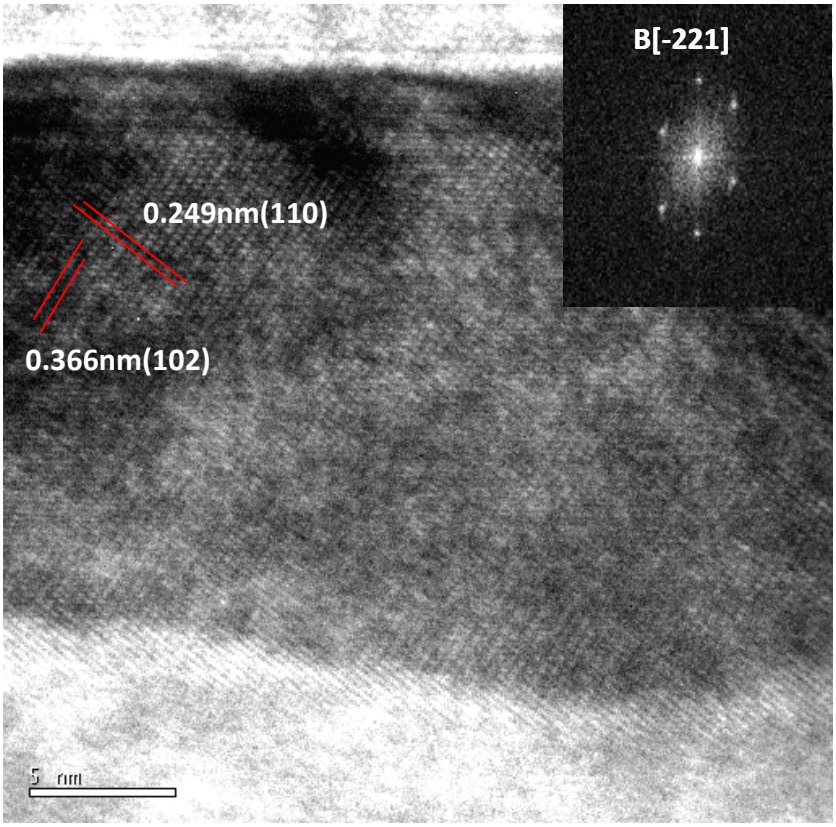

Figure 4.4-18 HRTEM microstructure of Fe_2O_3 with inserted corresponding FFT pattern of the image

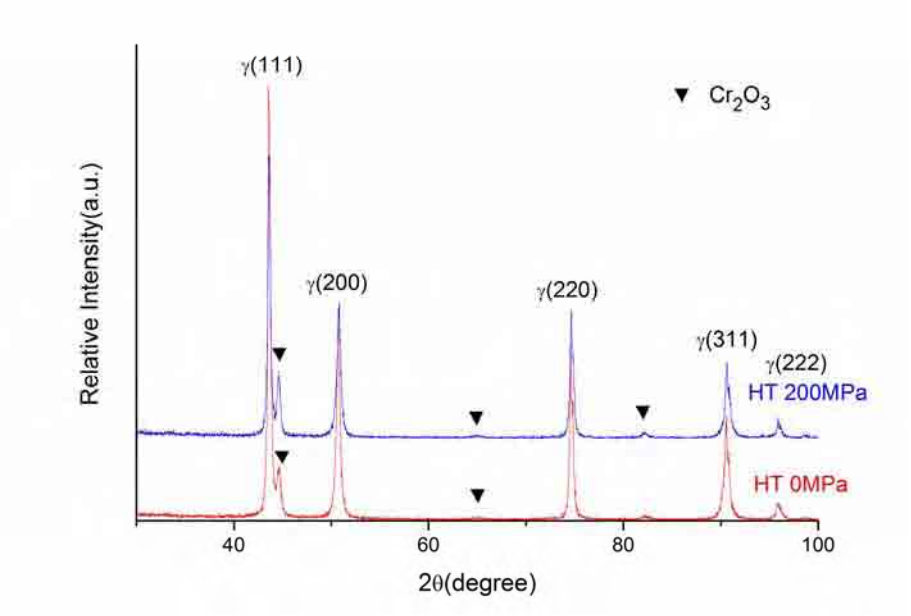

Figure 4.4-19 XRD patterns of heat treatment of 316 ASS at 500 °C for 100 hours with and without 200MPa tensile stress

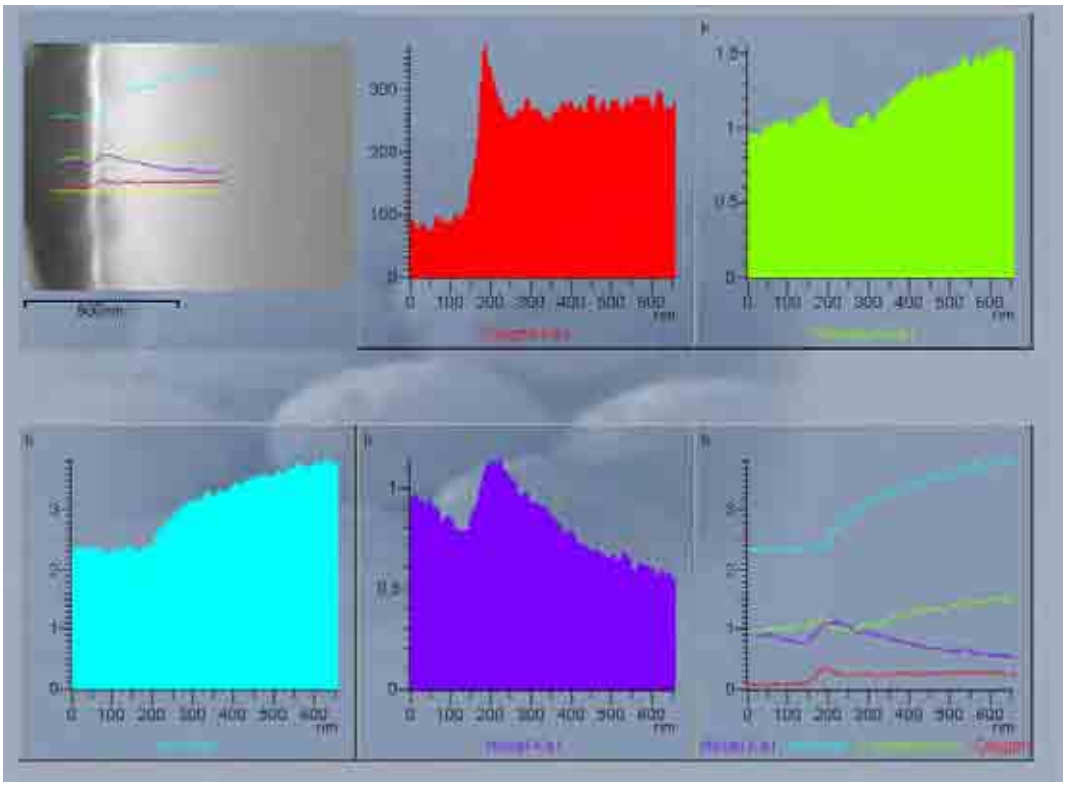

Figure 4.4-20 SEM line scan results of cross section of Sample '316 ASS' at 500 °C for 100 hours under 200MPa

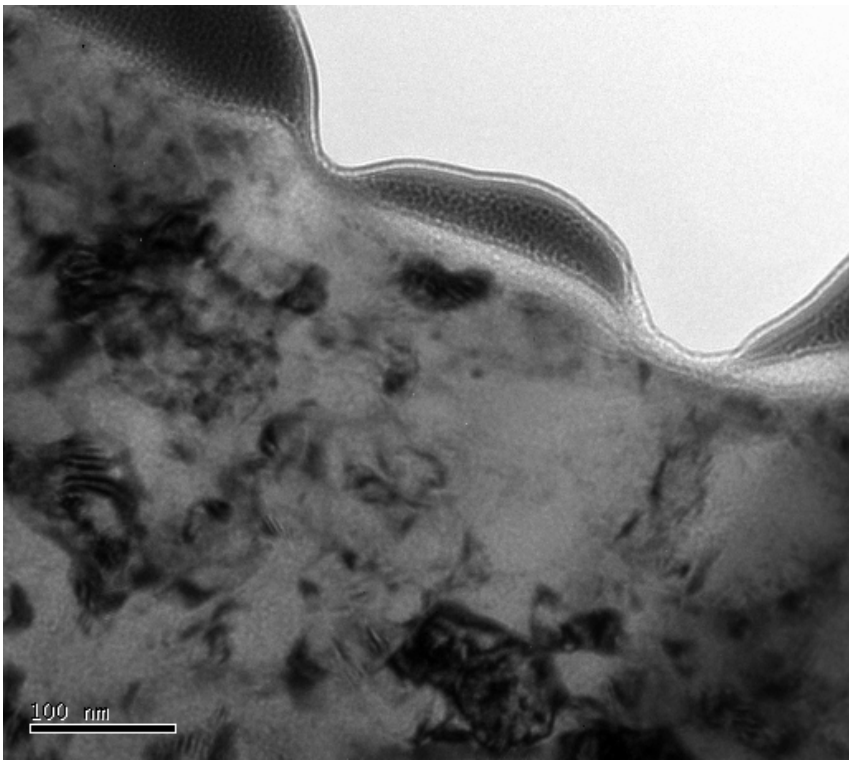

(a)

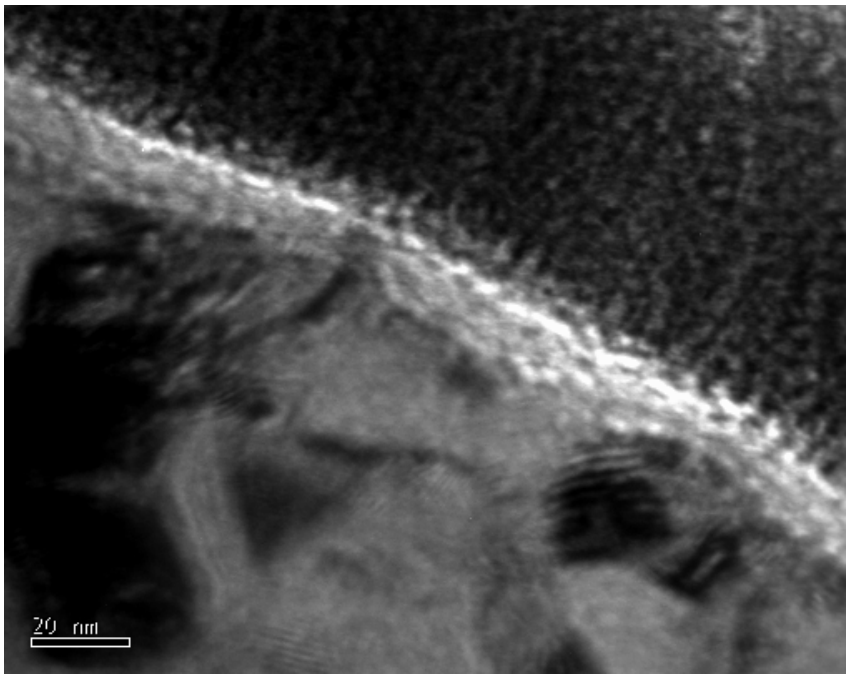

(b)

Figure 4.4-21 Cross sectional TEM images from 500°C 0MPa treatment of 316ASS

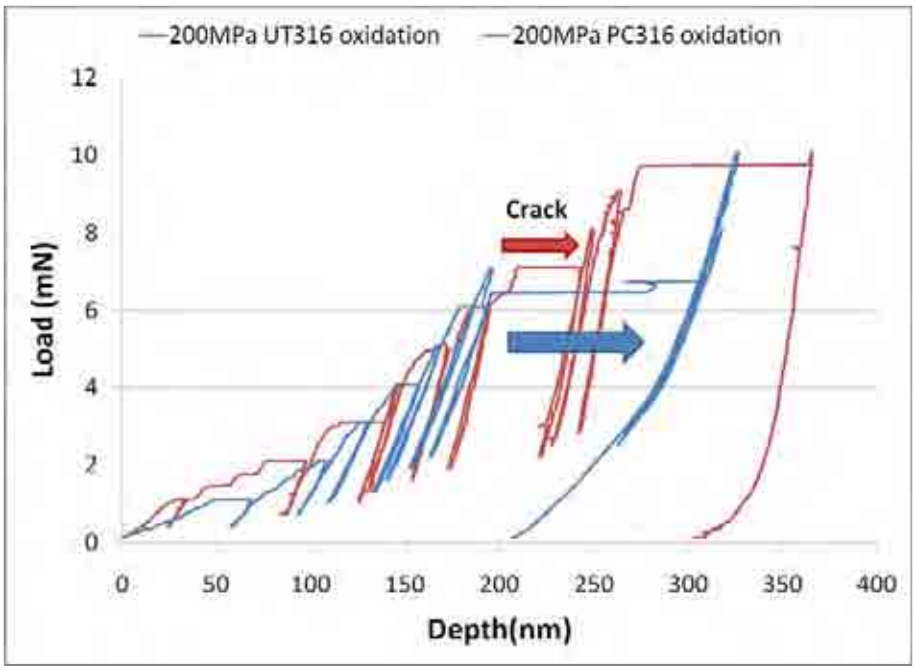

Figure 4.4-22 Load-displacement curves of the oxidised untreated and carburised 316ASS under 200MPa tensile stress

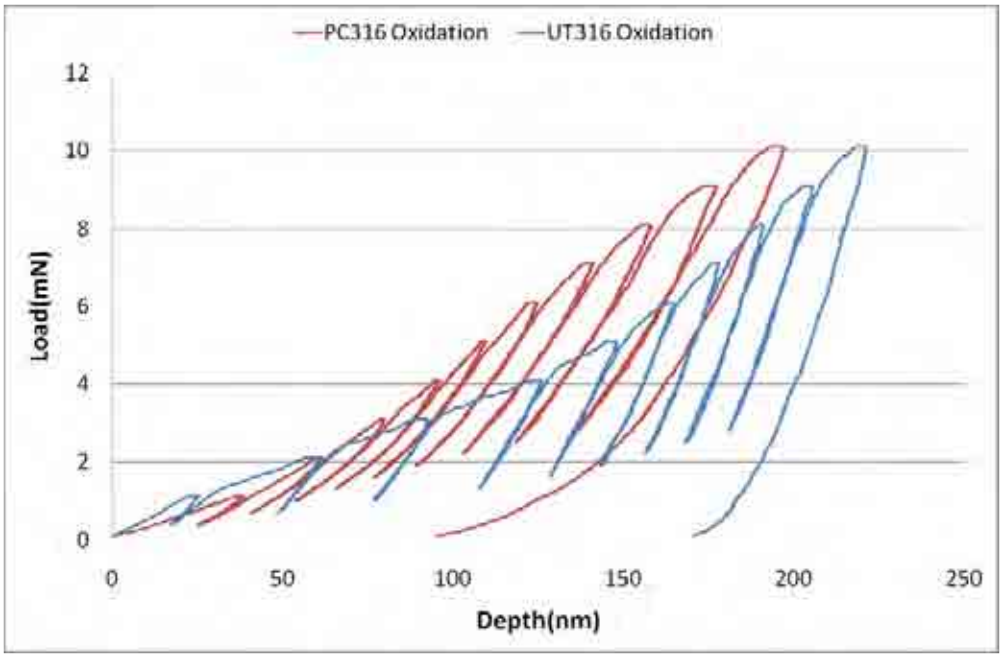

(a)

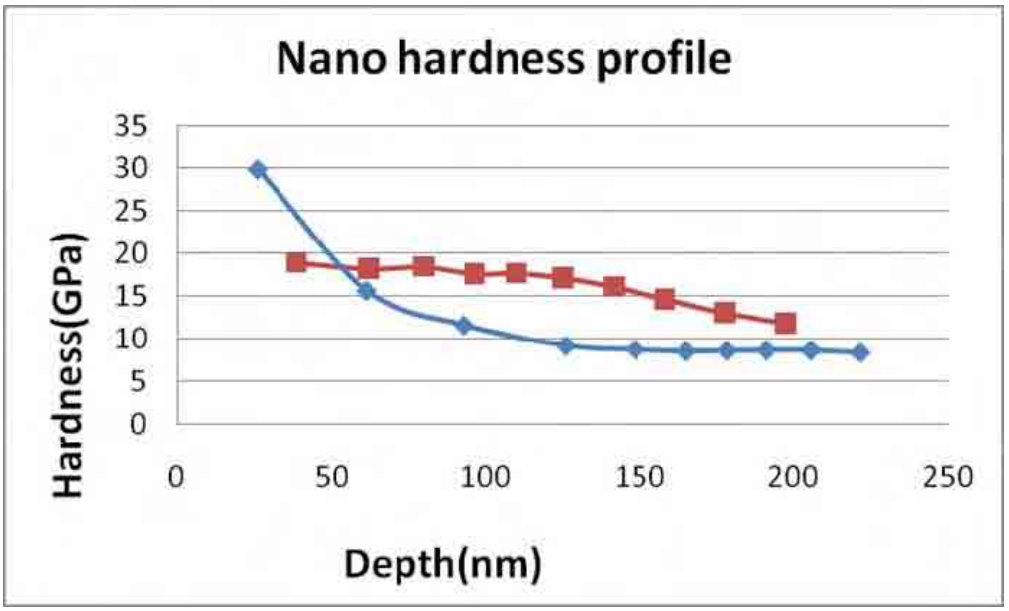

(b)

Figure 4.4-23(a) Load-displacement curves of the oxided untreated and carburised 316ASS without tensile stress; (b) calculated Hardness profiles obtained from (a)

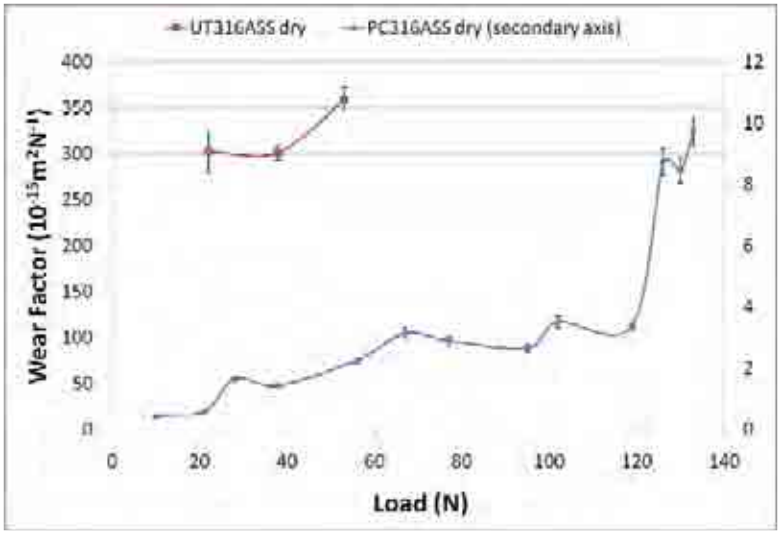

Figure 4.5-1 Wear factor results of untreated and carburised 316ASS tested in air

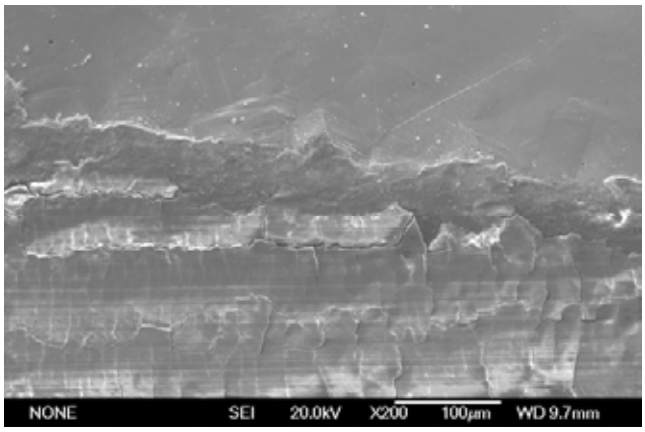

(a)

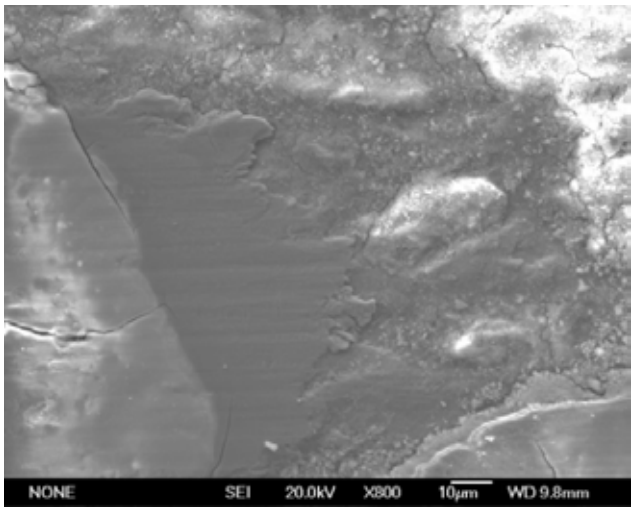

(b)

Figure 4.5-2 SEM micrographs of the wear track of untreated 316ASS tested in air at a load of 21N (a) cracking and (b) oxide particles

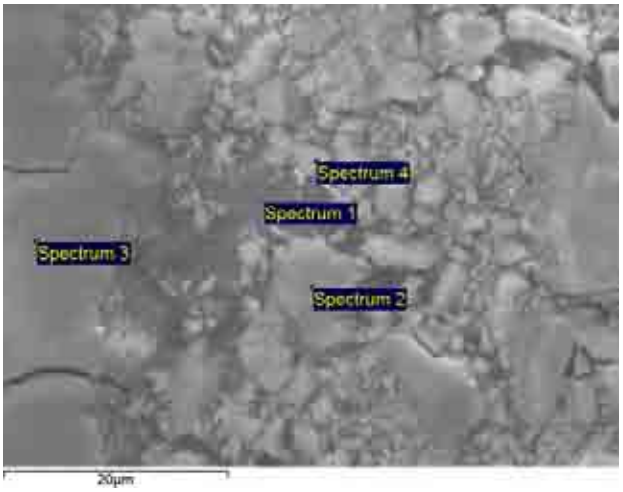

Figure 4.5-3 Measuring positions for EDX analysis in the wear track of untreated 316ASS tested in air at a load of 21 N

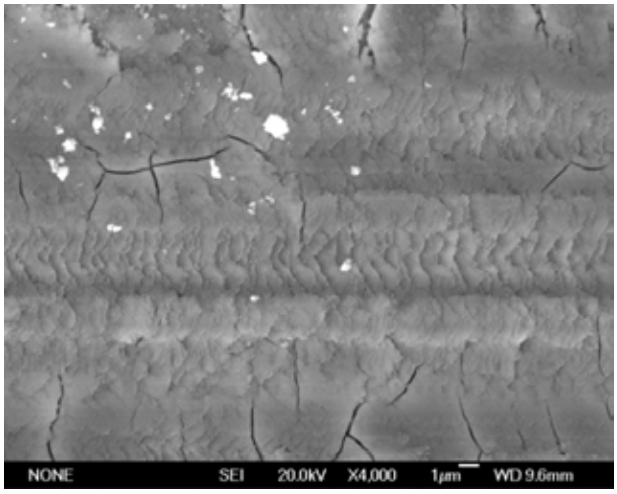

Figure 4.5-4 SEM micrographs of the dry wear track of carburised 316ASS tested in air at a load of 21N

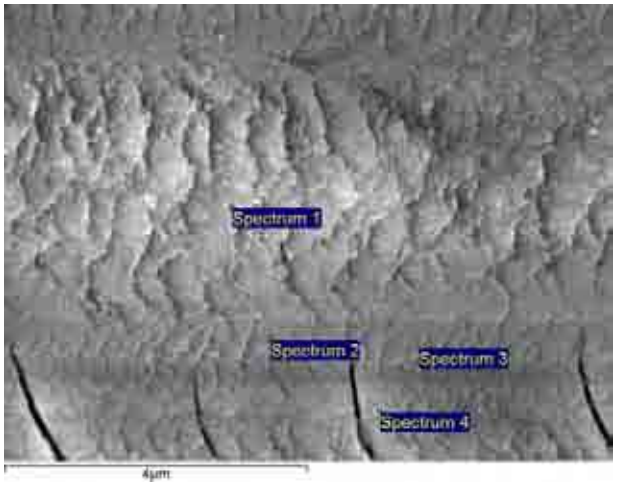

Figure 4.5-5 Measuring positions for EDX analysis in the wear track of PC 316ASS tested in air at a load of 21N

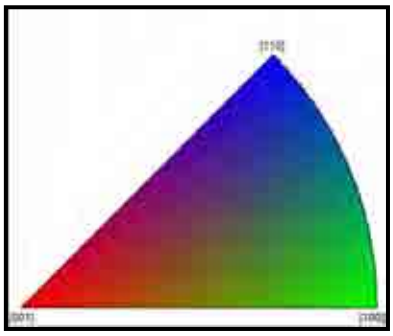

(a)

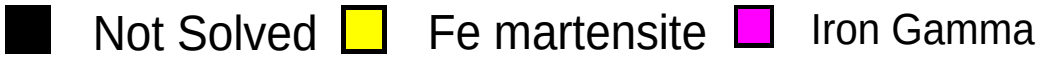

(b)

Figure 4.5-6 EBSD analysis keys: (a) EBSD orientation key; (b) EBSD phase key

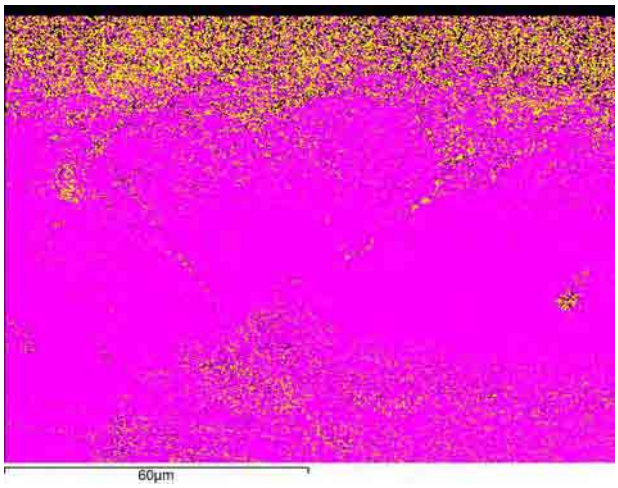

(a)

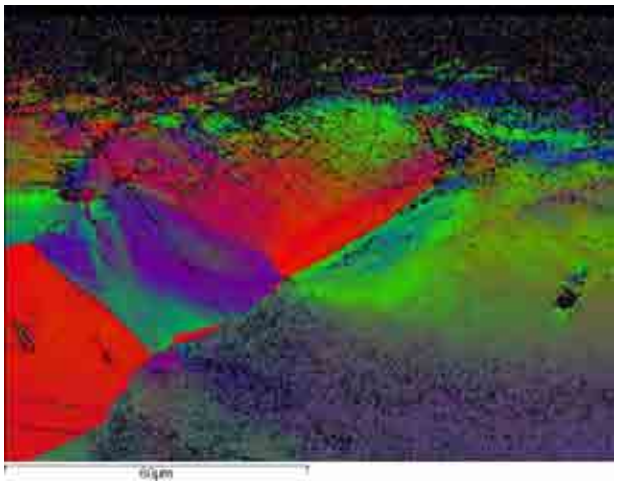

(b)

Figure 4.5-7 EBSD results of the wear track on untreated 316ASS tested in air at a load of 21N: (a) phases map; (b) orientations of austenitic FCC phase

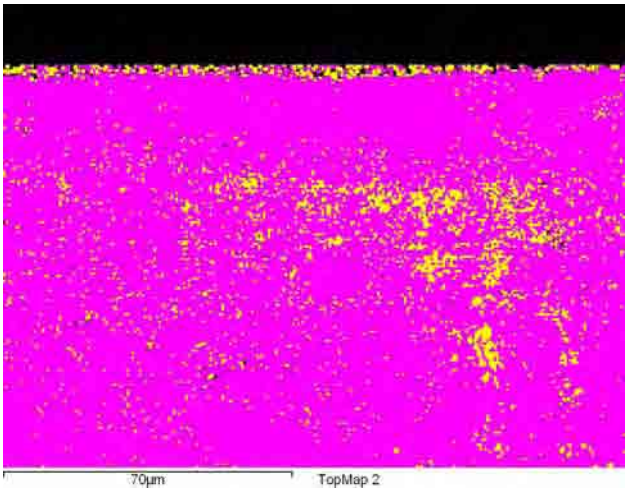

(a)

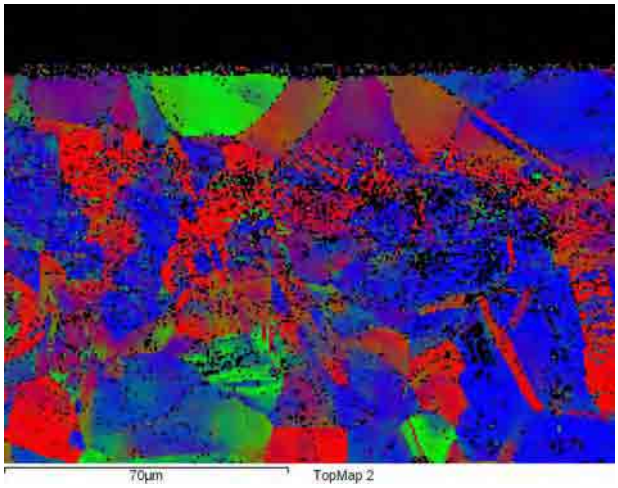

(b)

Figure 4.5-8 EBSD results of the wear track on PC 316ASS tested in air at a load of 95N: (a) phases map; (b) orientations of austenitic FCC phase

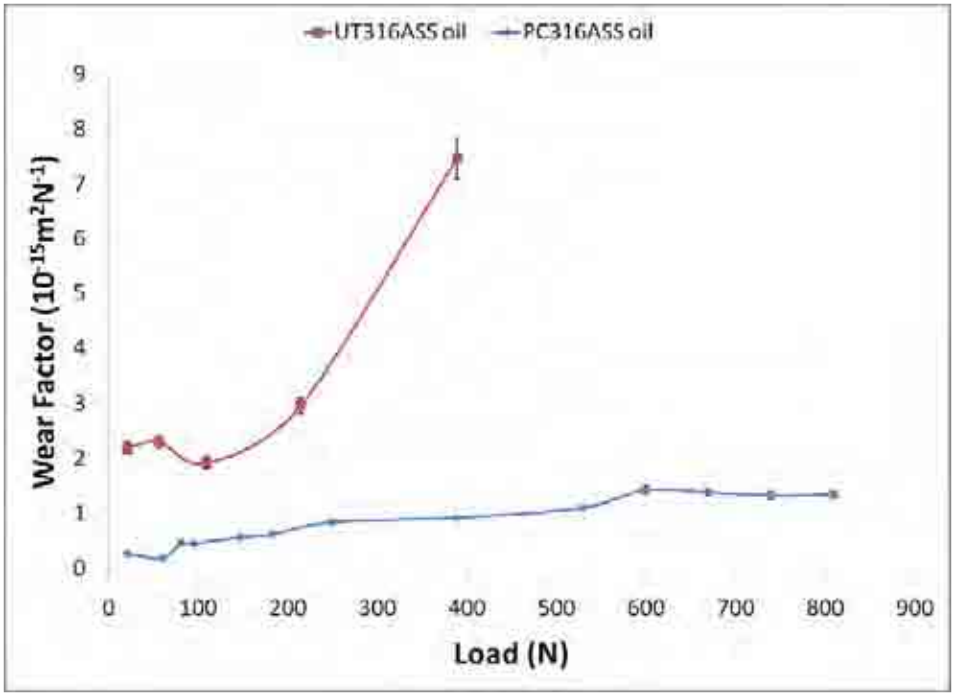

Figure 4.5-9 Wear factor of untreated and carburised 316ASS in oil lubricated reciprocating sliding wear

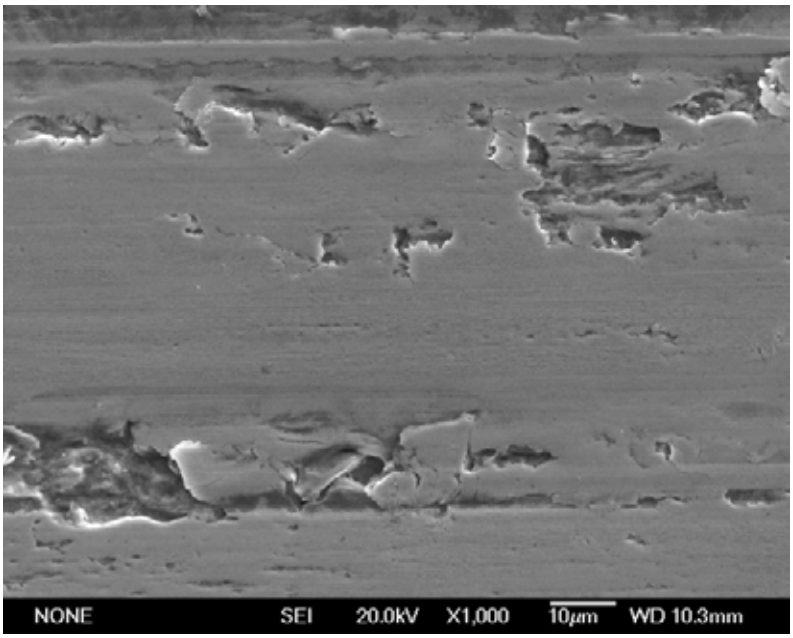

Figure 4.5-10 SEM micrograph of the wear track of untreated 316 ASS tested in oil lubricated reciprocating sliding wear at a load of 56N

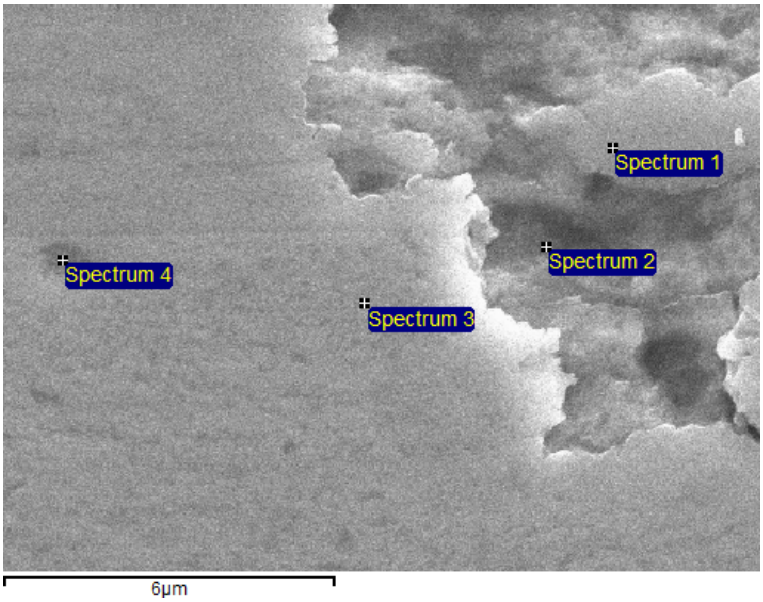

Figure 4.5-11 Measuring positions for EDX analysis in the wear track of PC 316ASS tested in oil reciprocating sliding wear at a load of 56N

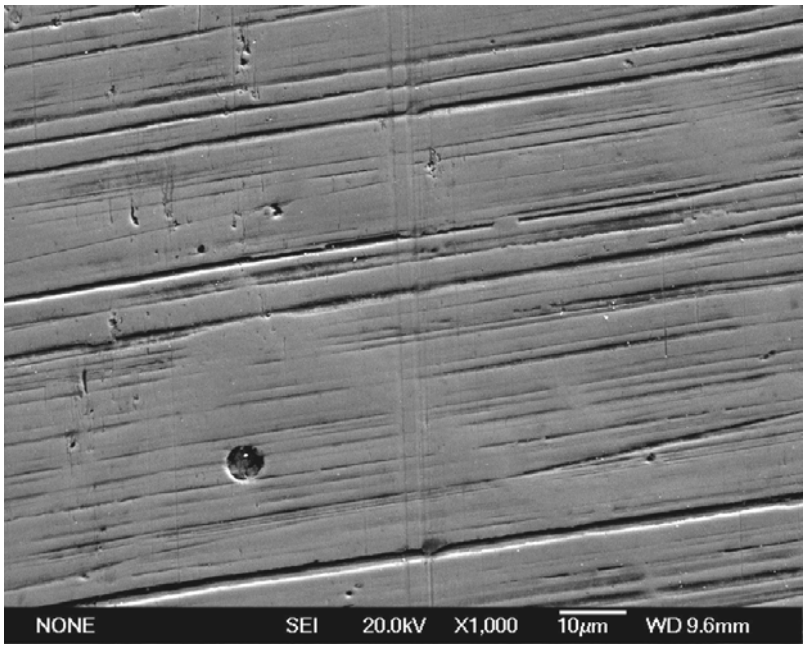

Figure 4.5-12 SEM micrograph of the wear track of PC 316ASS tested in oil lubricated reciprocating sliding wear at a load of 214N

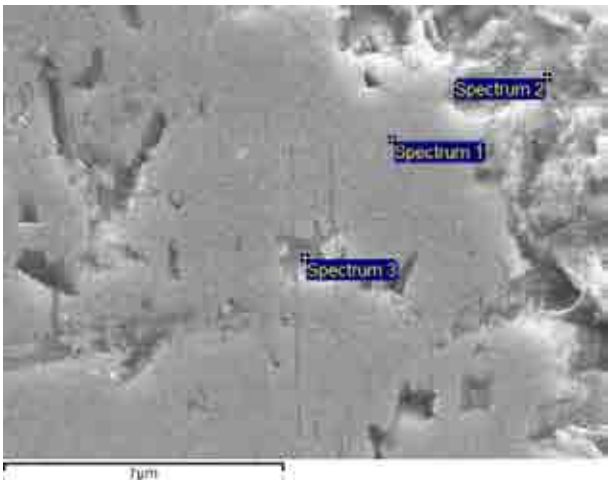

Figure 4.5-13 Measuring positions for EDX analysis in the wear track of PC 316ASS tested in oil lubricated reciprocating sliding wear at a load of 214N

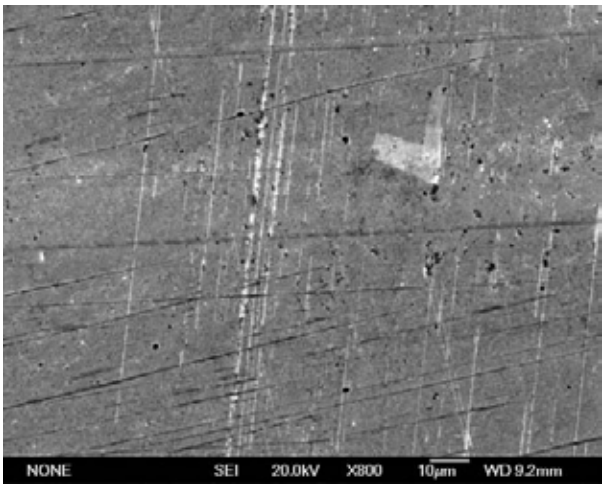

(a)

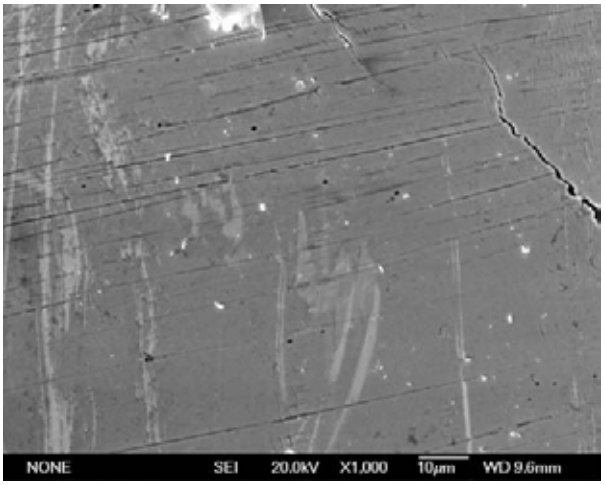

(b)

Figure 4.5-14 SEM micrographs of the wear tracks carburised 316ASS tested in oil lubricated reciprocating sliding wear at a load of (a) 529 N (b) 739 N

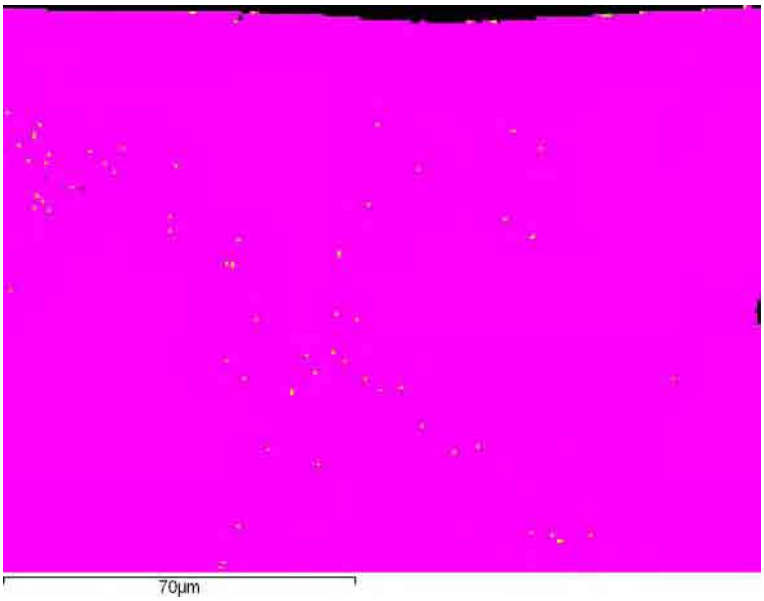

(a)

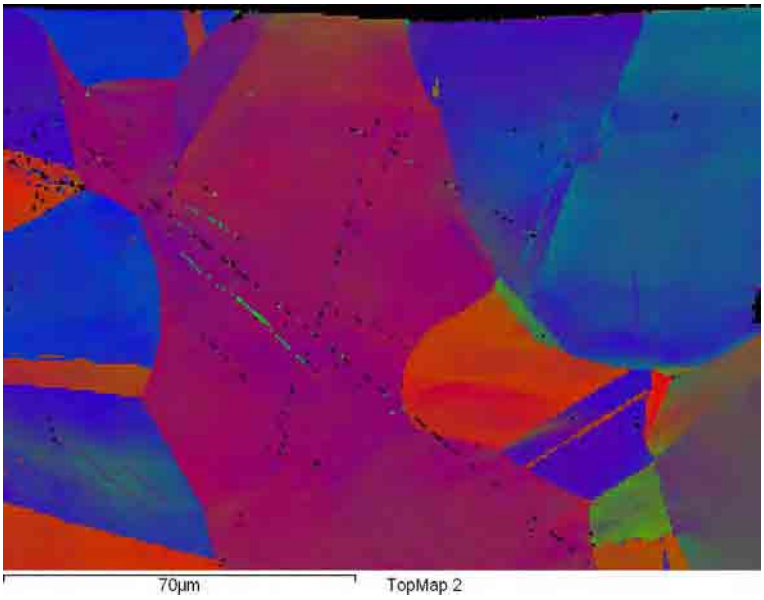

(b)

Figure 4.5-15 EBSD results of the wear tracks of carburised 316ASS tested in oil lubricated reciprocating sliding wear at a load of 95 N (a) phases map; (b) orientations of austenitic FCC phase

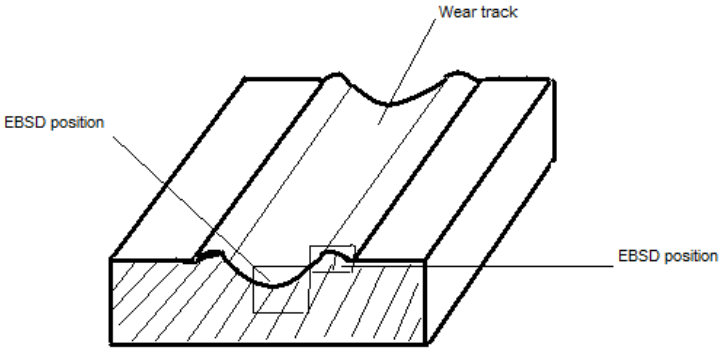

Figure 4.5.16 Schematic diagram of EBSD positions from the cross section of wear track

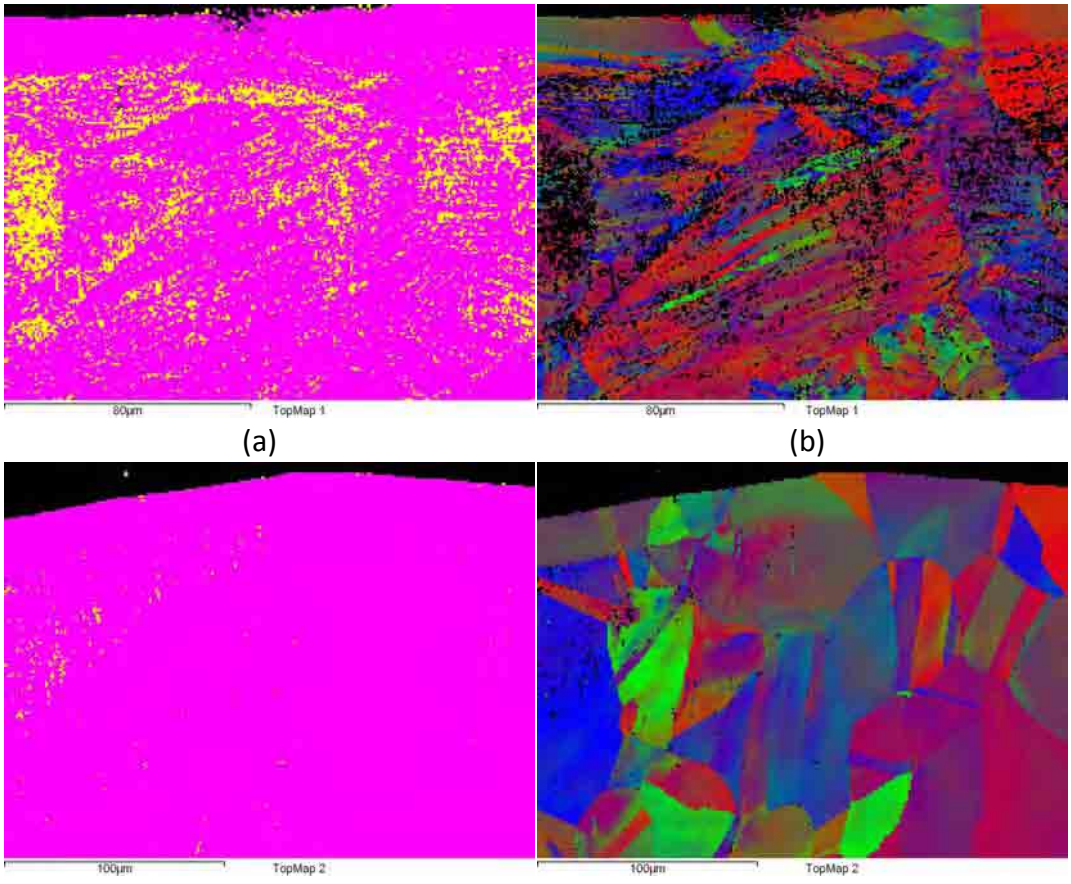

(a) (b)

(c) (d)

Figure 4.5-17 EBSD results of the wear tracks on PC 316ASS tested in oil lubricated reciprocating sliding wear at a load of 599 N (a) phases map; (b); (c) &(d) phase map& orientations of austenitic FCC phase near the edge of wear track

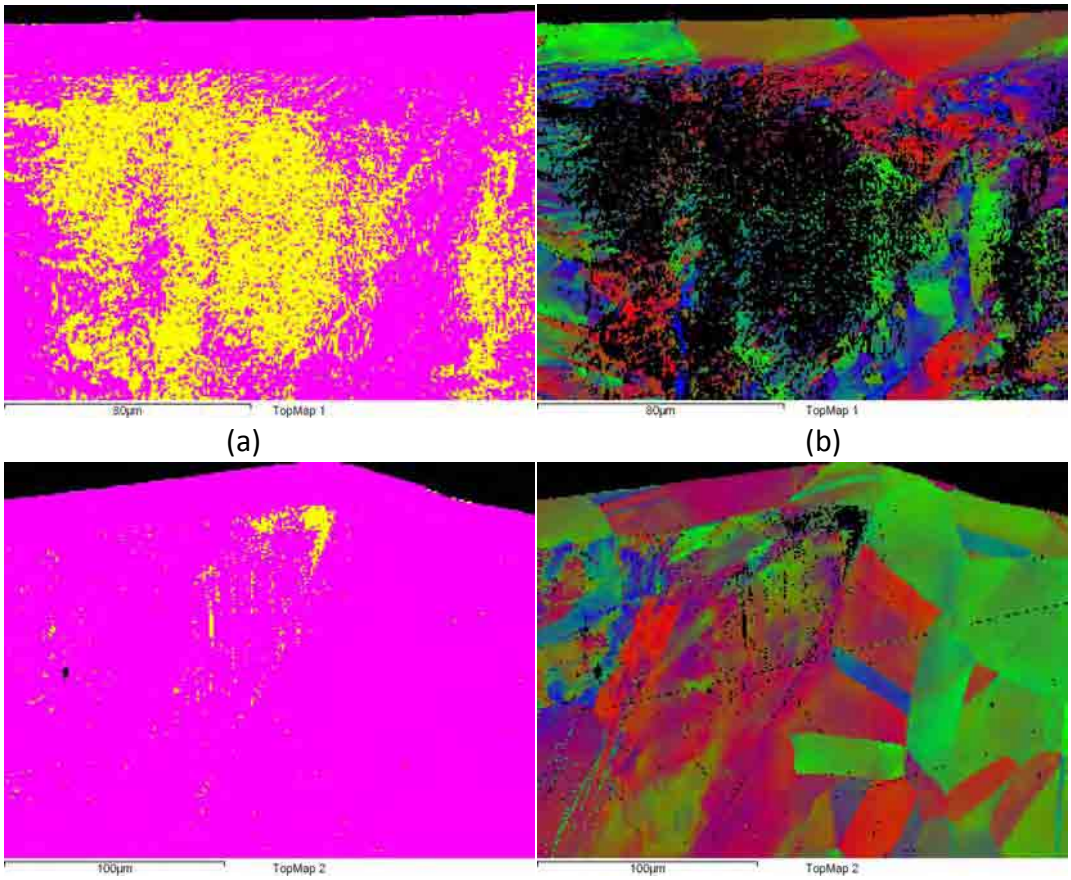

(a) (b)

(c) (d)

Figure 4.5-18 EBSD results of the wear tracks on PC 316ASS tested in oil lubricated reciprocating sliding wear at a load of 739 N (a) phases map; (b) orientations of austenitic FCC phase; (c) &(d) phase map& orientations of austenitic FCC phase near the edge of wear track

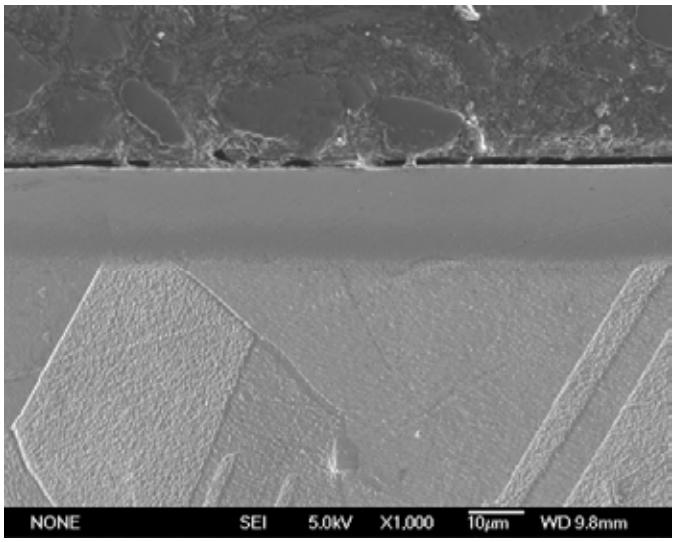

Figure 4.6-1 Cross sectional SEM showing S-phase formed by carburising for 10 hours at 450°C

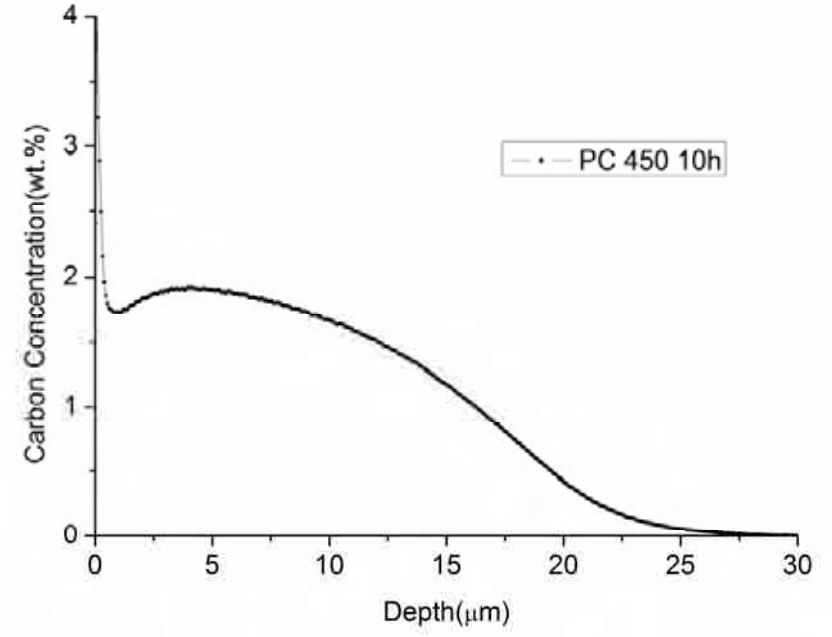

Figure 4.6-2 Carbon depth profiles of the plasma carburised 316ASS

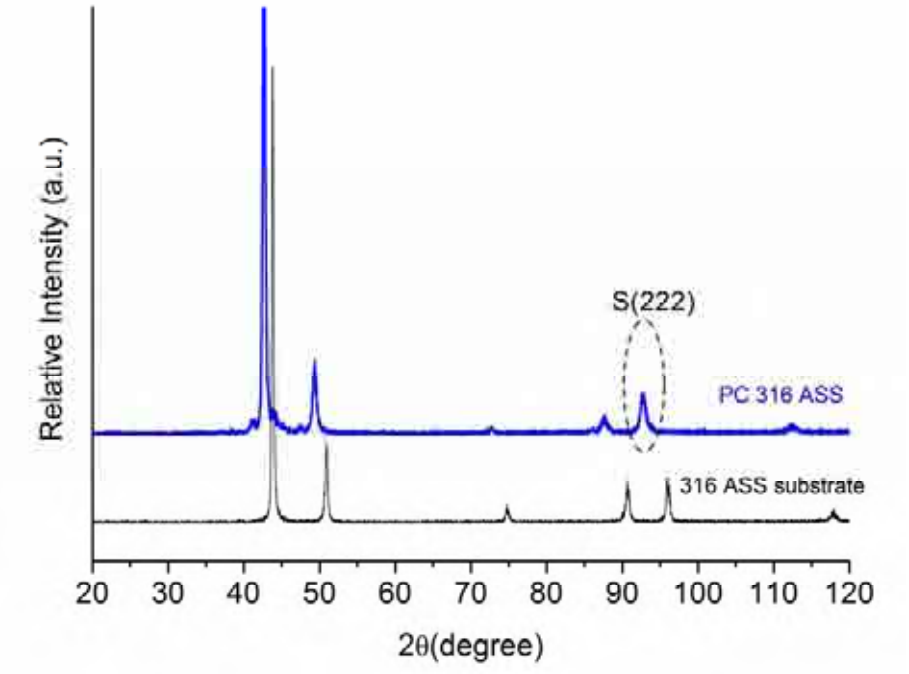

Figure 4.6-3 XRD patterns of untreated and carburised AISI 316 ASS. Peak (222) was taken for residual stress test

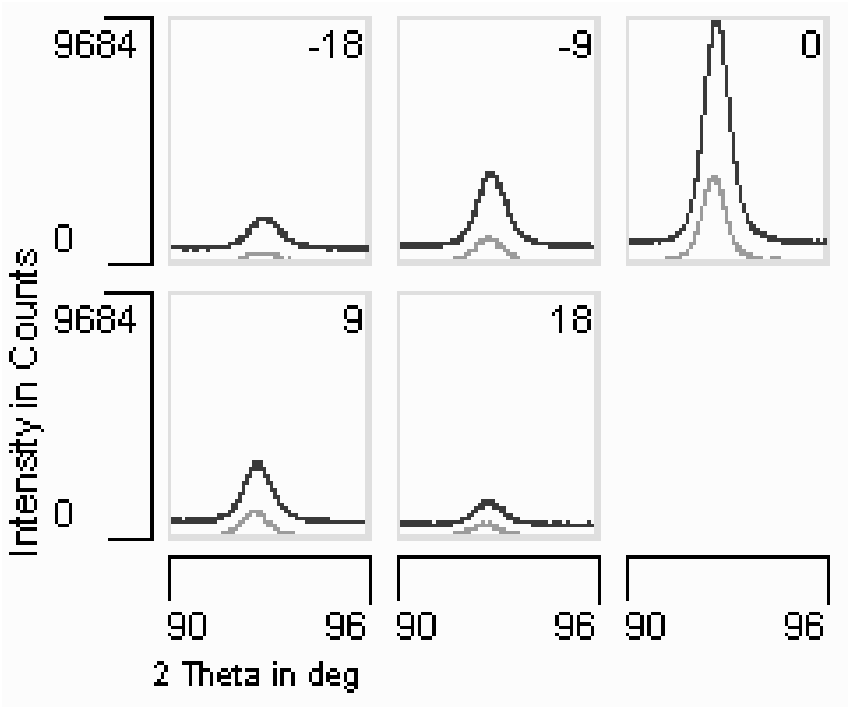

Figure 4.6-4 Peaks shift of S (222) at different ψ angles (original peaks in dark black colour and peaks after correction in grey colour)

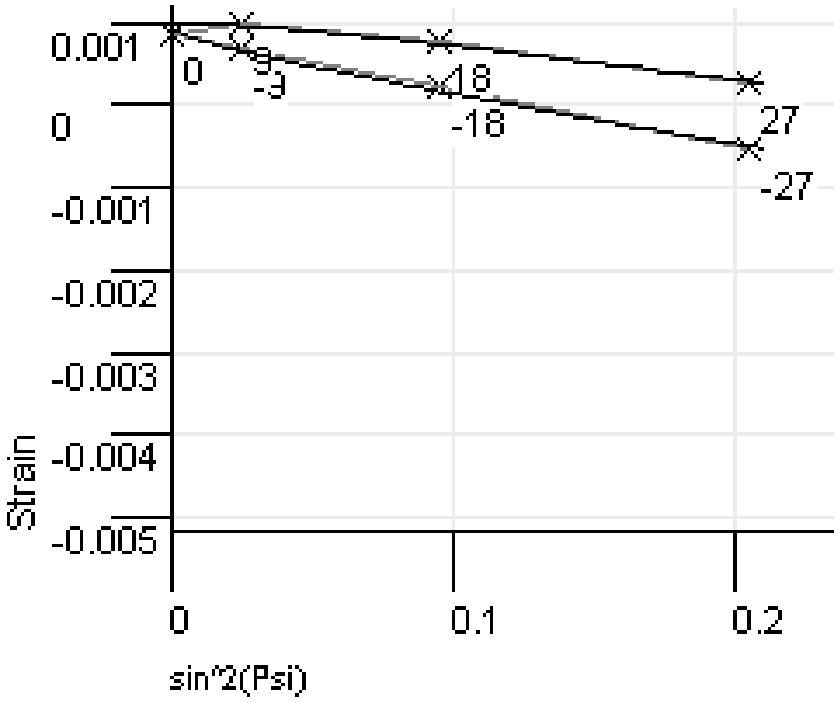

Figure 4.6-5 Elliptical fitting of strains versus $\sin^2 \psi$

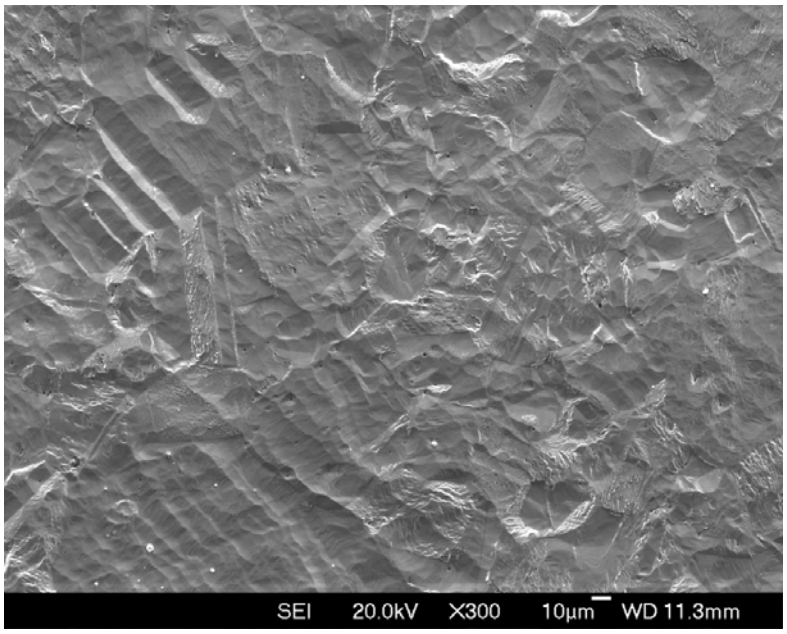

Figure 4.6-6 Surface morphology of AISI 316ASS after sputtering using GDS for 10 seconds

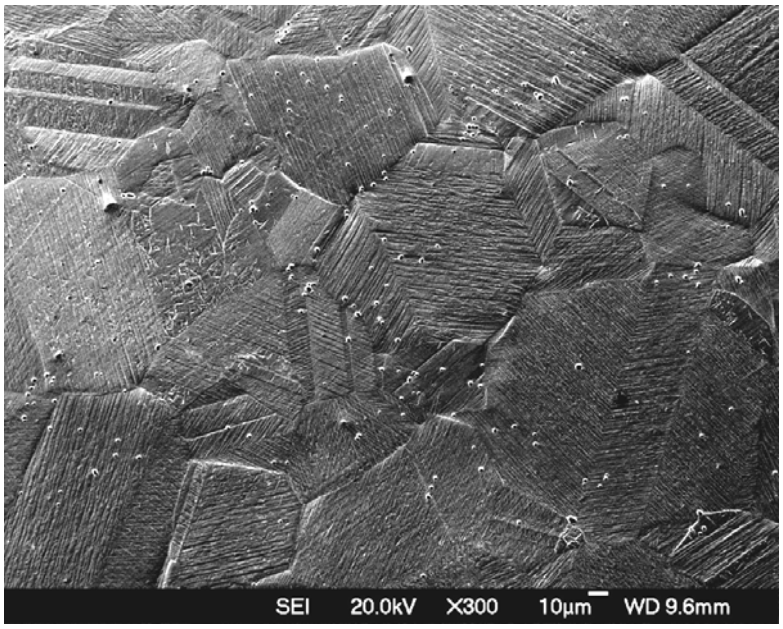

Figure 4.6-7 Surface morphology of PC AISI 316ASS after sputtering in GDS for 10 seconds.

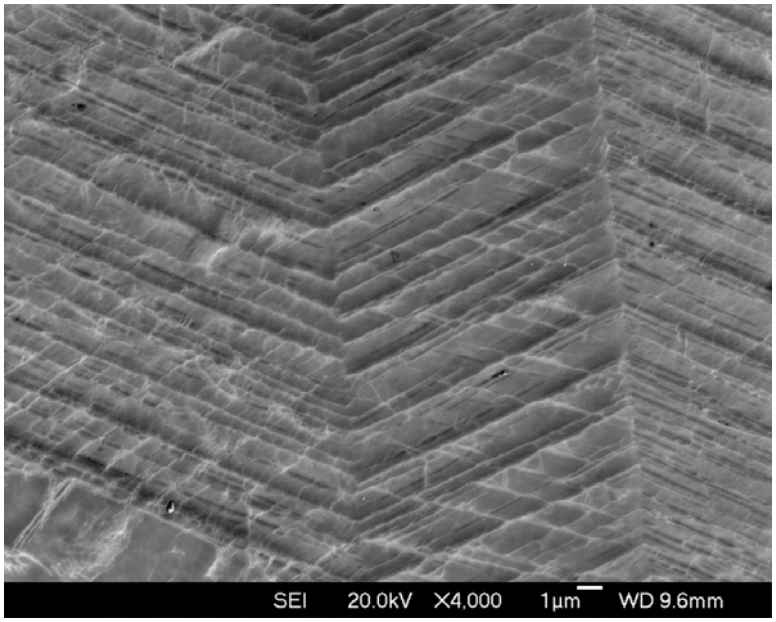

Figure 4.6-8 Magnified SEM morphology showing persistent slip bands

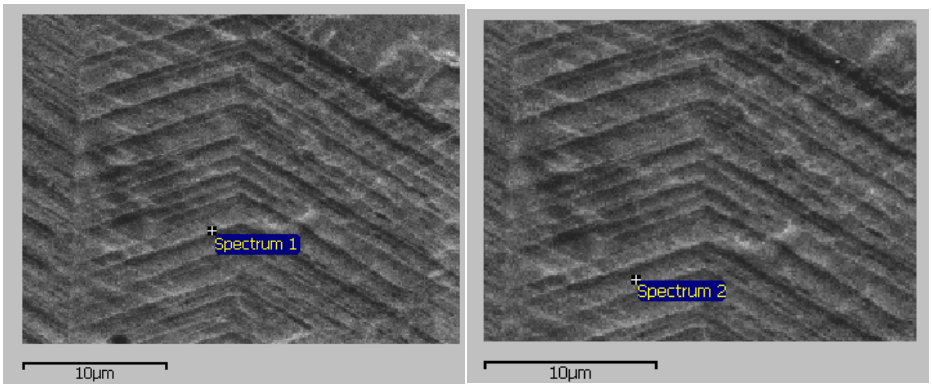

(a) (b)

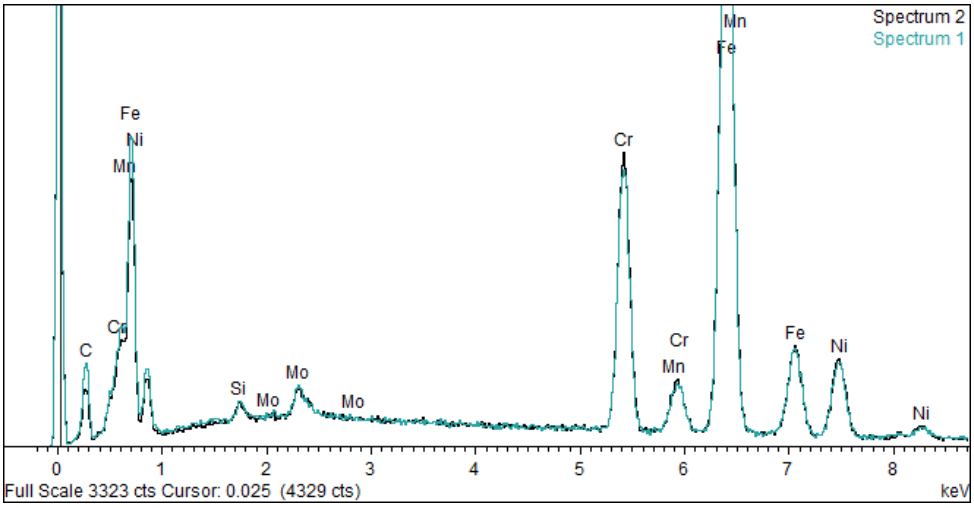

(c)

Figure 4.6-9 EDX analysis of two spectra from the extrusion and intrusion place

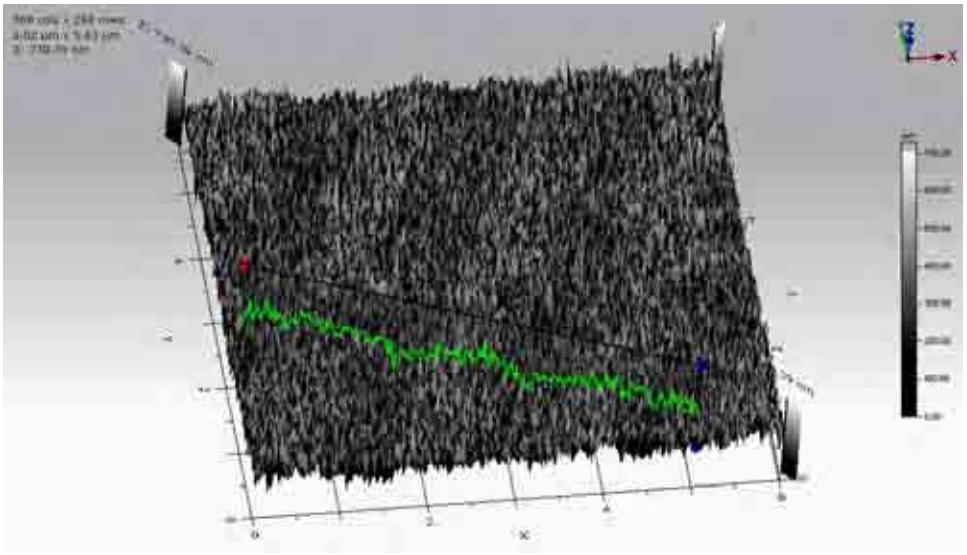

(a) Surface topological image

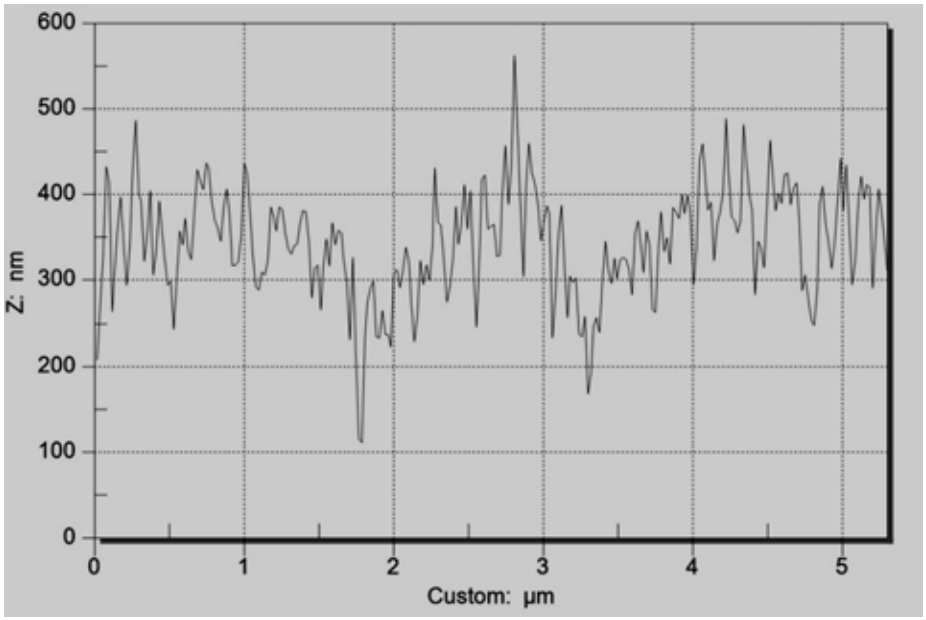

(b) Cross sectional height profile from (a)

Figure 4.6-10 AFM pictures showing 3D morphology from the surface of PC 450 10hours

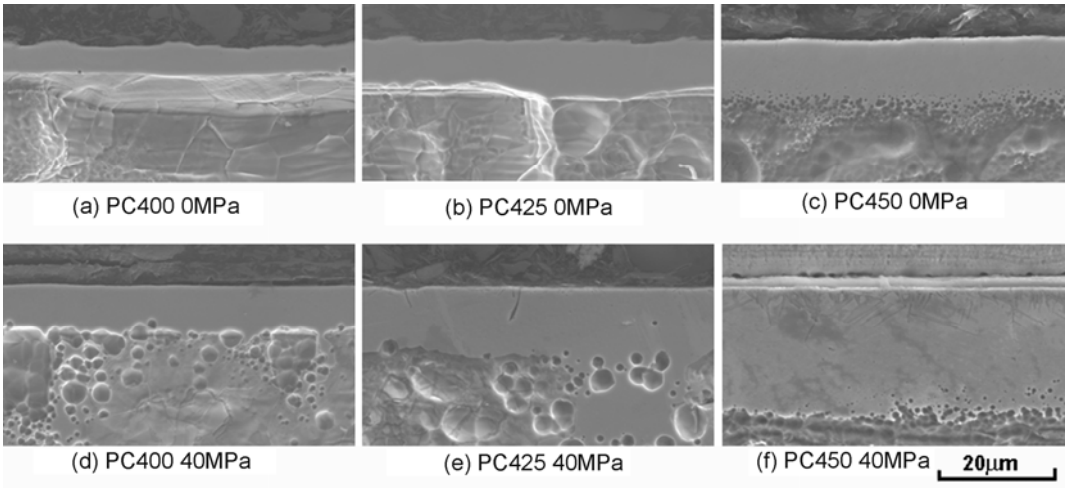

Figure 5.1-1 Cross sectional microstructure after carburising for 400,425 and 450°C under 0 and 40 MPa tensile stress for 10 hours

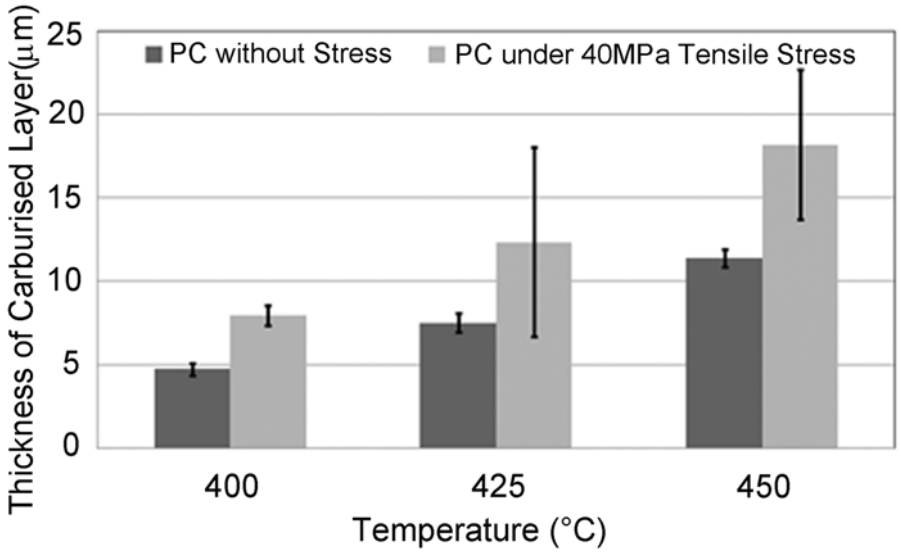

Figure 5.1-2 Thickness of plasma carburised layers as a function of the PC treatment temperature and applied *in situ* tensile stress.

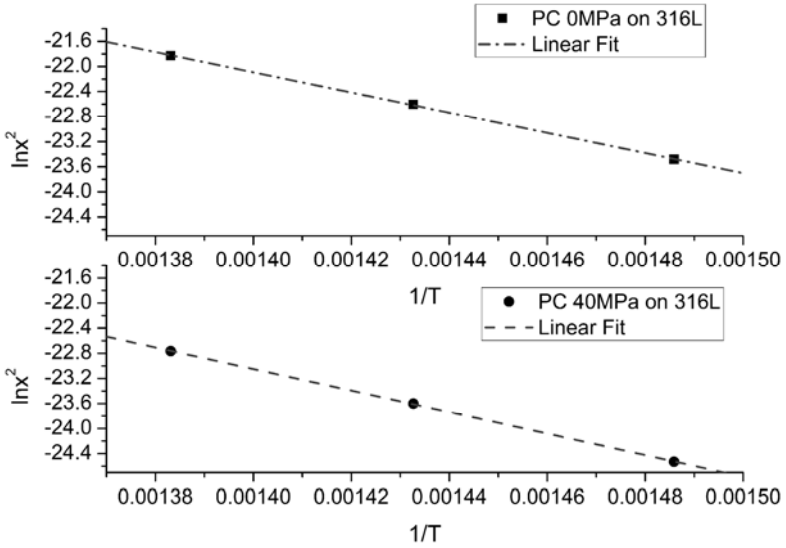

Figure 5.1-3 Experimental results and linear fitting of lnx^2 vs.1/T for 316L samples carburised at 400, 425, 450°C for 10 hours without stress and with 40 MPa tensile stress

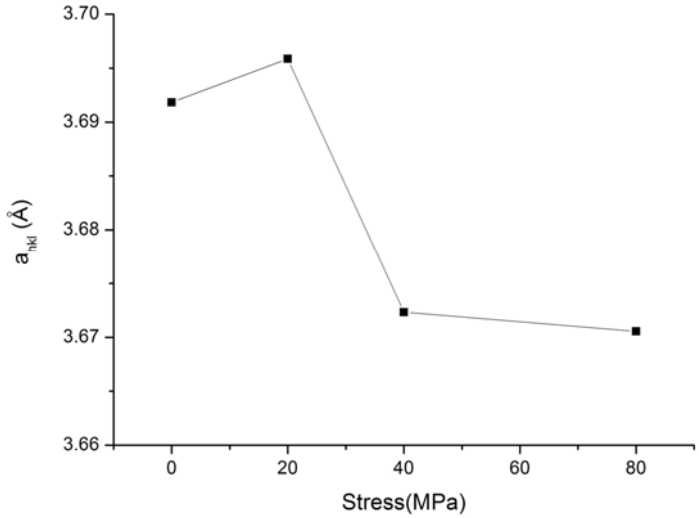

Figure 5.1-4 Lattice constants of S-phase obtained from (311) deflection of PC treated samples as a function of *in situ* tensile stresses.

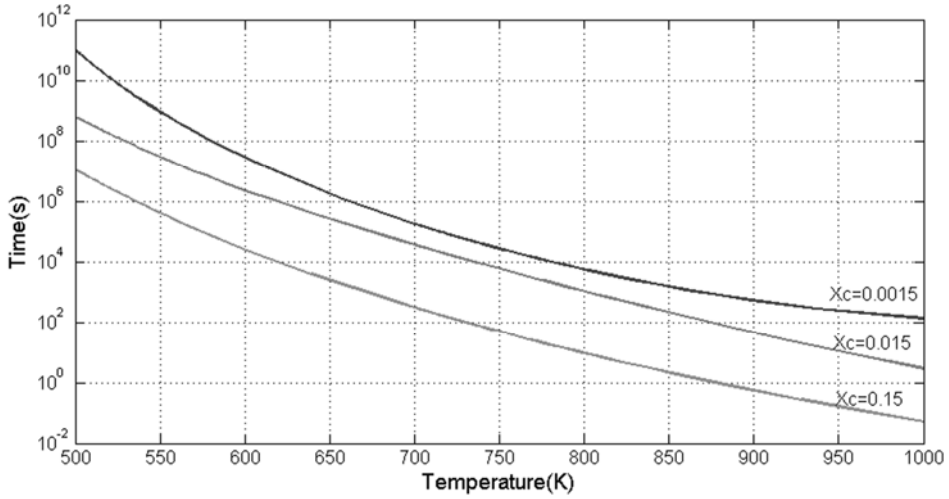

Figure 5.1-5 Incubation time of $Cr_{23}C_6$ precipitated from S-phase with different carbon concentrations (0.15, 1.5 and 15 at.%)

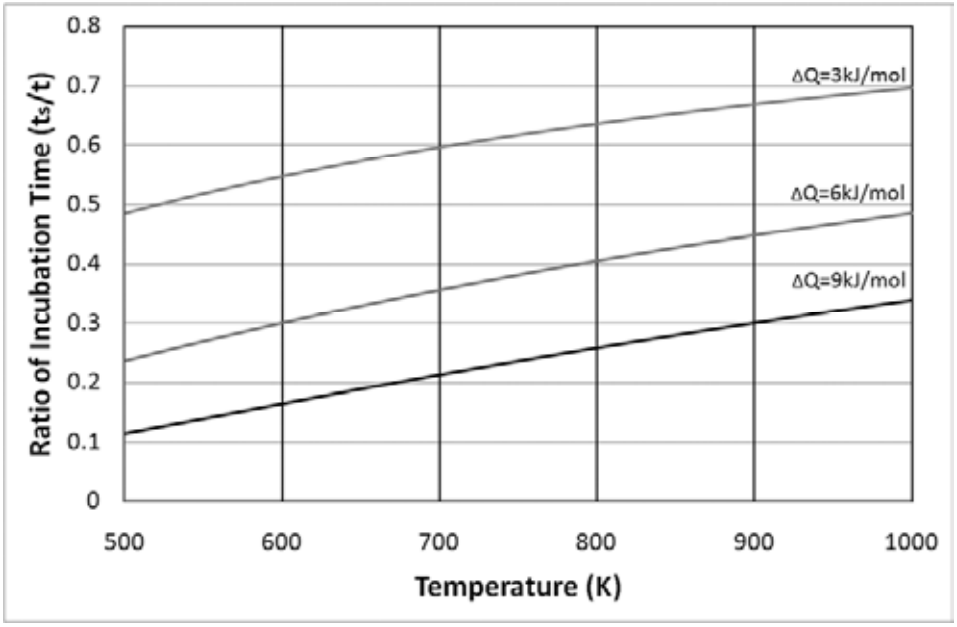

Figure 5.1-6 Ratio of incubation time at different temperatures as a function of the difference in the diffusion activation energy caused by *in situ* tensile stress.

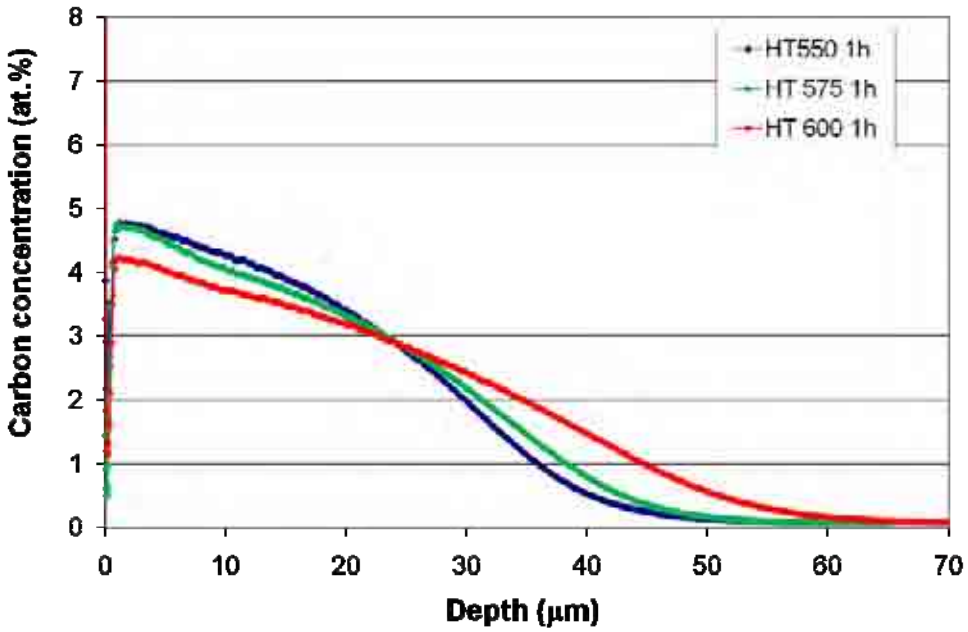

Figure 5.2-1 Carbon profiles of carburised samples after heat treatment s at 550°C, 575°C and 600°C for 1hour without stress

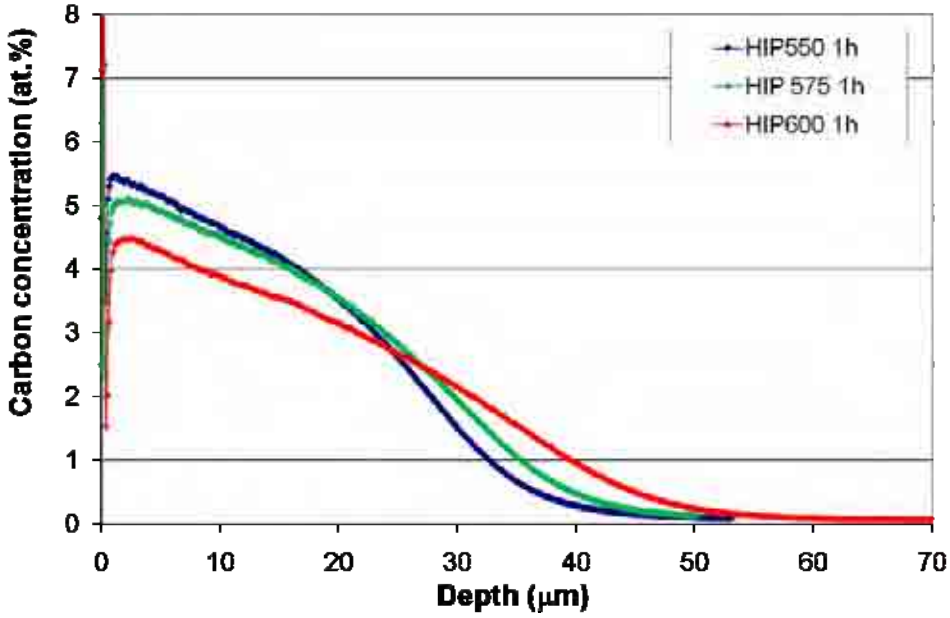

Figure 5.2-2 Carbon profiles of carburised samples after heat treatment at 550°C, 575°C and 600°C for 1hour under 180MPa isostatic compressive stress

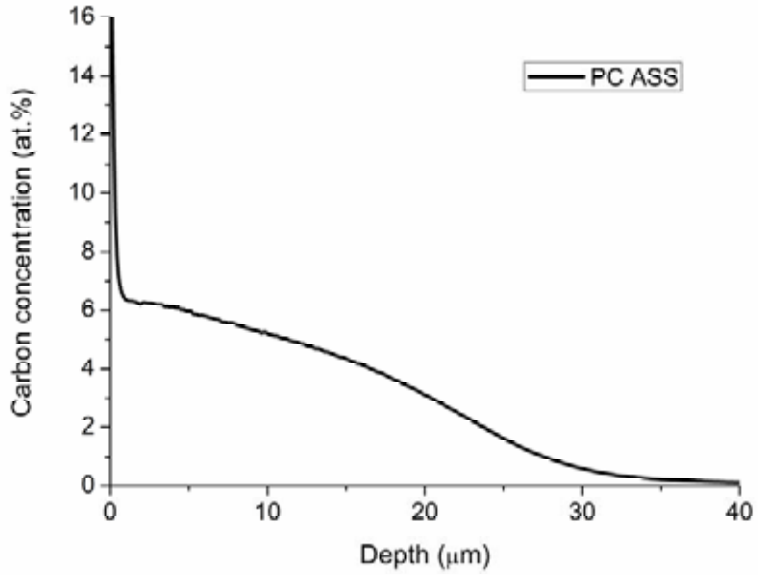

Figure 5.2-3 Carbon profile of Samples 'PC ASS' prior to HIPping and annealing treatments

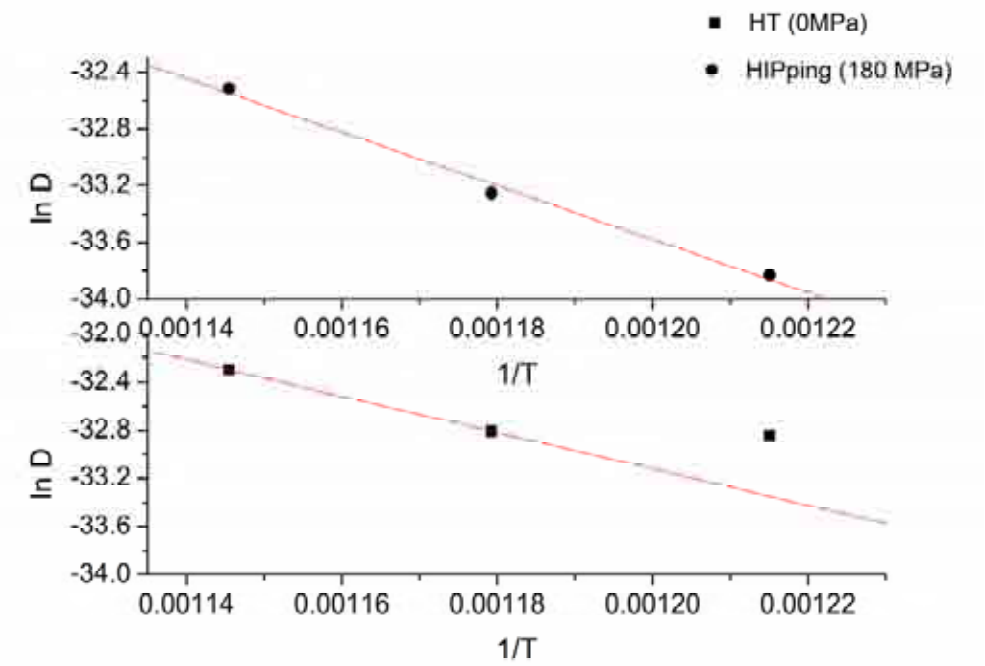

Figure 5.2-4 Linear relationship of ln D vs. 1/T calculated from Table 5.2-1.

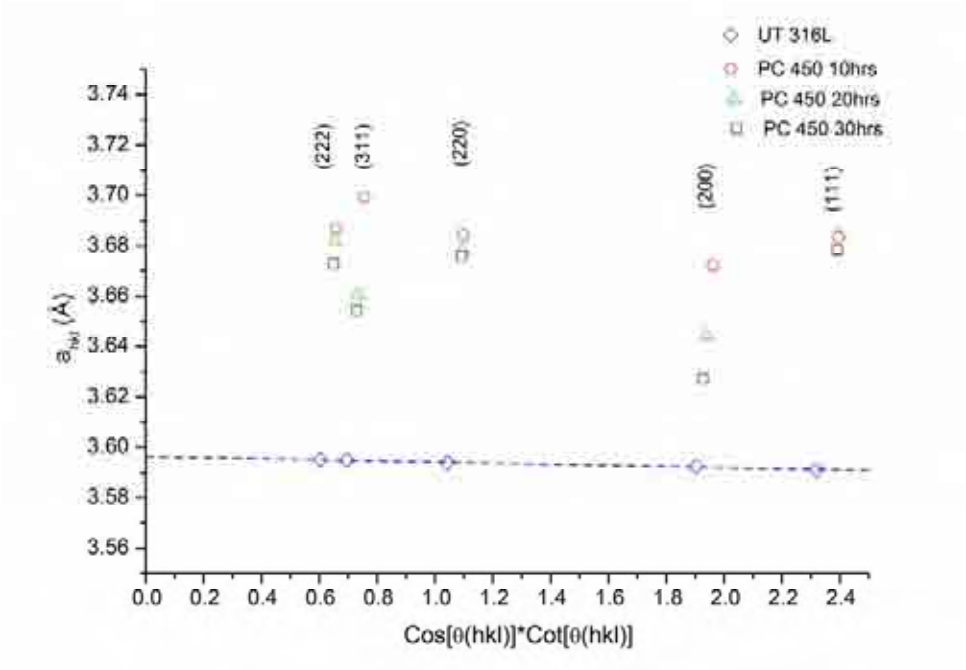

Figure 5.4-1 Nelson-Riley plots showing Influence of carburising time upon lattice expansion

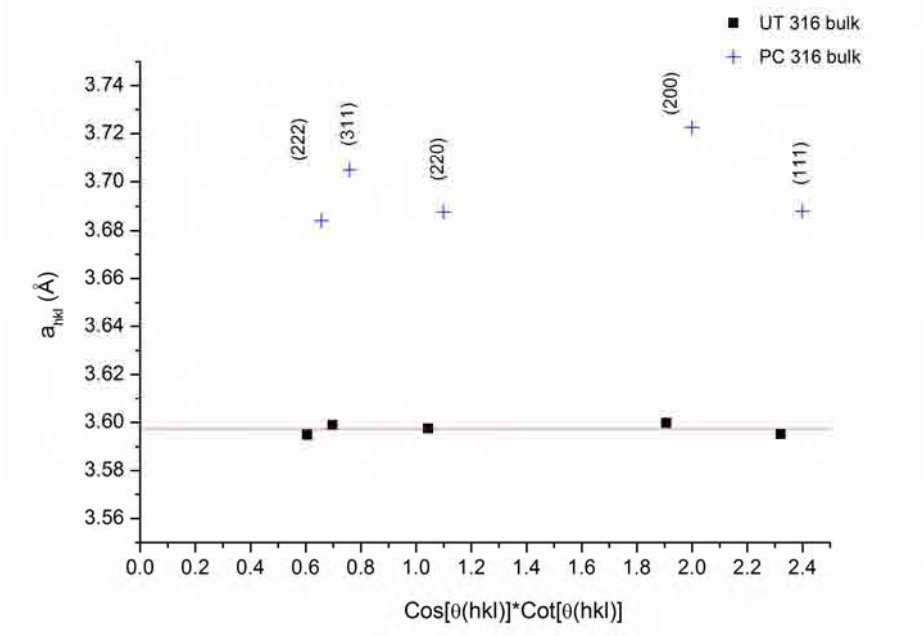

Figure 5.4-2 Nelson-Riley plots of untreated and carburising treatment on AISI316 bulk